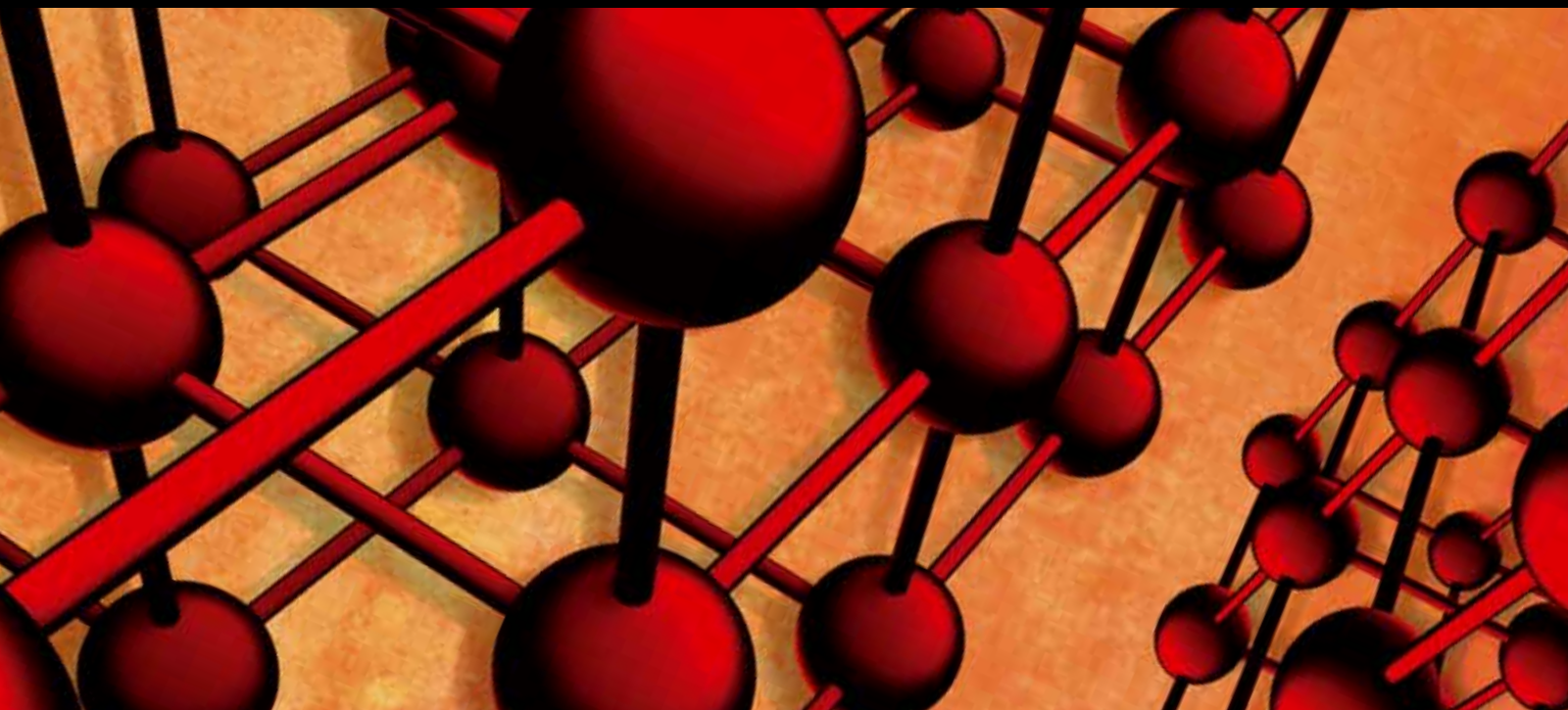


# Mechanical Properties and Nondestructive Testing of Advanced Materials

Guest Editors: Yan Yang, Xing Chen, and Young Soo Choi





---

# **Mechanical Properties and Nondestructive Testing of Advanced Materials**

Advances in Materials Science and Engineering

---

# **Mechanical Properties and Nondestructive Testing of Advanced Materials**

Guest Editors: Yan Yang, Xing Chen, and Young Soo Choi



---

Copyright © 2013 Hindawi Publishing Corporation. All rights reserved.

This is a special issue published in “Advances in Materials Science and Engineering.” All articles are open access articles distributed under the Creative Commons Attribution License, which permits unrestricted use, distribution, and reproduction in any medium, provided the original work is properly cited.

## Editorial Board

K. G. Anthymidis, Greece  
Robert S. Averbach, USA  
Amit Bandyopadhyay, USA  
Z. Barber, UK  
Yucel Birol, Turkey  
Susmita Bose, USA  
Steve Bull, UK  
Peter Chang, Canada  
Daolun Chen, Canada  
Manish U. Chhowalla, USA  
Martin Crimp, USA  
Jie Dai, Singapore  
C. K. Das, India  
J. Paulo Davim, Portugal  
Seshu Babu Desu, USA  
Yong Ding, USA  
Chunying Duan, China  
Nadia El-Masry, USA  
Sergi Gallego, Spain  
John W. Gillespie, USA  
Hiroki Habazaki, Japan  
Richard Hennig, USA  
Dachamir Hotza, Brazil  
Chun-Hway Hsueh, Taiwan  
Rui Huang, USA  
Shyh-Chin Huang, Taiwan  
Wei Huang, China  
Jacques Huot, Canada  
William A. Jesser, USA  
Jaehwan Kim, Korea  
S. Komarneni, USA  
Prashant Kumta, USA

Pavel Lejcek, Czech Republic  
Markku Leskela, Finland  
Bin Li, China  
Hai Lin, China  
Yuanhua Lin, China  
Zhimin Liu, China  
Meilin Liu, Georgia  
Tao Liu, China  
Jun Liu, China  
Ying Liu, USA  
Yuan Liu, China  
Gang Liu, China  
M. A. Loi, The Netherlands  
Hai Lu, China  
Peter Majewski, Australia  
A. S. H. Makhlof, Germany  
S. Miyazaki, Japan  
Paul Munroe, Australia  
Korukonda L. Murty, USA  
Ali Nazari, Iran  
Luigi Nicolais, Italy  
Tsutomu Ohzuku, Japan  
Xiaoqing Pan, USA  
Ganapathiraman Ramanath, USA  
Raju V. Ramanujan, Singapore  
Manijeh Razeghi, USA  
Mohd Sapuan Salit, Malaysia  
Chinnappa Sanjeeviraja, India  
Jainagesh A. Sekhar, USA  
Jiangbo Sha, China  
Liyuan Sheng, China  
You Song, China

Aloysius Soon, Korea  
Charles C. Sorrell, Australia  
Steven L. Suib, USA  
Sam-Shajing Sun, USA  
Wen-Hua Sun, China  
Weihua Tang, China  
Achim Trampert, Germany  
An-Pang Tsai, Japan  
Vladimir Tsukruk, USA  
Krystyn Van Vliet, USA  
Rui Vilar, Portugal  
Kunpeng Wang, China  
Min Wang, China  
Jörg M K Wiezorek, USA  
Wei Wu, USA  
Gongnan Xie, China  
Aiguo Xu, China  
Jianqiao Ye, UK  
Yadong Yin, USA  
Tao Zhang, China  
Bin Zhang, China  
Jun Zhang, China  
Ming-Xing Zhang, Australia  
Guan-Jun Zhang, China  
Rui Zhang, China  
Kai Zhang, China  
Yufeng Zhang, China  
Jian Zhang, Singapore  
Kai Zhang, China  
Jing Zhang, China

# Contents

**Mechanical Properties and Nondestructive Testing of Advanced Materials**, Yan Yang, Xing Chen, and Young Soo Choi  
Volume 2013, Article ID 589320, 2 pages

**Crack Detection in Single-Crystalline Silicon Wafer Using Laser Generated Lamb Wave**, Min-Kyoo Song and Kyung-Young Jhang  
Volume 2013, Article ID 950791, 6 pages

**Measurements of the Characteristics of Transparent Material Using Digital Holography**, Ding Yu, Shang Wenbin, Yang Hong, and Yang Yan  
Volume 2013, Article ID 598737, 7 pages

**Analysis and Testing of Chain Characteristics and Rheological Properties for Magnetorheological Fluid**, Song Chen, Jin Huang, Hongyu Shu, Tiger Sun, and Kailin Jian  
Volume 2013, Article ID 290691, 6 pages

**Evaluation of Ultrasonic Nonlinear Characteristics in Heat-Treated Aluminum Alloy (Al-Mg-Si-Cu)**, JongBeom Kim and Kyung-Young Jhang  
Volume 2013, Article ID 407846, 6 pages

**Deformation Properties and Fatigue of Bituminous Mixtures**, Frantisek Schlosser, Jan Mikolaj, Viera Zatkalikova, Juraj Sramek, Dominika Durekova, and Lubos Remek  
Volume 2013, Article ID 701764, 7 pages

**A Study on Contact Fatigue Performance of Nitrided and TiN Coated Gears**, Hongbin Xu, Hui Li, Jianjun Hu, and Song Wang  
Volume 2013, Article ID 580470, 7 pages

**Mechanical Performance Evaluation of Concrete Beams Strengthened with Carbon Fiber Materials**, Jun Ding, Xia Huang, Gang Zhu, Song Chen, and Guochao Wang  
Volume 2013, Article ID 572151, 9 pages


**Deposition of Low Stress Silicon Nitride Thin Film and Its Application in Surface Micromachining Device Structures**, Beirong Zheng, Chen Zhou, Quan Wang, Yifeng Chen, and Wei Xue  
Volume 2013, Article ID 835942, 4 pages

**Study of Alloying Process on 40Cr Surface with Electron Beam after Electroplated Cr Layer**, Xu Hongbin, Hu Jianjun, Li Hui, Mao Rongshan, Sun Fei, and Hou Tianfeng  
Volume 2013, Article ID 984231, 7 pages

**Scaling Analysis of the Tensile Strength of Bamboo Fibers Using Weibull Statistics**, Jiaying Shao, Fang Wang, Lu Li, and Junqian Zhang  
Volume 2013, Article ID 167823, 6 pages

**Vibration Analysis of Cylindrical Sandwich Aluminum Shell with Viscoelastic Damping Treatment**, Tai-Hong Cheng, Zhen-Zhe Li, and Yun-De Shen  
Volume 2013, Article ID 130438, 7 pages

**Characteristics Analysis and Testing of SMA Spring Actuator**, Jianzuo Ma, Haolei Huang, and Jin Huang  
Volume 2013, Article ID 823594, 7 pages



---

**Intelligent Detector of Internal Combustion Engine Cylinder Pressure and Sensitivity Temperature Coefficient Compensation**, Beirong Zheng, Chen Zhou, Xiaomin Pan, Quan Wang, and Wei Xue  
Volume 2013, Article ID 107582, 6 pages

**An Inverse Method to Reconstruct Complete Stiffness Information of Rubber Bushing**, Gang Lei, Qian Chen, Ying Liu, and Jingjing Jiang  
Volume 2013, Article ID 187636, 6 pages

**Analysis and Testing of MR Shear Transmission Driven by SMA Spring**, Jin Huang, Xu Chen, and Lirong Zhong  
Volume 2013, Article ID 307207, 6 pages

**Flexural Vibration Test of a Beam Elastically Restrained at One End: A New Approach for Young's Modulus Determination**, Rafael M. Digilov and Haim Abramovich  
Volume 2013, Article ID 329530, 6 pages

## Editorial

# Mechanical Properties and Nondestructive Testing of Advanced Materials

Yan Yang,<sup>1</sup> Xing Chen,<sup>2</sup> and Young Soo Choi<sup>3</sup>

<sup>1</sup> Key Laboratory of Manufacture and Test Techniques for Automobile Parts, Ministry of Education, Chongqing 400054, China

<sup>2</sup> Department of Electrical and Computer Engineering, University of British Columbia, Vancouver, Canada V6T 1Z4

<sup>3</sup> Department of Bioengineering, University of Washington, Seattle, WA 98195-5061, USA

Correspondence should be addressed to Yan Yang; yangyan@cqut.edu.cn

Received 15 December 2013; Accepted 15 December 2013

Copyright © 2013 Yan Yang et al. This is an open access article distributed under the Creative Commons Attribution License, which permits unrestricted use, distribution, and reproduction in any medium, provided the original work is properly cited.

Modern industry has been moving forward with unprecedented pace over past decades, while there is no doubt about the significant dedication by material science there. Of all the materials, advanced materials are becoming the driving source for extensive cutting-edge technologies, such as biomedical devices and wearable microelectronics. Generally speaking, the advanced material covers all the new materials, as well as existing materials but with modification for some specific applications, including ceramic materials, composites, metal alloys, and polymers.

Normally, any advanced materials should not be accepted by industry until their properties have been fully understood for the sake of reliability, especially for their mechanical properties that are of particular importance to engineering applications. With the advent of a huge number of new materials and continued evolution of other advanced materials, how to easily and quickly evaluate them remains challenging. Nondestructive testing presents the potential to be the solution for studying materials with both finance and time efficiency, which mainly relies on radiation, ultrasonic, and optical measurement methods.

This special issue thus focuses on mechanical properties and the nondestructive testing of advanced materials. Sixteen papers are invited herein to demonstrate the research on various advanced materials, such as shape memory alloy (SMA) and bamboo fibers. Many nondestructive testing methods and their implementation on advanced materials are introduced, including holography and laser-based lamb wave.

In the paper “*Crack detection in single-crystalline silicon wafer using laser generated lamb wave*,” a noncontact and reliable measurement that was based on laser generated lamb wave has been used to detect crack existence in the brittle silicon wafer. Two modes of lamb wave were generated and detected, yielding accurate measurements. In the paper “*Flexural vibration test of a beam elastically restrained at one end: a new approach for Young’s modulus determination*,” a new vibration beam technique for the fast determination of the Young’s modulus has been developed. The method is based on measuring the resonant frequency of flexural vibrations of a partially restrained rectangular beam. To validate this method, a number of industrial samples have been tested and the measured modulus was compared to the known values from the literature, showing good agreements. The work “*Measurements of the characteristics of transparent material using digital holography*” introduced a new method to optically measure characteristics of transparent materials by digital holography. The information of material surfaces was measured, and the characteristic was presented in 3D visualization with high fidelity which was validated by comparing it to the output from commercial counterpart. The paper “*Deposition of low stress silicon nitride thin film and its application in surface micromachining device structures*” talked about the work to deposit silicon nitride thin film with low stress and its application in surface micromachining.  $\text{SiH}_2\text{Cl}_2/\text{NH}_3$  gaseous ratio was adjusted to optimize the low stress recipe. The internal stress about 135 MPa has been detected.

In the research “*Evaluation of ultrasonic nonlinear characteristics in heat-treated aluminum alloy (Al-Mg-Si-Cu)*,” the ultrasonic nonlinear parameters in the heat-treated aluminum alloy (Al-Mg-Si-Cu) specimens have been measured. Its effectiveness to evaluate critical change in the elastic properties due to the thermal aging at high temperature was demonstrated. The paper “*A study on contact fatigue performance of nitrided and TiN coated gears*” discussed the effect of TiN coating on gear contact fatigue characteristics through contact fatigue experiment and gear rig test, which shows to be able to prolong the contact fatigue life of gears. In the study “*Characteristics analysis and testing of SMA spring actuator*,” authors have discussed the shape memory alloy spring working as actuator and studied its displacement versus temperature by both theoretical model and the experimental method. The theoretical results are basically consistent to the experimental data. The paper “*Analysis and testing of chain characteristics and rheological properties for magnetorheological fluid*” presented to use digital holographic microscopy to measure magnetorheological (MR) fluid in different volume fraction of particles and under different magnetic field strengths. The chain model of dipole interaction of MR fluid was established, and the relationship between the shear stress and magnetic induction with particle volume fraction was obtained.

J. Ding et al. in the work “*Mechanical performance evaluation of concrete beams strengthened with carbon fiber materials*” used both finite element analysis and experimental validation to study the effect of carbon fibers in the reinforced plates. The finding revealed a big mechanical performance enhancement compared to that without carbon fibers. The work “*Study of alloying process on 40Cr surface with electron beam after electroplated Cr layer*” studied the precoating of electroplated chromium layer for improving surface properties of 40Cr. Microcracks have been detected by some measurement means, which can be eliminated by orthogonal experimental optimum process though. J. Shao et al. in the paper “*Scaling analysis of the tensile strength of bamboo fibers using Weibull statistics*” worked on scaling analysis of the mechanical properties of bamboo fibers by Weibull statistics. This study verified that the use of Weibull parameters from specimen testing can predict the strength distributions of fibers of longer gauge lengths. In the paper “*Deformation properties and fatigue of bituminous mixtures*,” F. Schlosser et al. studied the deformation properties and fatigue of bituminous mixtures. Deformation properties can be used for empirical mixture design, and fatigue performance of asphalt mixtures in turn reflects the parameters of functional tests. Master curves express the properties of asphalt mixtures for various conditions and provide a time-efficient testing.

The work “*Analysis and testing of MR shear transmission driven by SMA spring*” described a novel transmission method of MR fluid in a cylindrical type that is driven by SMA spring. The transmit torque of MR fluid was controllable by the movement of coil-assembly with magnetic flux, which is actuated by SMA. By using this way, the transmission of mechanical torque can be controlled by temperature. In the paper “*Vibration analysis of cylindrical sandwich aluminum shell with viscoelastic damping treatment*,” the vibration

characteristics of a sandwiched cylindrical aluminum shell with viscoelastic damping treatment were investigated using layerwise theories. The cylindrical curved structure has been employed in many engineering applications, such as aircrafts, automobiles, ships, and other industrial machines. The results herein suggest that the sandwiched viscoelastic damping layer can effectively suppress vibration of cylindrical aluminum structure. Explosion pressure and compression pressure of internal combustion engine cylinder are two significant technical parameters affecting the total performance. By relying on microelectromechanical system (MEMS) technology, an intelligent pressure sensor with temperature coefficient compensation was demonstrated in the paper “*Intelligent detector of internal combustion engine cylinder pressure and sensitivity temperature coefficient compensation*.” This technology exhibits the great practical value on internal combustion engine to test cylinder pressure, and the potential for volume manufacturing. The last paper in this special issue “*An inverse method to reconstruct complete stiffness information of rubber bushing*” discussed an inverse finite element method for parameters identification of rubber busing.

In summary, this special issue presents a broad range of topics relating to mechanical properties and the nondestructive testing of advanced materials. Valuable theoretical models and experimental testing methods have been introduced and discussed. Mechanical properties of different advanced materials have been studied, which suggests the promising features of them for wide applications.

Yan Yang  
Xing Chen  
Young Soo Choi

## Research Article

# Crack Detection in Single-Crystalline Silicon Wafer Using Laser Generated Lamb Wave

Min-Kyoo Song<sup>1</sup> and Kyung-Young Jhang<sup>2</sup>

<sup>1</sup> Graduate School of Mechanical Engineering, Hanyang University, Seoul 133-791, Republic of Korea

<sup>2</sup> School of Mechanical Engineering, Hanyang University, Seoul 133-791, Republic of Korea

Correspondence should be addressed to Kyung-Young Jhang; [kyjhang@hanyang.ac.kr](mailto:kyjhang@hanyang.ac.kr)

Received 19 July 2013; Revised 16 November 2013; Accepted 18 November 2013

Academic Editor: Yan Yang

Copyright © 2013 M.-K. Song and K.-Y. Jhang. This is an open access article distributed under the Creative Commons Attribution License, which permits unrestricted use, distribution, and reproduction in any medium, provided the original work is properly cited.

In the semiconductor industry, with increasing requirements for high performance, high capacity, high reliability, and compact components, the crack has been one of the most critical issues in accordance with the growing requirement of the wafer-thinning in recent years. Previous researchers presented the crack detection on the silicon wafers with the air-coupled ultrasonic method successfully. However, the high impedance mismatching will be the problem in the industrial field. In this paper, in order to detect the crack, we propose a laser generated Lamb wave method which is not only noncontact, but also reliable for the measurement. The laser-ultrasonic generator and the laser-interferometer are used as a transmitter and a receiver, respectively. We firstly verified the identification of S0 and A0 lamb wave modes and then conducted the crack detection under the thermoelastic regime. The experimental results showed that S0 and A0 modes of lamb wave were clearly generated and detected, and in the case of the crack detection, the estimated crack size by 6 dB drop method was almost equal to the actual crack size. So, the proposed method is expected to make it possible to detect the crack in the silicon wafer in the industrial fields.

## 1. Introduction

Semiconductors have been applied to many fields including smart TVs, smart phones, smart PCs, automobiles, home appliances, and laptop computers. These fields have demanded that the semiconductor should be of high performance, high capacity, high reliability, small components, and low cost. Because of these demands, semiconductor fabrication processes have focused on the lithography for a nanometer-scaled line width. And especially, semiconductor packaging processes have focused on a few trends in recent years: multistacking components and thinner wafers [1–3]. The multistacking component implies that more chips have to be stacked up within the same size component for the high capacity, and the thinner wafer indicates that wafer thickness has to be very thin up to 30  $\mu\text{m}$  for the multistacking component. Moreover, an attempt to change from 12 inch-wafers to 18 inch-wafers is recently going on, since larger wafers which are able to put more chips have impact on the yield improvement. Because of these trends

that wafers are getting thinner and larger, silicon wafers are vulnerable to cracks during manufacturing. The cracks can also lead to the yield drop and reliability failure. Therefore, one of the most critical issues in the semiconductor packaging process is the crack. So, the online crack detection in silicon wafers is becoming more important than ever before and its importance cannot be stressed enough.

Previous articles about the online crack detection which deals with poly-crystalline silicon wafers commonly used in the solar cell industry are largely classified into two groups. One is the contact method by resonance ultrasonic vibrations and impact tests [4, 5]. The other is the noncontact method by an air-coupled ultrasonic lamb wave [6]. Resonance ultrasonic vibrations method can accurately detect the millimeter-length cracks and the impact testing method can also analyze defective wafers. But both of them are driven by external forces which are not adequate for thin silicon wafers under 100  $\mu\text{m}$  thickness used generally. Air-coupled ultrasonic lamb wave method demonstrates the crack detection successfully and lamb wave is suitable for the thin silicon wafer. However,

this method has the problem of high impedance mismatches which cause dissipation of most incident energies from the surface of materials. This is also not satisfied for very noisy environment caused from facilities or manufacturing machines.

For many years, laser-ultrasonic technology has been increasingly used for nondestructive crack detections [7–10]. The biggest advantage of this technology is noncontact without regard to external forces and surface conditions of materials. This technology has another advantage that can reduce the energy loss by adjusting the shape of the laser beam for the energy enhancement. Although laser-ultrasonic technology has these advantages, few studies have performed for the crack detection in silicon wafers. Therefore, we propose the laser generated lamb wave method, which not only is noncontact but also guarantees the reliable measurement. And this paper deals with single crystalline silicon wafers commonly used in the semiconductor industry other than previous papers which deal with poly-crystalline silicon wafers.

Laser-ultrasonic technology has two main regimes. One is thermoelastic regime and the other is ablation regime [11]. In the case of thermoelastic regime, the ultrasonic waves are generated from thermoelastic expansions of materials. Meanwhile, in the case of ablation regime, the ultrasonic waves are generated from the material removal. If the ablation regime is applied to silicon wafers, they will be damaged. So, thermoelastic regime has to be applied to silicon wafers in terms of the reliability. And also there are two possible generation mechanisms; thermal effect and electrostriction. However, the thermal effect is dominant at the high power input while the electrostriction is dominant at the low power input [12]. In our case, the input power was in the range of high power input, so that we did not consider the electrostriction effect.

If the thermoelastic regime is applied to a silicon wafer that has the comparable thickness to wavelength, lamb wave is generated. We are expected to detect the cracks in silicon wafers through analysis of this lamb wave.

## 2. Dispersion Curves of Lamb Wave in Silicon Wafer

Lamb wave is dispersive, which implies that the wave velocity is dependent on the frequency. So dispersion curves need to be analyzed first. The wave velocities in single-crystalline silicon wafers are listed in Table 1. The silicon wafer has three kinds of different velocities depending on the orientations [13]. But, since wafers have the characteristics that cracks are easily initiated and cleft in the (110) orientation, it is reasonable to consider only the (110) orientation in terms of easier experiments. Figure 1 shows dispersion curves of group velocity which are plotted from velocities at the (110) orientation in the silicon wafer whose thickness is 525  $\mu\text{m}$ . The curves in the dotted box area are mostly used for the practical applications, because other areas are more complicated. So the curves in this box area are supposed to be used for our experiments as well.

TABLE 1: Wave velocities in single-crystalline silicon wafer.

Orientation	Longitudinal wave velocity	Shear wave velocity
(100)	8436 (m/s)	5847 (m/s)
(110)	9138 (m/s)	4675 (m/s)
(111)	9360 (m/s)	5096 (m/s)

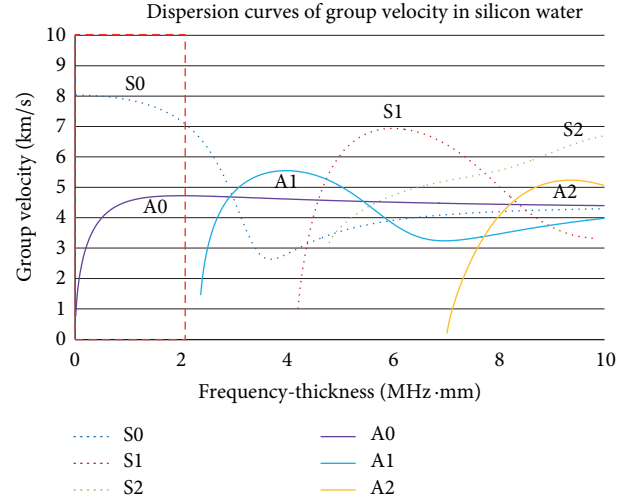


FIGURE 1: Dispersion curves of group velocity in silicon wafers whose thickness is 525  $\mu\text{m}$ .

## 3. Simulation

The thermoelastic mechanism is described by a few equations. First, the laser energy that has Gaussian spatial and temporal distributions is quickly absorbed in the wafer as shown in Figure 2. This process can be expressed as

$$Q = 2 \frac{E(1-R)}{S\tau} \exp\left(-2\frac{x^2}{r^2}\right) \exp\left(2.7726\frac{(t-2\tau^2)}{\tau^2}\right), \quad (1)$$

where  $Q$  means the heat source;  $E$  is the initial laser energy;  $R$  is the reflectivity;  $S$  is the surface area on which the laser is absorbed;  $\tau$  is the pulse duration;  $r$  indicates a distance that laser density is 1/2 times from the center;  $x$  is the spatial coordinates;  $t$  means time.

And then, the absorbed energy makes the temperature of the wafer increase sharply. The thermal conduction is caused by this large temperature gradient. This thermal conduction equation can be described as

$$\rho C_p \frac{\partial T}{\partial t} + \rho C_p u \nabla T = \nabla (k \nabla T) + Q, \quad (2)$$

where  $\rho$ ,  $C_p$ , and  $T$  are density, heat capacity, and temperature, respectively;  $u$  means the displacement;  $Q$  is the heat generated from the heat source.

TABLE 2: Properties of the wafer.

Properties	Value						Unit
Reflectivity	0.32						
Density	2330						kg/m <sup>3</sup>
Coefficient of thermal expansion	$2.6 \times 10^{-6}$						1/K
Thermal conductivity	130						W/(m·K)
Heat capacity at constant pressure	700						J/(kg·K)
Elasticity matrix	166	64	64	0	0	0	GPa
	64	166	64	0	0	0	
	64	64	166	0	0	0	
	0	0	0	80	0	0	
	0	0	0	0	80	0	
	0	0	0	0	0	80	

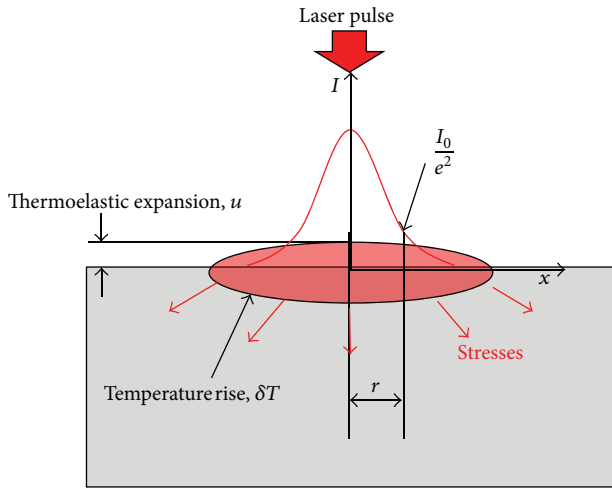


FIGURE 2: Schematic of thermoelastic mechanism.

At last, thermoelastic expansion is caused by the large temperature gradient. Thermoelastic stresses are finally generated and thermoelastic wave is rapidly propagated. This equation of motion can be represented as

$$(\lambda + 2\mu) \nabla (\nabla \cdot u) - \mu \nabla \times \nabla \times u - \alpha (3\lambda + 2\mu) \nabla T = \rho \frac{\partial^2 u}{\partial t^2}, \quad (3)$$

where  $\lambda$  and  $\mu$  are Lamé constants;  $\alpha$  is coefficient of thermal expansion.

All of these equations were applied to the simulation with COMSOL multiphysics 4.3. The incident laser density and the pulse duration were adopted as  $1.00 \times 10^{12} \text{ W/m}^2$  and 5 ns. And we considered the line beam as the elliptical beam which has 11.5 mm major axis and 0.5 mm minor axis, as shown in the next experiment section. Other properties used in the simulation are listed in Table 2. The geometrical dimensions of this simulation were modeled as shown in Figure 3: the diameter of the wafer, 4 inches and the thickness of the wafer, 525  $\mu\text{m}$ . The outside boundaries were considered as thermal insulations. And the mesh size was determined as 0.1 mm

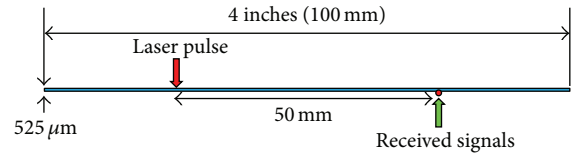


FIGURE 3: Geometrical dimensions of simulation model.

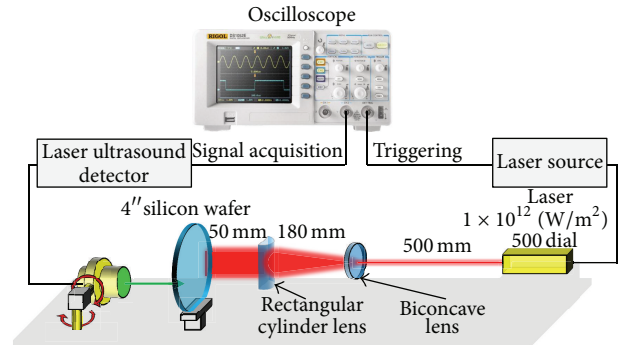


FIGURE 4: Experimental setup.

which is less than a 10th of the A0 mode wavelength and is small enough to get reasonable calculation accuracy [14]. Lamb wave was obtained at a distance of 50 mm from the laser source in this simulation.

#### 4. Experimental Procedures and Setup

We conducted two experiments that are mode identification and crack detection. Firstly, lamb wave modes were identified in the wafer without any crack, as comparing the experiment and the simulation. Secondly, the modes which were identified in the first experiment were used for the crack detection experiment in the wafer with an artificial crack.

Figure 4 illustrates the experimental setup. The materials we used for two experiments are (100) single-crystalline silicon wafers that are manufactured by ShinEtsu Chemical

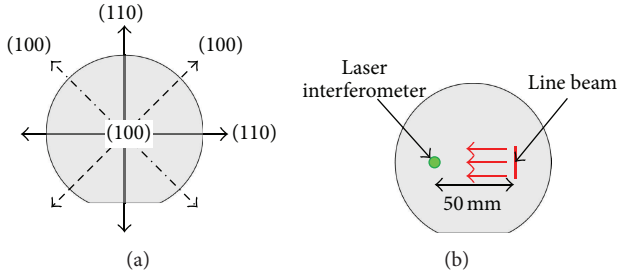


FIGURE 5: (a) Orientation in a (100) wafer and (b) the setup of the laser source and the laser interferometer.

Co., Ltd. The diameter and thickness of the wafers are 4 inches and  $525\ \mu\text{m}$ , respectively, which are the same in the previous simulation section. The pulsed laser made by Spectron Laser Systems was used as a transmitter. Its fundamental wavelength, beam diameter, pulse duration, and the repetition rate are  $1064\ \text{nm}$ ,  $4\ \text{mm}$ ,  $5\ \text{ns}$ , and  $1\ \text{Hz}$ , respectively. The laser interferometer made by TECNAR was used as a receiver. Its operating principle is described by two-wave mixing. This equipment detects out-of-plane displacement and the frequency bandwidth for the detection of lamb wave has upper limit,  $2\ \text{MHz}$ . An oscilloscope was used for triggering and signal acquisition.

Two lenses, which are able to transform the laser beam into a line beam, were used to make it clear to generate lamb wave: a biconcave lens and a rectangular cylinder lens. The biconcave lens was placed at a distance of  $500\ \text{mm}$  from the laser and then the distance between the biconcave lens and the rectangular cylinder lens was set to  $180\ \text{mm}$ , in order to make a beam diameter of  $23\ \text{mm}$ . The silicon wafer was located where the laser beam became a line beam whose width was  $1\ \text{mm}$  and length was  $23\ \text{mm}$ . Its distance was  $50\ \text{mm}$  from the rectangular cylinder lens. The laser intensity of the line beam was  $1.00 \times 10^{12}\ \text{W/m}^2$ , which is within the thermoelastic regime and less than the ablation threshold. The laser interferometer was installed behind the wafer due to the interference with other equipment. The oscilloscope was linked both to the laser source for the triggering and to the laser interferometer for the signal acquisition.

## 5. Mode Identification

The experimental setup for the mode identification was the same as in Figure 4. In addition, the orientation of the wafer was taken into account, because we supposed to only consider the (110) orientation where cracks are easily generated. Figure 5(a) illustrates the orientations in a (100) wafer. The line beam as a laser source was aligned perpendicular to the flat zone of the wafer, in order to generate lamb wave in the direction, (110), as shown in Figure 5(b) which describes the setup of the laser source and the laser interferometer.

In the case of the experimental result, the triggering signal is occupied by around  $4\ \mu\text{s}$  as shown in Figure 6(a). We can also see that S0 mode and A0 mode are clearly generated and received. S0 mode is received in  $6.24\ \mu\text{s}$  and A0 mode is measured from  $8.5\ \mu\text{s}$  to  $18\ \mu\text{s}$ .

In the case of the simulation result, S0 mode and A0 mode are also obviously generated and received. S0 mode is obtained in  $6.6\ \mu\text{s}$  and A0 mode is followed for the time which is similar to the experimental result, as shown in Figure 6(b).

As comparing the experiment with the simulation, the arrival times of S0 mode are almost the same. Likewise, the arrival times of A0 mode are also the same. In terms of the velocity, S0 mode is faster than A0 mode. In terms of the amplitude, however, it can be seen from both results that the amplitude of A0 mode is much larger than that of S0 mode. This is because A0 mode is dominant for out-of-plane on the surface of the wafer; on the other hand, S0 mode is dominant for in-plane on the surface of the wafer. Note that the equipment used for the receiver detects only the out-of-plane displacement. As a result of plotting the STFT result overlapped with the group velocity, A0 mode strongly appears around  $500\ \text{kHz}$  as shown in Figure 7. It implies that A0 mode is helpful for the crack detection.

However, considering that the nondispersive wave is preferable for the easier interpretation of wave signal, the higher frequency band of  $2\sim 4\ \text{MHz}$  looks better as we can see from the dispersion curve of A0 mode shown in Figure 7. But, in our experimental setup, the upper frequency limit of lamb wave detector was  $2\ \text{MHz}$  and the line beam width  $1\ \text{mm}$  was the least width for the safe generation in the thermoelastic regime. Thus, we did not have much flexibility to choose the frequency band.

In order to use the higher frequency lamb wave for the inspection, both sides of generation and detection should be considered. In the generation side, a simple way is the reduction of the line beam width. But, in this case, there exists a limit in the input laser power to keep the laser intensity of line beam within the thermoelastic range. In the detection side, the frequency bandwidth and the sensitivity should be considered. The frequency bandwidth of lamb wave detector is dependent on the beam spot size of detection laser. The smaller spot size can detect the higher frequency (or the shorter wavelength) lamb wave. Also, if we reduce the generation laser power to make the line beam width smaller within the thermoelastic regime, then the generated wave amplitude will be decreased. In this case, the higher sensitivity of detector may be required.

## 6. Crack Detection

A0 mode was used for the crack detection because of the large amplitude, as was mentioned in the former section. The experimental setup was nothing different from the setup for the mode identification. But, it is the difference that the reflection method was used by scanning the wafer that has the crack artificially made with a diamond cutter, as shown in Figure 8. The crack length, width, and depth are  $5\ \text{mm}$ ,  $0.5\ \text{mm}$ , and  $0.1\ \text{mm}$ , respectively.

We analyzed what kinds of modes are generated in the center of the crack prior to the crack detection experiment. The crack, the laser interferometer, and the line beam were positioned as shown in Figure 9(a). And then a variety of modes were received as shown in Figure 9(b). S0 mode arrives the earliest at  $2.5\ \mu\text{s}$ , but this is buried in the triggering

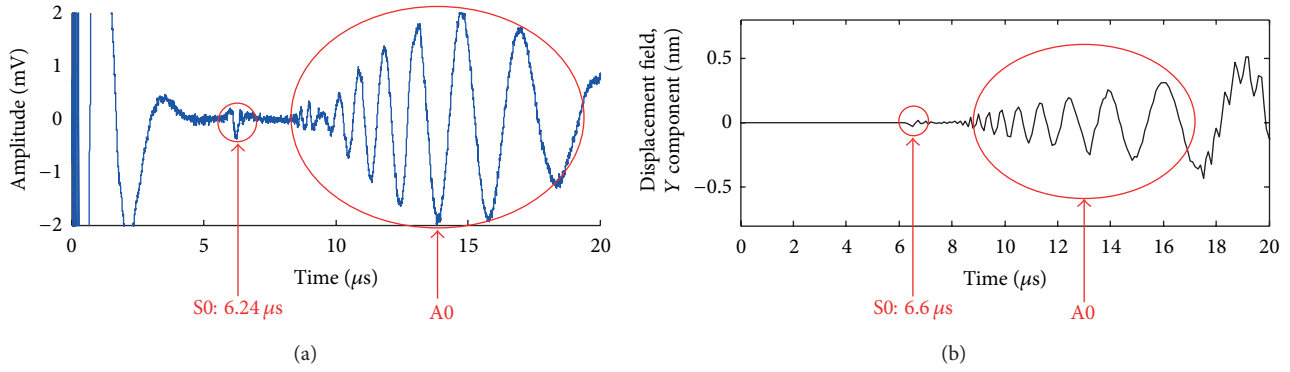


FIGURE 6: (a) Experimental result and (b) simulation result for mode identification.

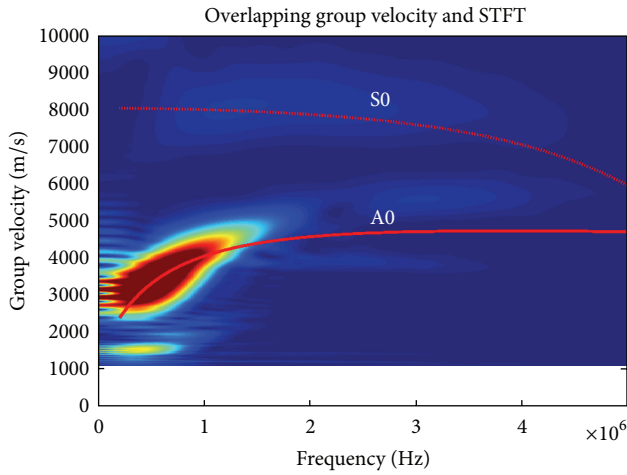


FIGURE 7: STFT result overlapped with group velocity.

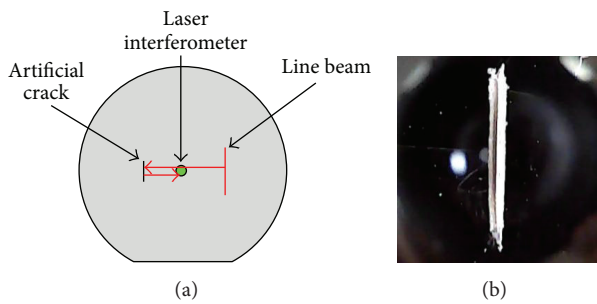


FIGURE 8: (a) Reflection method schematic and (b) artificial crack.

signal. Since S0 mode has very tiny amplitude, it will not be considered any more. And A0 mode arrives then at 6.07  $\mu\text{s}$ . Some part of A0 mode is also buried in the triggering signal. Next, A0 mode reflected from the crack is detected at 15.17  $\mu\text{s}$ . This is what we are looking for in this experiment. And then, the complicated signals are followed. So the reflected A0 mode from the crack is analyzed for the crack detection and its signal is in the range from 12 to 18  $\mu\text{s}$ .

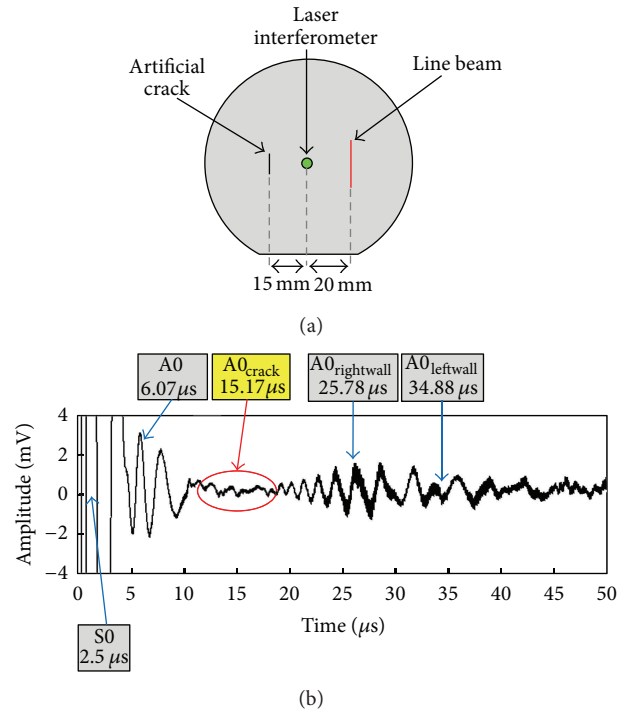


FIGURE 9: (a) Experimental setup and (b) received signals.

The crack was scanned with every 0.5 mm and the scan length was 10 mm as shown in Figure 10(a). So every datum corresponding to each A0 mode reflected from the crack was extracted and plotted based on the maximum amplitude in the range from 12 to 18  $\mu\text{s}$ . And then the 6 dB drop method is applied to decide the defect size, which has been widely used for the defect sizing based on the ultrasonic scan [15, 16]. Figure 10(b) shows the experimental result that the estimated crack length by 6 dB drop method is about 4.8 mm. In comparison with the actual crack length, 5 mm, we come to conclusion that the width more than 50% of the maximum signal level can be considered as an actual crack length. Therefore, the proposed method is expected to make it possible for the online crack detection in the silicon wafer.

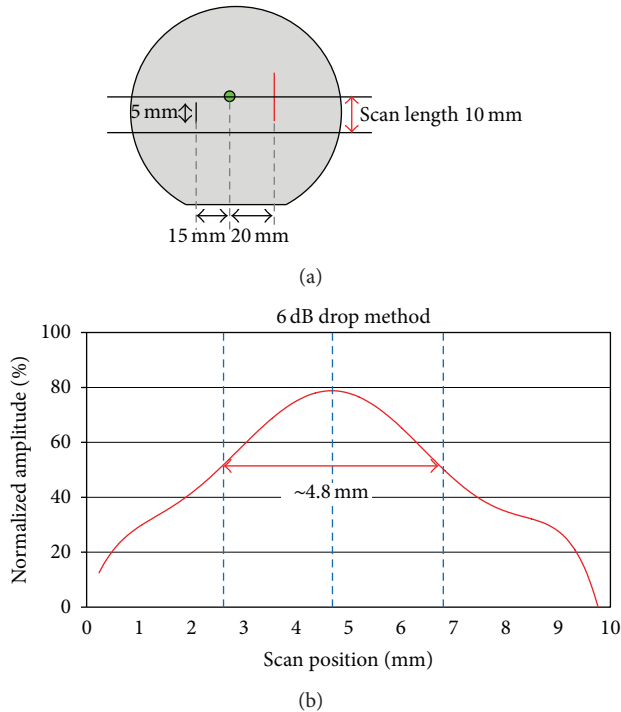


FIGURE 10: (a) Scan length and (b) experimental result by 6 dB drop method.

## 7. Conclusions

This paper proposed the laser generated Lamb wave which not only is noncontact method, but also guarantees the reliable measurement, in order to detect the crack in the single-crystalline silicon wafer. We verified the identification of S0 and A0 lamb wave modes and then conducted crack detection under the thermoelastic regime. At first, mode identification was carried out, as comparing the experiment with the simulation. The experimental result showed a good agreement with the simulation result. In particular, we could see that the amplitude of A0 mode is remarkably larger than that of S0 mode. This is because A0 mode is dominant for out-of-plane; on the other hand, S0 mode is dominant for in-plane. So A0 mode was used for the crack detection. It can be seen that the actual crack size was nearly identical to the estimated crack size by 6 dB drop method, as the crack was scanned. Finally, we concluded that laser generated lamb wave we proposed can be used for the crack detection in silicon wafer.

Although this paper deals with a single-crystalline silicon wafer as the beginning of the crack detection, our future work will deal with an individual chip separated from a thinner wafer by a saw machine.

## Acknowledgment

This work was financially supported by the National Research Foundation of Korea (NRF) as a grant funded by the Korean government (NRF-2013M2A2A9043241).

## References

- [1] E.-K. Kim, "Assessment of ultra-thin Si wafer thickness in 3D wafer stacking," *Microelectronics Reliability*, vol. 50, no. 2, pp. 195–198, 2010.
- [2] C.-C. A. Chen and L.-S. Hsu, "A process model of wafer thinning by diamond grinding," *Journal of Materials Processing Technology*, vol. 201, no. 1-3, pp. 606–611, 2008.
- [3] Y. S. Kim, N. Maeda, H. Kitada et al., "Advanced wafer thinning technology and feasibility test for 3D integration," *Microelectronic Engineering*, vol. 107, pp. 65–71, 2013.
- [4] W. Dallas, O. Polupan, and S. Ostapenko, "Resonance ultrasonic vibrations for crack detection in photovoltaic silicon wafers," *Measurement Science and Technology*, vol. 18, no. 3, article 038, pp. 852–858, 2007.
- [5] C. Hilmersson, D. P. Hess, W. Dallas, and S. Ostapenko, "Crack detection in single-crystalline silicon wafers using impact testing," *Applied Acoustics*, vol. 69, no. 8, pp. 755–760, 2008.
- [6] S. K. Chakrapani, M. J. Padiyar, and K. Balasubramaniam, "Crack detection in full size Cz-silicon wafers using lamb wave air coupled ultrasonic testing (LAC-UT)," *Journal of Nondestructive Evaluation*, vol. 31, pp. 46–55, 2012.
- [7] C. Ni, Y. Shi, Z. Shen, J. Lu, and X. Ni, "An analysis of angled surface-breaking crack detection by dual-laser source generated ultrasound," *NDT and E International*, vol. 43, no. 6, pp. 470–475, 2010.
- [8] S. Dixon, S. E. Burrows, B. Dutton, and Y. Fan, "Detection of cracks in metal sheets using pulsed laser generated ultrasound and EMAT detection," *Ultrasonics*, vol. 51, no. 1, pp. 7–16, 2011.
- [9] C. Ni, L. Dong, Z. Shen, and J. Lu, "The experimental study of fatigue crack detection using scanning laser point source technique," *Optics and Laser Technology*, vol. 43, no. 8, pp. 1391–1397, 2011.
- [10] S. J. Davies, C. Edwards, G. S. Taylor, and S. B. Palmer, "Laser-generated ultrasound: its properties, mechanisms and multifarious applications," *Journal of Physics D*, vol. 26, no. 3, pp. 329–348, 1993.
- [11] C. B. Scruby and L. E. Drain, *Laser Ultrasonics: Techniques and Applications*, Adam Hilger, Bristol, UK, 1990.
- [12] H. J. Shin, S. W. Noh, J. H. Lee, and J. S. Jang, "Pulsed laser induced photoacoustic effect in silicon, mainly caused by thermal expansion and electrostriction, is studied," *Journal of the Institute of Electronics Engineers of Korea*, vol. 3, pp. 42–44, 1988.
- [13] J. J. Wortman and R. A. Evans, "Young's modulus, shear modulus, and poisson's ratio in silicon and germanium," *Journal of Applied Physics*, vol. 36, no. 1, pp. 153–156, 1965.
- [14] H.-X. Sun, S.-Y. Zhang, and B.-Q. Xu, "Influence of viscoelastic property on laser-generated surface acoustic waves in coating-substrate systems," *Journal of Applied Physics*, vol. 109, no. 7, Article ID 073107, 2011.
- [15] J. Blitz and G. Simpson, *Ultrasonic Methods of Non-Destructive Testing*, Chapman and Hall, London, UK, 1996.
- [16] P. Ciorau, "Comparison between -6 dB and -12 dB amplitude drop techniques for length sizing," Ontario Power Generation, no. 11, 2011, <http://www.ndt.net/>.

## Research Article

# Measurements of the Characteristics of Transparent Material Using Digital Holography

Ding Yu,<sup>1</sup> Shang Wenbin,<sup>2</sup> Yang Hong,<sup>3</sup> and Yang Yan<sup>2</sup>

<sup>1</sup> Chongqing City Management College, Shapingba District, Chongqing 401331, China

<sup>2</sup> Mechanical Engineering, Chongqing University of Technology, No. 69 Hongguang Road, Banan District, Chongqing 400054, China

<sup>3</sup> Key Laboratory of Advanced Manufacturing Technology for Automobile Parts, Ministry of Education, No. 69 Hongguang Road, Banan District, Chongqing 400054, China

Correspondence should be addressed to Yang Yan; 40129784@qq.com

Received 31 July 2013; Revised 28 September 2013; Accepted 28 September 2013

Academic Editor: Xing Chen

Copyright © 2013 Ding Yu et al. This is an open access article distributed under the Creative Commons Attribution License, which permits unrestricted use, distribution, and reproduction in any medium, provided the original work is properly cited.

Digital holography is applied to measure the characteristics of transparent material. A digital hologram recording system to measure the surface of transparent material was established, and the digital holograms of transparent object were obtained in high quality. For postprocessing of hologram, the least-squares phase unwrapping algorithm was used in phase unwrapping, and the phase reconstruction image of transparent object was obtained. The information of material surfaces was measured and the characteristic was presented in 3D visualization. The validation experiment was conducted by NanoMap 500LS system; the results of validation experiment are well satisfied with the measurement by digital holography, which proved the feasibility of digital holographic technology as a good measurement tool for transparent material.

## 1. Introduction

In 1948, Gabor [1, 2] proposed holography, which can be used for reconstructing amplitude and phase of wave field. With the fast development of computer technology, recording and reconstruction are made possible by means of computer. Subsequently, Goodman and Lawrence [3] developed digital holography in 1960s.

Digital holography is a new image processing technology that uses a high-resolution charge-coupled device (CCD) camera for hologram recording and image reconstruction with a numerical method by a computer [4]. Compared with traditional holography, which uses a photographic plates as recording media, digital holography has a significant improvement; that is to say, it does not need complicated chemical processing [5], thus, adding more flexibility and improving the efficiency of the holographic process. In the past few years, with modern computer technology and CCD technology developing rapidly, digital holography has been established as an important scientific means applied in

metrology [6], surface measurement, deformation measurement [7], and more recently biological microscopy [8–10].

In general, the objects in applications of digital holography are not transparent, so the holograms were captured by the reflection of the object [11–13]. In this paper, we adopt the method of transmission to generate the hologram.

Noncontact surface measurement techniques are very important in many fields, such as science and engineering. It is very helpful to control the products quality and make the appropriate diagnosis. Digital holographic imaging as a new image processing technology, combined with optical holography and digital image processing of computer, is widely used in the field of surface measurements of objects. In addition to classical roughness values  $R_a$ ,  $R_t$ , and so forth, digital holography can also make full-field measurements of 3D surface material. Digital holographic measurement can measure the surface of the object with some important characteristics, such as no damage, high resolution, and noncontact fast processing.

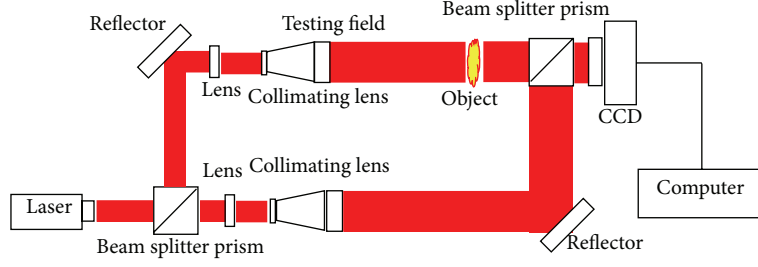


FIGURE 1: Off-line recording of digital hologram.

Compared with other image processing and measuring techniques, digital holography has a number of important advantages [4]. Firstly, it does not require much optical equipment, especially changing the hologram plates. Secondly, it captures the image with noncontact, nondestructive, and fast, height accuracy, sensitivity and resolution. Thirdly, there is no complex chemical processing in digital holography, so reproducing hologram and reconstructing the hologram are quicker than traditional optical holography. Fourthly, computer image processing allows to process the errors and noise so as to revise additional optical phase for improving the quality of the reconstructed image.

Holographic interferometry (HI) is a procedure which enables static and dynamic displacements of objects with optically rough surfaces to be measured with optical interferometer accuracy [4, 14]. Then, in digital holography, we can accurately measure the slight deformation of the objects by calculating the change of the information recorded by digital holograms [4]. In this paper, through digital holography and image processing, we can measure the height of the material surface. Otherwise, by recording the hologram, the phase diagram can be obtained and the surface of material can be measured quickly and accurately, making the three-dimensional visualization possible.

## 2. General Principles of Digital Holography

**2.1. Recording of Digital Hologram.** Digital holographic recording optical path and the traditional optical holography are consistent; only replace holographic plate with a CCD camera as the recording medium. The concept of outline digital hologram recording is shown in Figure 1.

The object wave  $O(x, y)$  and the reference wave  $R(x, y)$  interference occur to form a hologram on the CCD surface. In the hologram plane, the recorded intensity distribution  $I_H(x, y)$  can be printed as follows [4]:

$$H(x, y) = |O|^2 + |R|^2 + RO^* + R^*O, \quad (1)$$

where  $RO^*$  and  $R^*O$  represent the conjugation image and the original image, respectively.

So the intensity distribution of the recorded hologram by CCD is written as

$$H(m, n) = H(x, y) \text{rect}\left(\frac{x}{L_x}, \frac{y}{L_y}\right) \text{comb}\left(\frac{x}{\Delta_x}, \frac{y}{\Delta_y}\right). \quad (2)$$

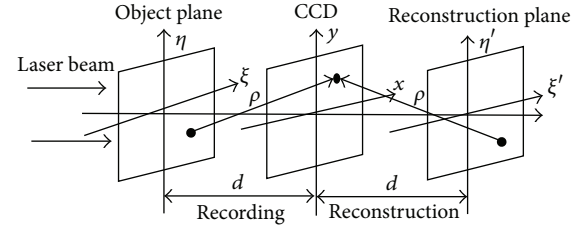


FIGURE 2: Coordinate system for image reconstruction.

The light intensity is collected by the data acquisition card and quantity. The 3D information of object is saved by the computer and formed as a digital hologram.

**2.2. Reconstruction of Digital Hologram.** In traditional holography, the reconstruction is carried out by means of illumination of the hologram intensity with the reference wave. A virtual image and a real image of the object are reconstructed. The digital hologram simulates the traditional optical reproduction processes, and its numerical reconstruction can be gained by computer.

The laser beam goes through the object and the part of the beam diffracted by objects and reaching the recording surface is considered the object beam, while the beam from the laser arriving without any distortion is considered as the reference beam. Two beams superposition create an interference pattern on the CCD sensor. This diffraction can be described by the Fresnel-Kirchhoff integral as [4]

$$R(\xi', \eta') = \frac{i}{\lambda} \iint_{-\infty}^{\infty} h(x, y) E_R(x, y) \frac{\exp(-i(2\pi/\lambda)\rho)}{\rho} dx dy, \quad (3)$$

with

$$\rho = \sqrt{(\xi' - x)^2 + (\eta' - y)^2 + d^2}. \quad (4)$$

The coordinates in (3) and (4) are illustrated in Figure 2.  $R(\xi', \eta')$  is the wave fields of the reconstruction image and  $h(x, y)$  is the hologram function. The  $\rho$  is the distance between a point in the hologram plane and the corresponding point in the reconstruction plane,  $d$  is the distance between two adjacent planes, and  $\lambda$  is the wavelength.

Different numerical reconstruction algorithms have been proposed, such as Fresnel approximation algorithm and

convolution approach algorithm [4]. The resolution of the reconstruction image by convolution approach algorithms is much better than that by the Fresnel approximation algorithm in [10]. Therefore, the convolution approach algorithm is adopted in this paper and the mathematical expression of the convolution approach algorithm is defined as follows:

$$\begin{aligned}
 R(\xi', \eta') &= F^{-1} \left\{ F[h(x, y)] \right. \\
 &\quad \cdot F \left[ \frac{i}{\lambda} \left( \exp \left[ -i \frac{2\pi}{\lambda} \sqrt{d^2 + (x - \xi')^2 + (y - \eta')^2} \right] \right) \right. \\
 &\quad \times \left. \left. \sqrt{d^2 + (x - \xi')^2 + (y - \eta')^2} \right] \right\}, \quad (5)
 \end{aligned}$$

where  $F[\cdot]$  and  $F^{-1}[\cdot]$  are the Fourier transform and the inverse Fourier transform, respectively.

In this paper, we use numerical simulation hologram to check the ability of our arithmetic for determination of the focal plane. For numerical simulation reconstruction of holograms, the Fresnel and convolution arithmetic based on the reconstruction equations has been used well in practice. The convolution arithmetic producing good holograms and reconstruction images and high quality of holograms does not change with different object distances. Therefore, convolution arithmetic will be importantly explained in this paper.

In Figure 2, the left and the right part are the same, which means the formula for reconstruction image from a hologram is the same as that for the generation of the hologram from the object image. Thus, after change of some parameters in (3), we will obtain the new hologram function as follows:

$$h(x, y) = \frac{i}{\lambda} \iint_{-\infty}^{\infty} O(\xi, \eta) E_R(\xi, \eta) \frac{\exp(-i(2\pi/\lambda)\rho)}{\rho} d\xi d\eta. \quad (6)$$

Because the form of (6) is the same as that of (3), the convolution algorithm can also be used to obtain the hologram function,  $h(x, y)$ , from the object function,  $O(\xi, \eta)$ . Then the replacement of (3) and (6) can be rewritten in the form of the superposition integral as follows:

$$h(x, y) = \iint_{-\infty}^{\infty} O(\xi, \eta) g(\xi, \eta, x, y) d\xi d\eta, \quad (7)$$

with

$$\begin{aligned}
 g(\xi, \eta, x, y) &= \frac{i}{\lambda} \frac{\exp \left[ -i(2\pi/\lambda) \sqrt{d^2 + (\xi - x)^2 + (\eta - y)^2} \right]}{\sqrt{d^2 + (\xi - x)^2 + (\eta - y)^2}}. \quad (8)
 \end{aligned}$$

This superposition integral can be considered as a convolution. So, (7) will become

$$\begin{aligned}
 h(x, y) &= F^{-1} \left\{ F[O(\xi, \eta)] \right. \\
 &\quad \cdot F \left[ \frac{i}{\lambda} \left( \exp \left[ -i \frac{2\pi}{\lambda} \sqrt{d^2 + (\xi - x)^2 + (\eta - y)^2} \right] \right) \right. \\
 &\quad \times \left. \left. \left( \sqrt{d^2 + (\xi - x)^2 + (\eta - y)^2} \right)^{-1} \right] \right\}. \quad (9)
 \end{aligned}$$

Equation (9) is used for numerical simulation of holograms by the convolution algorithm. Based on this equation, we can get the hologram function,  $h(x, y)$ , equivalent to some object image function,  $O(\xi, \eta)$  [4].

### 3. Theories of Surface Measurements by Digital Holography

**3.1. General Principles.** As the material surfaces are uneven, when irradiated by the laser, there will appear a different phase on the material surfaces. In Section 2, after recording and reconstruction of digital hologram, the intensity and phase distribution of the reconstructed image can be obtained by [4]

$$I(\xi, \eta) = |R(\xi, \eta)|^2 = \text{Re}^2 |R(\xi, \eta)| + \text{Im}^2 |R(\xi, \eta)|, \quad (10)$$

$$\Phi(\xi, \eta) = \arctan \frac{\text{Im} |R(\xi, \eta)|}{\text{Re} |R(\xi, \eta)|}, \quad (11)$$

where  $\text{Re} |R(\xi, \eta)|$  and  $\text{Im} |R(\xi, \eta)|$  denote the real and imaginary parts of the object complex amplitude, respectively.

**3.2. Phase Unwrapping.** Phase distribution value obtained by (11) is limited in the range of  $(-\pi, +\pi)$  for the theory of the arctan function, so also through phase unwrapping, the accurate phase information can be obtained [4]. Phase unwrapping is a method applied to wrapped phase images to remove the  $2\pi$  incoherence embedded within the phase diagram. It detects a  $2\pi$  phase jump and adds or subtracts an integer offset of  $2\pi$  to adjoining pixels following that phase jump based on a tolerance mechanism, thus, retrieving the continuous form of the phase map. The simulation of phase unwrapping process is illustrated in Figures 3(a) and 3(b).

Phase unwrapping is a technique which can generate a continuously phase distribution. It constitutes essential parts of optical metrology by heterodyne techniques. In surface measurement by digital holographic, the phase unwrapping is a key technique. Numerous phase unwrapping algorithms have been proposed in the past several years [15, 16]. Two types of strategy have been developed to solve the

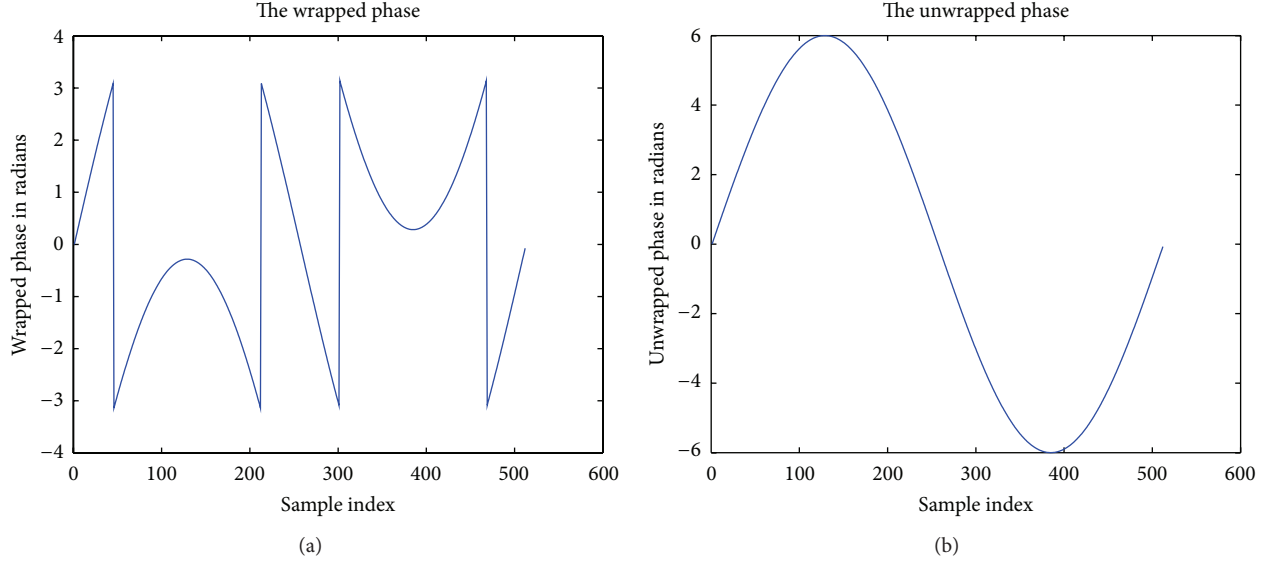


FIGURE 3: Phase unwrapping: (a) wrapped phase and (b) continuous phase.

phase unwrapping problem: path-following and minimum-norm methods. Path-following methods include Goldstein's branch cut algorithm [17], and minimum spanning tree algorithm [18]. Minimum-norm methods contain least-squares phase unwrapping algorithm [19], minimum Lp-norm phase unwrapping algorithm [16], and so on.

In this paper, the continuous phase image is acquired by least-squares phase unwrapping algorithm without weighing. The discrete cosine transforms (DCT) is used to solve the discrete Poisson equation in this method. The least-square solution of the unwrapped phase and the expanded phase is obtained.

**3.3. The Height Distribution of Surface.** As mentioned above, after the phase unwrapping with computer, the phase distribution  $\Phi(\xi, \eta)$  can be simply converted into the height distribution  $h(\xi, \eta)$  on the material surface. Then, the continuous phase distribution can be used for measurements of material surface. So the height of the material surface  $h(\xi, \eta)$  can be calculated by [4]

$$h(\xi, \eta) = \frac{\lambda}{4\pi} \Phi(\xi, \eta), \quad (12)$$

where  $\lambda$  is the wavelength.

The surface of homogenous optical properties was measured in the light of the reconstructed phase-contrast image [19], which showed the phase changes corresponding to optical path was less than 10 nm. In this paper, the target we choose is much bigger than 10 nm.

## 4. Experiments and Results

**4.1. Optical Experiment.** Since the height of the target surface is uniformly distributed, in this experiment a test target is used as the target surface. The optical experimental setup for recording test target (USFA 1950) holograms is shown in

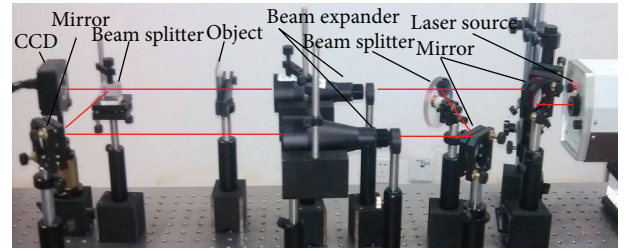


FIGURE 4: Experimental setup for recording test target holograms.

Figure 4. The experimental conditions are listed as follows: the pixel number  $N$  is equal to 1024; the pixel size of the CCD camera is  $5.2 \mu\text{m}$ ; the wavelength  $\lambda$  is equal to  $632.8 \text{ nm}$ . The laser with a maximum output power of  $6 \text{ W}$  is adopted.

As shown in Figure 4, the input He-Ne laser is divided into two parts by a beam splitter (BS): one beam goes through the test target as the object beam and another beam is expanded as the reference beam. The object and reference beams have an interference with BS, the hologram is recorded by a CCD detector, and then the image information is sent to the computer by a collection.

Figure 5 shows the recording of digital hologram by computer. The recording distance between the object and the CCD sensors is set to be  $78 \text{ mm}$ . Figure 6 shows the reconstruction intensity image of the test target. Then the height distribution  $h(\xi, \eta)$  can be obtained from (11) and (12). Through the powerful drawing function of MATLAB, the height distribution of the material surface can be displayed in the form of 3D; it was shown in Figure 7. 1002 points on material surface were measured in experiment, and the height distribution information is illustrated in Figure 8 and Table 1.

**4.2. Validation Experiment.** The verification experimental equipment uses NanoMap 500LS which is produced by AEP

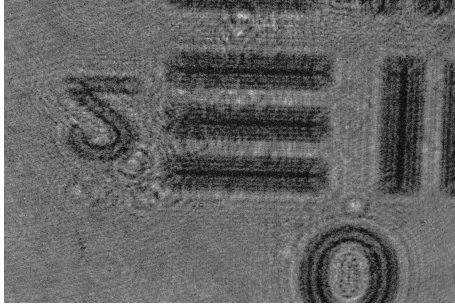


FIGURE 5: Recording of digital hologram.

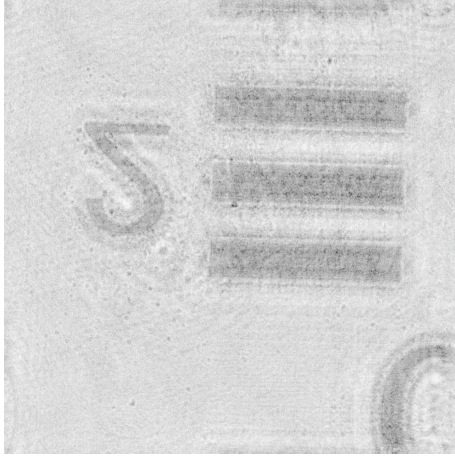


FIGURE 6: Reconstruction of digital hologram.

technology, and the composition of the equipment is the same as the one in Figure 9 [20]. NanoMap has many features: (a) seamless integration of conventional contact profile meter and scanning probe microscope (SPM) technology, (b) dual mode operation (tip scan and stage scan) optimized for small areas, (c) 3D mapping as well as long range profiling and 3D long scan range up to  $150 \text{ mm} \times 150 \text{ mm}$ , (d) stage scan by using high grade optical reference flat, (e) wide vertical range with high accuracy as a result of the dual optical and up to  $0.1 \text{ nm}$  vertical resolution with fine sensor, (f) constant contact forces suitable by software and automatic sample positioning with  $XY$  motorized stage. The NanoMap 500LS measurement flow chart is shown in Figure 10.

After loading the test target onto the stage and setting up scan parameters, we can get the scan curve shown in Figure 11. We process the data and curve fitting using MATLAB and obtain the result shown in Figure 12. The height distribution information is illustrated in Figure 13 and the height data in Table 2. From Figures 12 and 13, we can see so many more numbers whose values are smaller than zero, the reason for which is that the protruding part is less than the hollow one in the part we scan. In Figure 13 and Table 2, the average measurement result of the target surface by NanoMap 500LS is  $69.9 \text{ nm}$ .

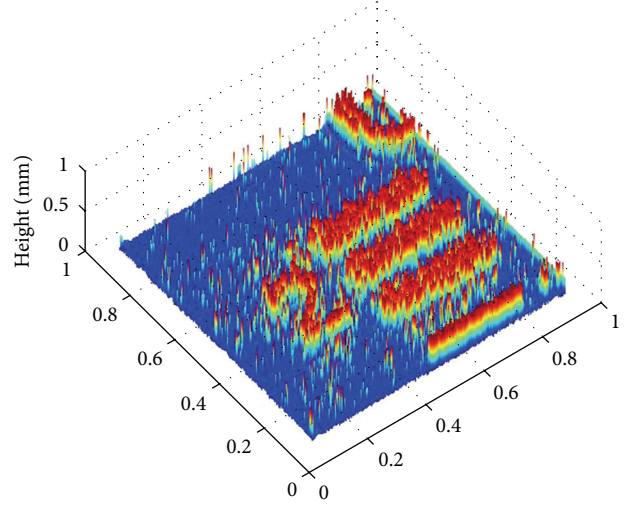


FIGURE 7: The reconstructed height distribution.

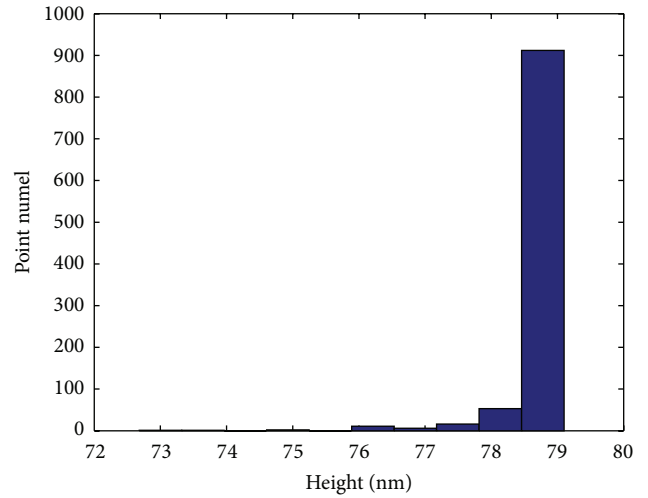


FIGURE 8: Height distribution.

TABLE 1: Data of heights.

Height	Min	Max	Average
Value (nm)	72.7	79.1	78.8

TABLE 2: Data of heights.

Height	Min	Max	Average
Value (nm)	60.4	87.6	69.9

**4.3. Experimental Results.** Tables 1 and 2 show the measurement results of the target surface by digital holography and NanoMap500LS. The comparison of two methods is shown in Table 3. The relative error can be obtain as follows:  $8.9/69.9 = 12.7\%$ . The digital holography can serve as an effective measurement method used in engineering.

TABLE 3: Comparison of the measurement results by two methods.

Methods	Digital holography (nm)	NanoMap 500Ls (nm)	Difference (nm)	Relative error (%)
Value	78.8	69.9	8.9	12.7

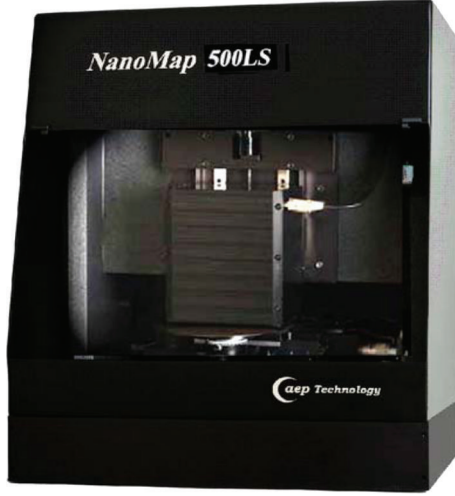


FIGURE 9: NanoMap 500LS.

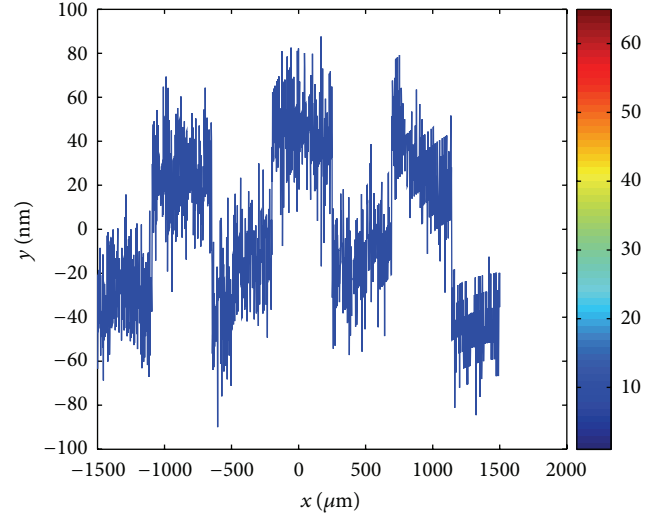


FIGURE 11: The scan curve.

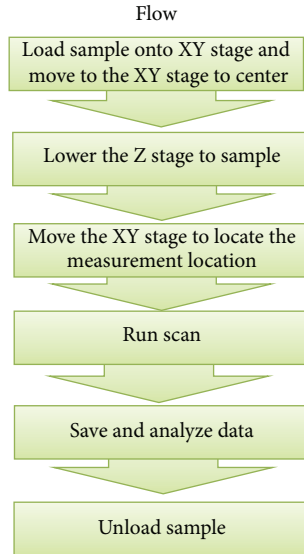


FIGURE 10: Flow chart for taking a profile measurement.

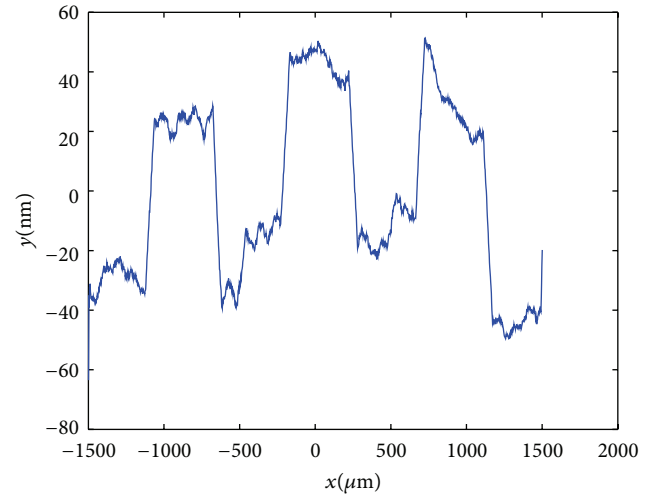


FIGURE 12: The fitting curve.

## 5. Conclusions

In this paper, we have presented the digital holography for measuring the material surface as an important technique. The principle of surface measurement by digital holography is analyzed. In this paper, we use a target as a test target. By recording and reconstruction hologram, we obtain the phase and height distribution of the object surface by noise, phase unwrapping, and so forth. Then we use NanoMap 500LS 3D profilometer as validation experiment. Comprised

of contact profilometer, the results of two measurement methods do not make much difference. However, digital holography measurement method has the larger advantage. Digital holographic measurement can obtain the surface of objects with no damage, high resolution, noncontact, and fast processing characteristics. And also, any measurement system has measuring error. Future research direction is to solve the measurement errors which exist.

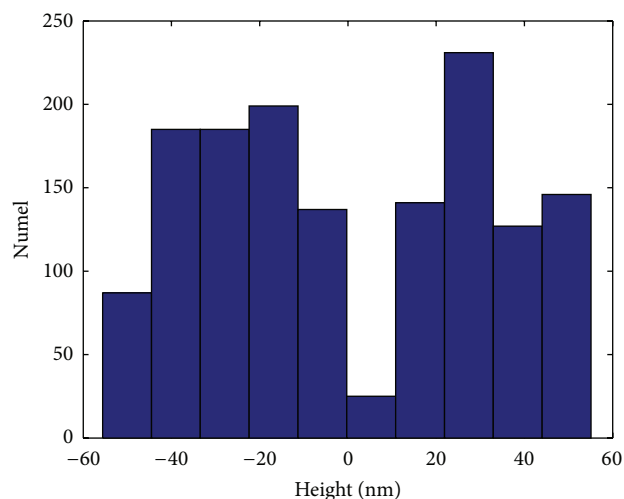


FIGURE 13: Height distribution.

## Acknowledgments

This work was supported by the National Natural Science Foundation of China (11272368) and the Natural Science Foundation of CSTC (cstc2013yykfB0198).

## References

- [1] D. Gabor, "A new microscopic principle," *Nature*, vol. 161, no. 4098, pp. 777–778, 1948.
- [2] D. Gabor, "Microscopy by reconstructed wavefronts: 2," *Proceedings of the Royal Society*, vol. 64, pp. 449–469, 1951.
- [3] J. W. Goodman and R. W. Lawrence, "Digital image formation from electronically detected holograms," *Applied Physics Letters*, vol. 11, no. 3, pp. 77–79, 1967.
- [4] Y. Yang, B.-S. Kang, and Y.-J. Choo, "Application of the correlation coefficient method for determination of the focal plane to digital particle holography," *Applied Optics*, vol. 47, no. 6, pp. 817–824, 2008.
- [5] Y. Yang and B.-S. Kang, "Experimental validation for the determination of particle positions by the correlation coefficient method in digital particle holography," *Applied Optics*, vol. 47, no. 32, pp. 5953–5960, 2008.
- [6] L. Xu, X. Peng, J. Miao, and A. K. Asundi, "Studies of digital microscopic holography with applications to microstructure testing," *Applied Optics*, vol. 40, no. 28, pp. 5046–5051, 2001.
- [7] G. Pedrini and H. J. Tiziani, "Quantitative evaluation of two-dimensional dynamic deformations using digital holography," *Optics and Laser Technology*, vol. 29, no. 5, pp. 249–256, 1997.
- [8] Y. Yang and B. Kang, "Measurements of the characteristics of spray droplets using in-line digital particle holography," *Journal of Mechanical Science and Technology*, vol. 23, no. 6, pp. 1670–1679, 2009.
- [9] G. Popescu, L. P. Deflores, J. C. Vaughan et al., "Fourier phase microscopy for investigation of biological structures and dynamics," *Optics Letters*, vol. 29, no. 21, pp. 2503–2505, 2004.
- [10] P. Marquet, B. Rappaz, P. J. Magistretti et al., "Digital holographic microscopy: a noninvasive contrast imaging technique allowing quantitative visualization of living cells with subwavelength axial accuracy," *Optics Letters*, vol. 30, no. 5, pp. 468–470, 2005.
- [11] A. Ettemeyer, "Applications of digital holography to microstructures," in *Proceedings of the SAE World Congress 2009*, Detroit, Mich, USA, April 2009.
- [12] S. Seebacher, W. Osten, and W. P. O. Jüptner, "Measuring shape and deformation of small objects using digital holography," in *Proceedings of SPIE*, pp. 104–115, July 1998.
- [13] B. Bowe and V. Toal, "White light interferometric surface profiler," *Optical Engineering*, vol. 37, no. 6, pp. 1796–1799, 1998.
- [14] T. Kreis, *Handbook of Holographic Interferometry*, Wiley-VCH, 2005.
- [15] R. M. Goldstein, H. A. Zebker, and C. L. Werner, "Satellite radar interferometry: two-dimensional phase unwrapping," *Radio Science*, vol. 23, no. 4, pp. 713–720, 1988.
- [16] D. C. Ghiglia and M. D. Pritt, *Two-Dimensional Phase Unwrapping: Theory, Algorithms, and Software*, John Wiley & Sons, Hoboken, NJ, USA, 1998.
- [17] R. M. Goldstein, H. A. Zebker, and C. L. Werner, "Satellite radar interferometry: two-dimensional phase unwrapping," *Radio Science*, vol. 23, no. 4, pp. 713–720, 1988.
- [18] J. Schöner, A. Ettemeyer, U. Neupert, H. Rottenkolber, C. Winter, and P. Obermeier, "New approaches in interpreting holographic images," *Optics and Lasers in Engineering*, vol. 14, no. 4-5, pp. 283–291, 1991.
- [19] D. Kerr, G. H. Kaufmann, and G. E. Galizzi, "Unwrapping of interferometric phase-fringe maps by the discrete cosine transform," *Applied Optics*, vol. 35, no. 5, pp. 810–816, 1996.
- [20] AEP Technology, "NanoMap 500LS 3D profilometer User's Manual," Revision B, 2009.

## Research Article

# Analysis and Testing of Chain Characteristics and Rheological Properties for Magnetorheological Fluid

Song Chen,<sup>1,2</sup> Jin Huang,<sup>2</sup> Hongyu Shu,<sup>1</sup> Tiger Sun,<sup>1</sup> and Kailin Jian<sup>1</sup>

<sup>1</sup> College of Resources and Environmental, Chongqing University, Chongqing 400044, China

<sup>2</sup> College of Mechanical Engineering, Chongqing University of Technology, Chongqing 400054, China

Correspondence should be addressed to Jin Huang; [jhuangcq@sohu.com](mailto:jhuangcq@sohu.com)

Received 16 July 2013; Accepted 9 October 2013

Academic Editor: Xing Chen

Copyright © 2013 Song Chen et al. This is an open access article distributed under the Creative Commons Attribution License, which permits unrestricted use, distribution, and reproduction in any medium, provided the original work is properly cited.

Digital holographic microscopy is presented in this study, which can measure the magnetorheological (MR) fluid in different volume fractions of particles and different magnetic field strengths. Based on the chain structure of magnetic particle under applied magnetic field, the relationships between shear yield stress, magnetic field, size, and volume fraction of MR fluid in two parallel discs are established. In this experiment, we choose three MR fluid samples to check the rheological properties of MR fluid and to obtain the material parameters with the test equipment of MR fluid; the conclusion is effective.

## 1. Introduction

Magnetorheological (MR) fluids are suspensions of micron-sized, magnetizable particles in a carrier fluid such as synthetic oil and silicone oil, which are regarded as the intelligent materials that respond to an applied magnetic field with a change in their rheological properties. In the absence of an applied magnetic field, MR fluids exhibit Newtonian fluid-like behavior. Upon application of a magnetic field, the polarization between two induced dipoles causes the suspended particles in the MR fluids to form a chain-like microstructure aligned with the direction of applied magnetic field. The magnetic chain structure changes the rheological properties of the suspension. Altering the strength of the applied magnetic field precisely and proportionally controls the shear yield strength of the fluids [1, 2]. Based on the mechanical characteristics, the fluids can be used in the controllable energy-dissipating applications such as dampers [3, 4], valves [5, 6], and clutches and brakes [7, 8].

Experiments showed that many other factors affect the macroscopic properties of an MR fluid. It mainly includes the applied magnetic field strength, the size and gradation, and the property and volume fraction of the particles; the property of the carrier fluid and the additives. Noma et al. [9] found that Fe nanoparticles synthesized by the arc plasma

method exhibited a high saturation magnetization and may be useful for MR fluids. Ekwebelam and See [10] explored the yielding behavior and enhanced stress response exhibited by bidisperse MR fluid over monodisperse systems. He found that the stress enhancement in bidisperse suspensions is likely to be due to the population and orientation of interacting large particles in the bidisperse suspensions. Jang et al. [11] studied the behavioral model for magnetorheological fluid under a magnetic field using Lekner summation method. Pacull et al. [12] studied the effect of polar interactions on the magnetorheology of silica-coated magnetite suspensions in oil media reported. He suggested that the nonnegligible interfacial interactions are responsible for both the absence of MR effect in hydrophobic samples and the low yield stress in hydrophilic suspensions. To resolve the sedimentation of carbonyl iron (CI) based MR fluid, Fang et al. [13] introduced fibrous single-walled carbon nanotube (SWNT) into carbonyl iron (CI) suspension as additives.

## 2. Chain Characteristics of MR Fluid

**2.1. Chain Process.** When a magnetic field is applied, the magnetic particles in MR fluid are moving orderly that causes the suspended particles to attract each other under the action

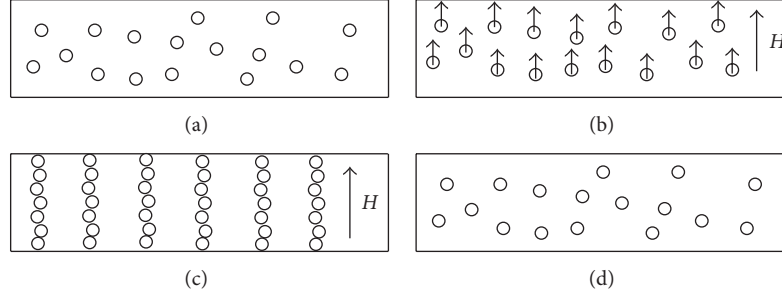


FIGURE 1: The chain process of MR fluid.

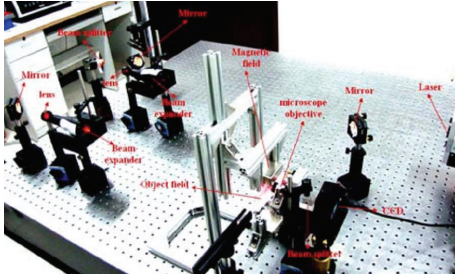


FIGURE 2: The experimental device of measurement of MR fluids by digital microholography.

of magnetic force to form a chain-like microstructure along the field direction; meanwhile the chain process of MR fluid occurs, as shown in Figure 1. The distribution of particles in MR fluid without the magnetic field is shown in Figure 1(a), the dynamic yield stress is zero in this case. The chain structure of particles in MR fluid under the magnetic field is shown in Figure 1(b). Figure 1(c) shows that the number and diameter of chain will increase with the applied magnetic field and the dynamic yield stress and apparent viscosity of MR fluid also increase. Figure 1(d) shows that the MR fluid recovers rapidly and response time is only few milliseconds when the applied magnetic field disappeared.

Figure 2 shows the experimental device for recording holograms of MR fluid. The experimental conditions are as follows: the pixel number  $N = 1024$ ; the pixel size of the charge coupled device (CCD) camera  $\Delta x = 5.2 \mu\text{m}$ ; the wavelength  $\lambda = 632.8 \text{ nm}$ ; the magnification of objective  $M = 40$ .

The hologram and reconstruction images of calibration target are shown in Figure 3. From Figure 3(b), we can easily obtain the length between two graduation lines based on counting the pixel numbers. Because the actual scale of calibration target is  $50 \mu\text{m}$ ,  $M'$  and actual  $d$  can be calculated [13].

After a strong magnetic field is applied to MR fluids, the microparticles will be polarized and aligned like chains along the direction of magnetic field. The continuous holograms of MR fluids under an applied magnetic field were encoded by CCD and the construction images of the chain configuration are shown in Figure 4. The figures also indicate the transform process from micro-particles to chains in a magnetic field.

The chaining process along the direction of magnetic field, that is, the responding speed of MR fluids for magnetic field, is easily calculated.

**2.2. Shear Yield Stress.** In order to analyze the relationship between the shear yield stress and the magnetic field, the size, the volume percentage of MR fluid. The assumptions for chain model of dipole are as follows.

- (1) The ordered arrangement of particles after magnetic polarization and the chain structure is steady. All of the particles occupy a fixed position in the stable chain.
- (2) The single chain formed by particles is along with the direction of magnetic field. The chain is parallel to magnetic field direction, and its length is equal to the distance between two plates. All of the chains are the same in geometry, so the analysis results of arbitrary chain can be representative of the others.
- (3) The acting force between adjacent particles in the chains is equal, which presents the tensile strength of chains.
- (4) The adjacent particles are magnetized and turn into dipoles. The direction of the centerline of particles is parallel to the magnetic field.
- (5) The interaction force in particles decides the strength of chains. When applied force is greater than the interaction force between particles, the chain will be pulled off. When the shear stress is perpendicular to the direction of magnetic field, the chain will be elongated and snapped.
- (6) The particles are supposed to be spherosome and uniform.

The analysis mode of shear yield stress in MR fluid is shown in Figure 5, where  $h$  represents the distance between two parallel plates and  $F_a$  is the external force [14]. The bottom plate is fixed, and external force is applied to upper plate. When the shear stress is perpendicular to magnetic field direction, the chain will deform and break. The  $\tau_y(H)$  represents the shear yield stress under unit area. The relationship between  $\tau_y(H)$  and  $F_a$  is indicated by  $\tau_y(H) = F_a \sin \theta$ , where  $\theta$  represents the angle between the centerline of chain and magnetic field direction, as shown in Figure 5.

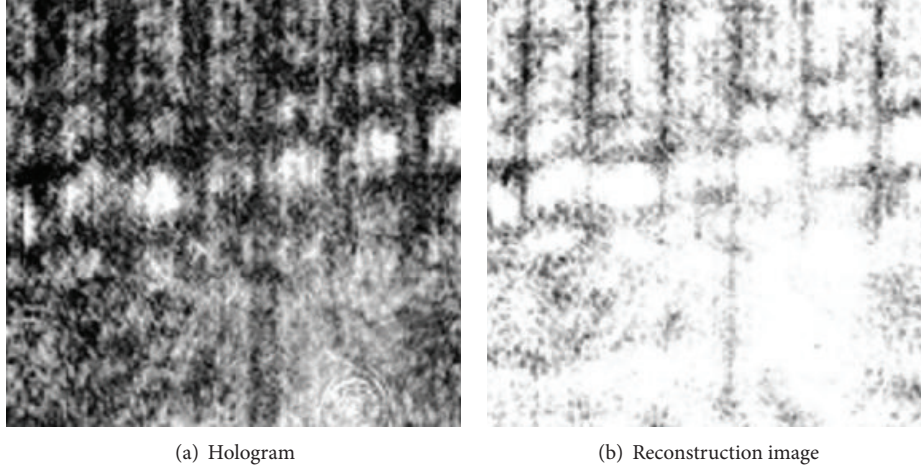


FIGURE 3: Hologram and reconstruction images of calibration target.

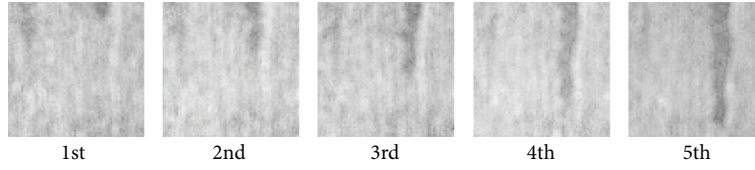


FIGURE 4: Reconstruction images (MR fluids under a magnetic field in different times).

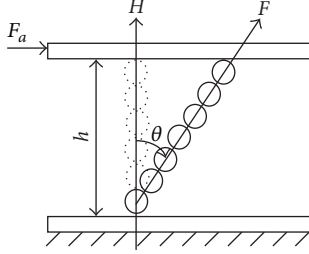


FIGURE 5: The analysis mode of shear yield stress.

With the applied magnetic field, the single magnetic particle is magnetized and forms dipoles in the MR fluid. The  $J$  represents the dipole moment which can be expressed as follows [15]:

$$J = \mu_0 V_1 M, \quad (1)$$

where  $\mu_0$  is the permeability of vacuum,  $V_1$  is the average volume of magnetic particles,  $V_1 = 4\pi r^3/3$ , and  $M$  is magnetization intensity:

$$M = \chi H, \quad (2)$$

where  $\chi$  is the magnetic susceptibility and  $H$  is the magnetic field strength.

The magnetic pole strength of the dipole can be expressed as follows:

$$m = \frac{J}{2r}. \quad (3)$$

The distance of dipoles which is formed by any two magnetic particles in the same chain is

$$d = \frac{n(2r + \delta)}{\cos \theta}, \quad (4)$$

where  $\delta$  is the average value of the gap between two adjacent particles in the chain.

The average value of acting force in particles in the same chain can be expressed as follows:

$$F = \frac{1}{4\pi\mu_0} \frac{m^2}{d^2}. \quad (5)$$

The shear yield stress of MR fluid under magnetic field is

$$\tau_y(H) = \frac{NF \sin \theta}{A}, \quad (6)$$

where  $A$  represents the area of the flat plate.

The number of chains in the unit area can be expressed as follows:

$$N = \frac{(\phi Ah/V_1)}{(h/R)}, \quad (7)$$

where  $\phi$  is the volume fraction of magnetic particles in MR fluid and  $R = 2r + \delta$ .

Combining (1), (3), (4), and (6), the shear yield stress of MR fluid under magnetic field is expressed as follows:

$$\tau_y(H) = \sum_{n=1}^k \frac{\mu_0}{12n^2} \frac{r\phi(\mu_r - 1)^2 H^2}{(2r + \delta)} \sin \theta \cos^2 \theta, \quad (8)$$

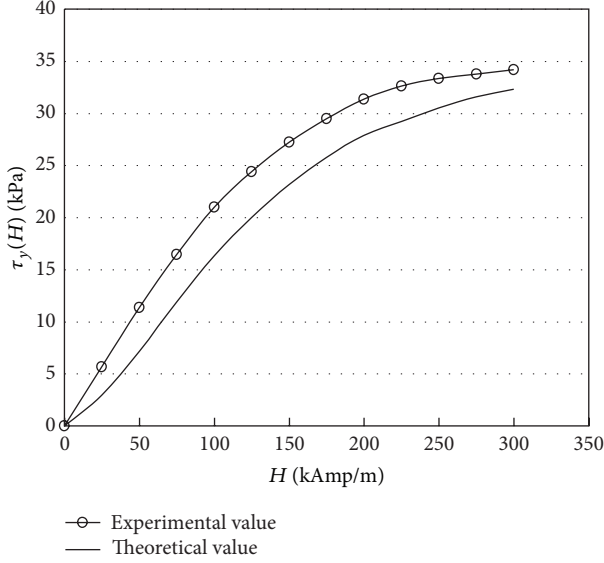


FIGURE 6: The yield stress versus applied magnetic field strength.

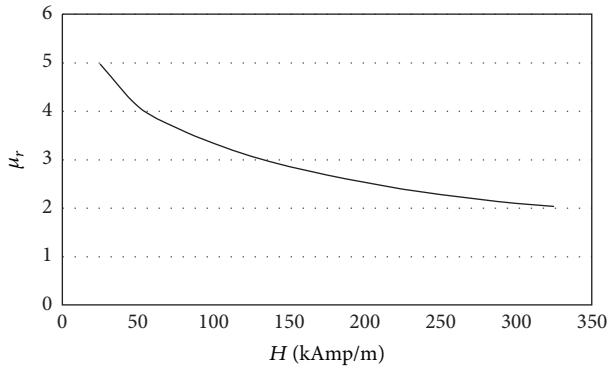


FIGURE 7: The relative magnetic permeability versus applied magnetic field strength.

where  $\mu_r$  represents the relative magnetic permeability of MR fluid,  $\mu_r = 1 + \chi$ ,  $k$  represents the average number of particles in each chain, and  $k = Ah/V_1 N$ .

The theoretical value and experimental value of yield stress versus applied magnetic field strength are shown in Figure 6. The magnetic particle is uniform spherosome in the MR fluid. Assume that  $\theta = 30^\circ$ ,  $\delta = 0$ ,  $\mu_0 = 4\pi \times 10^{-7} \text{ Tm/A}$ , and  $\phi = 37\%$ . The relationship between the relative magnetic permeability and the applied magnetic field strength can be drawn, as shown in Figure 7. As shown in Figure 6, the theoretical value is satisfied with the experimental value, the yield stress of MR fluid is increased with the applied magnetic field and its value can be controlled by applied magnetic field.

### 3. Rheological Properties of MR Fluid

**3.1. Test Equipment.** The performance experimental device for rheological properties of MR fluid between two discs is shown in Figure 8. Based on this test system, the transmission torques of MR fluids between two discs under zero magnetic

field and different applied magnetic fields are analyzed. The shearing rate of MR fluids between two discs can be adjusted by motor in the test system. The applied magnetic field strength can be controlled by electric current in coil. All parameters in system are measured in real time by gaussmeter, speed, and torque sensors.

**3.2. Test Principle.** For the properties of experimental system of MR fluid between two parallel disks, shown in Figure 8, the following assumptions are given: the fluid is incompressible. There is no flow in radial direction and axial direction, but only tangential flow. The flow velocity of MR fluid is a function of radius. The pressure in the thickness direction of MR fluid is constant. The strength of magnetic field in the gap of the activation region is well distributed. In cylindrical coordinates  $(r, \theta, z)$ , the distribution of the flow velocity is

$$V_r = 0, \quad V_\theta = r\omega(z), \quad V_z = 0, \quad (9)$$

where  $V_r$ ,  $V_\theta$ , and  $V_z$  are the flow velocity of the fluid in the  $r$ -direction, the  $\theta$ -direction, and  $z$ -direction, respectively;  $\omega(z)$  is the rotation angular velocity of the fluid in the  $\theta$ -direction. The angular velocity  $\omega(z)$  is the function of  $z$ -coordinate.

The fluid shear strain rate may be approximated as follows:

$$\dot{\gamma} = \omega_0 \frac{r}{h}, \quad (10)$$

where  $\omega_0$  is speed of rotating disk. The torque transmitted by the MR fluid between two parallel disks is calculated by integrating the shear stress of the MR fluid as follows:

$$T = 2\pi \int_{R_1}^{R_2} \tau r^2 dr, \quad (11)$$

where  $R_1$  and  $R_2$  are the effective inner and outer radius of the rotor-disc in the MR fluid exposed to the magnetic field, respectively. Based on the mean value theorem of integral, the torque  $T$  in (11) can be expressed as follows:

$$T = \frac{2\pi}{3} \tau^* (R_2^3 - R_1^3), \quad (12)$$

where  $\tau^*$  is the shear stress of the sample. When  $(R_2 - R_1) \ll R_0$ , the  $\tau^*$  is equal to the stress located at  $R_0 = (R_2 - R_1)/2$ , approximately. Using (10) and (12), the relationship between  $\tau$  and  $\dot{\gamma}$  can be obtained by the measuring torque  $T$  and speed  $\omega_0$ .

**3.3. Test Results.** In this experiment, we choose MR fluid samples MRM1, MRM2, and MRM3 to check the theory, as shown in Table 1. Then we make a comparison with the results.

When the magnetic displacement is small, shown in Figure 9, magnetic particle is far from reaching a magnetic saturation and the shear stress quickly increases. With the increase of the magnetic induction intensity, curves gradually become slow. This is mainly because of different magnetisability of the solid ferromagnetism particles. We

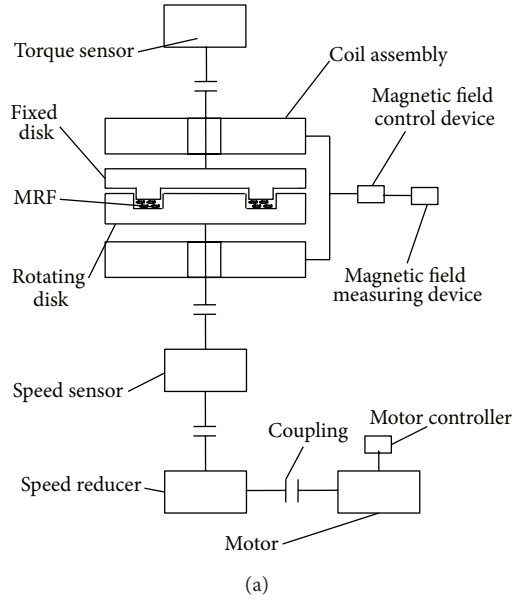


FIGURE 8: The performance experimental device for MR fluid rheological properties.

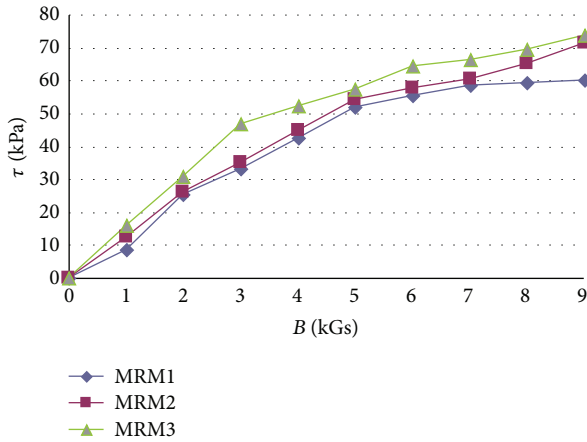


FIGURE 9: The shear stress of the different magnetic induction intensities.

TABLE 1: The MR fluid samples on different particle volume fractions.

List	Particle volume fraction/%	Zero field viscosity/(Pa·s)
MRM1	5	0.1
MRM2	15	0.2
MRM3	35	1.1

must increase the applied magnetic field strength in order to obtain a greater shear stress. If the magnetic induction intensity is large enough, the particles gradually reach magnetic saturation, particle interaction reaches the extreme value, and the shear stress at this time will not increase with the magnetic induction intensity and tends to a stable value.

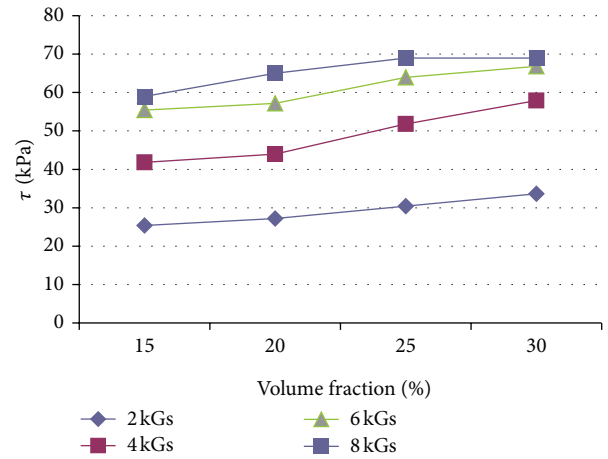


FIGURE 10: The shear stress of the different particle volume fractions.

The particles volume percentage refers to the percentage of the volume occupied by the dispersed phase of solid particles in the MR fluid. As Figure 10 shows, the shear stress also increases when the particle volume fraction increases. In the case of not very high magnetic field strength, both are rendering the approximate linear relationship. This can be explained by MR fluid microscopic mechanism. The solid particulate magnetic becomes dipole under the action of the magnetic field. Dipole of interaction form magnetic chain between the two plates. When the volume percentage is low, the number of solid particle is limited. In a magnetic field, a few of magnetic chains are formed and the shear stress is small. When the volume percentage is high, the number of magnetic chain increases and even forms column or mesh structure and the shear stress ensues to increase.

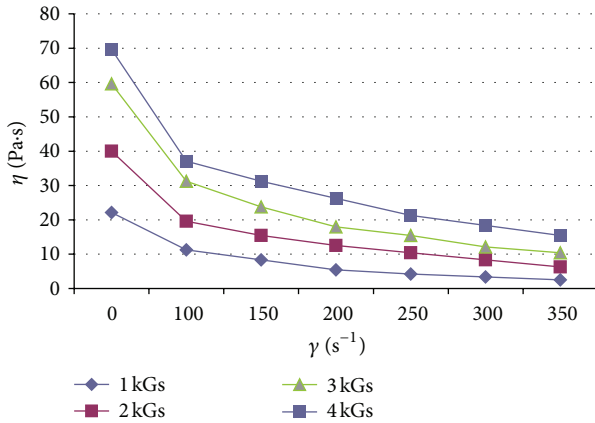


FIGURE 11: The relationship between viscosity and shear stress rate.

The apparent viscosity of MR fluid is the measure shear stress  $\tau$  under certain conditions divided by the shear strain rate  $\dot{\gamma}$ . Obviously, for a Newtonian fluid, the apparent viscosity is the dynamic viscosity, and the value of viscosity is a constant, independent of the shear strain rate. But for MR fluid, it is not so. As Figure 11 shows, the apparent viscosity of MR fluid changes with shear strain rate under different magnetic induction intensity. The apparent viscosity decreases with increasing shear strain rate and in the beginning it decreased rapidly and then leveled off.

#### 4. Conclusion

In order to predict the mechanical property of MR fluid under magnetic field and shear strain, the microstructures of chain at different magnetic fields strength were measured. The chain model of dipole interaction for MR fluid was established. The prediction model of yield stress for MR fluid is obtained. The influence of yield stress by magnetization intensity of magnetic particle and magnetic field strength were analyzed, respectively. In this experiment, we obtain the relationship between the shear stress and magnetic induction and particle volume fraction.

#### Acknowledgments

This work was financially supported by the National Natural Science Foundation of China (Grant no. 51175532); the Natural Science Foundation Key Project of Chongqing (Grant no. CSTC, 2011ba4028); Key Program of the Fundamental Research Funds for the Central Universities (Grant no. CDJXS10242206).

#### References

- [1] G. L. Gulley and R. Tao, "Structures of a magnetorheological fluid," *International Journal of Modern Physics B*, vol. 15, no. 6-7, pp. 851-858, 2001.
- [2] K. H. Song, B. J. Park, and H. J. Choi, "Effect of magnetic nanoparticle additive on characteristics of magnetorheological

fluid," *IEEE Transactions on Magnetics*, vol. 45, no. 10, pp. 4045-4048, 2009.

- [3] J. Huang, P. Wang, and G. Wang, "Squeezing force of the magnetorheological fluid isolating damper for centrifugal fan in nuclear power plant," *Science and Technology of Nuclear Installations*, vol. 2012, Article ID 175703, 6 pages, 2012.
- [4] E. Dragašius, V. Grigas, D. Mažeika, and A. Šulginas, "Evaluation of the resistance force of magnetorheological fluid damper," *Journal of Vibroengineering*, vol. 14, no. 1, pp. 1-6, 2012.
- [5] J. Huang, J. M. He, and J. Q. Zhang, "Viscoplastic flow of the MR fluid in a cylindrical valve," *Key Engineering Materials*, vol. 274-276, no. 1, pp. 969-974, 2004.
- [6] A. M. Afonso, M. A. Alves, and F. T. Pinho, "Analytical solution of mixed electro-osmotic/pressure driven flows of viscoelastic fluids in microchannels," *Journal of Non-Newtonian Fluid Mechanics*, vol. 159, no. 1-3, pp. 50-63, 2009.
- [7] P. Kielan, P. Kowol, and Z. Pilch, "Conception of the electronic controlled magnetorheological clutch," *Przegląd Elektrotechniczny*, vol. 87, no. 3, pp. 93-95, 2011.
- [8] J. Huang, J. Q. Zhang, Y. Yang, and Y. Q. Wei, "Analysis and design of a cylindrical magneto-rheological fluid brake," *Journal of Materials Processing Technology*, vol. 129, no. 1-3, pp. 559-562, 2002.
- [9] J. Noma, H. Abe, T. Kikuchi, J. Furusho, and M. Naito, "Magnetorheology of colloidal dispersion containing Fe nanoparticles synthesized by the arc-plasma method," *Journal of Magnetism and Magnetic Materials*, vol. 322, no. 13, pp. 1868-1871, 2010.
- [10] C. Ekwebelam and H. See, "Microstructural investigations of the yielding behaviour of bidisperse magnetorheological fluids," *Rheologica Acta*, vol. 48, no. 1, pp. 19-32, 2009.
- [11] K. I. Jang, J. Seok, B. K. Min, and S. J. Lee, "Behavioral model for magnetorheological fluid under a magnetic field using Lekner summation method," *Journal of Magnetism and Magnetic Materials*, vol. 321, no. 9, pp. 1167-1176, 2009.
- [12] J. Pacull, S. Gonçalves, Á. V. Delgado, J. D. G. Durán, and M. L. Jiménez, "Effect of polar interactions on the magnetorheology of silica-coated magnetite suspensions in oil media," *Journal of Colloid and Interface Science*, vol. 337, no. 1, pp. 254-259, 2009.
- [13] F. F. Fang, H. J. Choi, and M. S. Jhon, "Magnetorheology of soft magnetic carbonyl iron suspension with single-walled carbon nanotube additive and its yield stress scaling function," *Colloids and Surfaces A*, vol. 351, no. 1-3, pp. 46-51, 2009.
- [14] S. Chen, K. Jian, and X. Peng, "Cylindrical magnetorheological fluid variable transmission controlled by shape-memory alloy," *Science and Technology of Nuclear Installations*, vol. 2012, Article ID 856082, 6 pages, 2012.
- [15] X. Z. Zhang, X. L. Gong, P. Q. Zhang, and Q. M. Wang, "Study on the mechanism of the squeeze-strengthen effect in magnetorheological fluids," *Journal of Applied Physics*, vol. 96, no. 4, pp. 2359-2364, 2004.

## Research Article

# Evaluation of Ultrasonic Nonlinear Characteristics in Heat-Treated Aluminum Alloy (Al-Mg-Si-Cu)

JongBeom Kim<sup>1</sup> and Kyung-Young Jhang<sup>2</sup>

<sup>1</sup> Graduate School of Mechanical Engineering, Hanyang University, Seoul 133-791, Republic of Korea

<sup>2</sup> School of Mechanical Engineering, Hanyang University, Seoul 133-791, Republic of Korea

Correspondence should be addressed to Kyung-Young Jhang; [kyjhang@hanyang.ac.kr](mailto:kyjhang@hanyang.ac.kr)

Received 19 July 2013; Revised 7 October 2013; Accepted 21 October 2013

Academic Editor: Young Soo Choi

Copyright © 2013 J. Kim and K.-Y. Jhang. This is an open access article distributed under the Creative Commons Attribution License, which permits unrestricted use, distribution, and reproduction in any medium, provided the original work is properly cited.

The nonlinear ultrasonic technique has been known to be more sensitive to minute variation of elastic properties in material than the conventional linear ultrasonic method. In this study, the ultrasonic nonlinear characteristics in the heat-treated aluminum alloy (Al-Mg-Si-Cu) have been evaluated. For this, the specimens were heat treated for various heating period up to 50 hours at three different heating temperatures: 250°C, 300°C, and 350°C. The ultrasonic nonlinear characteristics of each specimen were evaluated by measuring the ultrasonic nonlinear parameter  $\beta$  from the amplitudes of fundamental and second harmonic frequency components in the transmitted ultrasonic wave. After the ultrasonic test, tensile strengths and elongations were obtained by the tensile test to compare with the parameter  $\beta$ . The heating time showing a peak in the parameter  $\beta$  was identical to that showing critical change in the tensile strength and elongation, and such peak appeared at the earlier heating time in the higher heating temperature. These results suggest that the ultrasonic nonlinear parameter  $\beta$  can be used for monitoring the variations in elastic properties of aluminum alloys according to the heat treatment.

## 1. Introduction

To evaluate material degradation, destructive tests such as tensile test, impact test, and bending test are commonly used. However, the destructive tests require preparation of specimens separately from the operating structures and the specimens cannot be reused after test. Therefore, in order to save time and cost, the nondestructive evaluation technique is preferred.

Ultrasonic method is a common nondestructive method to evaluate the material degradation, since the propagation characteristics of ultrasonic wave is very closely associated with the elastic properties of material [1]. Generally, when the material is degraded, the elastic property of material will be changed, so that if we can monitor the change of elastic properties, then the degradation can be evaluated. For this purpose, most of ultrasonic methods measure the sound velocity or attenuation of amplitude: the linear elastic constant can be estimated by measuring the longitudinal wave velocity and the shear wave velocity [2]. Also, the

correlation between the attenuation of ultrasonic wave and the microstructural change such as phase transformation or grain size growth has been reported [3]. And resonant frequency is dependent on the elastic properties of material as well. So, the linear elastic constant also can be estimated by using resonant frequency method [4].

Nevertheless, those techniques are still less sensitive to the minute degradation affected by precipitation or dislocation [5]. Thus, those conventional ultrasonic methods will not be able to evaluate the degradation induced by heat treatment in aluminum alloy effectively, since the thermal degradation in aluminum alloy by heat treatment is generally known to be related to the behavior of precipitation [6].

On the other hand, the nonlinear ultrasonic technique has been considered as a potential method since it has higher sensitivity to the minute degradation [7, 8]. When an ultrasonic wave is transmitted in a material, the waveform is distorted by the nonlinear elastic property of material and the harmonic waves are generated. The nonlinear ultrasonic technique uses this nonlinear ultrasonic effect to evaluate

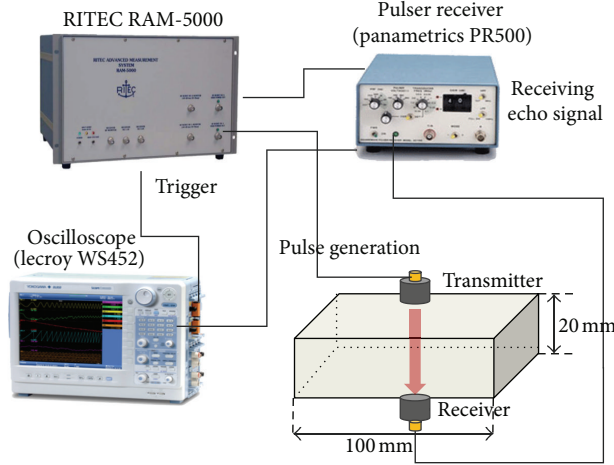


FIGURE 1: Experimental system to measure the ultrasonic nonlinear parameter.

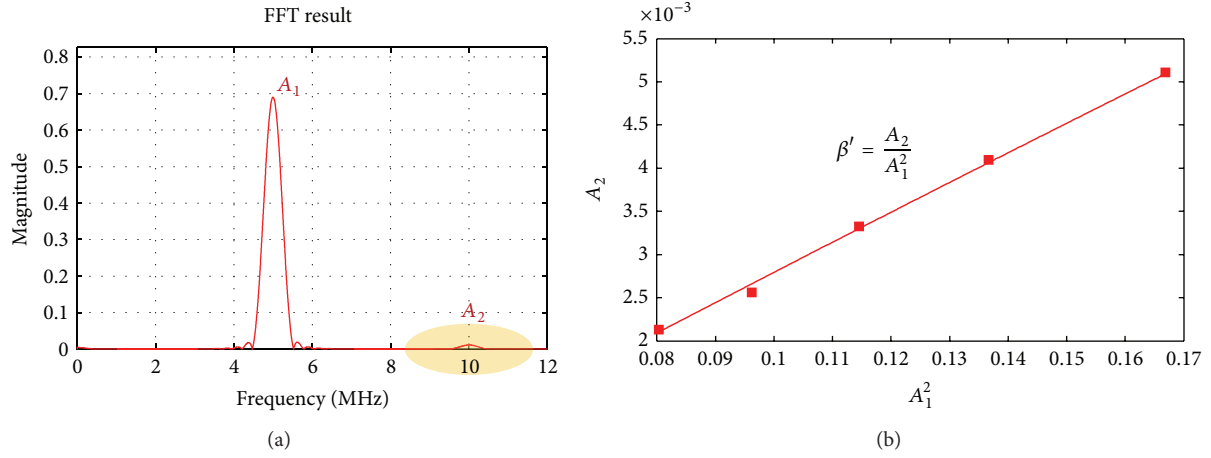


FIGURE 2: (a) Magnitude spectrum of the received signal and (b) experimental result to show the dependency of the second-harmonic amplitude on the power of fundamental frequency component.

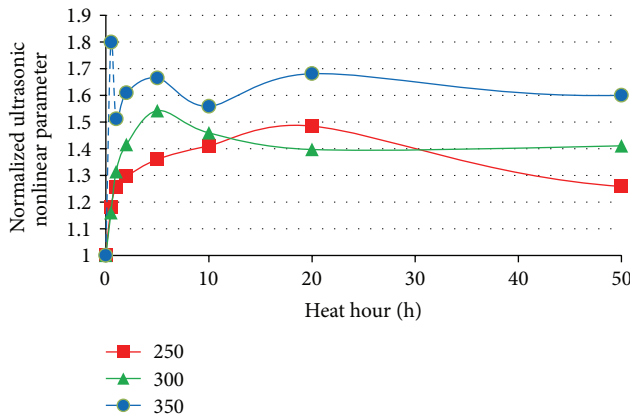


FIGURE 3: The ultrasonic nonlinear parameter obtained from three heating temperatures (250°C, 300°C, and 350°C), where the data was normalized by the value of ultrasonic nonlinear parameter obtained from no heat-treated specimen.

changes in elastic property of material, which measures the ultrasonic nonlinear parameter  $\beta$  defined by the ratio of the second-order harmonic amplitude and the power of fundamental frequency component [7, 9]. The ultrasonic nonlinear parameter is related to the nonlinear elastic constants [10, 11], which is expected to be more sensitive to the minute degradation of material than the linear elastic constant.

This paper is to demonstrate the effectiveness of ultrasonic nonlinear parameter for the evaluation of thermal degradation in the heat treated aluminum alloy (Al-Mg-Si-Cu). For this purpose, the specimens were heat treated for various heating periods up to 50 hours (1, 2, 5, 10, 20, and 50) at three different heating temperatures: 250°C, 300°C, and 350°C. 5 MHz tone burst longitudinal wave was used to measure the ultrasonic nonlinear parameter. The amplitudes of 5 MHz and 10 MHz components of the received signal were estimated by using (fast Fourier transform) FFT to obtain the ultrasonic nonlinear parameter. After the ultrasonic test,

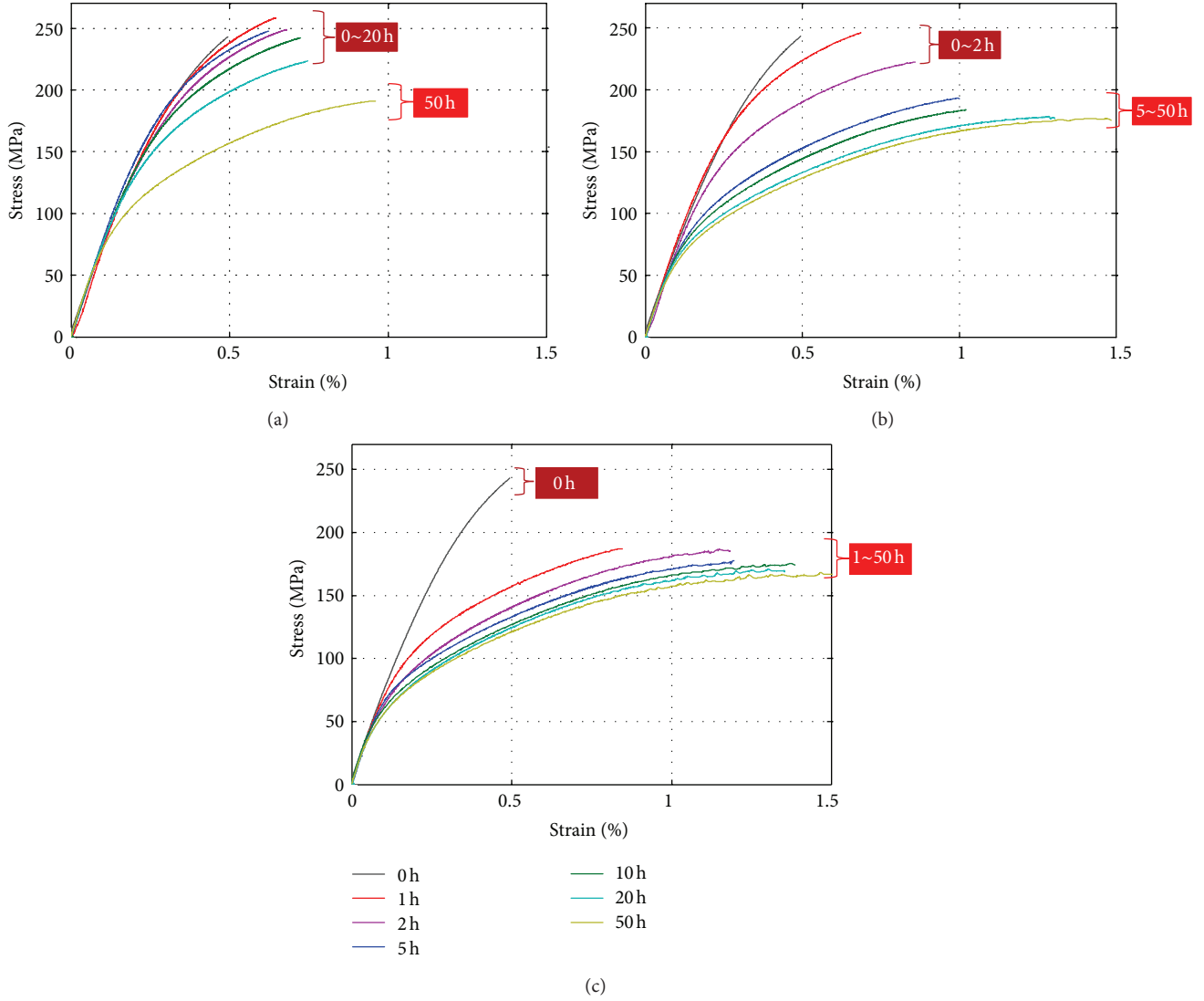


FIGURE 4: Stress-strain curve obtained from the tensile test for three heating temperatures: (a) 250°C, (b) 300°C, and (c) 350°C.

tensile strengths and elongations were obtained by the tensile test to be compared with the parameter  $\beta$ .

## 2. Ultrasonic Nonlinear Parameter

To evaluate the ultrasonic nonlinear characteristics, a single-frequency ultrasonic wave is launched into the specimen, and the signal of the ultrasonic wave transmitted through the material is received. In this process, the single-frequency ultrasonic wave is distorted due to the elastic nonlinearity and the second harmonic wave is generated. Thus, the received signal is composed of not only the fundamental frequency wave but also the second harmonic wave. The measurement of harmonic generation for microstructural characterization is typically aimed at determining the value of ultrasonic nonlinear parameter  $\beta$  defined as follows:

$$\beta = \frac{8A_2}{A_1^2 k^2 x}, \quad (1)$$

where  $A_1$  and  $A_2$  are the amplitudes of fundamental wave and the second harmonic wave, respectively,  $k$  is the wave number, and  $x$  is the wave propagation distance. In our experiments, since  $k$  and  $x$  are constants, the quantity  $\beta'$  is measured as follows [12]:

$$\beta \propto \beta' = \frac{A_2}{A_1^2}. \quad (2)$$

## 3. Experimental Procedure

The material of specimen is aluminum casting alloy, and its chemical proportion is shown in Table 1.

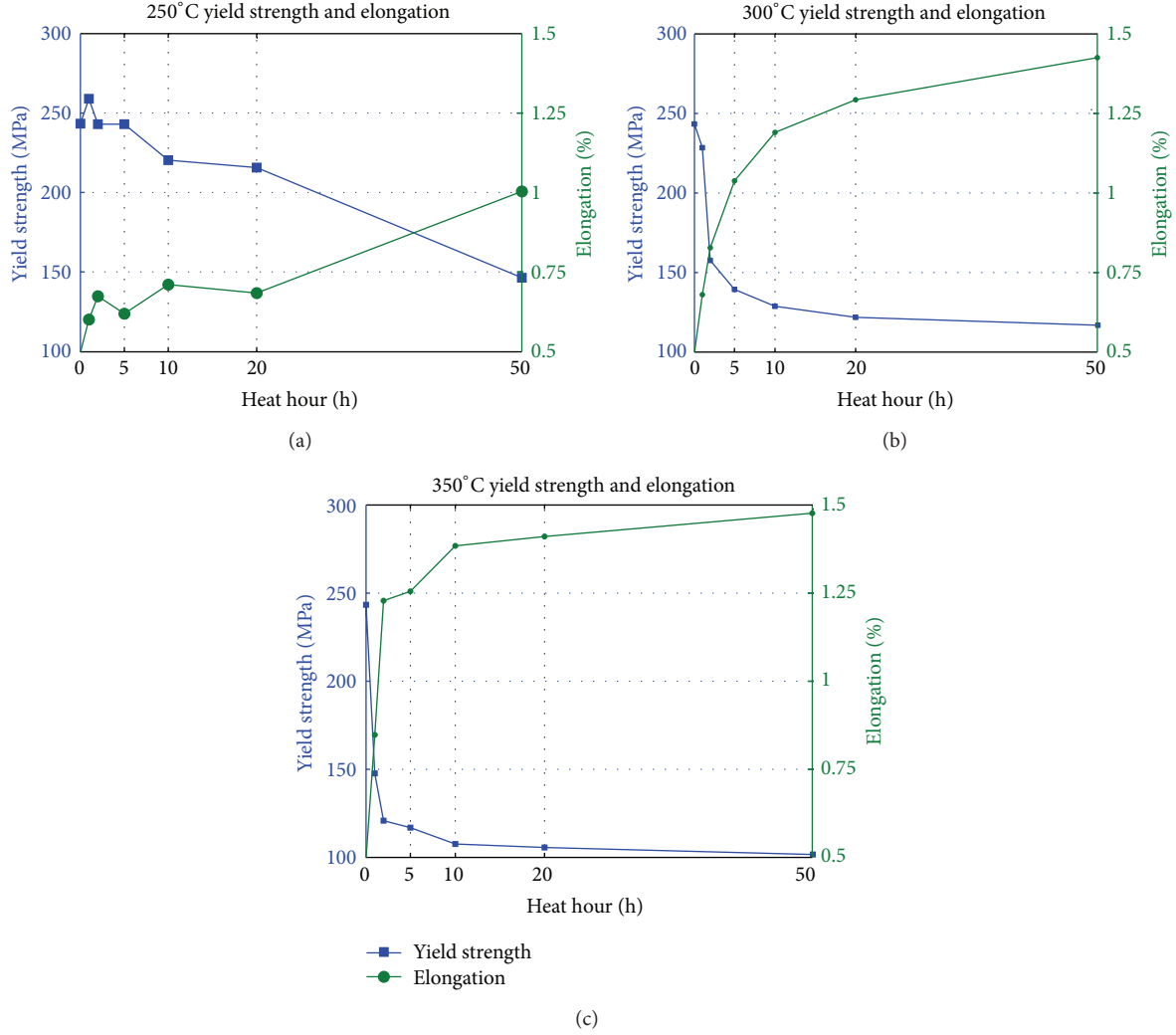


FIGURE 5: Yield strength and elongation obtained from the result of the tensile test for three heating temperatures: (a) 250°C, (b) 300°C, and (c) 350°C.

TABLE 1: Chemical proportion of aluminum alloy (in wt%).

	Al	Si	Ni	Cu	Zn	Mg	Fe
Chemical proportion (%)	77.0	13.8	1.11	3.69	3.14	0.90	0.36

The size of specimen is 100 mm × 100 mm × 20 mm. We prepared 18 specimens heat-treated in 18 different heating conditions, three different heating temperatures (250°C, 300°C, and 350°C), and six different heating period (1H, 2H, 5H, 10H, 20H, and 50H) at each heating temperature. This heat treatment is a kind of accelerated reliability test condition to generate degradation in the tensile properties. Including an intact specimen without heat treatment, the total number of specimen is 19.

In experiment, a measurement system with contact transducers was constructed as shown in Figure 1. Signal control is mainly based on the high power pulser (RAM 5000, RITEC, USA) that drives a transmitter. Transmitting frequency was set to 5 MHz, so that a 5 MHz narrowband transducer is used as the transmitter. The receiver detects the ultrasonic wave transmitting the specimen. A 10 MHz narrowband transducer was used as the receiver to detect second harmonic wave sensitively.

In order to measure the parameter  $\beta'$ , the amplitude of the fundamental frequency component and the second-harmonic amplitude were obtained by FFT of the received signal as shown in Figure 2(a). Figure 2(b) shows the relationship between  $A_1^2$  and  $A_2$ , which is obtained by increasing the input power for the intact specimen before the heat treatment. We can see clearly the linear relationship satisfying (2), and then the ultrasonic nonlinear parameter  $\beta'$  is determined

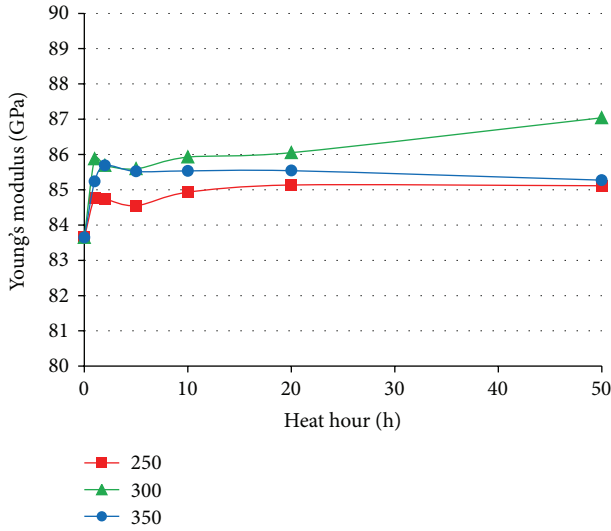


FIGURE 6: Young's modulus obtained by ultrasonic measurement of longitudinal wave velocity and shear wave velocity for three heating temperatures: (a) 250°C, (b) 300°C, and (c) 350°C.

from the slope of the fitted line. For all specimens, we measured the ultrasonic nonlinear parameters in this way.

#### 4. Results

Figure 3 shows the ultrasonic nonlinear parameter obtained for all specimens. Three curves are corresponding to three heating temperatures (250°C, 300°C, and 350°C), where the data was normalized by the value of ultrasonic nonlinear parameter obtained from the intact specimen. Maximum fluctuation in the repetition of measurement was less than 3%. Results showed that a typical peak appeared; that is, at 250°C heating temperature the peak appeared at 20-hour heat (48.5% increase as compared with intact specimen), and in 300°C heating temperature the peak appeared at 5-hours heat (54.3% increase as compared with intact specimen). From these results, it is expected that the peak appeared earlier in the higher heating temperature. At 350°C heating temperature, however, we could not see a peak earlier than 5-hours heat. We can predict only that the peak of ultrasonic nonlinear parameter might occur earlier than 1-hour heat. The data shown in dotted line in the figure is just hypothetical.

Figure 4 shows the stress-strain curves obtained from the tensile test. We can see a dramatic change at some heat-treatment hours. That is, at 250°C and 300°C heating temperatures, the stress-strain curves were dramatically changed at heat treatment time between 20 and 50 hours (16.5% increase of elongation, 32.2% decrease of yield strength) and between 2 and 5 hours (11.7% increase of elongation, 31.0% decrease of yield strength), respectively. These results showed that the heat treatment time causing drastic change of curvature in the stress-strain curve is very similar to the heat treatment time showing a peak in the ultrasonic nonlinear parameter. At 350°C heating temperature, such dramatic change appeared at heat treatment time between 0 and 1 hour (38.7% increase

of elongation, 72.1% decrease of yield strength) which means that the critical microstructural change already happened prior to 1 hour heat. This result proves our hypothesis that the first peak of ultrasonic nonlinear parameter may occurred earlier than 1-hour heat at 350°C heating temperature. From these, we can conclude that the first peak in the ultrasonic nonlinear parameter is strongly correlated with the drastic change of curvature in the stress-strain curve.

Figure 5 shows the changes in elongation and yield strength according to the heat treatment time, which were obtained from the tensile test. The increment of elongation and the decrement of yield strength are bigger at the higher heating temperature. Also, at the heating hours specifically mentioned perviously, the elongation drastically increased and the yield strength rapidly decreased.

Physically, the ultrasonic nonlinear parameter is related to the third order nonlinear elastic constant and this nonlinear elastic constant is very sensitive to the change in composition of material. The aluminum alloy tested in this study is the casting alloy (Al-Mg-Si-Cu). Generally, this alloy is thermally aged when exposed to high-temperature environment, and the precipitations (such as  $\text{Al}_2\text{Cu}$ ,  $\text{Mg}_2\text{Si}$ ) are created and transformed, which is reduced to the change of elastic property. Resultantly, the curvature in the stress-strain curve varies. The ultrasonic nonlinear parameter detected well such variation. Contrarily, the linear elastic constant obtained from the conventional ultrasonic method based on the sound velocity measurement did not show any typical change according to the heat-treatment time and the heating temperature. Figure 6 shows the measurement result of the linear elastic constant (Young's modulus).

#### 5. Conclusions

The ultrasonic nonlinear parameters in the heat-treated aluminum alloy (Al-Mg-Si-Cu) specimens have been measured and its effectiveness to evaluate the critical change in the elastic properties due to the thermal aging at high temperature was demonstrated. Specimens were heat treated at three different heating temperatures (250°C, 300°C, and 350°C) with six different heat treatment periods (1H, 2H, 5H, 10H, 20H, and 50H). After the ultrasonic test, tensile strengths and elongations were obtained by the tensile test to compare with the ultrasonic nonlinear parameter.

A typical peak appeared in the measured ultrasonic nonlinear parameter according to the heating time at each heating temperature and this peak appeared earlier in the higher heating temperature. That is, in 250°C the peak appeared at 20-hours heat, and in 300°C the peak appeared at 5-hour heat. In 350°C, such peak was expected to occur earlier than 1-hour heating. From the tensile tests, these heating periods were found to be identical to those when the curvatures of stress-strain curve were dramatically changed with the rapid increment of elongation and the sharp decrement of yield strength.

From these, we can conclude that the first peak in the ultrasonic nonlinear parameter is strongly correlated with the drastic change of curvature in the stress-strain

curve and that the nonlinear ultrasonic method is useful to evaluate the critical change of elastic property by thermal degradation in heat treated aluminum alloys. Note that the linear elastic constant measured by conventional ultrasonic method based on the sound velocity measurement did not show any critical change according to the heating time and the heating temperature.

## Acknowledgment

This work was financially supported by the National Research Foundation of Korea (NRF) Grant funded by the Korean government (NRF-2013M2A2A9043241).

## References

- [1] S. H. Baek, T. H. Lee, C. S. Kim, and K. Y. Jhang, "Ultrasonic nonlinearity measurement in heat treated SA508 alloy: influences of grains and precipitates," *Journal of the Korean Society for Nondestructive Testing*, vol. 30, no. 5, pp. 451–457, 2010.
- [2] M. Kikuchi, M. Takahashi, and O. Okuno, "Elastic moduli of cast Ti-Au, Ti-Ag, and Ti-Cu alloys," *Dental Materials*, vol. 22, no. 7, pp. 641–646, 2006.
- [3] A. Badidi Bouda, S. Lebaili, and A. Benchaala, "Grain size influence on ultrasonic velocities and attenuation," *NDT & E International*, vol. 36, no. 1, pp. 1–5, 2003.
- [4] MAGNAFLUX, *Magnaflux Quasar 4000 Quality Test Systems*, 2013, <http://www.quasarintl.com/ndt-products>.
- [5] U. S. Park, I. K. Park, and C. S. Kim, "A study on the evaluation of material degradation for 2.25Cr-1Mo steel by ultrasonic measurements," *Transactions of the Korea Society of Machine Tool Engineer*, vol. 10, no. 3, pp. 61–67, 2001.
- [6] P. Palanichamy, M. D. Mathew, S. Latha et al., "Assessing microstructural changes in alloy 625 using ultrasonic waves and correlation with tensile properties," *Scripta Materialia*, vol. 45, no. 9, pp. 1025–1030, 2001.
- [7] K.-Y. Jhang, "Applications of nonlinear ultrasonics to the NDE of material degradation," *IEEE Transactions on Ultrasonics, Ferroelectrics, and Frequency Control*, vol. 47, no. 3, pp. 540–548, 2000.
- [8] G. E. Dace, P. B. Thompson, and L. J. H. Brash, "Nonlinear acoustics, a technique to determine microstructural changes in material," in *Review of Progress in Quantitative Nondestructive Evaluation*, vol. 10, pp. 1685–1692, Plenum Press, New York, NY, USA, 1991.
- [9] J. K. Na, J. H. Cantrell, and W. T. Yost, "Linear and nonlinear ultrasonic properties of fatigues 410Cb stainless steel," in *Review of Progress in Quantitative Nondestructive Evaluation*, vol. 15, pp. 1347–1351, Plenum Press, 1996.
- [10] T. Kundu, *Ultrasonic and Electromagnetic NDE for Structure and Material Characterization-Engineering and Biomedical Application*, CRC Press, 2012.
- [11] J.-Y. Kim, L. J. Jacobs, J. Qu, and J. W. Little, "Experimental characterization of fatigue damage in a nickel-base superalloy using nonlinear ultrasonic waves," *Journal of the Acoustical Society of America*, vol. 120, no. 3, pp. 1266–1273, 2006.
- [12] I. H. Choi, T. H. Lee, and K. Y. Jhang, "Evaluation of fatigue degradation using nonlinear ultrasonics," *Review of Progress in Quantitative Nondestructive Evaluation*, vol. 29, pp. 1433–1438, 2011.

## Research Article

# Deformation Properties and Fatigue of Bituminous Mixtures

Frantisek Schlosser,<sup>1</sup> Jan Mikolaj,<sup>1</sup> Viera Zatkalikova,<sup>2</sup> Juraj Sramek,<sup>1</sup>  
Dominika Durekova,<sup>1</sup> and Lubos Remek<sup>1</sup>

<sup>1</sup> Department of Construction Management, Faculty of Civil Engineering, University of Zilina, Univerzitna 8215/1,  
01026 Zilina, Slovakia

<sup>2</sup> Department of Materials Engineering, Faculty of Mechanical Engineering, University of Zilina, Univerzitna 8215/1,  
01026 Zilina, Slovakia

Correspondence should be addressed to Lubos Remek; [lubos.remek@fstav.uniza.sk](mailto:lubos.remek@fstav.uniza.sk)

Received 11 July 2013; Accepted 10 September 2013

Academic Editor: Young Soo Choi

Copyright © 2013 Frantisek Schlosser et al. This is an open access article distributed under the Creative Commons Attribution License, which permits unrestricted use, distribution, and reproduction in any medium, provided the original work is properly cited.

Deformation properties and fatigue performance are important characteristics of asphalt bound materials which are used for construction of pavement layers. Viscoelastic asphalt mixtures are better characterized via dynamic tests. This type of tests allows us to collate materials with regard to axle vibrations which lie usually in the range of 6 Hz–25 Hz for standard conditions. Asphalt modified for heat sensitivity in the range from  $-20^{\circ}\text{C}$  to  $+60^{\circ}\text{C}$  has significant impact on the overall characteristics of the mixture. Deformation properties are used as inputs for empirical mixture design, and fatigue performance of asphalt mixtures reflects the parameters of functional tests. Master curves convey properties of asphalt mixtures for various conditions and allow us to evaluate them without the need of time expensive testing.

## 1. Asphalt Binders and Asphalt Mixtures

Deformation properties, resistance to deformation, and fatigue performance of asphalt mixtures have a significant influence on operational performance of asphalt pavements. Within the pavement construction, the asphalt serves as a binder for mineral aggregate of surfacing layer. Asphalt is a bituminous material obtained as a residue of vacuum distillation process during the refining of crude oil [1]. Mechanical properties of asphalt mixture are mostly affected by the properties of applied asphalt binder. In regard to mixing process, asphalt binder must be fluid enough at high temperatures—about  $160^{\circ}\text{C}$ —to create homogenous coating of the aggregate. Local climate plays a role as the binder has to maintain prescribed stiffness at the highest summer temperature to resist rutting deformation, yet it has to remain flexible enough at low temperatures during the winter season [2].

The assessment of deformation properties is performed by means of dynamic impact test and fatigue life of particular asphalt mixture. Evaluation of fatigue life is based on resistance decrease or deformation increase in different binders and mixtures. Concurrently, the evaluation itself is performed

in accordance with standard for measurement of complex modulus [3] and fatigue [4] of asphalt reinforced materials, that is, mixtures; these regulations represent realistic traffic-car axle during normal operation at the frequency from 6 to 25 Hz.

**1.1. Asphalt Binder Laboratory Tests.** Asphalt binders are thermoplastic liquids which behave as viscoelastic materials [5]. Their deformation behaviour can be determined by their rheological parameters. The changes in both viscous and elastic properties related to temperature and time are measured as response of the material to deformation induced by periodic forces-vibration or small-amplitude oscillatory stress. Phases of induced stress and responding deformation do not match exactly; the strain phase lags behind the stress by a certain phase angle. If the oscillatory deformation is sinusoidal, shear stress  $\tau$  is expressed as [6, 7]

$$\tau(t) = \tau_0 \cdot e^{i\omega t} = \tau_0 (\cos \omega t + i \cdot \sin \omega t), \quad (1)$$

where  $\tau_0$  is the stress amplitude,  $\omega$  is the angular frequency,  $t$  is the time, and  $i = \sqrt{-1}$ .

TABLE 1: Basic properties of tested bituminous binders.

Type of binder	Unmodified binders	
	B 50/70	B 70/100 (Q8)
Softening point (°C); STN EN 1427	46–54	43–51
Penetration at 25°C (0,1 mm); STN EN 1426	50–70	70–100

The complex dynamic modulus  $G^*$  [Pa] is defined as [6, 7]

$$G^* = \frac{\tau(t)}{\gamma(t)}. \quad (2)$$

Equation (2) can be divided into two parts:

$$G^* = G' + i \cdot G'' = \frac{\tau_0}{\gamma_0} (\cos \delta + i \cdot \sin \delta). \quad (3)$$

The first  $G'$  is in phase with strain, and the second  $G''$  is out of phase with strain with angle  $\delta$ . Therefore, two dynamic modules are defined [6, 7]:

$$G' = \frac{\tau_0}{\gamma_0} \cos \delta, \quad (4)$$

$$G'' = \frac{\tau_0}{\gamma_0} \sin \delta. \quad (5)$$

$G'$  is called storage modulus and its value is strain energy stored by the sample during the shear process. Thus, it represents the elastic behaviour. The value of loss modulus  $G''$  is measured as strain energy used up by the sample during the shear process; therefore, they represent the viscous behaviour of the material. A part of this energy heats the sample and is released as heat to the environment. Sample with high loss modulus exhibits irreversible deformation [6, 7].

The complex dynamic viscosity  $\eta^*$  [Pa·s] is defined by

$$\eta^* = \frac{\tau(t)}{\dot{\gamma}(t)}, \quad (6)$$

where  $\dot{\gamma}$  [s<sup>-1</sup>] represents the shear rate [6, 7].

## 2. Performed Testing

The comparison of rheological parameters  $\eta^*$ ,  $G'$ , and  $G''$  was performed for selected unmodified and polymer modified asphalt binders at the temperatures of 46°C–60°C (80°C). Rheological properties were determined and compared for unmodified bituminous binders B 50/70 and B 70/100 (Q8). Basic properties of tested materials are in Table 1. The composition of aggregate is equal for both mixtures, it is shown in Table 2.

Measurements were performed on the oscillatory Physica Rheometer MCR301 with convection heating device CTD 450. The applied method was the frequency sweep test (FS). FS method uses parallel plate system—PP system: lower plate is stationary; upper plate performs oscillatory motion and thus creates a shear in the sample. The distance between the plates—shearing interval—is well defined (Figure 1).

TABLE 2: Tested mix designs for AC 11 pavement layer.

Mixture	Mixture 1 (A1) %	Mixture 2 (A2) %
	B 70/100 (Q8)	PmB 70/100-83
Filler		7,1%
0/2 mm		29,3%
2/4 mm		15,6%
4/8 mm		22,6%
8/11 mm		19,8%
Binder		5,6%
Sum		100,00%

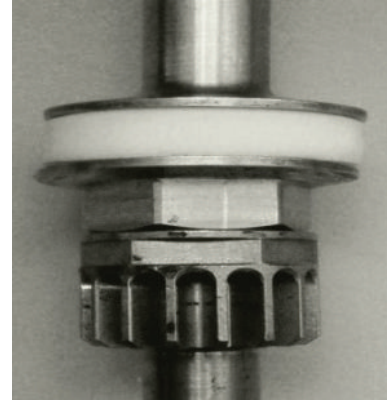


FIGURE 1: PP system, Physica Rheometer MCR301.

FS test is performed at a constant temperature. This measurement method enables simultaneous monitoring of rheological parameters  $G'$ ,  $G''$ , and  $\eta^*$  in the selected interval of angular frequencies [6]. Each test sample was placed between the two parallel plates with a diameter of 25 mm (PP25 system), with 1 mm distance from each other—shearing interval = 1 mm.

The trend of monitored rheological parameters  $G'$ ,  $G''$ , and  $\eta^*$  in dependence on angular frequency is linear except for storage modulus  $G'$  at angular frequencies 400–600 s<sup>-1</sup> at 60°C (Figure 2). Except for the above mentioned case, the  $G'$  and  $G''$  curves are nearly parallel. Ratio between viscous and elastic properties remains the same; this means that degradation which would be shown by changes in molecular weight—networking or macromolecular chains breaking—is not probable [6].

In addition, the modified binders were also tested. The chart curves expressing storage modulus  $G'$  are losing their linearity at angular frequencies of 400–600 s<sup>-1</sup>. The sharp decrease of  $G'$  denotes higher ratio between loss modulus  $G''$  and storage modulus  $G'$ , that is, damping factor. This points to degradation related to the loss of elasticity.

Knowledge ascertained from measurements is as follows:

- polymer-modified binder achieves the highest values of evaluated rheological parameters  $G'$ ,  $G''$ , and  $\eta^*$  in the considered interval of angular frequencies at the temperature of 60°C. The lowest values of rheological parameters were measured for unmodified binder Q8 70/100;

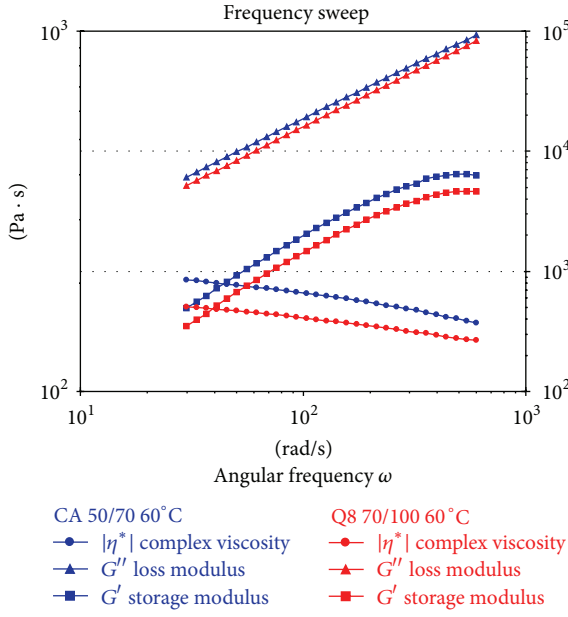


FIGURE 2: Comparison of rheological parameters of unmodified binders at 60°C.

- (ii) modified binders show more significant reduction in complex viscosity with the increase of angular frequency in comparison to unmodified binders;
- (iii) according to the obtained results, from the set of tested binders, the modified binders are most suitable for heavy duty pavements in climate with strong temperature fluctuations.

In order to obtain required properties, asphalt binders are not used exclusively in the form of pure asphalt, that is, unmodified asphalt binders; instead, they can be modified by synthetic polymers. Polymer modified bitumen (PMB) has higher softening point and lower breaking point than unmodified ones. Therefore, it is recommended for construction of heavy duty pavements in climates with large temperature fluctuations [3–5].

**2.1. Laboratory Tests of Asphalt Mixtures.** Complex modulus ( $E^*$ ) is a ratio of strain and deformation at steady, harmonically variable oscillation in consideration of their mutual time shift [8]:

$$E^* = \frac{\sigma_0}{\varepsilon_0} = (E_1^2 + E_2^2)^{1/2}. \quad (7)$$

Complex modulus is measured on samples exposed to short-term alternating harmonic load. It conveys the proportion of maximum amplitude of excitation tension ( $\sigma_0$ ), maximum amplitude of induced deformation ( $\varepsilon_0$ ), and phase shift of their amplitudes ( $\varphi$ ). The stress, that is, load, which varies sinusoidally in time, is applied to the element of linear viscoelastic material. The strain varies in time with the same frequency as the stress, but it lags behind by the phase. The measured values for particular mixtures are graphically presented in chart shown in Figure 3. Graphical representation

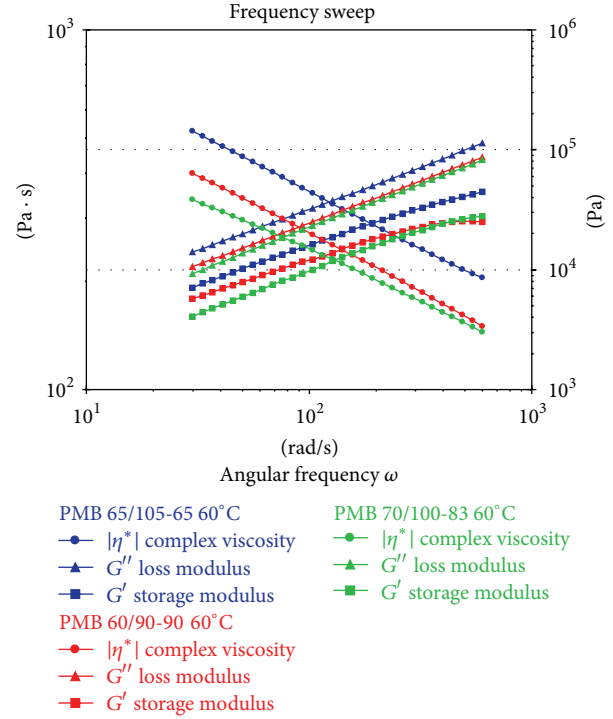


FIGURE 3: Comparison of rheological parameters of 3 modified binders at 60°C.

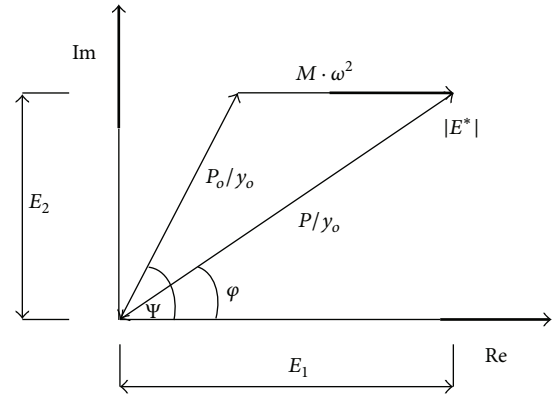


FIGURE 4: Scheme of complex modulus.

of measurement and complex modulus evaluation is shown in Figures 4 and 5.

An accurate assessment of the fatigue life of asphalt mixtures depends on the criteria used in the fatigue analysis [9].

Fatigue is reduction of strength of a material under repeated loading when compared to the strength under a single load [10]. The value  $\varepsilon_6 = 1 \cdot 10^6$  cycles (in m/m) is the strain corresponding to  $10^6$  cycles [10].

According to the Slovak dimensioning method, the fatigue is given by

$$S = a - b \cdot \log N_i, \quad (8)$$

where  $a, b$  are the fatigue coefficients and  $N_i$  is the number of load cycles.

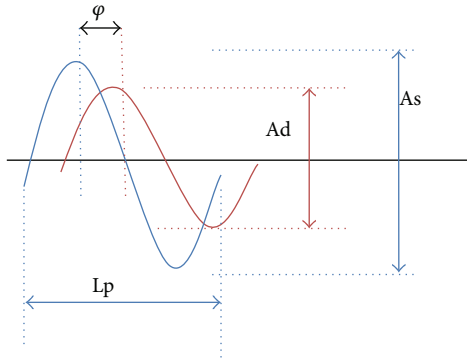


FIGURE 5: Measurement of complex modulus:  $L_p$ : length of period,  $\varphi$ : phase-shift,  $A_s$ : amplitude forces, and  $A_d$ : amplitude deformations.



FIGURE 6: Two-point trapezoidal bending beam machine used at the University of Zilina.

The tests of the complex modulus and fatigue performance were carried out in the laboratory of the Department of Construction Management of the University of Zilina (Figure 6). The equipment works with constant deviation. It is possible to change the frequency from 0.1 to 30 Hz and temperature for the tests from  $-20^{\circ}\text{C}$  to  $+30^{\circ}\text{C}$ .

Bending tests are used to ascertain the complex modulus and fatigue resistance of asphalt pavement surfacing materials. The two-point bending test on trapezoidal sample is arguably the most repeatable and reproducible bending test method detailed in the relevant EN 12697 directives [8, 10]. The samples were carefully stored on a flat surface protected from the sun at a temperature of  $<30^{\circ}\text{C}$  to prevent distortion. The samples were measured with an accuracy of 0.1 mm.

In this test, the bottom of the sample is fixed and the free top is moved sinusoidally with constant displacement amplitude. The trapezoidal samples are tested simultaneously; they are subjected to constant strain amplitude at a selected frequency and temperature until the stiffness modulus decreases. Fatigue life of a sample is the number of cycles  $N_{i,j,k}$  corresponding to the conventional failure criterion at

the set of test conditions  $k$ -temperature, frequency, and loading mode, for example, constant deflection level, or constant force level, and or any other constant loading condition. It is a number of load applications,  $N_f/50$ , during which the complex modulus decreases to half of its initial value [10].

### 3. Tested Mix Designs and Measurements Results

Complex modulus and fatigue performance were tested for two mix designs. The aggregate content and ratios stay the same for both mixtures. However, the 1st mixture (A1) contains generic asphalt binder B 70/100 (Q8) compared to the 2nd mixture (A2) which contains polymer modified bitumen PmB 70/100-83. Both mixtures can be applied for the AC11 pavement layer. In general, pavement performance properties are affected by the bitumen binder properties; it is known that the conventional bitumen has a limited range of rheological properties and durability that are not sufficient enough to resist pavement distresses [11]. Therefore, the testing was aimed to show us the magnitude of impacts on mixture properties attained through binder modification.

**3.1. Results: Complex Modulus.** Both samples were tested at temperatures ranging from  $-10^{\circ}\text{C}$  to  $+27^{\circ}\text{C}$ . The frequency varied from 1 Hz to 20 Hz. The measured results of complex modulus of mixture A1 are listed in Table 3 and Figure 7. The complex modulus ( $E^*$ ) is different for temperatures of  $+10^{\circ}\text{C}$  and  $+15^{\circ}\text{C}$  during the same frequency (10 Hz):

$$E_{T=10^{\circ}\text{C}; F=10\text{ Hz}}^* = 8364,7 \text{ MPa},$$

$$E_{T=15^{\circ}\text{C}; F=10\text{ Hz}}^* = 5938,0 \text{ MPa}.$$

With identical approach, the same types of results were measured for mixture A2:

$$E_{T=10^{\circ}\text{C}; F=10\text{ Hz}}^* = 5844 \text{ MPa},$$

$$E_{T=15^{\circ}\text{C}; F=10\text{ Hz}}^* = 4032 \text{ MPa}.$$

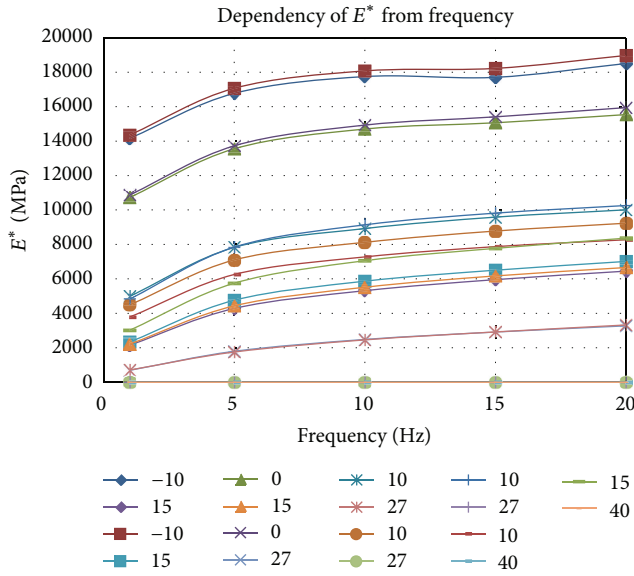
In addition, deformation properties were verified for a third mix design A3rec, which is prepared from mixture A2 with 40% of the aggregate made of asphalt recycled material—recycle aggregate. For the A3rec mix design, less favourable deformational properties were ascertained. These were probably the consequence of brittleness of old asphalt in the new mixture and altered grain distribution curve as a result of added recycled material.

Complex modulus was measured by  $\varepsilon < 50 \cdot 10^{-6}$  (microstrains). The reason to introduce this mix design to the test was that as natural aggregate sources are becoming depleted due to high demand in road construction and as the amount of disposed waste material keeps increasing, researchers are exploring the use of alternative materials which could preserve natural sources and save the environment [12].

**3.2. Results: Fatigue Performance.** Fatigue life was measured on samples, which were loaded at  $+10^{\circ}\text{C}$  with frequency of 25 Hz. The fatigue line is estimated in a bilogarithmic system

TABLE 3: Complex modulus of mixture A1 in MPa.

Temperature (°C)	Complex modulus $E^*$ (MPa)				
	Frequency (Hz)				
	1	5	10	15	20
−10	14158	16769	17744	17700	18503
−10	14351	17063	18073	18219	18970
0	10727	13551	14698	15062	15538
0	10874	13723	14927	15407	15943
10	4991	7827	8923	9586	10009
10	4494	7098	8122	8778	9233
10	4832	7844	9138	9818	10260
10	3786	6256	7276	7873	8272
15	3021	5749	7055	7773	8366
15	2151	4284	5315	5958	6451
15	2339	4759	5867	6506	7014
15	2216	4436	5515	6173	6660
27	695	1798	2487	2915	3275
27	713	1755	2460	2922	3327

FIGURE 7: Dependency of complex modulus ( $E^*$ ) from frequency ( $F$ ) for mixture A1 for temperatures ranging from  $-10^\circ\text{C}$  to  $+27^\circ\text{C}$ .

as a linear regression of fatigue life versus amplitude levels. Using these results, the strain corresponds to an average of  $10^6$  cycles ( $\epsilon_6$ ) and the slope of the fatigue line  $1/b$ . The parameters are

- (a)  $\epsilon_6$ ,
- (b)  $\Delta\epsilon_6$ ,
- (c) slope  $1/b$ ,
- (d) estimated residual standard deviation  $s_N$ ,
- (e) correlation coefficient  $r^2$ .

The evaluation was performed in accordance with

$$\lg(N) = a + \left(\frac{1}{b}\right) \times \lg(\epsilon). \quad (9)$$

For  $n$  results, the following were calculated:

- (i) the estimation of the strain at  $10^6$  cycles (10),
- (ii) the estimation of the residual standard deviation  $s_N$  (11),
- (iii) the quality index  $\Delta\epsilon_6$  (12),

$$\epsilon_6 = 10^{b \times (6-a)}, \quad (10)$$

$$S_N = S_{\lg(N)} \times \sqrt{\frac{(1-r_2^2) \times (n-1)}{n-2}}, \quad (11)$$

$$\Delta\epsilon_6 = 0.5\epsilon_6 \times (10^{-2b \times S_0} - 10^{2b \times S_0}), \quad (12)$$

where

$$S_0 = S_N \times \sqrt{\left[ \frac{1}{n} + \frac{(\lg(\epsilon_6) - \lg(\epsilon))^2}{(n-1) \times S_{\lg(\epsilon)}^2} \right]}. \quad (13)$$

The samples were subject to fatigue testing for three deformation values of the trapezoid's unfastened end, whereby the testing ended when the complex modulus decreased by half of its initial value. The fatigue is expressed as a value of  $\epsilon_6$ , which is ascertained from linear regression for measurement on 18 testing samples. For mixtures A1, A2, and A3rec, ascertained values are presented in Table 4. The graphical representation of measured results is shown in Wöhler's diagram (Figure 8).

#### 4. Evaluation: Master Curves

All three mixtures were subject to evaluation of maser curves. The evaluation was performed by means of master curves—after introducing the gas constant—at the frequency from 3

TABLE 4: Fatigue of mix designs A1 and A2.

Mix.	Temp. (°C)	Freq. (Hz)	$\epsilon_6 \cdot 10^6$ (microstrain)	$N_i$ (cycles)	$b$ (—)	$r^2$ (—)	$s_N$	$\Delta\epsilon_6$	Category
A1	+10	25	87,44	10908–2156738	−0,2060	0,9554	0,1437	$4,61E-10$	$\epsilon_{6-80}$
A2	+10	25	193,10	40500–2382028	−0,1310	0,5726	0,4481	$4,41E-09$	$\epsilon_{6-190}$
A3rec	+10	25	166,38	300–2369414	−0,0397	0,8039	0,6119	$1,24E-09$	$\epsilon_{6-60}$

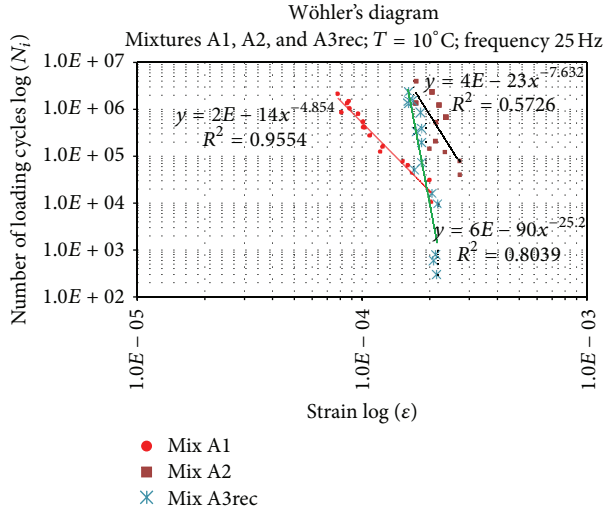
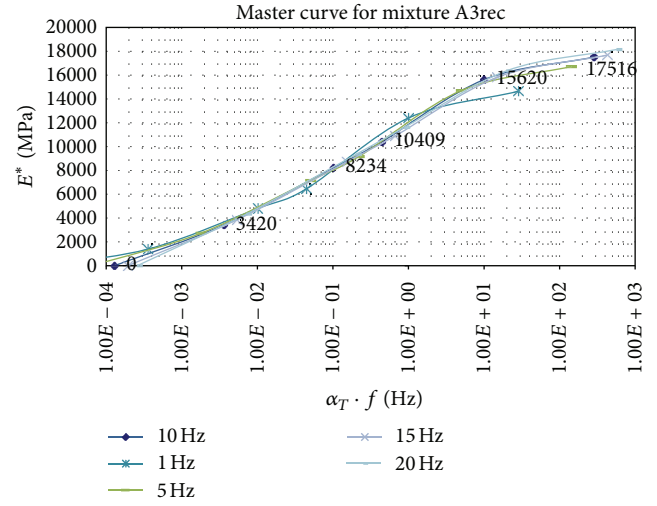


FIGURE 8: Fatigue life of mixtures with asphalt B 70/100 (A1), PmB 70/100-83 (A2), and 40% of recycling material (A3rec).

FIGURE 9: Master curve for mixture A3rec in MPa for temperature ranging from  $-10^\circ\text{C}$  to  $+27^\circ\text{C}$  and frequency ranging from 1 Hz to 20 Hz.

to 97 Hz. The values are computed according to the following [8]:

$$\alpha_T = \exp \frac{\Delta H}{R} \left( \frac{1}{T} - \frac{1}{T_s} \right), \quad (14)$$

where  $\Delta H$  is the apparent energy activation ( $2 \cdot 10^5 \text{ Jmol}^{-1}$ ),  $R$  is the universal gas constant ( $8.31434 \text{ Jmol}^{-1} \text{ K}^{-1}$ ), and  $T$ ,  $T_s$  are the temperatures expressed in  $^\circ\text{K}$  ( $T_s$  is the reference temperature).

The advantage of master curves is that they allow the evaluation of properties of asphalt mixtures for different temperatures and frequencies with lower number of tests—recomputed values that express deformation properties of asphalt mixtures. The master curves convey the changes of complex modulus induced by temperatures affecting the pavement during its life span.

Figure 9 shows the master curves for mixture A3rec. We can observe the changes of complex modulus at different temperatures and the frequencies of excitation force—continuous lines. Discrete values in Figure 9 show the change in complex modulus at a constant temperature but at various frequencies of the excitation force.

## 5. Conclusions

According to the performed measurements, we ascertained that the mixture A1 with unmodified binder has superior deformation properties ( $E^*$ ), while the modified binder mixture A2 has superior fatigue life parameter ( $\epsilon_6$ ). Asphalt,

from the viewpoint of fatigue parameters, has a paramount influence on asphalt mixtures used for construction of pavement surface layers. Deformation characteristics and fatigue of asphalt binder influence normatively prescribed characteristics of pavement layers. Evaluated asphalts have varying complex modulus values in dependence on temperature. In spite of the fact that modified asphalt has higher values of shear modulus, the deformation properties are inferior, whereas fatigue life is superior. This knowledge was confirmed by measurements of other mixtures. The empirical mixture design methods usually use deformation properties; fatigue life characteristics are pivotal for functional testing. All three mixtures are satisfactory from the viewpoint of physicomaterial properties. Design of asphalt bound materials for pavement layers is empirical and utilizes deformation properties like complex modulus. However, for functional tests, fatigue life characteristic ( $\epsilon_6$ ) is more important. For different values of deformation properties and fatigue life, it is pivotal that the designed mixture is evaluated for required bearing capacity and resiliency against climate conditions.

Measurements show that superior modified asphalt mixture is defined by auspicious fatigue parameters. Deformation properties and fatigue life were validated also on mixture A3rec. The recycled aggregate was a milled-out pavement surfacing material. The A3rec mixture has lower fatigue life parameter, the angle of regression line is more acute, and the value of proportional deformation for one million cycles ( $\epsilon_6$ ) is lower. Despite this, the mixture is applicable for pavement construction layers and can be utilized for subbase layers.

## Acknowledgments

The research was supported partially by Scientific Grant Agency of Ministry of Education, Science and Sport of Slovak Republic and Slovak Academy of Science Grant VEGA no. 1/0485/12.

## References

- [1] V. Simanzhnnkov and R. Idem, *Crude Oil Chemistry*, CRC Press, New York, NY, USA, 2003.
- [2] D. Leseueur, "The thermo-rheological complexity and relaxation of asphalt cements," *Journal of Rheology*, vol. 43, pp. 1701–1704, 1999.
- [3] G. D. Airey, "Rheological properties of styrene butadiene styrene polymer modified road bitumens," *Fuel*, vol. 82, no. 14, pp. 1709–1719, 2003.
- [4] G. D. Airey, "Styrene butadiene styrene polymer modification of road bitumens," *Journal of Materials Science*, vol. 39, no. 3, pp. 951–959, 2004.
- [5] J. L. Goodrich, "Asphalt and polymere modified asphalt properties related to the performance of asphalt concrete mixes," *Proceedings of the Association of Asphalt Paving Technologists*, vol. 57, pp. 116–175, 1988.
- [6] T. G. Mezger, *The Rheology Handbook*, Vincentz Network, Hannover, Germany, 2nd edition, 2006.
- [7] J. Kahovec, *Rheology of Polymer Systems*, Wiley-VCH, Praha, Czech Republic, 2000.
- [8] "Bituminous mixtures—test methods for hot mix asphalt—part 26: stiffness," EN, 12697-26:2007 (S), 2007.
- [9] M. J. Khattak and G. Y. Baladi, "Analysis of fatigue and fracture of hot mix asphalt mixtures," *ISRN Civil Engineering*, vol. 2013, Article ID 901652, 10 pages, 2013.
- [10] "Bituminous mixtures—test methods for hot mix asphalt—part 24: resistance to fatigue," EN12697-24:2003 (E), 2003.
- [11] N. S. Mashaan, A. H. Ali, S. Koting, and M. R. Karim, "Performance evaluation of crumb rubber modified stone mastic asphalt pavement in Malaysia," *Advances in Materials Science and Engineering*, vol. 2013, Article ID 304676, 8 pages, 2013.
- [12] M. R. Hainin, N. I. Md. Yusoff, M. F. M. Sabri, M. A. Abdul Aziz, M. A. A. Hameed, and W. F. Reshi, "Steel Slag as an aggregate replacement in Malaysian hot mix asphalt," *ISRN Civil Engineering*, vol. 2012, Article ID 459016, 5 pages, 2012.

## Research Article

# A Study on Contact Fatigue Performance of Nitrided and TiN Coated Gears

Hongbin Xu,<sup>1</sup> Hui Li,<sup>2</sup> Jianjun Hu,<sup>2</sup> and Song Wang<sup>2</sup>

<sup>1</sup> Key Laboratory of Manufacture and Test Techniques for Automobile Parts, Ministry of Education, Chongqing 400054, China

<sup>2</sup> Material Science and Engineering College, Chongqing University of Technology, Chongqing 400054, China

Correspondence should be addressed to Hui Li; 28406053@qq.com

Received 19 July 2013; Accepted 1 September 2013

Academic Editor: Xing Chen

Copyright © 2013 Hongbin Xu et al. This is an open access article distributed under the Creative Commons Attribution License, which permits unrestricted use, distribution, and reproduction in any medium, provided the original work is properly cited.

This paper discusses the effects of TiN coating on gear contact fatigue performance through contact fatigue experiment and gear rig test. The results reveal that the deposition on gears with hard coating TiN could provide the subsurface protection and improve the contact fatigue life, and the contact fatigue strength of nitrided+TiN coated 32Cr2MoV is 1557 MPa at survival probability of 99%, 284 MPa higher than that of nitrided 32Cr2MoV. Although TiN coating on the the edge of the meshing zone wore out, there is no obvious pitting at the site and the rest of meshed zone of TiN coated gear keeps well without pittings and wear grooves, which is opposite to nitrided gears with pittings and peeling off. TiN coating is dense and smooth with lower surface roughness, and it wraps up the gear tooth so that the gear surface no longer contacts with lubricant and prevents the cracks initiation, prolonging the contact fatigue life of gears.

## 1. Introduction

The development in trend of gears, focusing on high-speed, heavy-duty, light weight, and small sizes, makes hardness promotion of gear face through traditional surface treatment and improvement of the bearing capacity of gears by enlarging module faces many limitations. Special work conditions require new type of surface strengthening methods as well as new gear materials with high performance. The hard thin coatings with lower friction and higher wear-resistance, for instance, MoS<sub>2</sub> [1], DLC [2], WC/C [3, 4], TiN [5, 6], or the others [5, 7], have been studied for enhancing the surface contact fatigue life. In most cases, the effects of hard coatings on rolling contact fatigue have been mainly investigated by using a roller tester, pin-on-ring tester, three ball-on-rod tester, and so on, which reveals that coatings deposited by PVD could improve the wear resistance and contact fatigue life of substrate. However, it is not always easy to evaluate the tribological properties of tooth surface in meshingly using these fundamental testers [8, 9].

Among the common ceramic coatings, the titanium nitride (TiN) is featured by excellent wear-resistance, low friction against metals, and more mature technology, making

it widely used in tool and die industry [10, 11]. To confirm the effects of surface engineering on load carrying capacity of gears, this paper dwelled on load carrying capacity of nitrided and TiN deposited gears by means of contact fatigue experiment and gear rig test; additional tooth surface failure was investigated.

## 2. Experiment Details

According to Chinese Standard, 32Cr2MoV whose composition was reported in Table 1 was selected to proceed with the experiment, and the geometrical characteristic of gears used in test was presented in Table 2. Heat treatments of samples were as follows: (1) austenitizing at 940°C for 1 h, (2) oil cooling to room temperature, and (3) heating up to 640°C and holding for 1.5 h, then air cooling. After tempering and machining, all samples have been plasma nitrided at 530°C~550°C for 20 hours.

To synthesize the TiN coating by multi-arc ion plating, the work chamber was first vacuumed to pressure of  $6.67 \times 10^{-4}$  Pa, and then Ar gas was introduced into the chamber to clean the workpiece surface by sputtering for 5 minutes.

TABLE 1: The composition of 32Cr2MoV (Wt/%).

Material	C	Si	Mn	Cr	Mo	V
32Cr2MoV	0.30~0.34	0.34~0.38	0.48~0.60	2.10~2.23	1.3~1.6	0.24

TABLE 2: Gear specification.

Gear type	Tooth profile	Accuracy	Module/mm	Number of teeth	Pressure angle	Surface hardness
Drive gears	Standard involutes	5	1.75	17	20°	>HRC 58
Driven gears		5	1.75	32		>HRC 58

TABLE 3: Operating conditions in gear test.

Torque $T/N \cdot m$	Rotational speed $R$ r/min	Normal load $L/N$	Contact stress $\sigma/MPa$	Time $t/h$
16.71	2000	1250	1235	84

A DC bias voltage 200 V was applied on the Ti target to motivate the ionic Ti coated on the surface for 3 minutes. Then,  $N_2$  of  $4.0 \times 10^{-1}$  Pa work pressure was introduced into the chamber to deposit the TiN film onto the nitrided substrate.

Technical specification of samples and fatigue experiment procedure followed the experiment method of metal line contact rolling fatigue (Chinese National Standard GB10622-89). The fatigue experiment conditions were as follows: the four stress levels were 2500 MPa, 2200 MPa, 2000 MPa, and 1800 MPa, slip ratio was 10%, the rotational speed of drive samples was 1400 r/min, temperature of lubricant kept  $<40^\circ C$ . The five valid samples were chosen at every stress level to achieve the accurate numbers of cycles.

After the contact fatigue strength was obtained by contact fatigue experiment, the load carrying capacity of TiN coated gears has been analyzed by means of gear rig contact test; the conditions were as shown in Table 3.

The failure surface of gears was firstly examined by stereomicroscope and microscope, in particular the fracture surfaces prior to being observed by scanning electron microscopy (SEM). Also, the surface roughness of gears was measured.

### 3. Results and Discussion

The numbers of cycles in different contact stress levels for the nitrided and nitrided+TiN coated samples were presented in Table 4, which illustrated that the numbers of cycles of nitrided+TiN coated samples were larger than those of nitrided samples under the same failure criterion and experimental condition.

By analyzing numbers of cycles with Fixed Emitting Point Method-An Accelerated Test Program [12], fatigue curves of different survival ratio from the test gears have been drawn and fatigue limit was acquired, as shown in Figure 1. The P-S-N curve indicated that the fatigue life and the increment of fatigue lives of nitrided+TiN coated samples were higher than those of the nitrided samples with the descending of stress levels. It was obvious that TiN coating could provide the

subsurface protection and that properties of high cycle fatigue of nitrided samples could be improved by deposition of TiN. The contact fatigue strength of nitrided+TiN 32Cr2MoV is 284 MPa higher than that of nitrided 32Cr2MoV.

Figure 2 was the photograph of gear surface before gear rig contact test at contact stress 1235 Mpa. Both tooth faces with different surface treatment showed the uniform state without the scratches and defects.

After long time running test, there was significant comparison between the two kinds of tooth faces, which was demonstrated by Figure 3. It could be seen that the fatigue load obviously damaged the nitrided gears surfaces, and base metal is exposed with deep scratches, grooves, and spallings on tooth surface. As a distinction, nitrided+TiN coated gears were in good conditions relatively with less Horizontal grooves than the nitrided gears, few scratches and grooves were observed on nitrided+TiN coated driven gears, but it could be found that TiN coatings of driving gears on the edge of meshed zone were peeling off. There were some indentations on the nitrided+TiN coated driven gears but meshing zone kept original color and luster without the TiN coating peeling off. Macro-observation of tooth surface showed that TiN coating could increase the wear-resistance and resistance to contact fatigue.

The results of gears surfaces magnified 50 times were shown in Figure 4. Long time running caused serious fatigue wear on nitrided gear surface which emerged in forms of pitting and grooves. However, few pitting were observed on the nitrided+TiN coated gears, and wear of gear surface was too slight to exhaust the TiN coatings. According the gear status without TiN peeling off in Figure 4(d), The circle concave should not be pittings, which revealed that wear of TiN was uniform during the gear test.

The area of pitch line and edge of meshed zone of nitrided gears were investigated by SEM, as shown in Figure 5. All of the gears at the pitch line have the serious superficial injury, whose characteristics were also the fine pits and scratches with direction along the flank profiles (Figures 5(a) and 5(c)), while on the edge of the meshing zone there were obviously large areas of peeling off (Figures 5(b) and 5(d)). The SEM micrograph and EDS results of nitrided+TiN gears are shown in Figure 6. The peeling off of TiN coated gears was less than that of nitrided gears, and TiN coatings on pitch line still existed and were covered on the tooth surface. However substrate exposed on the edge of meshed zone, which revealed that TiN coatings have peeling off. an explanation for this phenomenon was contact interference

TABLE 4: Contact fatigue life of gears under different contact stress levels.

Contact stress $\sigma$ /MPa	Contact fatigue life $N/\times 10^5$									
	Nitreded and TiN coated 32Cr2MoV					Nitrided 32Cr2MoV				
2500	1.45	1.74	9.56	1.51	1.17	1.23	1.34	1.01	1.31	1.06
2200	4.94	4.66	5.44	5.18	4.65	3.88	3.31	3.97	3.92	3.10
2000	13.85	11.46	16.01	15.72	14.22	6.92	5.77	7.51	7.23	7.04
1800	49.75	53.85	50.72	47.86	43.75	19.91	22.63	21.73	17.86	16.40

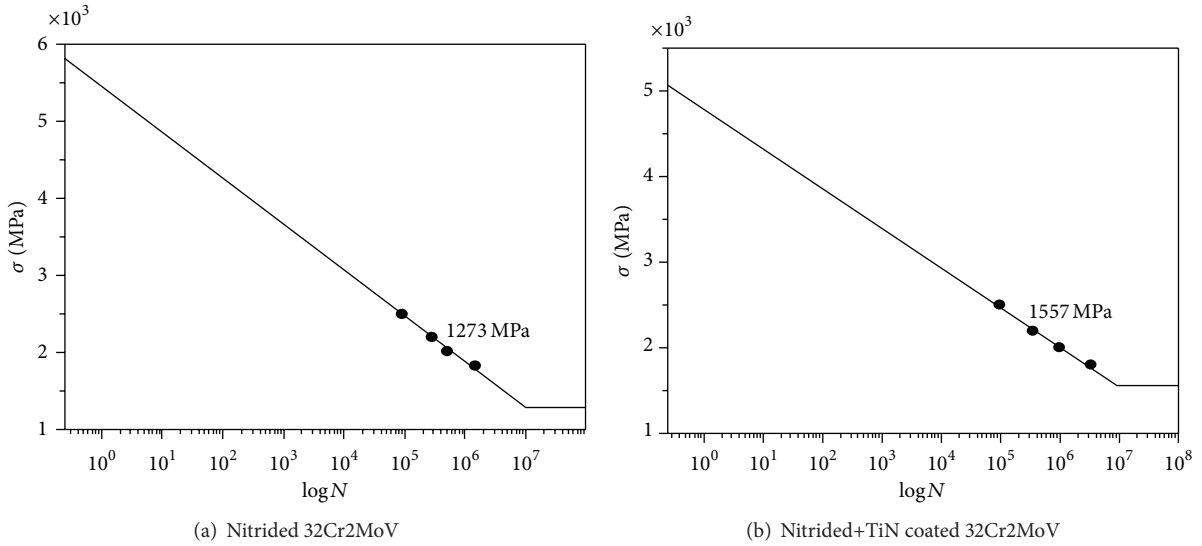


FIGURE 1: 99% survival probability P-S-N curves.

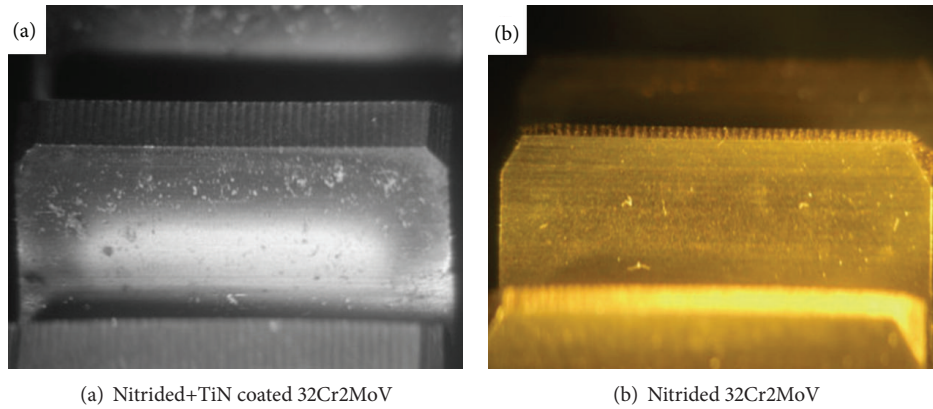


FIGURE 2: Tooth surface before gear rig contact test.

of gear shape between driven gears and drive gears [8, 13]. Furthermore, the residual TiN coatings of all nitrided+TiN gears maintained a uniform state and color, without the wear scar and plowing grooves along the tooth profile, which sharply contrasted with the nitrided gears. The EDS results of coated gears were consistent with previous analysis. Normally, the element Fe could not be detected by EDS after TiN coatings have been deposited onto surface, which misfits the result of Figure 6 and demonstrates that wear of TiN coating has occurred during the gear running. The content of Ti and Fe in the different area revealed that wear of TiN

on the edge of meshed zone was more severe than that on the pitch line zone. After running test some round spots and strip pits, the size of which was larger than that of the liquid-drop spots within  $10\ \mu\text{m}$  found in the TiN surface by different PVD technology were observed on the TiN coated driven gears (Figures 3(d) and 4(d)). However, morphology of spots and strip pits was quite different from the warp or bulge of film and similar to the indentation, showing that the TiN coating has good toughness and deformation capacity. The indentation illustrated that the driven gear surface was deformed during the repeated sliding and rolling, and

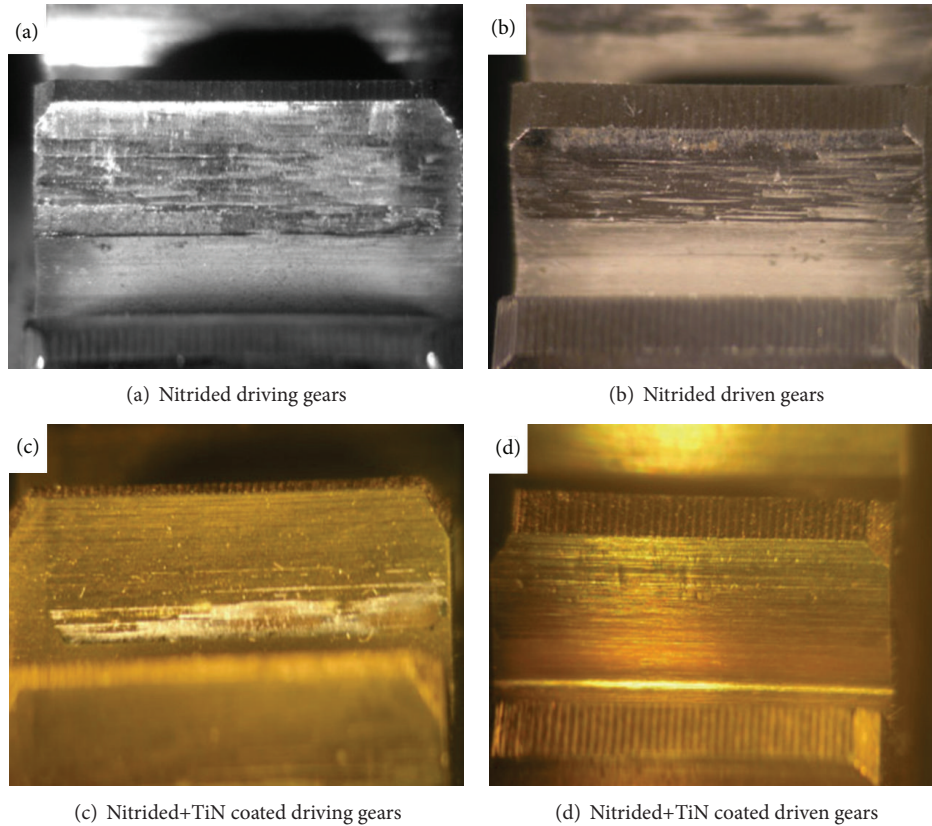


FIGURE 3: The macrophotograph of tooth surface after running test.

the deformed material will rupture if the accumulated strain exceeds the critical value of plastic strain [14]. The failure characteristic of TiN coated gears was consistent with contact fatigue of traditional hardened gears, but TiN could improve the contact fatigue performance.

The observation of nitrided gears is consistent with gear failure rules: pittings usually occur on the site near tooth root and below the pitch line, and it is easier for generating pittings on the driving gears than driven gears; additionally heavy load may cause spalling [15, 16]. Compared with the severe tooth damage of all nitrided gears, the TiN coated gears show an excellent resistance of pitting and spalling. TiN coatings within thickness  $3\text{ }\mu\text{m}$  still remain on the most of gear surface, which demonstrated wear of TiN coated gears is slighter. On the basis of the contact fatigue model, main failure type of hardened gears is pitting owing to its shallower nitride case and important role of surface cracks. Micro cracks caused by surface machining and repeated plastic deformation interact with lubricant and result in nucleation and propagation of fatigue cracks [8, 14, 15]. Deposition with TiN coating wrapped up the gear tooth so that the gear surface no longer contacts with lubricant and prevents the cracks initiation; furthermore, brittle TiN coating combined with hard case may weaken the surface plastic deformation, prolonging the contact fatigue life of gears. After the TiN coating wore out, the conditions of nitrided+TiN gears are the same as nitrided gears, and pitting process is similar to nitrided gears.

The changes in surface roughness also reflected the wear of gears, as shown in Figure 7. The surface roughness of nitrided gears increased to about  $\Delta R_a\ 0.6\sim 0.7\text{ }\mu\text{m}$ , which indicated that pitting destroyed the smoothness of nitrided gears. Reversely, surface roughness  $R_a$  of TiN coated gears decreased, making tooth surface smoother, and helping reduce the friction and wear, and improving and inhibiting pitting of gears.

#### 4. Conclusions

From the previous discussion, the conclusion can be summarized as follows.

- (1) The deposition on gears by hard coating TiN can provide subsurface protection and improve the contact fatigue life. The contact fatigue strength of nitrided+TiN coated 32Cr2MoV is 1557 Mpa at survival probability of 99%, and it is 284 MPa higher than that of nitrided 32Cr2MoV.
- (2) Due to the protection of TiN coatings with good toughness and deformation capacity, feature of gear surface fatigue exhibit indentation instead of pittings, which is different from the pittings and liquid-drop spots within  $10\text{ }\mu\text{m}$  found in the TiN deposition. The meshing zone of coated TiN gear face keeps well basically without pittings and wear grooves, which is opposite to nitrided gears with pittings and

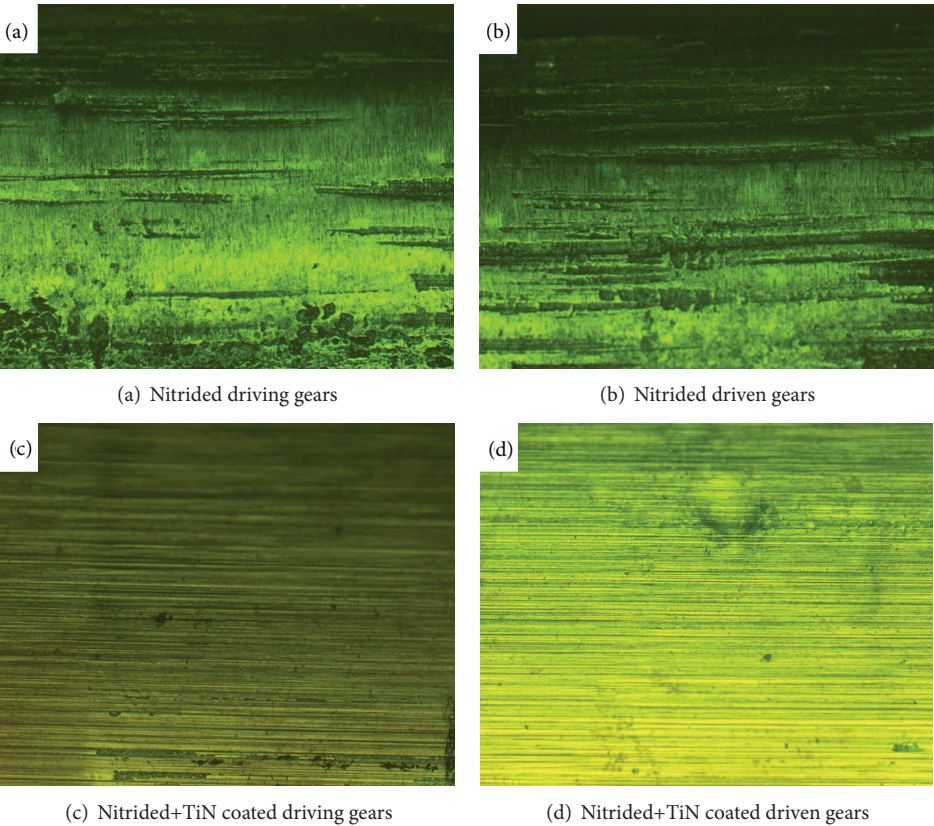


FIGURE 4: The photograph of tooth surface after running test magnified 50 times.

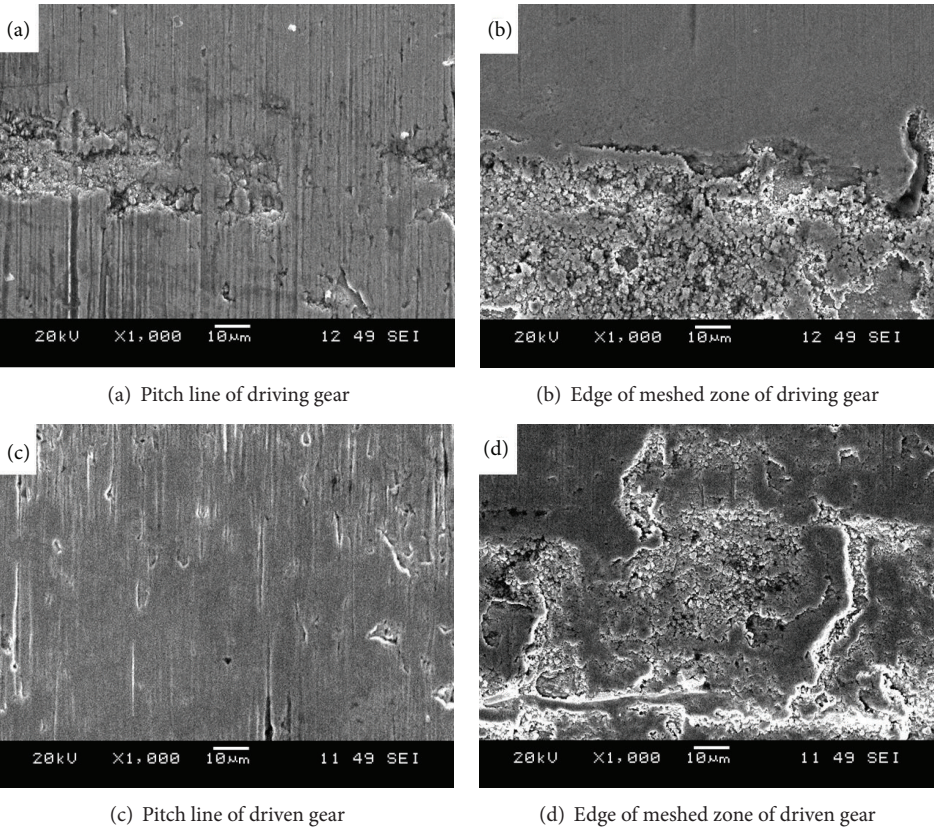


FIGURE 5: The SEM micrograph of nitrided gears after running test.

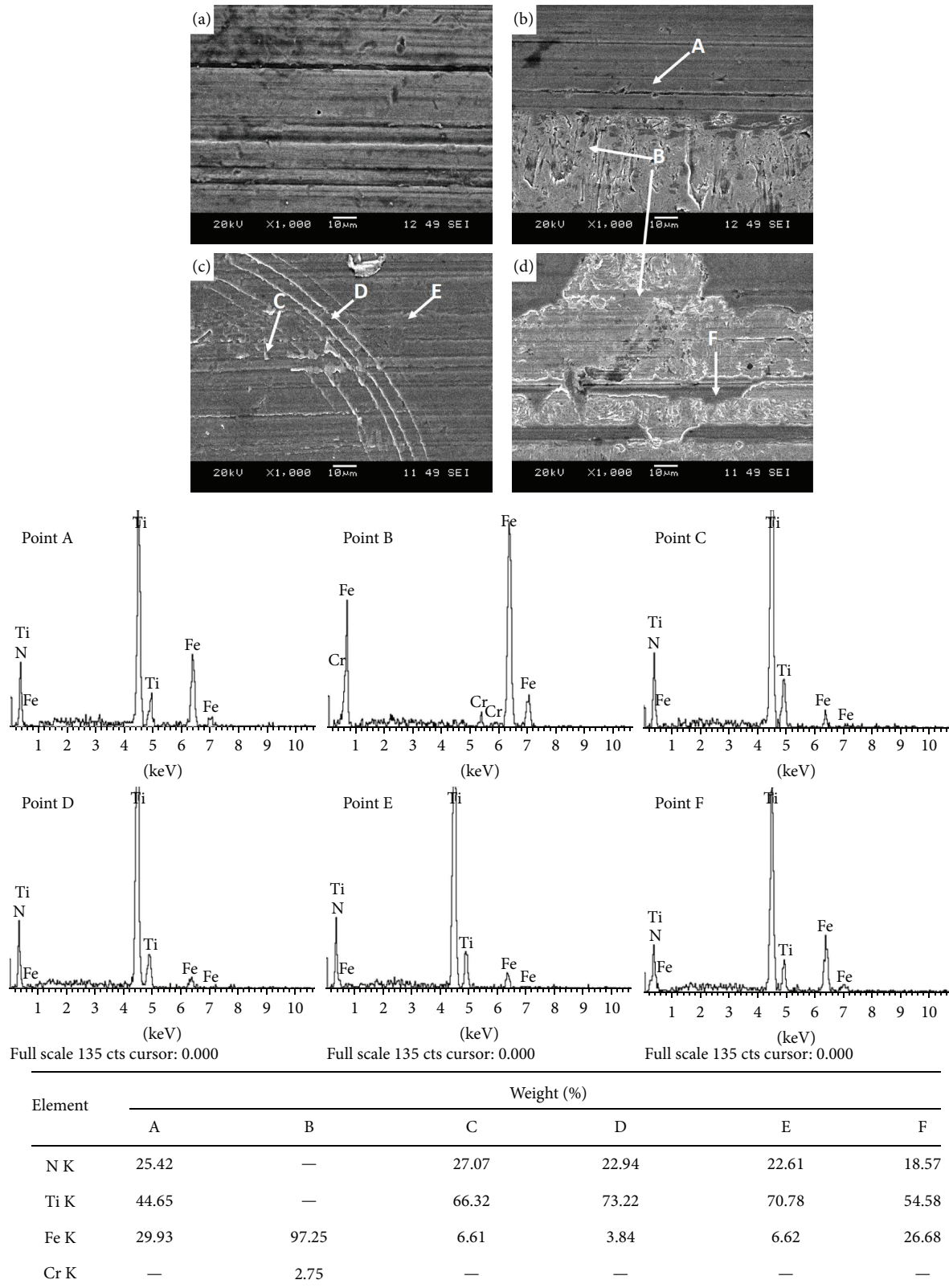


FIGURE 6: The SEM micrograph of nitrided+TiN gears after running test; (a) pitch line of driving gear, (b) edge of meshed zone of driving gear, (c) pitch line of driven gear, and (d) edge of meshed zone of driven gear.

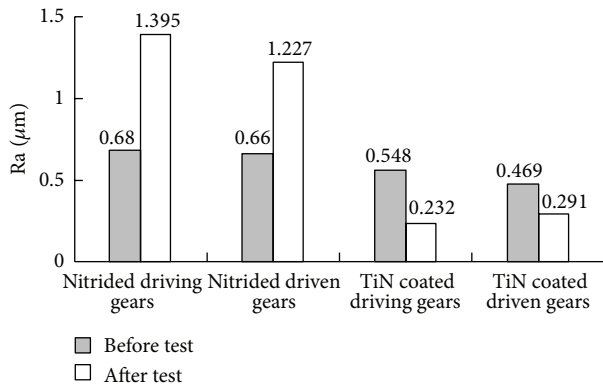


FIGURE 7: Surface roughness of gears.

peeling off. Even on the edge of the meshing zone TiN coatings have been worn out, the gear face kept well without pittings. The surface of the TiN coating is dense and smooth with lower surface roughness, and it wraps up the gear tooth so that the gear surface no longer contacts with lubricant and prevents the cracks initiation. During the running test, surface roughness of TiN coated gears decreased, making tooth surface smoother and helping reduce the friction and wear, improving contact fatigue properties.

## Acknowledgments

This work has been supported by National Natural Science Foundation of China (no. 51275548), Chongqing Science and Technology Commission (no. cstc2012jjB70002), and International Cooperation Special Project in Science and Technology of China (2013DFA70730). Authors are grateful to State Key Laboratory of Mechanical Transmission in Chongqing University for providing the specimens and gear experimental equipment.

## References

- [1] R. C. Martins, P. S. Moura, and J. O. Seabra, "MoS<sub>2</sub>/Ti low-friction coating for gears," *Tribology International*, vol. 39, no. 12, pp. 1686–1697, 2006.
- [2] M. Kalin and J. Vizintin, "The tribological performance of DLC-coated gears lubricated with biodegradable oil in various pinion/gear material combinations," *Wear*, vol. 259, no. 7–12, pp. 1270–1280, 2005.
- [3] J. C. Jiang, W. J. Meng, A. G. Evans, and C. V. Cooper, "Structure and mechanics of W-DLC coated spur gears," *Surface and Coatings Technology*, vol. 176, no. 1, pp. 50–56, 2003.
- [4] C. Mercer, A. G. Evans, N. Yao, S. Allameh, and C. V. Cooper, "Material removal on lubricated steel gears with W-DLC-coated surfaces," *Surface and Coatings Technology*, vol. 173, no. 2–3, pp. 122–129, 2003.
- [5] S. Baragetti, "Fatigue resistance of steel and titanium PVD coated spur gears," *International Journal of Fatigue*, vol. 29, no. 9–11, pp. 1893–1903, 2007.
- [6] J. Luo, H. Dong, and T. Bell, "Model-based contact fatigue design of surface engineered titanium gears," *Computational Materials Science*, vol. 35, no. 4, pp. 447–457, 2006.
- [7] Q. Wenfu, C. Xingjin, L. Long et al., "Surface treatment and coating technologies on gears," *Journal of Chongqing University*, vol. 2, pp. 1–4, 2005 (Chinese).
- [8] M. Fujii, M. Seki, and A. Yoshida, "Surface durability of WC/C-coated case-hardened steel gear," *Journal of Mechanical Science and Technology*, vol. 24, no. 1, pp. 103–106, 2010.
- [9] L. Lu, F. Xu, T. Jiang, Q. Zhang, and S. Lyu, "Characteristic evaluation of friction and wear in the C-N and TiN coated gear," *International Journal of Precision Engineering and Manufacturing*, vol. 11, no. 1, pp. 107–111, 2010.
- [10] N. Dingremont, E. Bergmann, and P. Collignon, "Application of duplex coatings for metal injection moulding," *Surface and Coatings Technology*, vol. 72, no. 3, pp. 157–162, 1995.
- [11] S. Ma, Y. Li, and K. Xu, "The composite of nitrided steel of H13 and TiN coatings by plasma duplex treatment and the effect of pre-nitriding," *Surface and Coatings Technology*, vol. 137, no. 2–3, pp. 116–121, 2001.
- [12] M. B. Feng and Y. L. Chen, "Fixed emitting point method—an accelerated test program to determine fatigue limit of automotive components," SAE Technical Paper 2004-01-1646, SAE International, 2004.
- [13] M. Murakawa, T. Komori, S. Takeuchi, and K. Miyoshi, "Performance of a rotating gear pair coated with an amorphous carbon film under a loss-of-lubrication condition," *Surface and Coatings Technology*, vol. 120–121, pp. 646–652, 1999.
- [14] G. W. Stachowiak, *Engineering Tribology*, Elsevier, 3rd edition, 2006.
- [15] J. W. Blake and H. S. Cheng, "A surface pitting life model for spur gears," *Tribology*, vol. 113, pp. 712–718, 1991.
- [16] T. E. Tallian, "Simplified contact fatigue life prediction model," *Journal of Tribology*, vol. 2, pp. 207–220, 1992.

## Research Article

# Mechanical Performance Evaluation of Concrete Beams Strengthened with Carbon Fiber Materials

Jun Ding,<sup>1,2</sup> Xia Huang,<sup>1</sup> Gang Zhu,<sup>1</sup> Song Chen,<sup>1</sup> and Guochao Wang<sup>1</sup>

<sup>1</sup> College of Mechanical Engineering, Chongqing University of Technology, Chongqing 400054, China

<sup>2</sup> Key Laboratory of Manufacture and Test Techniques for Automobile Parts, Ministry of Education, Chongqing 400054, China

Correspondence should be addressed to Jun Ding; [dingjunawen@126.com](mailto:dingjunawen@126.com)

Received 16 July 2013; Accepted 12 September 2013

Academic Editor: Xing Chen

Copyright © 2013 Jun Ding et al. This is an open access article distributed under the Creative Commons Attribution License, which permits unrestricted use, distribution, and reproduction in any medium, provided the original work is properly cited.

As a kind of novel material of high strength and light weight, carbon fiber materials have been widely used in construction industry to repair the damaged bridges improving its mechanical performance. In this work, the reinforced plates made of carbon fiber materials (for short CFRP) are externally bonded to the bottom of concrete beams to enhance load capacity of beams. The strain energy release rates are calculated at the interest crack in concrete beams based on virtual crack closure technology using FEM and are chosen as the criterion to determine whether the mechanical properties of beams are strengthened by being externally bonded with CFRP. The effects of main crack propagation on plain concrete beam, on concrete beam strengthened with CFRP, and on inclined crack are also discussed. The comparison between the beams with and without CFRP shows that the CFRP significantly increases the loading capacity and crack resistance. It also shows that the main crack propagation can reduce loading capacity and crack resistance regardless of strengthening. The experiment observation also supports this. It proves the validity of the method, and it is concluded that in order to increase the loading capacity and crack resistance effectively, controlling over the crack propagation is necessary.

## 1. Introduction

Due to the excellent mechanical properties such as light weight, high strength at tension and superior resistance to aggressive environment, the reinforcement and strengthening technique bonded with the reinforced plates made of carbon fiber materials (for short CFRP) to concrete beam is widely accepted and considered as an effective and convenient method among various methods of strengthening infrastructure construction [1–4]. According to structural mechanics, an important concern over the effectiveness and safety for the method strengthening concrete beam with CFRP is the enormous potential for load capacity and decrease in failure mode in service.

So far, many researches [5–11] have been conducted to investigate the mechanical properties of the retrofitted members externally bonded with CFRP. It can be concluded that the bonding of the CFRP plates has a significant effect on enhancing the overall performance even for plates with a relatively low modulus of elasticity. The strengthening technology externally bonded with CFRP can considerably

increase the strength at bending, reduce the deflections as well as crack width in area of tension, and also change the mechanical behavior and failure pattern during service. The researches [5, 8–10] demonstrated that the cracking moment in reinforced concrete beams with CFRP can significantly increase by 218%, from 12% to 230%. They also found that in strengthened flexural members, cracks are seen in bigger numbers and closer to each other; however, they are narrower than in beams without strengthened reinforcement.

However, the review for the previous works shows that the reinforced concrete beams used to be strengthened with CFRP are essentially intact, that is, without any greater cracks and obvious defects in advance. As a matter of fact, some bigger defects and macrocracks such as holes and cracks are already pre-existed in flexural members in construction before it is strengthened. Such imperfection can severely reduce the structural strength and stiffness of members, and it receives more and more attention for earlier design and later maintenance. Moreover, the strengthened member fails often in a brittle way due to the loss of connection between

composite material and the concrete itself in the process of strengthening. Consequently, it is necessary to consider the effect of pre existed macrocracks on the performance of the flexural members externally bonded with CFRP systematically.

For the convenience of investigating the mechanical properties theoretically, the plain concrete beams, not reinforced with steel bars, have been chosen for this work to examine the mechanical behaviors such as structural strength, stiffness, and strain energy release rates. Considering that the purpose of this work focuses on exploring the loading capacity and crack resistance for the flexural beams externally bonded with CFRP, the choice of the purely plain beam as being studied will not lose the generality of research. In order to emphasize the influence of existence of crack on the loading capacity of beams, the macrocracks with different length were in advance made in the plain concrete beams and subsequent researches serve for it. According to fracture mechanics, in order to predict crack propagation, the strain energy released rate (abbreviated as SERR for convenience of later description),  $G$ , must be evaluated and compared with the critical fracture energy of the constituent materials,  $G_{IC}$ , determined from experiments. The calculation for SERR at the interest crack was based on virtual crack closure technology (VCCT) together with the finite element method (FEM). The values for SERR were then selected as a criterion to determine whether the mechanical properties of the beam are strengthened by being externally bonded with CFRP in comparison to those beams without bonded CFRP. We focus upon the effect of crack propagation that occurred at the initial crack, edge crack, and the mutual interaction between them on the loading capacity and failure mechanism of strengthened with CFRP.

## 2. Materials and Methods

**2.1. The Description in the Model of the Concrete Beam.** In order to experimentally investigate the improvement in mechanical properties of concrete beams due to the bond of CFRP, our previous work [11] made some experiments for beams at the test setup, as shown in Figure 1. Figure 2(a) shows the failure mode of the concrete beam without CFRP strengthened, and Figures 2(b)–2(d) show the failure mode with CFRP strengthened for the length of 0.1 m, 0.2 m and 0.35 m, respectively.

According to the previous experimental measurement, the geometry model has been constructed, shown as in Figure 3(a). It includes two models, plain concrete beam with and without CFRP. The geometry dimension for the concrete beam is about 0.1 m  $\times$  0.1 m  $\times$  0.4 m each with an initial crack length of 20 mm, marked as  $a_0$  in Figure 3. The plain concrete beam externally bonded with CFRP is illustrated as in Figure 3(b). In experiment test, the length of the CFRP varies with the different case study to investigate the effect of the length of CFRP on the reinforcement. The details about the experiment can refer to the work [11].



FIGURE 1: The test setup for concrete beams.

**2.2. The Crack Criterion Based on SERR.** There are common three fracture criteria,  $K$  (stress intensity factor),  $J$  integral, and Strain Energy Release Rate (SERR) in linearly elastic fracture mechanics, which are used to determine whether and when crack propagates [12]. The criteria for both  $K$  and SERR are for linearly elastic material, while  $J$  is integral criterion for plastic material. Concrete behaves in brittle material behavior and it is considered as elastic material [13]. Generally, in numerical simulation, the calculation for the value of  $K$  requires strict conditions for the mesh to discrete the geometry model, especially at the tip of the crack, due to its numerical radius singularity [12]. Meanwhile, the calculation for SERR usually does not need a more special element type near the area around crack tip, and it even employs fewer elements.

The SERR refers to the energy dissipated during fracture per unit of newly created fracture surface area, which is an essential quantity in fracture mechanics because the energy that must be supplied to a crack tip for it grows must be balanced by the amount of energy dissipated due to the formation of new surfaces [12].

For calculation, SERR is defined as

$$G = -\frac{\partial(U - V)}{\partial A}, \quad (1)$$

where  $U$  is the potential energy available for crack growth,  $V$  is the work associated with any external forces, and  $A$  is the crack area (crack length for two-dimensional problems). The failure criterion of energy release rate states that the crack will grow when the available energy release rate  $G$  is greater than or equal to the critical value  $G_C$ . The quantity  $G_C$  is the fracture energy and is considered to be a material property which is independent of the applied loads and the geometry configuration of the body.

For two-dimensional geometry configuration with isotropic elastic material property, the value of  $K$  and SERR for the case of problem of plane strain can follow (2), where  $K_I$  is the stress intensity factor,  $E$  is Young's modulus, and  $\nu$  is the Poisson ratio.  $G$  is the fracture energy and is considered to be

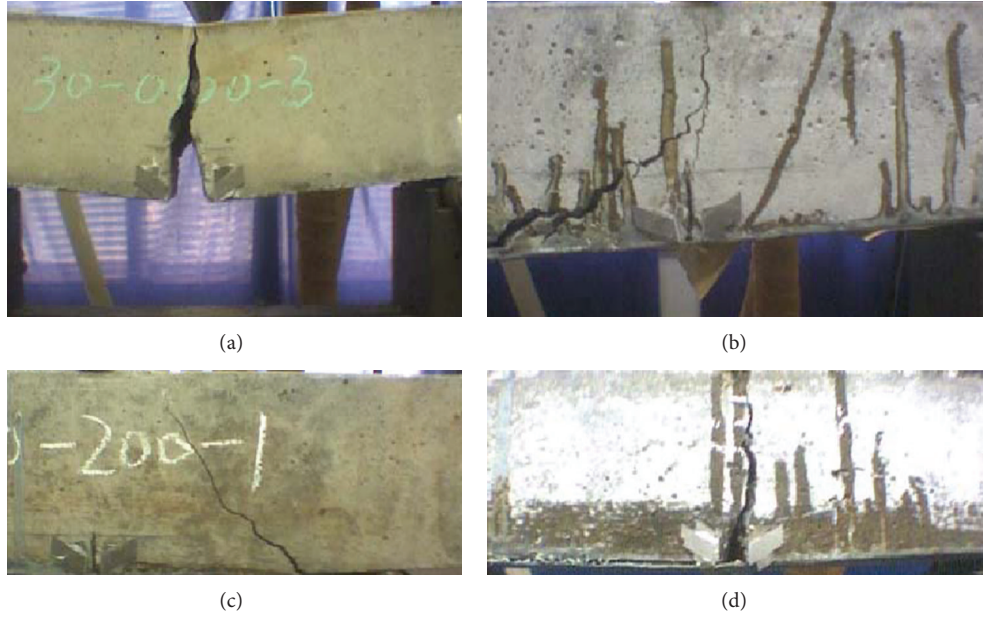


FIGURE 2: The photos of experimental measurement [11]. (a) Failure mode of the beam without CFRP. (b) Failure mode of the beam with CFRP of 0.1 m. (c) Failure mode of the beam with CFRP of 0.2 m. (d) Failure mode of the beam with CFRP of 0.35 m.

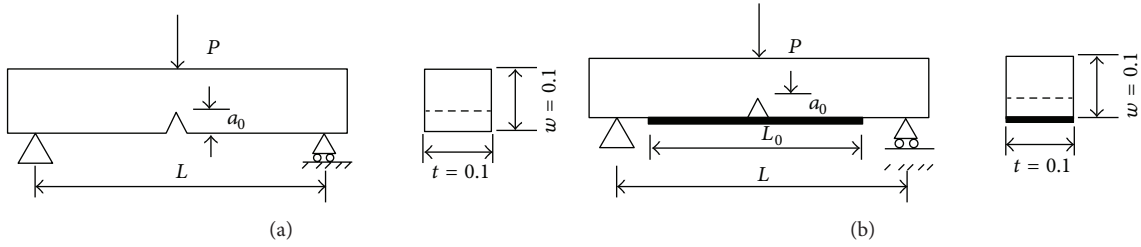


FIGURE 3: The geometrical model of the concrete beam. (a) The plain concrete beam. (b) The beam strengthened with CFRP.

a material property which is independent of the applied loads and the geometry configuration of the body. Consider

$$G = \frac{K_I^2}{E} (1 - \nu^2). \quad (2)$$

For the three-point bending concrete beam, illustrated as in Figure 3, the expression calculating the value for  $K_I$  follows (3), wherein  $P$  is the load applied at the midspan of the concrete beam,  $S$  is the span distance between two supports of the concrete beam,  $t$  is the thickness of the concrete beam,  $a$  is the crack length, and the expression for  $F(\alpha)$  can follow (4). Consider

$$K_I = \frac{3SP}{2tW^2} \sqrt{\pi a} F(\alpha), \quad (3)$$

$$F(\alpha) = \frac{1.99 - \alpha(1 - \alpha)(2.15 - 3.93\alpha + 2.7\alpha^2)}{\sqrt{\pi}(1 + 2\alpha)(1 - \alpha)^{3/2}}, \quad (4)$$

$$\text{where } \alpha = \frac{a}{w}.$$

In a word, for the geometric configuration illustrated as in Figure 3, the value of  $K$  can be numerically calculated

by substituting the parameters such as the crack length, the width of the cross section, the span between supports, and the load. Then taking on (2) can derive the value of SERR.

**2.3. The Virtual Crack Closure Technique (VCCT).** The virtual crack closure technique (VCCT) is widely used for computing SERR based on results from finite element analysis to supply the mode separation required when using the mixed-mode fracture criterion [14].

This method is mainly based on Irwin's crack closure integral and on the assumption that the energy  $\Delta E$  released when the crack is extended by  $\Delta a$  from  $a$  to  $a + \Delta a$  is identical to the energy required to close the crack between locations  $l$  and  $i$ , as illustrated in Figure 4. Additionally, however, it is assumed that a crack propagation of  $\Delta a$  from  $\Delta a$  to  $a + \Delta a$  (node  $i$ ) to  $a + 2\Delta a$  (node  $k$ ) does not significantly alter the state at the crack tip. Therefore, when the crack tip is located at node  $k$ , the displacements behind the crack tip at node  $i$  are approximately equal to the displacements behind the crack tip at node  $l$  when the crack tip is located at node  $i$ . Further, the energy  $\Delta E$  released when the crack is extended by  $\Delta a$  from

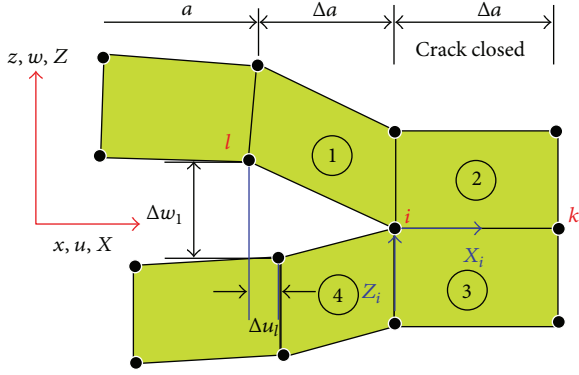


FIGURE 4: The specimens were tested in the three-point bending configuration, and the load was applied with cylindrical rollers as line load across the top width of the beams. To spread the load and avoid stress concentrations, elastomeric pads were placed between the roller supports and the lower surface of the specimens and between the loading device and the top surface of the specimens. During experimental measurement, the ultimate load which makes crack propagate or makes the reinforced concrete beam fail in fiber, in concrete, or at the interface between them can be achieved according to instrument reading. Virtual crack closure technique (VCCT).

$a + \Delta a$  to  $a + 2\Delta a$  is identical to the energy required to close the crack between locations  $i$  and  $k$ .

For a crack modeled with two dimensional, four-node elements, as shown in Figure 4, the work  $\Delta E$  required to close the crack along one element side therefore can be calculated as follows

$$\Delta E = \frac{1}{2} [X_i \Delta u_l + Z_i \Delta w_l], \quad (5)$$

where  $X_i$  and  $Z_i$  are the shear and opening forces at the nodal point  $i$  and  $\Delta u_l$  and  $\Delta w_l$  are the shear and opening displacements at node  $l$  as shown in Figure 4. Thus, forces and displacements required to calculate the energy  $\Delta E$  to close the crack may be obtained from one single finite element analysis.

However, Figure 3(a) shows that the dominant separation mode at the central crack of the concrete beam should be mode I crack. The term of shearing force  $X_i$  and of shear displacement  $\Delta u_l$  can disappear in (5), only the terms for opening force and displacement leave in the equation. Meanwhile, in Figure 3(b), both opening and shearing effects must be taken into account when calculating SERR for the crack failure that occurred at the interface between concrete and CFRP and the failure at the bottom of CFRP.

**2.4. Calculation of SERR Based on VCCT.** In this section, we discuss the scheme employed to calculate SERR from finite element analysis based on VCCT. The finite element model has firstly been created in ABAQUS software [15]. Because the calculation for SERR based on VCCT only involves the nodal forces and nodal displacements at the element side, more refined mesh or special treatment element types are not necessary for the discretization in FEM at the crack tip. The fewer elements with four-node plane strain elements are used at the crack tip.

TABLE 1: The value of SERR for various numbers of elements.

Numbers of elements	300	600	1000	1400
SERR from FEA	10.404	9.819	9.232	9.047
Relative error	15.3%	8.83%	2.32%	0.265%

The details of mesh configuration around the crack tip are also expressed as in Figure 4. The location of  $i$  is the crack tip. In ABAQUS software, in order to obtain the value of nodal force at node  $i$ , it needs define elements 1 and 2 as one element set using command \*ELSET, and using \*ELPRINT command to output the nodal force. Since the node  $i$  is shared by elements 1 and 2, the total nodal force at node  $i$  in  $Z$  direction is the sum of the contribution at node  $i$  by element 1 and that at node  $i$  by element 2. The displacements in  $Z$  direction at node  $l$  can also be known in finite element analysis. Thus, SERR at the crack tip based on VCCT using finite element analysis can be easily calculated.

In this case, the load applied on the concrete beam is 5000 N, and the crack length is 20 mm, taken into (2)–(4), the value of SERR  $G$  is  $9.024 \text{ J/m}^2$ . In order to check the mesh dependency on computation, four various numbers of elements, 300, 600, 1000, and 1400, are used to discrete the plain concrete beam in FEA. The calculated SERR for different numbers of elements is summarized in Table 1. Comparison between the value for SERR from FEA and theoretical calculation indicates that 1400 elements are the best choice which results in the minor error with the theoretical one.

### 3. Results and Discussion

**3.1. The Effect of Main Crack Propagation.** Firstly, the effects of crack propagation for the main crack seam (the location illustrated as in Figure 3(a)) on the overall strength of the plain concrete beam (i.e. without externally bonded CFRP at the bottom of the beam) are studied as follows. The finite element analysis for the concrete beam under three different loading case is performed in advance, and then the calculation method the same as that previously described in Section 2.4 is employed to calculate the value of SERR. The initial crack length is taken as 20 mm. We model the main crack propagation by means of varying the lengths of cracks, 20, 25, 30, 35, and 40 mm to simulate crack growth in service.

Figure 5 shows the plot of the calculated SERR for various load cases against the crack propagation of the main crack. Suppose that crack extends under the load from 20 mm to 40 mm. It can be seen from the figure that SERR for any case of load can increase slightly with the main crack propagation. The bigger the magnitude of SERR is, the closer it approaches  $G_C$  of the concrete material. It implies that the strength of the beam decreases with the increase of SERR. For a certain fixed crack length, the value for SERR also increases with the load, which indicates that the bigger load applied at the concrete beam can reduce the loading capacity and make the concrete beam closer to the critical load.

According to Section 3.1, SERR will increase with the load applied to the beam and also with the crack propagation.

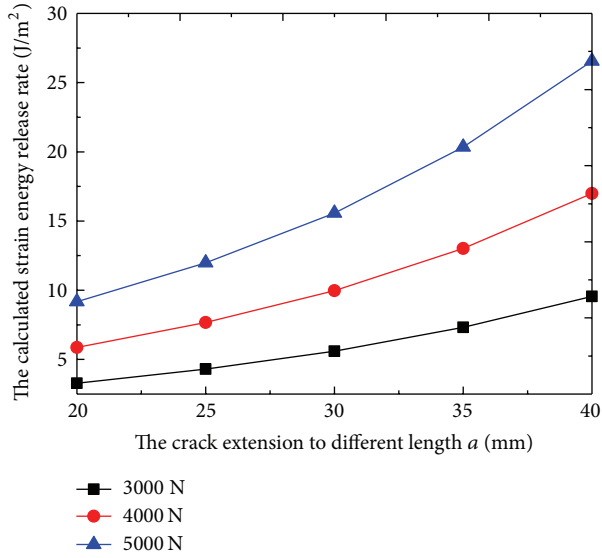


FIGURE 5: The plot of calculated SERR against the main crack propagation.

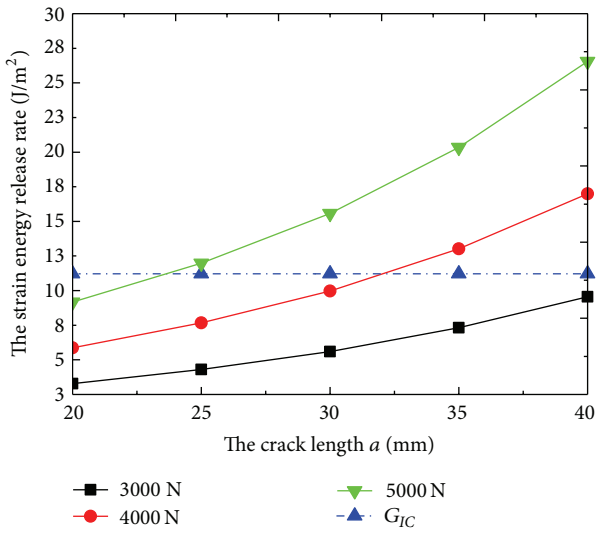


FIGURE 6: The comparison of SERR between the different load and the critical case.

Figure 6 shows a comparison made between the value of SERR for various loads and the critical SERR. For the crack length of 20 mm, the crack propagation will not occur even if the load exceeds 5000 N. However, as the crack length increases, the magnitude of load at which SERR exceeds  $G_{IC}$  decreases significantly indicating that the load capacity of the beam weakens.

**3.2. The Prediction for the Critical Load.** According to Figure 6, it can be seen that for a given length of crack, the ultimate load applied at the plain concrete beam can be predicated in theory. Figure 7 shows the calculated SERR for various loads at the crack length of 20 mm. The formula that

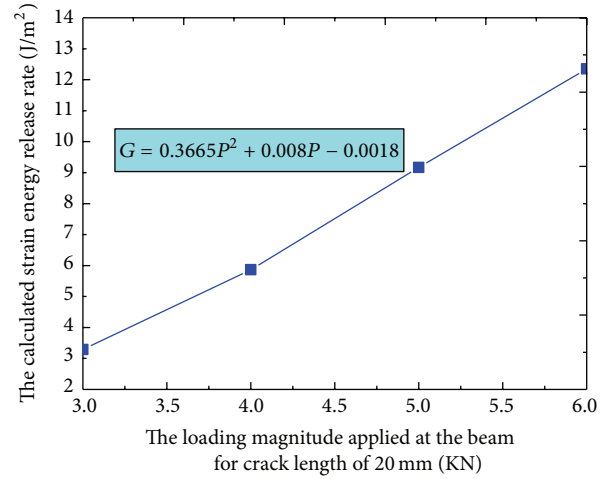


FIGURE 7: The calculated SERR for different load at the crack length of 20 mm.

calculates the ultimate load could be derived based on curve fitting. Consider

$$G = 0.3665P^2 + 0.0008P - 0.0018. \quad (6)$$

The magnitude of ultimate load can be calculated when the value of  $G \geq G_{IC}$ . Then we can derive the magnitude of load is 5580 N which makes the initial crack propagates. It is close to the value of 5752 N observed from the experimental measurement [11, 16] indicating the validity and accuracy of the method used to calculate the value for SERR.

**3.3. The Determination for Location of Potential Crack.** In this section, we focus on the case in which the plain concrete beam was strengthened with CFRP externally bonded at the bottom surface to the beam. Under the load, there exist many cracks possibly initiated at the end of the CFRP or at the interface between concrete and CFRP. Such potential cracks in turn significantly influence the stability of the main crack. Consequently, the determination for the location of potential crack seems enormously important to investigate the increase or decrease in strength of a concrete beam bonded externally with CFRP.

As illustrated in Figure 3(b), the length of CFRP bonded at the bottom of the concrete beam is taken as  $L_0 = 0.2$  m, the initial crack length  $a_0$  is 20 mm, and the length of the total concrete beam is  $L = 0.4$  m. For the convenience of comparison with experimental measurements, the load applied to the beam is  $P = 20$  KN. Due to the symmetry of the model, half of the concrete beam was considered and performed in finite element analysis. According to [11], the maximum tensile stress for concrete material is 5.15 MPa. In terms of strength theory for brittle material, the concrete is considered to break or debond when the maximum tensile stress under the load in concrete beam exceeds the critical stress, 5.15 MPa. Figure 8 shows the distribution of maximum tensile stress in concrete beam, while the dark black region stands for the stress greater than critical stress value, that is, potential crack initiation.

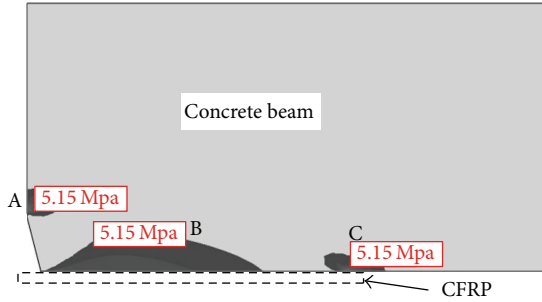


FIGURE 8: The distribution of the maximum tensile stress in the plain concrete beam strengthened with externally bonded CFRP.

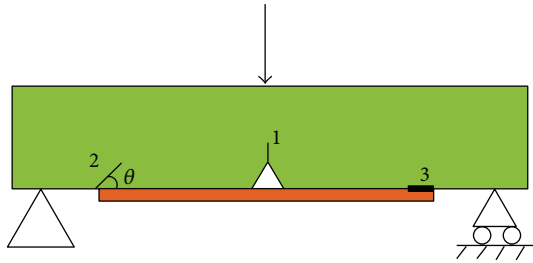


FIGURE 9: The potential crack initiation in concrete beam with CFRP.

Seen from the figure, the potential crack possibly occurs at three sites, near the main crack (denoted as A), at the interface between concrete and CFRP (denoted as B), and at the end of CFRP (denoted as C), respectively. For CFRP, it will not break through since the maximum tensile stress in CFRP is much smaller than its critical tensile stress, 4640 MPa. Subsequently, suppose that the strength of bonding between concrete material and epoxy resin and the bond force between epoxy resin and CFRP are sufficient enough to resist the tensile stress. The initiation of crack should occur at the side of the concrete beam. Therefore, the distribution of the potential crack in the concrete beam is sketched as in Figure 9. For the convenience of subsequent description, the main crack in the middle of the concrete beam, the crack probably initiated at the end of the CFRP, and the debonding cracks at the end of the CFRP are labeled as main crack 1, inclined crack 2, and delamination crack, respectively.

Cracks 1, 2, 3 illustrated in Figure 9 are possible to coexist at the same time, or one of them or both of them exist one time. Meanwhile, they will probably influence another to decrease the strength and the stiffness of the concrete beam.

**3.4. The Effect of Main Crack Propagation on the Strengthened Beam.** In order to investigate the effect of the main crack propagation on the performance of the strengthened beam, it is supposed in this section that the main crack only exists but the other cracks such cracks 2 and 3 did not.

Employing the similar method calculating SERR as previously described, SERR for the strengthened concrete beam is calculated, and the variation of SERR versus the main crack propagation is illustrated in as Figure 10. The horizontal line in figure with the value of  $11.22 \text{ J/m}^2$  represents

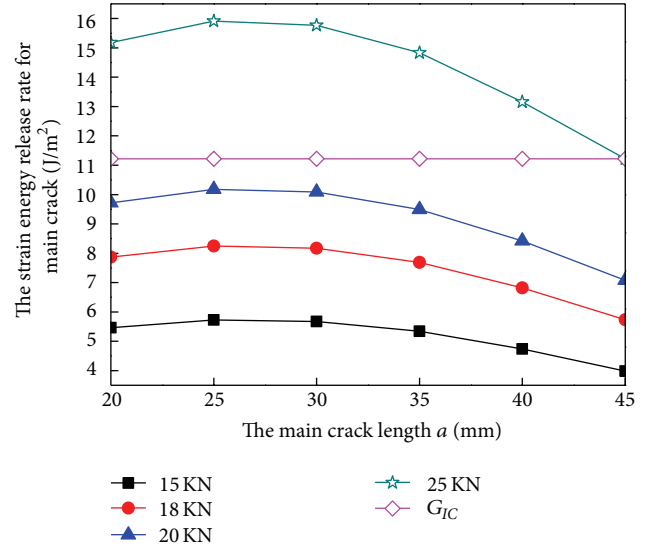


FIGURE 10: The plot of SERR against the main crack propagation.

the critical SERR for concrete material at which the concrete can probably break off. It can be seen from Figure 10 that when concrete beam is strengthened by CFRP, the SERR can significantly increase with the applied load, showing that the loading capacity of the beam is improved.

As the load increase to the extent at which SERR is greater than critical value, crack propagation will occur at the main crack. We can also find that the concrete beam strengthened with CFRP cannot sufficiently sustain the applied load at the initial stage of loading, because the main crack does not start to propagate and the subsequently increased load are mainly carried by concrete beam itself.

However, as the main crack extends to some certain length, CFRP begins to carry the load and the maximum tensile stress in CFRP starts to increase. As shown in Figure 10, for each load, SERR slightly increases as cracks extend but it decreases rapidly with crack propagation, and the case for load of 20 KN strongly supports this point.

Figure 11 shows the comparison of SERR between before and after strengthening for various loads, 3000, 4000, and 5000 N, respectively. From the figure, we can easily see that the strengthening beam with CFRP significantly improves the performance of the concrete beam, supported by the SERR for strengthened beam smaller than that without strengthening. The value of SERR for the beam with CFRP is almost 1/10 of that without CFRP. It is CFRP that decreases the value of SERR and increases the strength and stiffness of the concrete beam.

### 3.5. The Effect of Main Crack Propagation on Inclined Crack

**3.5.1. The Determination for the Inclined Angle.** Observed from Figure 9, as load applied at the midspan of the CFRP concrete beam increases, the deflection at the bottom of the concrete beam continually increases and CFRP bonded at the bottom of the beam starts to sustain the tension force. Since

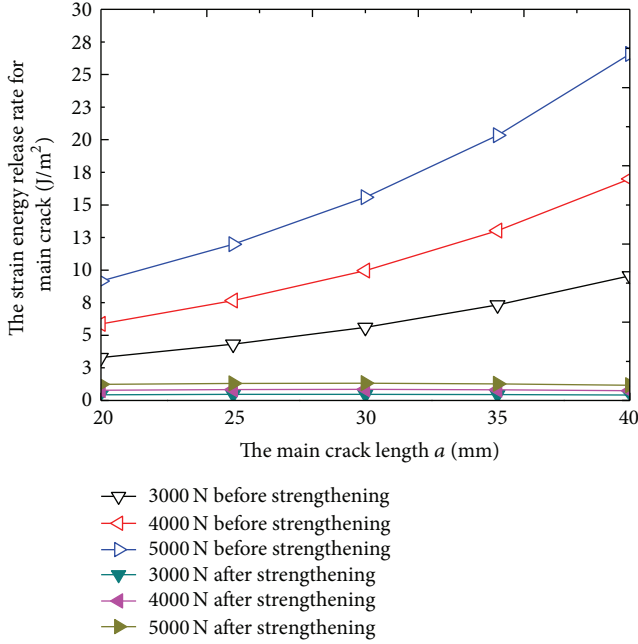


FIGURE 11: The comparison of SERR before and after strengthening.

the strength of CFRP is sufficient enough, it will not break due to a strength problem. The concrete material at the end of the CFRP can probably fail, and the inclined crack can initiate at this site. According to experiment observation, the direction of crack propagation makes an angle with the horizontal axis of a beam.

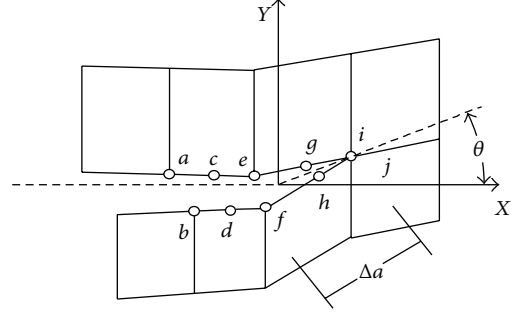
Based on the predication for crack path in bimaterial composites plate under uniform mechanical load and temperature load, suppose that an inclined crack can propagate along the direction of angle with the horizontal axis by the length of  $\Delta a$ , as illustrated in Figure 12.

The SERR for inclined crack extended by  $\Delta a$  can be calculated as follows:

$$\begin{aligned} G_I(a \rightarrow a + \Delta a, \theta) &= A \sin^2 \theta - B \sin \theta \cos \theta + C \cos^2 \theta, \\ G_{II}(a \rightarrow a + \Delta a, \theta) &= A \cos^2 \theta + B \sin \theta \cos \theta + C \sin^2 \theta, \\ G(a + \Delta a, \theta) &= G_I(a \rightarrow a + \Delta a, \theta) \\ &\quad + G_{II}(a \rightarrow a + \Delta a, \theta) = A + C, \end{aligned} \quad (7)$$

in which

$$\begin{aligned} A &= \frac{1}{2t\Delta a} \left[ F_x^f (u_x^e - u_x^f) + F_x^h (u_x^g - u_x^h) \right], \\ B &= \frac{1}{2t\Delta a} \left[ F_x^f (u_y^e - u_y^f) + F_x^h (u_y^g - u_y^h) \right. \\ &\quad \left. + F_y^f (u_x^e - u_x^f) + F_y^h (u_x^g - u_x^h) \right], \\ C &= \frac{1}{2t\Delta a} \left[ F_y^f (u_y^e - u_y^f) + F_y^h (u_y^g - u_y^h) \right] \end{aligned} \quad (8)$$

FIGURE 12: The finite element mesh configuration at the tip of crack with an angle against horizontal axis extended by the length of  $\Delta a$ .

in which  $F_x^i, F_y^i$  ( $i = f, h$ ) are the  $x$  and  $y$  components of nodal force at the node  $i$  before the crack extends by  $\Delta a$ , and  $u_x^i, u_y^i$  ( $i = e, f, g, h$ ) are the  $x$  and  $y$  components of displacement at the node  $i$  once crack extends by  $\Delta a$ .

Combined with the results from finite element analysis for concrete beam, the SERR of  $G, G_I$ , and  $G_{II}$  can be easily calculated from (7)-(8). In terms of brittle fracture mechanics, the inclined crack always extends along the direction at which  $G_{II} = 0$  when  $G_I \geq G_{IC}$ . Since the angle is unknown, now an arbitrary angle is assumed and the angle is desired if it just makes  $G_{II} = 0$ .

First, we forced  $G_{II}(\theta)$  to be zero to find a solution of the angle:

$$G_{II}(\theta) = A \cos^2 \theta + B \sin \theta \cos \theta + C \sin^2 \theta = 0. \quad (9)$$

In this case, the length of CFRP is 0.2 m, the initial length of crack is 20 mm, and the load is 20 kN. Substituting such known parameters into (7)-(9), we can obtain the solution to the angle,  $\theta = 45^\circ$  along which the inclined crack extends.

**3.5.2. The Effect of Main Crack Propagation on Inclined Crack.** In this section, the effects of main crack propagation on the inclined crack for various lengths of inclined crack have been discussed. Figures 13(a)–13(f) show the variation of SERR calculated at the inclined crack 2 with the propagation of main crack, (a) for the inclined crack length of 0 mm, (b) for 1 mm, (c) for 2 mm, (d) for 3 mm, (e) for 4 mm, and (f) for 5 mm, respectively. The increase in the inclined crack length means the progressive propagation of inclined crack as the load. The SERR calculated at the inclined crack is a good choice to reflect the influence of main crack propagation on the inclined crack and on the overall stiffness and strength of the concrete beam.

It can be seen from Figure 13 that for each given length of inclined crack, the value for SERR increases as the main crack grows, approaching the critical SERR of the concrete material and showing that the inclined crack with main crack propagation tends to crack. On the other hand, as illustrated in Figure 13(a), the value for SERR firstly appears to be a decrease as the main crack propagates, and then it seems to be an increase with the propagation of main crack, which implies that stress concentration exists in the concrete material at the end of the bonded FRP. As the main crack

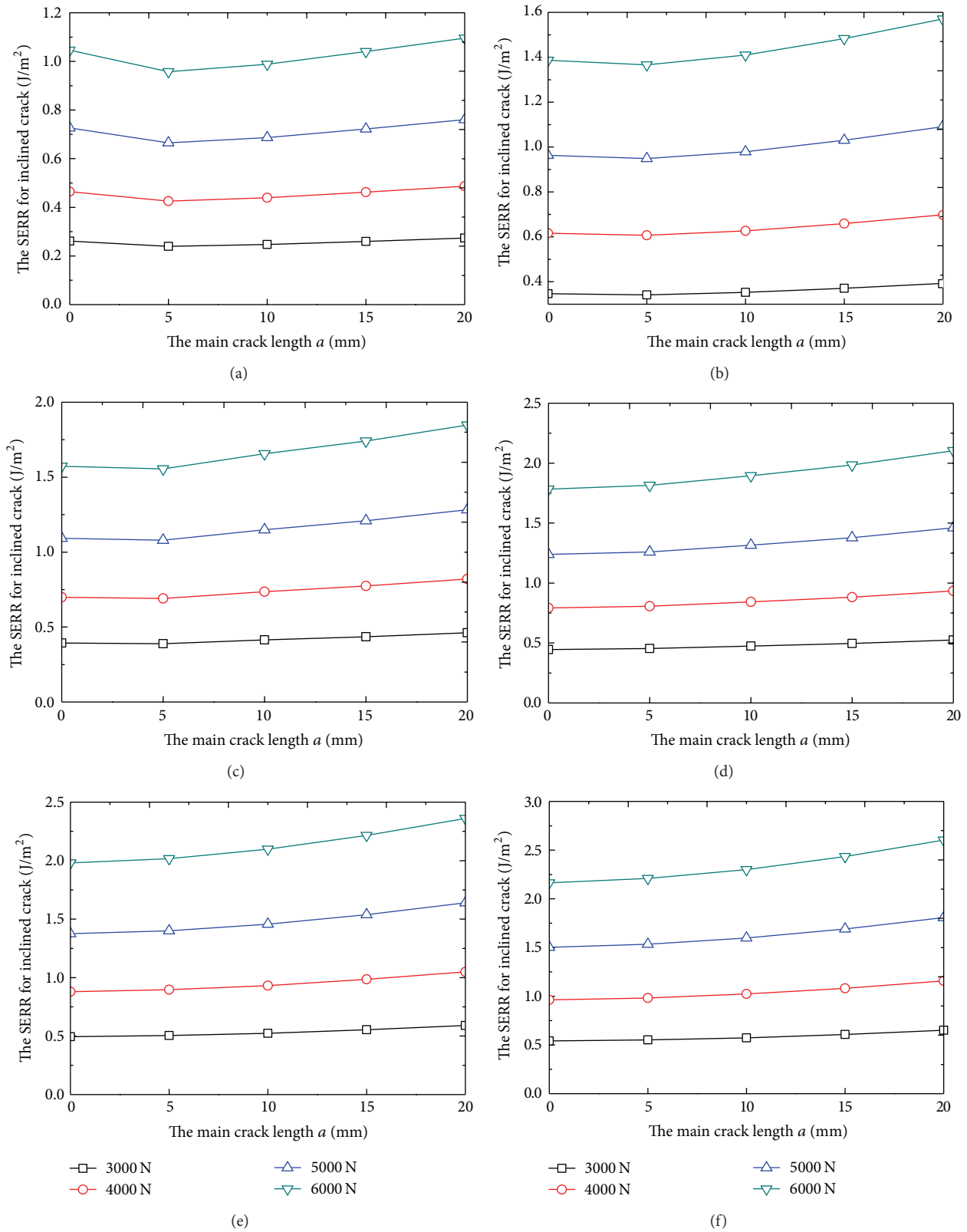


FIGURE 13: The plot of SERR against main crack propagation for various length of inclined crack. (a) 0 mm of inclined crack length, (b) 1 mm of inclined crack length, (c) 1 mm of inclined crack length, (d) 2 mm of inclined crack length, (e) 3 mm of inclined crack length, and (f) 0 mm of inclined crack length.

does not propagate, the value for SERR at the end of the plate seems to be larger while it will decrease rapidly when main crack starts to propagate. Next, the phenomenon of stress concentration at the end of plate has been effectively released. Meanwhile, as the main crack progressively propagates to a fixed crack length, the magnitude of stress at the crack tip of the main crack can dramatically decrease due to the tension of FRP externally bonded at the bottom of the concrete beam. At this time, CFRP begins to become tensile more than before and it considerably releases the stress concentration occurring at the main crack. The higher tension in CFRP due to its high stiffness and modulus can effectively prevent the main crack in concrete beam from propagating continually. However, SERR for inclined crack in turn increases slightly because the tensile stress in CFRP drastically increases the concentration of stress at the end of CFRP, building up the risk of crack propagation. With the inclined crack proceeding to propagate, the value for SERR at the inclined crack tends to increase slightly regardless of the applied load, seen from Figures 13(a)–13(f), showing that the propagation of inclined crack makes the SERR for itself much closer to the critical value and increases the risk of crack formation.

#### 4. Conclusion

The concrete beams with and without CFRP strengthened are considered to investigate the improvement in loading capacity and analyze the failure mechanism of the concrete beam. The main conclusions can be drawn as follows.

- (1) Strain energy release rate (SERR) for a specified crack has been chosen as an indicator to show the strengthening effect of CFRP bonded at the bottom of concrete beams. The strain energy release rate are calculated at an interest crack based on virtual crack closure technology (VCCT) using FEM to determine whether the mechanical properties of the beam are strengthened by being externally bonded with CFRP.
- (2) For plain concrete beam without being strengthened by CFRP, the calculated SERR for any case of load can increase slightly with the main crack propagation. The bigger the magnitude of SERR is, the closer it approaches  $G_C$  of the concrete material. It implies that the strength of the beam decreases with the increase of SERR.
- (3) For plain concrete beam externally bonded with CFRP, the value for SERR can significantly increase with the applied load, showing that the loading capacity of the beam is improved. However, as the main crack extends to some certain length, the value for SERR slightly increases as cracks extend, but it decreases rapidly with crack propagation.

#### Acknowledgments

This work is financially supported by the Natural Science Foundation of China (11302272), by the Natural Science Foundation of China (11272368), by the Natural Science

Foundation Project of Chongqing Municipality (CSTC, 2010BB4085), and by the Science and Technology Project Affiliated to the Education Department of Chongqing Municipality (KJ120801).

#### References

- [1] A. K. M. Anwarul Islam, "Effective methods of using CFRP bars in shear strengthening of concrete girders," *Engineering Structures*, vol. 31, no. 3, pp. 709–714, 2009.
- [2] M. C. Sundarraja and S. Rajamohan, "Strengthening of RC beams in shear using GFRP inclined strips—an experimental study," *Construction and Building Materials*, vol. 23, no. 2, pp. 856–864, 2009.
- [3] H. C. Biscaia, C. Chastre, and M. A. G. Silva, "Nonlinear numerical analysis of the debonding failure process of FRP-to-concrete interfaces," *Composites B*, vol. 50, pp. 210–223, 2013.
- [4] J. Michels, R. Christen, and D. Waldmann, "Experimental and numerical investigation on postcracking behavior of steel fiber reinforced concrete," *Engineering Fracture Mechanics*, vol. 98, pp. 326–349, 2013.
- [5] X.-S. Yang, J. M. Lees, and C. T. Morley, "Modelling crack propagation in structures: comparison of numerical methods," *Communications in Numerical Methods in Engineering*, vol. 24, no. 11, pp. 1373–1392, 2008.
- [6] J. F. Guan, L. B. Qing, and S. B. Zhao, "Research on numerical simulation on the whole cracking processes of three-point bending notch concrete beams," *Chinese Journal of Computational Mechanics*, vol. 30, pp. 143–148, 2013.
- [7] S. S. Pendhari, T. Kant, and Y. M. Desai, "Application of polymer composites in civil construction: a general review," *Composite Structures*, vol. 84, no. 2, pp. 114–124, 2008.
- [8] C. Mazzotti, M. Savoia, and B. Ferracuti, "An experimental study on delamination of FRP plates bonded to concrete," *Construction and Building Materials*, vol. 22, no. 7, pp. 1409–1421, 2008.
- [9] W. Xue, L. Zeng, and Y. Tan, "Experimental studies on bond behaviour of high strength CFRP plates," *Composites B*, vol. 39, no. 4, pp. 592–603, 2008.
- [10] J. Valivonis and T. Skuturna, "Cracking and strength of reinforced concrete structures in flexure strengthened with carbon fibre laminates," *Journal of Civil Engineering and Management*, vol. 13, no. 4, pp. 317–323, 2007.
- [11] S. S. Niu, *The experimental study on concrete beams strengthened with CFRP [M.S. thesis]*, Chongqing University, Chongqing, China, 2008.
- [12] T. L. Anderson, *Fracture Mechanics: Fundamentals and Applications*, CRC Press, 2005.
- [13] A. M. Navier, *Material Properties of Concrete*, China Building Industry Press, 2011.
- [14] R. Krueger, "Virtual crack closure technique: history, approach, and applications," *Applied Mechanics Reviews*, vol. 57, no. 1–6, pp. 109–143, 2004.
- [15] J. Ding, *Crack failure study of CFRP reinforced concrete beams [M.S. thesis]*, Chongqing University, Chongqing, China, 2008.
- [16] K. P. Herrmann and M. Dong, "Thermal cracking of two-phase composite structures under uniform and non-uniform temperature distributions," *International Journal of Solids and Structures*, vol. 29, no. 14–15, pp. 1789–1812, 1992.

## Research Article

# Deposition of Low Stress Silicon Nitride Thin Film and Its Application in Surface Micromachining Device Structures

Beirong Zheng,<sup>1</sup> Chen Zhou,<sup>1</sup> Quan Wang,<sup>2</sup> Yifeng Chen,<sup>1</sup> and Wei Xue<sup>1</sup>

<sup>1</sup> College of Mechanical and Electrical Engineering, Wenzhou University, Wenzhou 323035, China

<sup>2</sup> State Key Lab of Transducer Technology, Chinese Academy of Sciences, Shanghai 200050, China

Correspondence should be addressed to Wei Xue; [xue\\_wenzhou@163.com](mailto:xue_wenzhou@163.com)

Received 26 July 2013; Accepted 23 September 2013

Academic Editor: Yan Yang

Copyright © 2013 Beirong Zheng et al. This is an open access article distributed under the Creative Commons Attribution License, which permits unrestricted use, distribution, and reproduction in any medium, provided the original work is properly cited.

Surface machining processes are responsible for creating microstructures that reside near the surfaces of a substrate and are characterized by the fabrication of micromechanical structures from deposited thin films. These films can be selectively removed to build three-dimensional structures whose functionality typically requires that they should be freed from the planar substrate. Silicon nitride thin film is one of these important materials. In this paper, by adjusting the  $\text{SiH}_2\text{Cl}_2/\text{NH}_3$  gaseous ratio, low stress silicon nitride (LS SiN) is deposited by the low pressure chemical vapor deposition (LPCVD) process. The internal stress generally in 135 MPa has been detected using an FLX-2320 film stress tester. Based on the wide application in surface micromachining devices, the mechanical properties of LS SiN are measured by nanoindentation, giving the value of Young's modulus of 224 GPa and the hardness of 22.5 GPa, respectively. Dry etching and wet etching are utilized to fabricate the LS SiN thin film for structural layers. The etching rate compared with normal  $\text{Si}_3\text{N}_4$  film by LPCVD is demonstrated for silicon chip manufacture.

## 1. Introduction

Bulk micromachining is an important class of micromechanical electronics system (MEMS) process [1, 2]. In bulk processes, a portion of the substrate (bulk) is removed in order to create freestanding mechanical structures (such as beam and membranes) or unique three-dimensional features (such as cavities, through-wafer holes, and mesas). There are two major categories of processes for bulk etching according to the medium of the etchant: wet etching and dry etching. Wet silicon etching processes use liquid chemical solutions in contact with silicon. Dry etching uses plasma (high energy gas containing ionized radicals) or vapor phase etchants to remove materials. Currently, the focus on the bulk etching has been transformed from the etching geometric structures to improving etching accuracy, uniformity, surface roughness, and compatibility with CMOS.

Surface micromachining is so named because the process takes place on the surface of the wafer, where films are used for structural elements and deposited using a technique such as low temperature chemical vapor deposition (LPCVD) [3, 4]. Originally, employed for integrated circuits, films

composed of materials such as polysilicon, silicon nitride, and silicon dioxides can be sequentially deposited and selectively removed or machine three-dimensional structures whose functionality typically requires that they should be freed from the planar substrate. Bulk micromachining is not easily integrated with IC processing. Surface micromachining can easily be integrated with CMOS processing, allowing signal processing circuitry and MEMS devices to exist on the same chip.

There are two key process steps in surface micromachining. The first is deposition of low stress thin films that can be used for structural elements. The second is the use of a sacrificial layer to allow the structural layer to be detached from the substrate, thus allowing the motion of the structural layer. The deposition of controlled stress films is an essential process step for surface micromachining. With excellent characteristics [5, 6], silicon nitride film can block the diffusion of water and ions (such as sodium) effectively. Due to the capability of antioxidization and anticorrosion, it can be used as masks for deep etching, electronic insulation layer, and ion implantation. In this paper, we focus on the preparation process of low stress silicon-rich nitride

(LS SiN) films. The mechanical parameter of LS SiN is presented by nanoindentation. The film pattern in the surface micromachining process is demonstrated, which provides a strong basis for the MEMS device design and silicon chip fabrication.

## 2. Deposition of Low Stress Silicon Nitride Thin Film

Normal  $\text{Si}_3\text{N}_4$  film is deposited at temperature over  $800^\circ\text{C}$  using dichlorosilane (DCS) and ammonia in a flow ratio of approximately 1:5 (DCS: $\text{NH}_3$ ) on a silicon wafer. This process yields a stoichiometric  $\text{Si}_3\text{N}_4$  film with high tensile stress. By reversing the flow ratio to 10:1, a silicon-rich nitride film is deposited, and the tensile stress level is considerably lower. Table 1 lists the parameters; the reaction is



Figure 1 depicts the stress map of LS SiN tested by FLX2320. The stress can be calculated using the Stoney equation as follows:

$$\sigma = \frac{\delta}{t} \frac{E}{1-\nu} \frac{T^2}{3R^2}, \quad (2)$$

where  $\delta$  and  $t$  are the deflection of wafer center and film thickness, respectively.  $R$  and  $T$  are the radius and thickness of silicon, respectively.  $E$  is Young's modulus, and  $\nu$  is Poisson's ratio. The fitted stress is less than 135 MPa.

## 3. Mechanical Properties of LS SiN

In MEMS/NEMS design, Young's modulus of the thin film is one of the important mechanical properties. Young's modulus of a single-crystal material reflects the details of interatomic bond energy and lattice structure. With the rapid development of NEMS technologies, ultrathin cantilevers have been used as sensitive sensors for applications involving ultrafine resolution. Young's modulus,  $E$ , has a strong effect on the resonant cantilevers because it is proportional to the square of the resonance frequency. The fundamental resonance frequency of a cantilever is [7]

$$f_0 \approx 0162 \frac{t}{l^2} \sqrt{\frac{E}{\rho}}, \quad (3)$$

where  $t$  is the thickness,  $l$  is the length, and  $\rho$  is the material density of the cantilever.

Nanoindentation is a useful technique for measuring the mechanical properties of small volumes of materials. Its attractiveness stems largely from the fact that mechanical properties can be determined directly from measurements of indentation and displacement, without the need to image the hardness impression. Based on the depth-sensing indentation method of Oliver and Pharr, the elastic modulus of the

TABLE 1: LS SiN deposition parameter.

Temperature ( $^\circ\text{C}$ )			Pressure (mTorr)	Gas (sccm)	
Handle	Centre	Source		$\text{NH}_3$	DCS
835	875	860	289	8	80

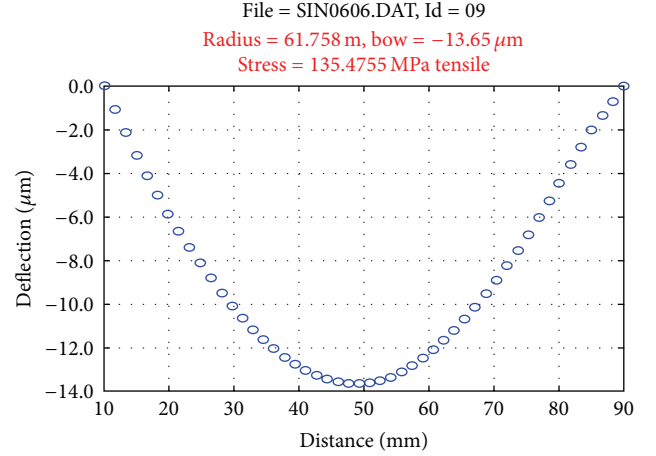


FIGURE 1: Internal stress measurement of LS SiN.

specimen was related to the measured reduced modulus,  $E_r$ , by using the equation [8, 9]

$$\frac{1}{E_r} = \frac{(1-\nu^2)}{E} + \frac{(1-\nu_i^2)}{E_i}, \quad (4)$$

$$E = \frac{1-\nu^2}{E_i - (1-\nu_i^2)} E_i E_r = \frac{1-\nu^2}{E_i/E_r - (1-\nu_i^2)} E_i,$$

where  $E_i$  and  $\nu_i$  are Young's modulus and Poisson's ratio of the diamond tip. Here,  $E_i$  and  $\nu_i$  are equal to 1140 GPa and 0.07, respectively.  $E_r$  is referred to as the reduced modulus and is expressed as a function of the displacement per unit load which is applied as follows:

$$E_r = \frac{1}{2} \frac{\sqrt{\pi}}{\sqrt{A}} \frac{dP}{dh}. \quad (5)$$

In the previous equation (5),  $P$  is the applied load,  $h$  is the displacement, and  $A$  is the contact area.

Nanoindentation tests were carried out on a Triboindenter (Hysitron Inc.), with a Berkovich indenter tip, whose radius was estimated to be 100 nm. Because the thickness of the LS SiN film was around  $1.2 \mu\text{m}$ , the maximum indentation depth was restricted to 120 nm to avoid the influence of the substrate. Figure 2 shows the load-displacement relationship of the sample during nanoindentation.

Figure 3 shows the load and unload time. Since the SiN film thickness is around  $1.2 \mu\text{m}$ , the 4 mN maximum load, the 5 s loading time, the 5 s unloading time, and the 5 s no-load time are selected to avoid phase change of the material [10, 11]. The maximum penetration depth to press is less than 120 nm to avoid the impact of the substrate. Four measurement locations are selected in each sample, each adjacent point

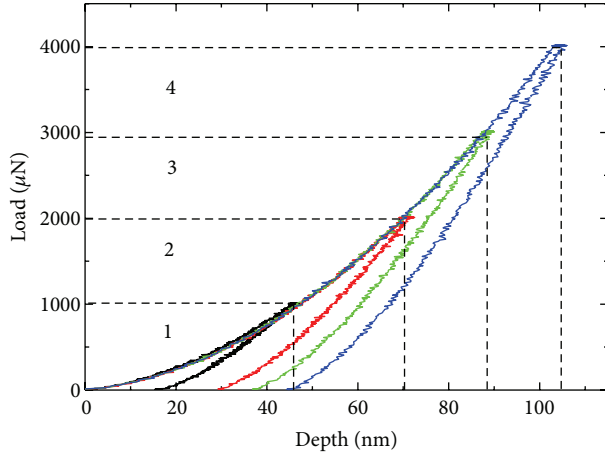


FIGURE 2: Load-displacement relationship of LS SiN sample during nanoindentation.

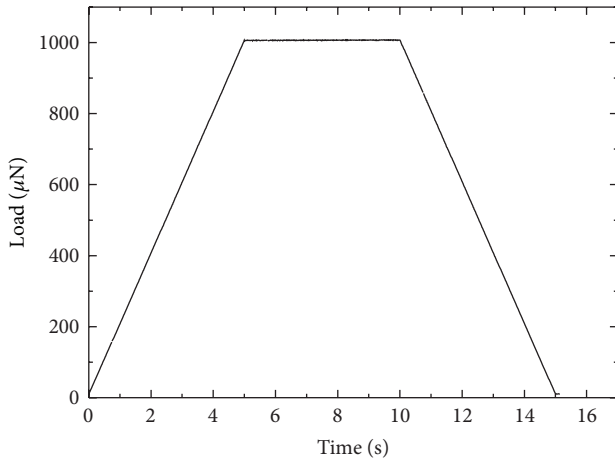


FIGURE 3: Indentation profile used for the indentation experiments.

keeping a distance above  $3 \mu\text{m}$ . Young's modulus of the four samples calculated is shown in Table 2. The average Young's modulus of LS SiN is 224 GPa.

#### 4. Application of Low Stress Silicon Nitride Film

Surface micromachining process can fabricate the micromechanical structures adhered to substrate surface by depositing structural layer on the sacrificial one. This can provide support for structural layer and play a role on space-based positioning during processing. The sacrificial layer was then removed to release the structural layer on it. Generally, silicon nitride films deposited by LPCVD can be used as a structural layer for their internal tensile stress and native nonporous morphology. In practical applications, except for long process time (high cost), silicon nitride films by LPCVD are less than  $1.5 \mu\text{m}$ . If the thickness is too large, the film under tensile stress will bend and even fracture. As the structural layer of devices, films with appropriate internal tensile stress are

TABLE 2: LS SiN Young's modulus experiment.

Sample	$E_r$ (GPa)				Average	$E$ (GPa)
	1	2	3	4		
1P19	197.29	181.02	183.15	196.27	189.43	214.92
1P20	219.53	221.14	203.86	201.09	211.40	245.48
1P21	211.28	188.60	191.03	191.17	195.52	223.24
1P22	187.31	186.96	187.41	189.42	187.78	212.67
Average (GPa)						224.08

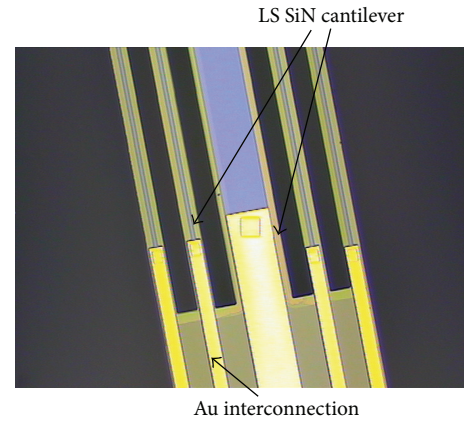
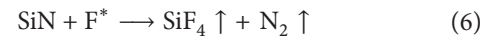


FIGURE 4: Cantilever structure made from LS SiN as the structural layer.

beneficial for the stability of the device and possess good mechanical properties [12]. Figure 4 shows the cantilever beam structure fabricated by LS SiN films. The resistor was formed after depositing polysilicon, ion implantation doping, and photolithography. A circuit compatible with CMOS by sputtering metals was constituted to fulfill low cost mass production of the devices.

The LS SiN patterning process can be divided into dry and wet etching. LS SiN dry etching mainly includes reaction ion etching (RIE) and ion beam etching (IBE). Reaction ion etching (RIE) is a technology that uses chemical reaction and physical ion bombardment to remove material. In general, the  $\text{CF}_4$  is used as corrosive gas and dissociated into  $\text{F}^*$ ,  $\text{CF}_3$ ,  $\text{CF}_2$  and  $\text{CF}$ , and so forth. With the highest chemical activity, fluoride free radicals  $\text{F}^*$  can react with LS SiN; the reaction is as follows:



Ion beam bombardment, using the inert gas Argon (Ar) rather than chemical incorporation of etching matter, is an absolute micromachining process with two significant advances of directionality and practicality. Since ions in the ion beam are accelerated by a strong vertical electric field and the pressure in the reactor is extremely low, the impossibility of collisions between atoms leads to the directionality of etching. Firstly, the velocity when atoms impinge the silicon surface is almost vertical. The anisotropic etching to every material can be achieved as a result of its nonchemical property. Secondly, different raw materials used for corrosion

TABLE 3: LPCVD nitride etching rate comparison.

Etchants	Temperature (°C)	Ratio (Å/min)	
		Normal Si <sub>3</sub> N <sub>4</sub>	LS SiN
BOE	38	26.36	11.17
BOE	25	7.68	2.66
KOH	50	0.05	0.01
40% HF	25	112.76	41.54
H <sub>3</sub> PO <sub>4</sub>	160	32.56	9.95

include compounds and alloys. Due to its capabilities to etch graphics on different materials, the serious disadvantages are the optical photoresistance and the selectivity of lower levels close to 1:1.

Due to the selectivity of etching, silicon nitride film commonly functions as a mask for wet etching of polysilicon, silicon oxide, and other materials. A comparison of the etching velocity of normal Si<sub>3</sub>N<sub>4</sub> and LS SiN using common etchants was studied. The result of the test is shown in Table 3. Results of the comparison show that the etching rate of normal Si<sub>3</sub>N<sub>4</sub> is faster than LS SiN in five different etching solutions (38°C BOE, ambient BOE, 50°C KOH, ambient 40% HF, and 160°C H<sub>3</sub>PO<sub>4</sub>).

The etching rate of LS SiN in the KOH and the ambient BOE is so slow that it can be used as a good etching resistant barrier. In the ambient 40% HF, due to the sensitivity to the oxygen residue in the film, the etching rate as the content of oxygen increased, while it is slow in H<sub>3</sub>PO<sub>4</sub>.

## 5. Conclusions

The preparation of low stress silicon-rich nitride films (LS SiN) is presented in this paper. By adjusting the SiH<sub>2</sub>Cl<sub>2</sub>/NH<sub>3</sub> gaseous ratio, LS SiN is deposited by the low pressure chemical vapor deposition (LPCVD) process. The internal stress, generally in 135 MPa, has been detected using an FLX-2320 film stress tester. Based on the wide application in surface micromachining devices, the mechanical properties of LS SiN are measured by nanoindentation, gaining the value of Young's modulus of 224 GPa and the hardness of 22.5 GPa, respectively. Dry etching (reaction ion etching and ion beam etching) and wet etching (38°C BOE, ambient BOE, 50°C KOH, ambient 40% HF, and 160°C H<sub>3</sub>PO<sub>4</sub>) are utilized to fabricate the LS SiN thin film for structural layers. The etching rate compared with normal Si<sub>3</sub>N<sub>4</sub> film by LPCVD is demonstrated for the device silicon chip manufacture.

## Acknowledgments

This work was financially supported by the Science and Technology Development Plan of Zhejiang Province (Public Technology Research and Industrial Projects, Grant no. 2012C21088), Natural Science Foundation of Zhejiang province (Grant no. LY13E050016), and the Opening Foundation of Jiangsu Province Naterial Tribology Key Laboratory (no. kjsmcx1001).

## References

- [1] G. T. A. Kovacs, N. I. Maluf, and K. E. Petersen, "Bulk micromachining of silicon," *Proceedings of the IEEE*, vol. 86, no. 8, pp. 1536–1551, 1998.
- [2] M. Zahedinejad, S. D. Farimani, M. Khaje et al., "Deep and vertical silicon bulk micromachining using metal assisted chemical etching," *Journal of Micromechanics and Microengineering*, vol. 23, no. 5, Article ID 055015, 2013.
- [3] F. Nabki, T. A. Dusatko, S. Vengallatore, and M. N. El-Gamal, "Low-stress CMOS-compatible silicon carbide surface-micromachining technology-part I: process development and characterization," *Journal of Microelectromechanical Systems*, vol. 20, no. 3, Article ID 5742665, pp. 720–729, 2011.
- [4] J. M. Bustillo, R. T. Howe, and R. S. Muller, "Surface micromachining for microelectromechanical systems," *Proceedings of the IEEE*, vol. 86, no. 8, pp. 1552–1574, 1998.
- [5] P. Morin, G. Raymond, D. Benoit, P. Maury, and R. Beneyton, "A comparison of the mechanical stability of silicon nitride films deposited with various techniques," *Applied Surface Science*, vol. 260, pp. 69–72, 2012.
- [6] M. Cazzanelli, F. Bianco, E. Borga et al., "Second-harmonic generation in silicon waveguides strained by silicon nitride," *Nature Materials*, vol. 11, no. 2, pp. 148–154, 2012.
- [7] C. Liu, *Foundation of MEMS (2nd Edited)*, China Machine Press, Beijing, China, 2011.
- [8] W. C. Oliver and G. M. Pharr, "Measurement of hardness and elastic modulus by instrumented indentation: advances in understanding and refinements to methodology," *Journal of Materials Research*, vol. 19, no. 1, pp. 3–20, 2004.
- [9] W. C. Oliver and G. M. Pharr, "Improved technique for determining hardness and elastic modulus using load and displacement sensing indentation experiments," *Journal of Materials Research*, vol. 7, no. 6, pp. 1564–1583, 1992.
- [10] S. Ruffell, J. E. Bradby, and J. S. Williams, "High pressure crystalline phase formation during nanoindentation: amorphous versus crystalline silicon," *Applied Physics Letters*, vol. 89, no. 9, Article ID 091919, 2006.
- [11] J. W. Yan, H. Takahashi, J. Tamaki, X. Gai, and T. Kuriyagawa, "Transmission electron microscopic observation of nanoindentations made on ductile-machined silicon wafers," *Applied Physics Letters*, vol. 87, no. 21, Article ID 211901, pp. 1–3, 2005.
- [12] L. W. Lin, H. C. Chu, and Y. W. Lu, "Simulation program for the sensitivity and linearity of piezoresistive pressure sensors," *Journal of Microelectromechanical Systems*, vol. 8, no. 4, pp. 514–522, 1999.

## Research Article

# Study of Alloying Process on 40Cr Surface with Electron Beam after Electroplated Cr Layer

**Xu Hongbin, Hu Jianjun, Li Hui, Mao Rongshan, Sun Fei, and Hou Tianfeng**

*Chongqing University of Technology, Chongqing 400054, China*

Correspondence should be addressed to Hu Jianjun; [hujj@qq.com](mailto:hujj@qq.com)

Received 13 July 2013; Accepted 11 September 2013

Academic Editor: Xing Chen

Copyright © 2013 Xu Hongbin et al. This is an open access article distributed under the Creative Commons Attribution License, which permits unrestricted use, distribution, and reproduction in any medium, provided the original work is properly cited.

The electroplated hard chromium coat was selected as precoating to improve surface properties of 40Cr. Then electron beam alloying process was experimentalized. The relation rules were summarized between alloying process parameters and overall surface properties by surface morphology observation, surface energy spectrum analysis, EDX analysis in section, and XRD. Experiment results showed that the microcracks appeared on surface of electron beam alloying specimen. Microcracks could disappear when the orthogonal experimental optimum process was used. The matrix metal elements diffused into metal coating surface after electron beam treatment. The maximum depth of alloyed layer could reach 8  $\mu\text{m}$  after electron beam alloying treatment, and electron beam alloying process generated new residual austenite phase.

## 1. Introduction

Gear is the key basic part in machinery products. Practice showed that gear failure appeared on tooth surface primarily. So it was the basic scientific problem to improve tooth surface performance of gears [1]. 40Cr steel was widely used in manufacturing industry as a driving part (such as gear wheel and bearings). However, it was easy to wear and tear in working which makes part discard as useless. Therefore, keeping 40Cr steel work piece away from the failure caused by corrosion, wear, oxidation, and fatigue is always an attractive objective [2].

The use of alloying for improving the properties of gear surface had been studied and developed widely because the strength of the material surface, wear, and fatigue strength properties could be improved significantly. But elements, processes, and mechanisms of alloying were not the same based on different materials [3, 4]. Cr was usually used as an alloying element to join into steel and alloys. Chrome plating was widely used because of higher hardness, good wear and corrosion resistance, and low cost.

High-current pulsed electron beam (HCPEB) was a new surface processing technology. When high energy density electron beam acted on the material surface, the coating alloy layer was melted, and substrate surface micromelting

occurred. Coated alloy formed metallurgical combination with surface alloy layer due to diffusion melt into internal metal substrates, which made big changes in the material's surface properties, such as high hardness, high wear resistance, and strong corrosion resistance [5].

Therefore, here hard chrome plating was selected as precoating on 40Cr then dealt with electron beam. Excellent surface overall performance was expected to obtain.

## 2. Materials and Methods

**2.1. Preparation of Specimen.** 40Cr was chosen as experiment material (the chemical composition is 0.40 wt-%C, 0.8 wt-%Cr, Ni  $\leq$  0.30 wt-%, 0.23 wt-%Si, 0.7 wt-%Mn, and Fe balance). The heat treatment pattern involved the first 850°C quenching and then tempering at 300°C. So its organizational form was tempered martensite.

**2.2. Experimental Scheme.** The orthogonal experiment was taken and three factors were selected: electron beam accelerating voltage, pulse frequency, and film thickness. Alloying process was investigated on the basis of surface morphology, element diffusion, and microstructural changed. The precoat thickness was selected as 1  $\mu\text{m}$ , 2  $\mu\text{m}$ , and 3  $\mu\text{m}$  because

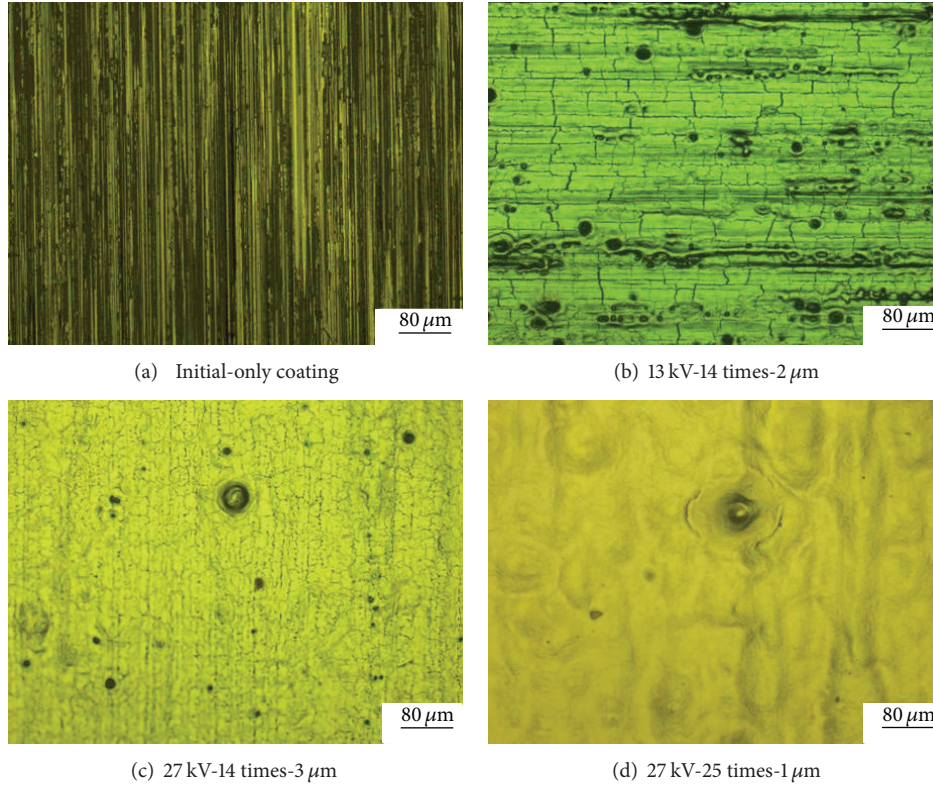


FIGURE 1: Surface morphology after electron beam treatment.

TABLE 1: The level and factors of orthogonal experiment.

Level	Accelerating voltage (kV)	Pulse frequency (times)	Film thickness ( $\mu\text{m}$ )
1	13	3	1
2	20	14	2
3	27	25	3

electron beam melting depth was not more than  $3\mu\text{m}$  [6]. Influencing factors and levels were shown in Table 1.

Coating specimens were irradiated with electron beam equipment "RITM-2M", which was made in Russia. It had the operating parameters as follows: electron energy 10–40 keV, pulse duration 5–10 ms, peak current density  $1\text{--}6\text{ J/cm}^2$ , and cross-section area  $30\text{ cm}^2$ .

**2.3. Organization and Performance Testing.** The surface topography was examined using an Axio Imager A10 optical microscope and a JSM-6460LV scanning electron microscope. The chemical composition was studied by using DX-2500 X-ray diffraction.

### 3. Results and Discussion

**3.1. Surface Topography.** The coating surface morphology before and after electron beam treatment was shown in Figure 1. Figure 1(a) was the chromium plating layer after machining, where mechanical wear scar dwelt on surface.

The crater could be observed on surface after electron beam irradiation, which was a typical feature of electron beam treatment [6]. The crack could be observed clearly on surface which could be caused by tensile stress.

Figure 1(b) showed the surface morphology of the voltage 13 kV, irradiation 14 times, and coating  $2\mu\text{m}$ . The mechanical grinding scar of the surface got some heal. Theoretically speaking, material surface melted quickly under electron beam irradiation, then molten metal flowed from the peak of the surface to the depressions rapidly on microscopic [7].

With increasing of accelerating voltage, the wear scar morphology was less clear and smoothing effect was more obvious. The crack became smaller with the acceleration voltage and the number of pulses increases. Figure 1(c) showed the surface morphology under the condition that the voltage was 27 kV, radiation 14 times, and coating depth  $3\mu\text{m}$ .

The surface cracks were not observed under the condition that voltage was 27 kV, radiation 25 times, and coating depth  $1\mu\text{m}$ , as shown in Figure 1(d).

The reason could be a result of the combined action of several factors. (1) High-energy electron beam was deposited on the surface of the material, which caused the metal surface layer of vaporization and enhanced diffusion [8]. So the chromium content of thin layer reduced or even disappeared. (2) The rapid heating of electron beam treatment caused thermal expansion, eventually rendering the surface compressive residual stress distribution [9]. (3) Chromium layer was in electron beam irradiation remelting zone and had completely fused with the base metal.

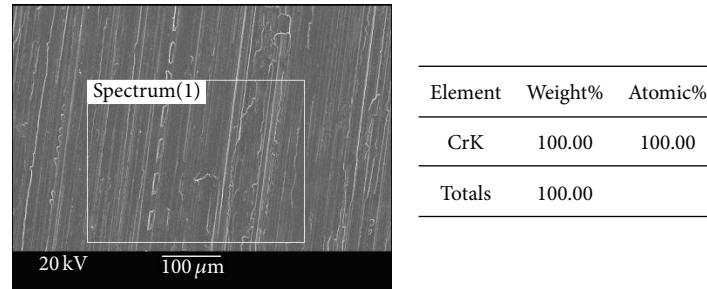
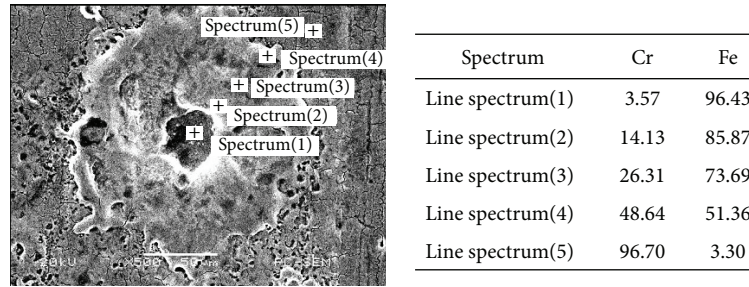
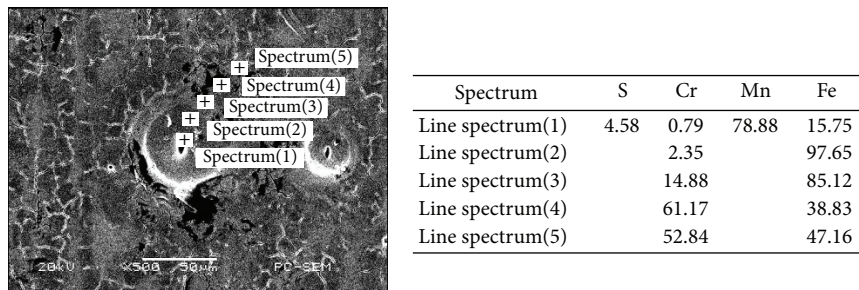
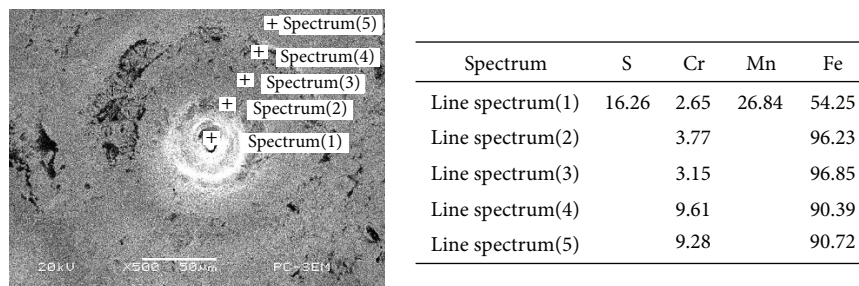
(a) Chromium plating 2  $\mu\text{m}$  surface spectrum before electron beam treatment(b) Surface spectroscopy after 13 kV-14 times-2  $\mu\text{m}$  parameters treated(c) Surface spectroscopy after 20 kV-25 times-2  $\mu\text{m}$  parameters treated(d) Surface spectroscopy after 27 kV-25 times-1  $\mu\text{m}$  parameters treated

FIGURE 2: Spectroscopy analysis results of surface crater.

**3.2. Surface Energy Spectrum Analysis.** Figure 2 showed surface energy spectrum analysis of the electron beam processing under the part parameters. As shown in Figure 2(a), plating surface was completely a Cr element before electron beam treatment. The Crater morphology was observed on the surface after electron beam treatment. The melting pit of representative specimen was selected to perform energy spectrum analysis and element diffusion was observed from the melt hole center location to the surface.

The analysis results of 5 points were shown in Figure 2(b) from the melting pit center to the material surface at electron

beam parameters 13 kV voltage, irradiation 14 times, and plating thickness 2  $\mu\text{m}$ . Cr elements' concentration of the points 1–4 was gradually increasing from melting pit center location to the material surface. Fe elements showed opposite distribution. The points 1, 2, 3, and 4 were in the melting pit eruption position, so Fe matrix elements were brought to the surface by volcanic crater eruption, which showed high concentration of center and low distribution of edge. Element concentrations of Cr and Fe varied widely from the measuring point 4 to 5, which may be because the measuring point 5 was outside the area impact crater eruption.

Figure 2(c) showed test result at 20 kV voltage, irradiation 25 times, and plating thickness  $2\text{ }\mu\text{m}$ . The element distribution trend was the same as shown in Figure 2(b). But the surface portion of Cr-Fe element concentration decreased about 95% than the previous specimen. It maybe because that diffusion of elements was promoted with the increasing of radiation voltage and frequency.

Figure 2(d) showed the analysis results at 27 kV voltage, irradiation 25 times, and the plating thickness  $1\text{ }\mu\text{m}$ . Fe concentration of the specimen improved greatly after treatment. There may be several reasons as follows. Firstly, as the radiation voltage and frequency increased, the diffusion between the elements was further promoted. Secondly, the chromium layer and substrate of the molten layer produced by electron beam irradiation had been completely melted, which caused content of Cr reducing in surface because they spread to sub-surface. Finally, high energy of electron beam depositing on the material surface could lead to vaporization and enhanced diffusion of the surface layer metal and other physical chemical phenomena, which makes chromium content of thin layer reduced or even disappeared.

**3.3. Morphologies and EDX Analysis in Section.** The specimen discussed previously was selected to perform interface energy spectrum analysis to explore element diffusion and the effect of alloying after the electron beam processing, as shown in Figure 3. Plating specimens were shown in Figure 3(a) before electron beam processing. Cr-Fe element intensity distribution was very steep at the interface curve, and diffusion almost did not happened between Cr and Fe element.

The molten layer formed after electron beam irradiation could be clearly observed in Figures 3(b), 3(c), and 3(d). Chromium layer which had completely melted fused together with the portion of melted base metal. In addition, the grain refinement of base material after electron beam treatment could be observed.

When voltage was 13 kV, irradiation was 14 times, and the plating thickness was  $2\text{ }\mu\text{m}$ , it was shown that the elements Cr-Fe diffusion layer depth was about  $2.5\text{ }\mu\text{m}$  in spectrum analysis, while the molten layer coating was about  $2\text{ }\mu\text{m}$  depth and grain refinement layer depth was about  $1.8\text{ }\mu\text{m}$ , as was shown in Figure 3(b). The Fe element was not detected on surface maybe because of its low concentration, which was confirmed by the surface EDS analysis results of the previous paper.

When the voltage was 20 kV, irradiation was 25 times, and the plating thickness was  $2\text{ }\mu\text{m}$ , it was shown that the elements Cr-Fe diffusion layer depth was about  $5.5\text{ }\mu\text{m}$  in spectrum analysis. The molten layer coating was about  $2.7\text{ }\mu\text{m}$  depth and grain refinement layer depth was about  $2\text{ }\mu\text{m}$ , as was shown in Figure 3(c). This was because the accelerating voltage, increasing pulse number, enhanced deposition energy of surface unit area, which prompted Fe element in the substrate diffusing to the surface of coating.

When the voltage was 27 kV, irradiation was 25 times, and the plating thickness was  $1\text{ }\mu\text{m}$ , because of the higher accelerating voltage and thinner plating Cr layer, the molten layer coating was about  $3.5\text{ }\mu\text{m}$  depth and grain refinement layer depth was about  $3.8\text{ }\mu\text{m}$ . The depth of the diffusion layer

was more than  $8\text{ }\mu\text{m}$ , and the intensity in the surface layer containing Fe was greater than Cr.

Thus, it was easy to summarize that with the increasing of electron beam acceleration voltage, pulses number, depth of the surface molten layer, grain refinement, and diffusion layer was increased gradually to obtain a good effect of alloying. The interdiffusion between coating and the matrix elements turned their mechanical bond into metallurgical bond. The electron-beam remelting and rapid cooling could cause grain refinement near the surface. And diffusion of elements caused solid solution strengthening. All these things provided conditions for improving surface properties of material.

**3.4. XRD Analysis.** Figure 4 shows that XRD diffraction spectrum of specimens corresponds to electron beam treatment. 40Cr original specimen was shown in Figure 4(a) before electron beam treatment and XRD diffraction spectrum of different thickness chromium layer specimens. The diffraction peak height of the specimen after plating was lower than before, and width increased significantly. The value of peak width achieved maximum when the coating thickness was  $3\text{ }\mu\text{m}$ .

XRD diffraction spectrum of specimens was shown in Figure 3(b) with different Cr layer thickness and pulses number under 13 kV voltage. Compared with the samples of only electroplating sample, the diffraction peak height was improved to some extent, and the diffraction peak width became narrow down. And it was more obvious with the increasing of the pulses number. It performed most obviously in the (110) lattice plane, which showed that as the integrity of the grain after the electron beam treatment improves, grain grows. When the Cr layer thickness was  $1\text{ }\mu\text{m}$  and  $2\text{ }\mu\text{m}$ , the corresponding diffraction spectrum appeared new characteristic peaks [10]. So new phase at produced, which was residual austenite, through analysis.

XRD diffraction spectrum of specimens was shown in Figure 4 with different Cr layer thickness and pulses number under 20 kV voltage. It was found that the surface crystal of specimen occurred preferred orientation from the original (110) lattice plane more than that from the (200). At the same time, the residual austenite phase appeared on surface of the chromium layer thickness  $1\text{ }\mu\text{m}$  and  $2\text{ }\mu\text{m}$ .

When accelerating voltage was increased to 27 kV, as shown in Figure 4(d), the preferred orientation of (200) lattice plane disappeared. The diffraction peak of residual austenite phase became very high at the irradiation of 25 pulse number, showing that the content increased significantly as a result of the very thin chromium layer at the moment. Within the scope of the electron beam melting layer, the deposited energy of electron beam bombarding material was sufficient to make the chromium layer and the substrate realized the full metallurgical melting of the matrix and coating metal under the action of mechanical stir at high voltage and pulse frequency. At the same time the austenite retained down and formed residual austenite under the rapid cooling speed.

By comparing the XRD diffraction of the orthogonal experiment specimens comprehensively, it could be found that residual austenite phase was often produced in the lower thickness chromium layer and its content also gradually

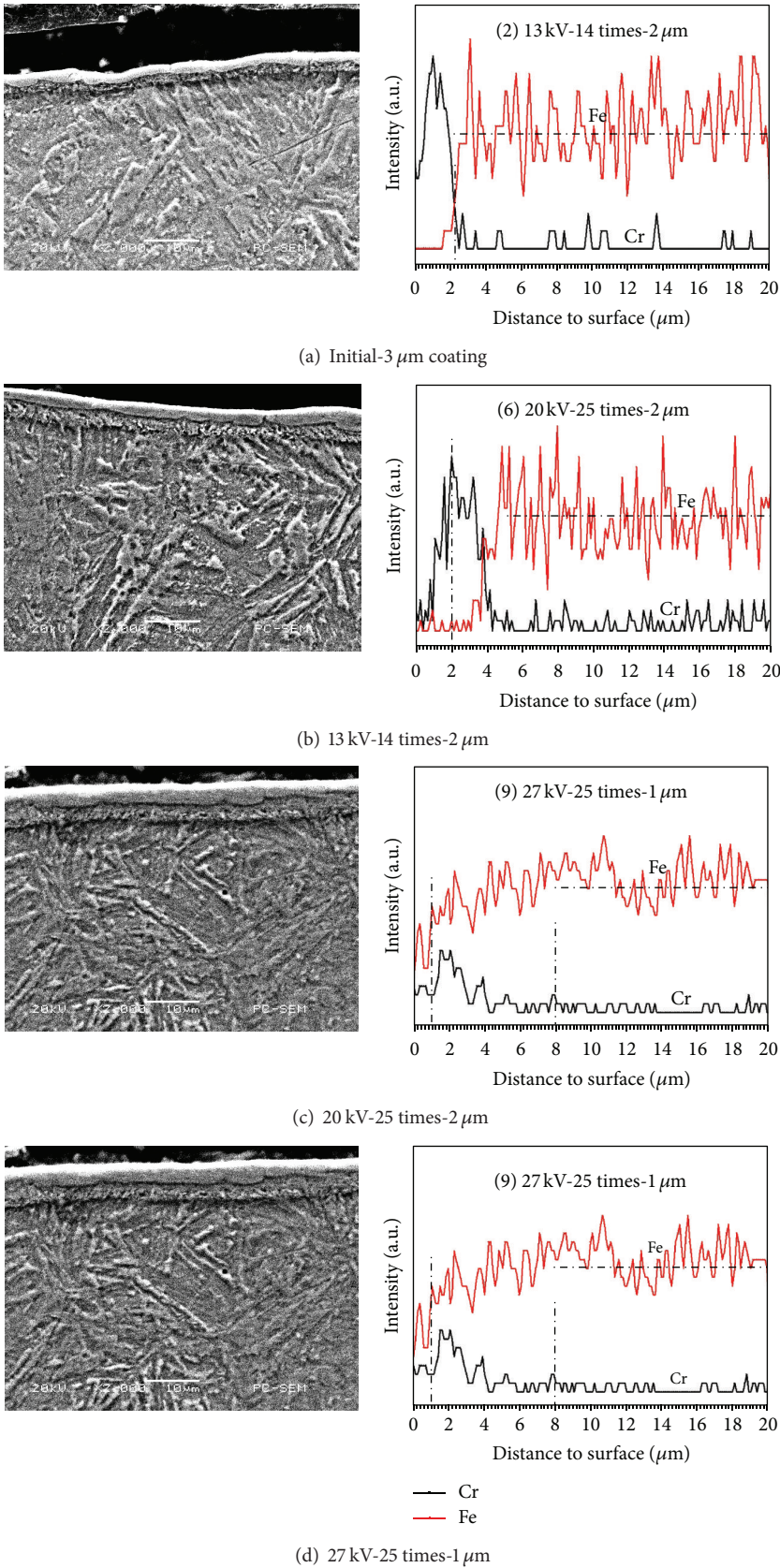


FIGURE 3: Cross-section morphology and spectral analysis.

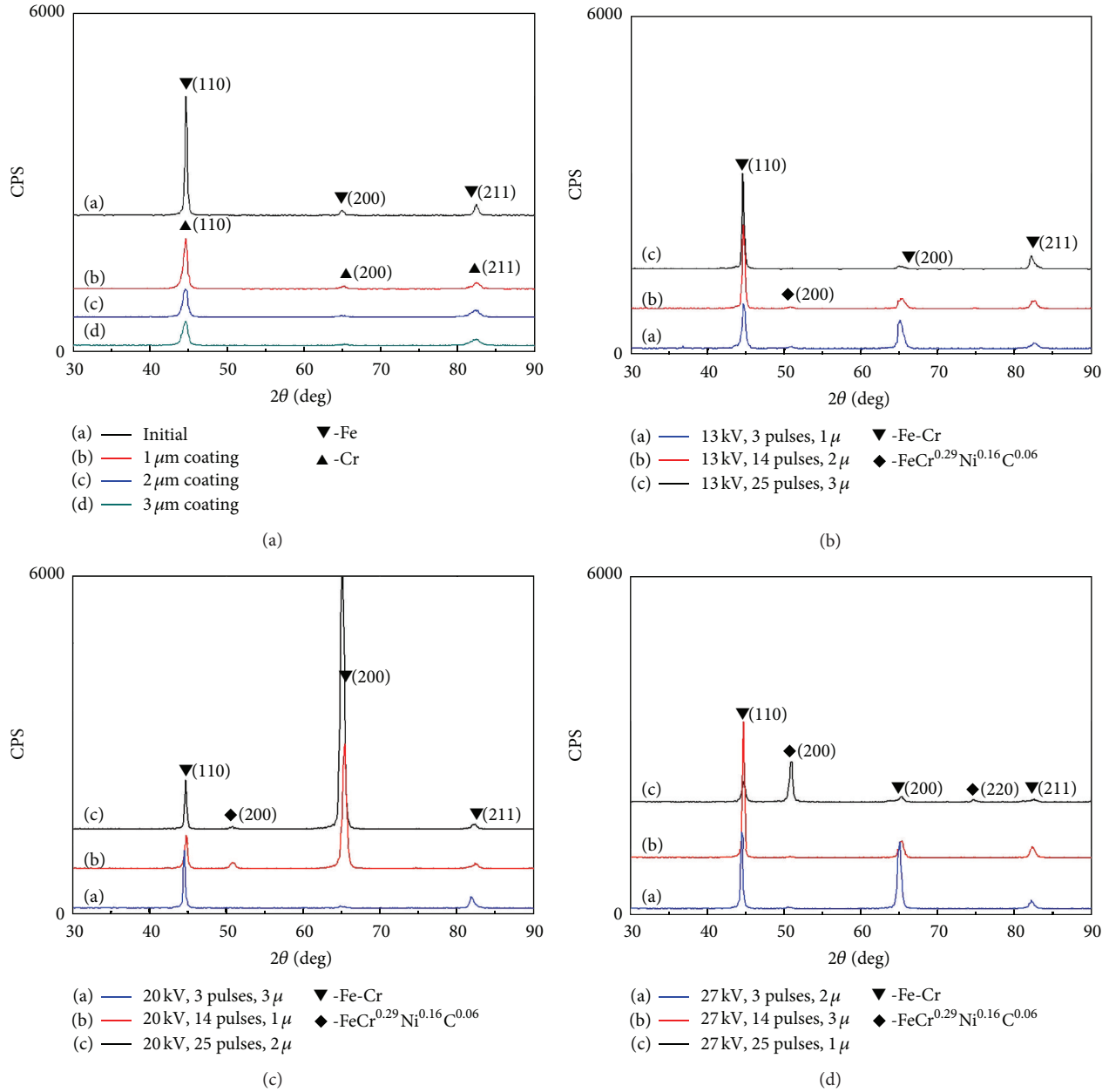


FIGURE 4: XRD diffraction spectrum.

increased with the increasing of acceleration voltage and pulse numbers. When the acceleration voltage reaches 27 kV, pulse number was 25 times, and coating thickness was 1  $\mu\text{m}$ , the surface residual austenite phase generated mostly [11].

By comparing the specimens treated with three different groups of accelerating voltages, it could be found that diffraction peaks had a certain degree of excursion to the right after electron beam treatment, indicating that the existing compressive stress or tensile stress releases. And it illustrated that the surface tensile stress could be reduced indirectly with the increasing of pulse number and make the surface present residual compressive stress state, finally. The comprehensive performance of surface could also be improved significantly.

#### 4. Conclusion

40Cr was precoated with electroplating hard chromium, and orthogonal experiment was used to realize the electron beam alloying processing. The conclusions could be drawn as following.

- (1) After the coating surface was treated with electron beam, a certain disagree of microcrack appeared on the surface, which became less and even disappeared with the increasing of accelerating voltage and pulse frequency.
- (2) After electron beam treatment, it was promoted that metal matrix elements spread to the coating surface.

With increasing of irradiation voltage and pulse frequency, the diffusion of surface element became stronger.

- (3) The alloying layer depth could reach  $8\text{ }\mu\text{m}$  treated by electron beam alloying maximum. And melting layer and grain refinement layer depth were increased gradually with the increasing of accelerating voltage and pulse frequency.
- (4) Contrasting with the original only electroplated, the chromium layer grain phases of specimens treated by electron beam were significantly larger. The residual austenite was produced on the surface. And the diffusion caused by electronic beam alloying could not only form solid solution making crystal lattice distorted, but also produce complex internal stress changes.

## Acknowledgments

The work has been supported by the National Natural Science Foundation of China (51275548), Chongqing Science and Technology Commission (cstc2012jjB0002 and cstc2012ggyys70019), and Innovation team of Chongqing Education Commission.

## References

- [1] D. T. Jelaska and S. Podrug, "Gear tooth root fatigue assessments by estimating the real stress cycle," in *Proceedings of the International Design Engineering Technical Conferences & Computers and Information in Engineering Conference (ASME '07)*, pp. 887–894, September 2007.
- [2] J. J. Hu, G. B. Zhang, H. B. Xu et al., "Microstructure characteristics and properties of 40Cr steel treated by high current pulsed electron beam," *Materials Technology*, vol. 27, no. 4, pp. 300–303, 2012.
- [3] Z. Tiejun, G. Bo, T. Xiaomei et al., "Modification and alloying of high purity magnesium surface with high current pulsed electron beam," *Chinese Journal of Vacuum Science and Technology*, vol. 28, no. 1, pp. 11–15, 2008.
- [4] H. Jianjun, Z. Genbao, C. Yuanfang et al., "Surface property of 40Cr alloyed Al with high current pulsed electron beam," *Materials Review*, vol. 26, no. 10, pp. 9–11, 2012.
- [5] K. Lee, K. Euh, D.-H. Nam, S. Lee, and N. J. Kim, "Wear resistance and thermal conductivity of Zr-base amorphous alloy/metal surface composites fabricated by high-energy electron beam irradiation," *Materials Science and Engineering A*, vol. 449–451, pp. 937–940, 2007.
- [6] C. Yuan-fang, X. Hong-bin, H. Jianjun et al., "Effect of HCPEB on frictional wear resistance of 3Cr2W8V mould steel," *Journal of Wuhan University of Technology*, vol. 33, no. 11, pp. 19–23, 2011.
- [7] H. Jianjun, Z. Genbao, X. Hongbin et al., "Gear bending fatigue strength with pulsed electron beam on different finished surface," *China Mechanical Engineering*, vol. 24, no. 3, pp. 380–385, 2013.
- [8] G. E. Ozur, D. I. Proskurovsky, V. P. Rotshtein, and A. B. Markov, "Production and application of low-energy high-current electron beams," *Laser and Particle Beams*, vol. 21, no. 2, pp. 157–174, 2003.
- [9] K. Jun, L. Gang, X. Jun, J. Mengdong, and L. Zigang, "Alloying Al on the surface of magnesium AZ31 alloy by high current pulsed electronic beam," *Special Casting and Nonferrous Alloys*, vol. 29, no. 11, pp. 1064–1067, 2009.
- [10] J. Zou, K. Zhang, C. Dong et al., "Selective surface purification via crater eruption under pulsed electron beam irradiation," *Applied Physics Letters*, vol. 89, no. 4, Article ID 041913, 3 pages, 2006.
- [11] M. Rongshan, *Study on Electron Beam Alloying Process and Properties of 40Cr Surface D*, Chongqing University of Technology, Chongqing, China, 2013.

## Research Article

# Scaling Analysis of the Tensile Strength of Bamboo Fibers Using Weibull Statistics

Jiaxing Shao,<sup>1,2</sup> Fang Wang,<sup>1,2</sup> Lu Li,<sup>1,2</sup> and Junqian Zhang<sup>3</sup>

<sup>1</sup> School of Materials Science and Engineering, Southwest University, Chongqing 400715, China

<sup>2</sup> Faculty of Materials and Energy, Southwest University, Chongqing 400715, China

<sup>3</sup> Department of Mechanics, Shanghai Key Laboratory of Mechanics in Energy and Environment Engineering, Shanghai University, Shanghai 200444, China

Correspondence should be addressed to Fang Wang; wangfang\_cq1978@163.com

Received 12 July 2013; Accepted 19 September 2013

Academic Editor: Xing Chen

Copyright © 2013 Jiaxing Shao et al. This is an open access article distributed under the Creative Commons Attribution License, which permits unrestricted use, distribution, and reproduction in any medium, provided the original work is properly cited.

This study demonstrates the effect of weak-link scaling on the tensile strength of bamboo fibers. The proposed model considers the random nature of fiber strength, which is reflected by using a two-parameter Weibull distribution function. Tension tests were performed on samples that could be scaled in length. The size effects in fiber length on the strength were analyzed based on Weibull statistics. The results verify the use of Weibull parameters from specimen testing for predicting the strength distributions of fibers of longer gauge lengths.

## 1. Introduction

In recent decades, natural fiber reinforcement has gained much attention as realistic, environmental-friendly alternatives to synthetic fibers. As typical biological materials with unique multiscale structures, natural fibers approximate or even exceed the specific mechanical properties of man-made fibers [1]. Among many natural fibers used as composite materials, bamboo fiber is one that offers the most potential because of its low density, low cost, high specific strength, and stiffness [2]. Understanding the mechanical properties of bamboo fiber is necessary for ensuring the reliability of such materials for designing proper composite structures.

Fibers are the main load-bearing elements of a fiber-reinforced composite, which means that most of the mechanical properties of fiber-reinforced composites are primarily affected by fiber strength distribution [3] and gauge length dependence [4]. The properties of bamboo fibers depend on growing condition, including growth duration and procedures involved in extracting the fiber from the plant [5]. In addition, bamboo fibers are typically brittle [6]. The strength of brittle materials and the effect of size have drawn the attention of scientists and technologists [7–11]. The statistical weakest link theory, which was formulated

based on conventional brittle fracture study, is based on the assumption that a material can be divided into smaller elements that are linked together, with the fracture beginning in the weakest link, and failure occurs when any of the links fail [12]. Considering that fiber strength is not constant even with uniform length and diameter, the statistical strength of fibers depends on the distribution of defects within the fiber. Although many studies have tried to predict fiber strength [5, 10, 13], very few statistical strength models have tried to describe the failure behavior of bamboo fibers. Therefore, we need an efficient method for evaluating bamboo strength for design and manufacturing.

The aim of the present paper is to investigate the scaling effects involved in predicting the ultimate tensile strength of bamboo fibers. Tension tests were performed to describe the statistical strength distributions of bamboo fibers. The measured fiber strengths at different gauge lengths were analyzed according to a two-parameter Weibull distribution. Thus, we established a method for determining statistical parameters used for characterizing strength distribution. Fibers 20, 30, 40, 50, and 60 mm long were used to investigate the dependence of strength on fiber size. The accuracy of using weak-link scaling statistics for fiber strength was also examined.

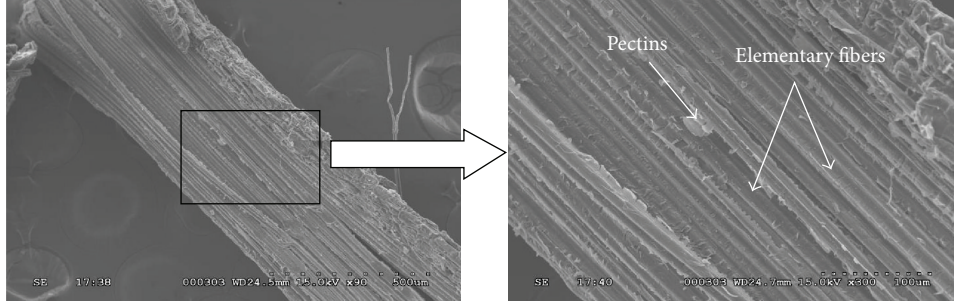


FIGURE 1: Longitudinal photomicrographs of bamboo fiber.

## 2. Experimental Procedure

The bamboo fibers were produced by Ban Ltd., Tokushima, Japan. The scanning electron micrograph of the longitudinal section of a bamboo fiber measured in the present study is shown in Figure 1. Bamboo fibers were clearly composed of elementary fibers connected by constituents, such as considerable amounts of pectins [14]. Although the microstructural framework of bamboo fibers could be called “elementary bamboo fiber bundles,” it was treated as a single fiber during macroscale tensile deformation [15]. In the present study, fiber diameter ranged from  $150\ \mu\text{m}$  to  $450\ \mu\text{m}$ . To study size effects on fiber length, the samples used in all tests had the same diameters, approximately  $200 \pm 15\ \mu\text{m}$ .

To fix the fiber as straight as possible between the clamps, a fiber specimen is mounted on a paper frame that matches the gauge length chosen for the test. The ends of the fiber were glued to the tab using a double-sided adhesive. The frame was cut after clamping in the jaws of the testing machine. The opening of the paper frame determined the gauge length. For this experiment, the gauge lengths were set to 20, 30, 40, 50, and 60 mm. Fifty individual fibers were tested at each of the five gauge lengths. Fiber length was measured to an accuracy of  $\pm 1\ \text{mm}$  at each end. Tests were performed on a variety of lengths to investigate the effects of fiber length on tensile strength. To prevent additional flaws caused by the clamping force, samples broken near the edge of the clamps were excluded from the analysis.

Fiber specimens were mechanically tested on a WDW3050 computer-controlled universal testing machine. All static tests were conducted in displacement control mode at a rate of  $0.5\ \text{mm/min}$  and at ambient temperature under atmospheric pressure. All samples were maintained under load until mechanical failure occurred, with failure being defined as the point in which the laminate no longer supported the externally applied load. The forces applied and the testing machine displacements were directly recorded by an acquisition system and on a chart recorder. Therefore, tensile strength was taken as the ratio of the maximum load applied to the cross-sectional area of the specimen. Based on a typical load-displacement response shown in Figure 2, the tensile load increased proportionally with increasing strain until the point of ultimate load, which is the point at which the bamboo fibers broke and exhibited brittle fractures with no apparent yielding.

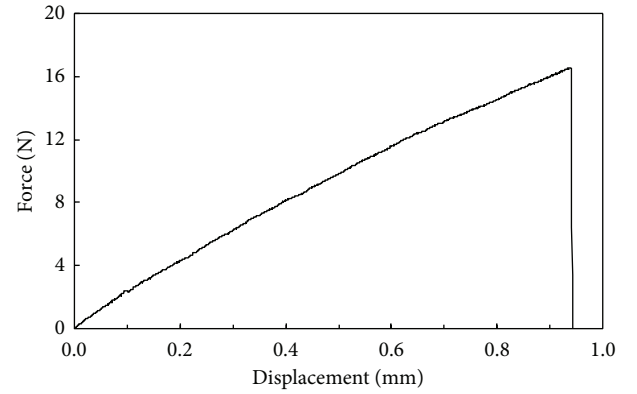


FIGURE 2: The experimental results of a classical load-displacement curve of bamboo fiber.

## 3. Weibull Statistics

Brittle fibers typically exhibit wide variability in strength, which is determined by the microstructural flaws that act as stress concentrations. These internal defects occur randomly along the length of the fiber. Fracture stresses measured on specimens with identical dimensions have a statistical distribution because of the widely varying severity of flaws caused by variability in shape, size, and location with respect to stress state [11]. Weibull statistical analysis is the best candidate for characterizing variations in fiber strength [8, 16]. Fiber strength,  $\sigma_f$ , is a stochastic variable that can be described by a two-parameter Weibull cumulative distribution function  $P(\sigma_f)$ :

$$P(\sigma_f) = 1 - \exp \left\{ - \left( \frac{\sigma_f}{\sigma_0} \right)^\beta \right\}, \quad (1)$$

where  $P$ , in the range of  $[0, 1]$ , is the failure probability of single fibers under an applied stress less than or equal to  $\sigma_f$ .  $\sigma_0$  is the Weibull scale parameter or characteristic stress for a reference length  $L_0$ .  $\beta$  is the Weibull modulus or shape parameter, which describes the variability of the failure strengths. The common values for  $\beta$  of pristine fibers range from 2 to 20 [3].

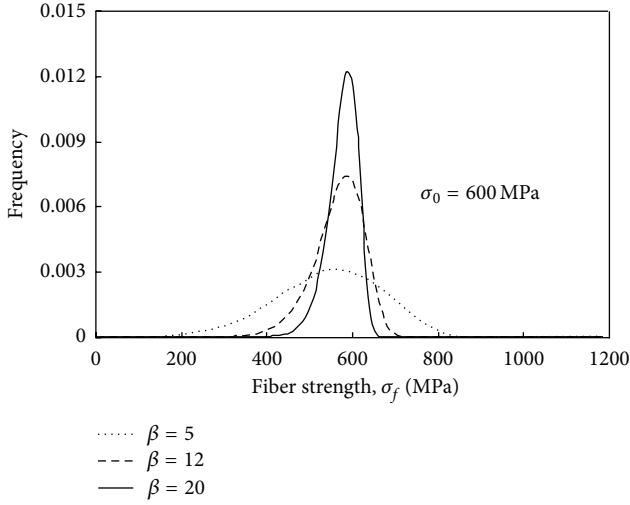


FIGURE 3: Weibull distribution of fiber strength.

Since  $\sigma_f$  follows a Weibull distribution, the probability density function (PDF) of  $\sigma_f$  is obtained from (1), which is

$$f(\sigma_f) = \frac{\beta}{\sigma_0} \left( \frac{\sigma_f}{\sigma_0} \right)^{\beta-1} \exp \left( - \left( \frac{\sigma_f}{\sigma_0} \right)^\beta \right). \quad (2)$$

Figure 3 presents the effect of scale parameter  $\beta$  on the shape of the probability density function when  $\sigma_0 = 600$  MPa. This finding indicates that  $\beta$  variations significantly affect the distribution of fiber tensile strength; that is, smaller  $\beta$  values indicate larger spreads in fiber strength and vice versa. A peak of probability density function is observed when  $\sigma_f$  is equal to  $\sigma_0$ . The parameters  $\beta$  and  $\sigma_0$  can be calculated statistically as follows:

$$E(\sigma_f) = \sigma_0 \Gamma \left( 1 + \frac{1}{\beta} \right), \quad (3)$$

$$D(\sigma_f) = \sigma_0^2 \left\{ \Gamma \left( 1 + \frac{2}{\beta} \right) - \left[ \Gamma \left( 1 + \frac{1}{\beta} \right) \right]^2 \right\},$$

where  $E(\sigma_f)$  and  $D(\sigma_f)$  are the mean and variance of random variable, respectively.  $\Gamma$  is the gamma function.

Expressing (1) in a linear form would facilitate using the equation to describe the experimental data. Rearranging and taking logarithms twice resulted in the following equation:

$$\ln \left( \ln \left( \frac{1}{1-P} \right) \right) = \beta \ln(\sigma_f) - \beta \ln(\sigma_0). \quad (4)$$

Hence, a plot of  $\ln(\sigma_f)$  versus  $\ln(\ln(1/(1-P)))$  should give a straight line if the material strength variability is described by the Weibull distribution. The shape parameter  $\beta$  and the scale parameter  $\sigma_0$  can both be obtained from the slope and  $y$ -intercept of this line, respectively.

$P$  can be calculated using a statistical approximation technique.  $N$  samples of  $\sigma_f$  are ranked in an ascending order,  $\sigma_{fi}$ ,  $i = 1 - N$ .  $\sigma_{fi}$  is denoted by the  $i$ th strength value ( $i = 1$  corresponds to the smallest and  $i = n$  corresponds to the

highest strength value). Then, the  $i$ th value is computed as follows:

$$P(\sigma_{fi}) = \frac{i}{N+1}. \quad (5)$$

#### 4. Weak-Link Scaling

Weak-link theory, which accurately describes the failure of many brittle materials, is based on the assumption that the material can be divided into smaller linked elements and that the fracture of a specimen is identified with the unstable propagation of the most “critical” crack [12].

Based on the weakest link theory, Weibull [8] proposed a strength  $\sigma_f$  distribution

$$P(\sigma_f) = 1 - \exp \left\{ -n \left( \frac{\sigma_f}{\sigma_0} \right)^\beta \right\} \\ = 1 - \exp \left\{ - \left( \frac{V}{V_0} \right) \left( \frac{\sigma_f}{\sigma_0} \right)^\beta \right\}, \quad (6)$$

where  $P$  is the failure probability of a long fiber that is connected by  $n$  independent segments and  $V$  is the tested volume.  $V_0$  is the volume of a unit link or segment, which is a scaling constant [17].

If the diameter,  $D$ , of all fibers is assumed to be the same, (6) can be written as

$$P(\sigma_f) = 1 - \exp \left\{ - \left( \frac{L}{L_0} \right) \left( \frac{\sigma_f}{\sigma_0} \right)^\beta \right\}, \quad (7)$$

where  $L_0$  is the reference length and  $L$  is the fiber gauge length.

From (7), the average strength is a power function of gauge length  $L$  [18],

$$\bar{\sigma}_f = \sigma_0 \left( \frac{L}{L_0} \right)^{-(1/\beta)} \Gamma \left( 1 + \frac{1}{\beta} \right). \quad (8)$$

If the strength of a material is determined by weak-link statistics, longer fibers have a larger number of links than shorter fibers and have a higher probability of encountering a more severe flaw along the fiber [19]. Furthermore, longer fibers have lower average fracture strengths than shorter fibers. In other words, the strength of the materials decreases with increasing size [9]. Therefore, weak-link scaling predictions assume that the strength can be scaled for any fiber length, from a single weak-link point estimate at a chosen fiber gauge length [13].

Considering (7) for the same probability of failure for two specimens with identical stress distributions, the strength values obtained at any given gauge length can be scaled to predict the strength of another length of fiber and for a similar probability of failure as follows:

$$\frac{\sigma_2}{\sigma_1} = \left( \frac{L_1}{L_2} \right)^{1/\beta}, \quad (9)$$

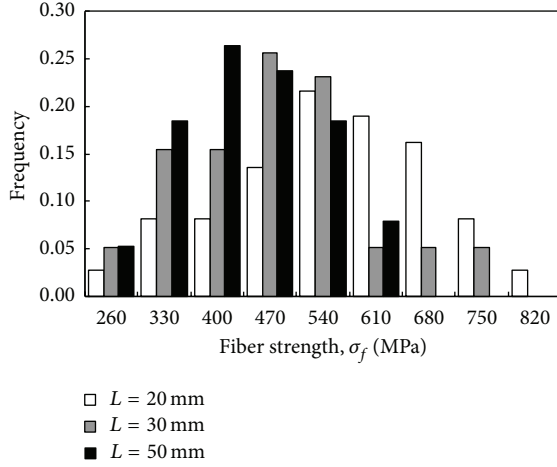


FIGURE 4: The experimental probability density function for ultimate strength of bamboo fiber.

where  $\sigma_2$  and  $\sigma_1$  are the fiber strengths at gauge lengths  $L_2$  and  $L_1$ , respectively. This equation directly links strength to volume; therefore, this equation quantifies the size effect, which is the basis for the statistical weakest link model.

The work by Curtin [20] indicated that a large system could be formally considered to be composed of a collection of independent subsystems linked in series, so that failure in the weakest subsystem causes failure across the entire system. Therefore, the cumulative probability of failure  $P_{f,V_2}$  of a fiber with volume  $V_2$  loaded with stress  $\sigma_f$  is related to the cumulative probability of failure  $P_{f,V_1}$  of a fiber with volume  $V_1$  as follows:

$$P_{f,V_2}(\sigma_c) = 1 - [1 - P_{f,V_1}(\sigma_c)]^{V_2/V_1}. \quad (10)$$

With constant fiber diameter, (10) becomes

$$P_{f,L_2}(\sigma_f) = 1 - [1 - P_{f,L_1}(\sigma_f)]^{L_2/L_1}. \quad (11)$$

## 5. Results and Discussion

**5.1. Statistical Distribution of Tensile Strength.** Figure 4 shows the histogram of the tensile strength distribution under three fiber lengths ( $L = 20, 30$ , and  $50$  mm). Tensile strength is clearly not homogeneous. Ultimate strength is more scattered in shorter fibers than in longer fibers. Therefore, the mean decreases with increased scattering of fiber tensile strength [21].

A typical Weibull plot of bamboo fracture strength at 20 mm gauge length based on (1) is shown in Figure 5. The linear relationship of  $X = \ln(\sigma_f)$  versus  $Y = \ln(\ln(1/(1 - P)))$  determined using the least squares method is shown in Figure 5. The  $R^2$  coefficient is 0.9883, which indicates a good degree of linearity. From this plot, the statistical parameters of the Weibull distribution can be obtained as listed

$$\beta = 4.02, \quad \sigma_0 = 612 \text{ MPa}, \quad L_0 = 20 \text{ mm}. \quad (12)$$

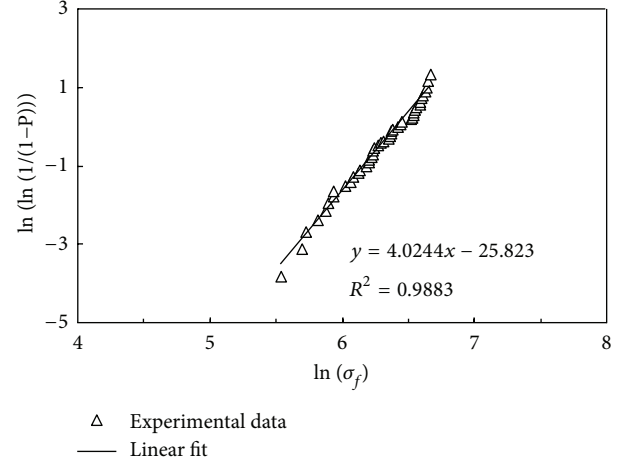


FIGURE 5: Strength distributions of bamboo fibers with  $L = 20$  mm.

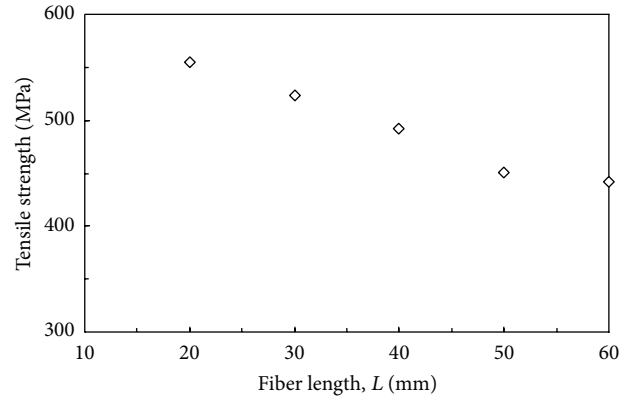


FIGURE 6: Length dependence of the mean tensile strength of bamboo fibers.

**5.2. Effect of Specimen Length on Ultimate Strength.** The relationship between the mean tensile strength of bamboo fiber and the testing gauge length is plotted on Figure 6. Fifty filaments are measured for each data point. The finding shows that the tensile strength depends on the specimen length of the fibers. A decrease in tensile strength was observed with increasing test length, which is attributed to the increasing probability of encountering more severe flaws with larger test lengths. Hence, longer fibers should on average have lower strengths than shorter fibers.

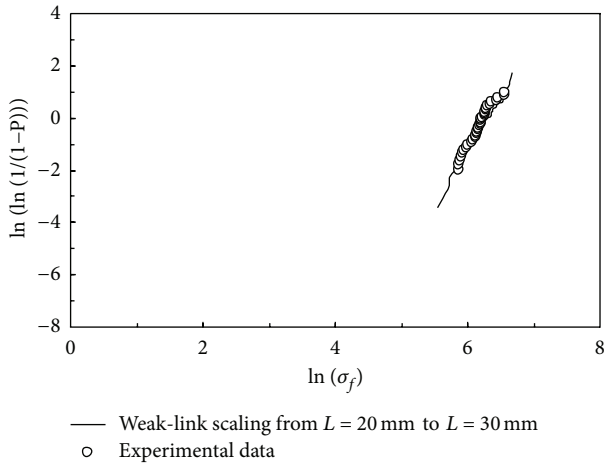
If the characteristic strength at a given gauge length is known, the mean strength at other gauge lengths can be calculated based on (8). In Table 1, the tensile strengths predicted through size scaling from  $L = 20$  mm are presented as a function of fiber test length; these findings are in excellent agreement with the experimental measurements. The Weibull theory clearly accounted for the correlation of strength variations with size [22].

**5.3. Strength Prediction by Weak-Link Scaling.** Predictions of the tensile strengths were made by size scaling data from samples of longer gauge lengths to access the accuracy of

TABLE 1: Comparison of measured and predicted fracture strengths of bamboo fibers.

Fiber test length (mm)	Tensile strength		Difference (%)
	Measured by experiment* (MPa)	Predicted by (8) (MPa)	
20	555	—	—
30	523	502	4.26
40	492	467	5.35
50	451	442	2.12
60	442	422	4.60

\* Average value of 50 results.

FIGURE 7: Strength distributions for bamboo fibers with  $L = 30$  mm.

weak-link scaling. An example comparing the experimental and predicted bamboo strength distribution for  $L = 30$  mm is presented in Figure 7. The distribution of open circles is the experimental result for fiber length of  $L = 30$  mm. The solid line represents the  $L = 20$  mm (fiber gauge length) distribution weak link scaled to  $L = 30$  mm (fiber gauge length) using (11). The results show that weak-link scaling works well, except at the lowest or highest fiber strengths. This exception is due to greater distributed damage in  $L = 20$  mm fibers than in  $L = 30$  mm fibers. The studies in the literature [16, 20] show that a critical damage size is necessary for weak-link scaling, which is the subject of our future study.

## 6. Conclusions

The tensile strength distribution of fibers is a key constitutive property of fiber-reinforced composites. Thus, understanding the scaling effects in the tensile properties of natural fibers is important. In the present study, bamboo fibers were tested with tension at several different gauge lengths. For each gauge length, 50 individual fibers were measured. The experimental fiber strength values were compared with the predicted values through weak-link scaling. The following conclusions were drawn.

- (1) Tensile strength of bamboo fibers exhibits statistical Weibull-type distribution, which is not necessarily constant. The two statistical parameters,  $\beta$  and  $\sigma_0$ , were used to quantify the variations in strength, which can be readily determined from static tensile tests on several fibers at a given gauge length  $L_0$ .
- (2) Ultimate fiber strength depends on specimen length, which is dominated by flaws statistics. This dependence is due to the increased probability of flaws that cause failure with larger material volumes. The gauge length effect on bamboo fiber strength can be predicted through weak-link scaling.
- (3) The simulated cumulative failure probability from the scaling model is consistent with the test data. These results verify the use of Weibull parameters from specimen testing for predicting the strength distributions of fibers of longer gauge lengths.

## Acknowledgments

The authors gratefully acknowledge the financial support of National Science Foundation of China under Grant no. 11102169, National Science Foundation Project of CQ CSTC under Grant no. 2012JJA70002, and Fundamental Research Funds for the Central Universities under Grant nos. XDJK2013B019, XDJK2013D011.

## References

- [1] H. P. S. Abdul Khalil, I. U. H. Bhat, M. Jawaid, A. Zaidon, D. Hermawan, and Y. S. Hadi, "Bamboo fibre reinforced biocomposites: a review," *Materials and Design*, vol. 42, pp. 353–368, 2012.
- [2] A. V. R. Prasad and K. M. Rao, "Mechanical properties of natural fibre reinforced polyester composites: jowar, sisal and bamboo," *Materials and Design*, vol. 32, no. 8-9, pp. 4658–4663, 2011.
- [3] S. Mahesh, I. J. Beyerlein, and S. L. Phoenix, "Size and heterogeneity effects on the strength of fibrous composites," *Physica D*, vol. 133, no. 1-4, pp. 371–389, 1999.
- [4] Z. P. Bažant, "Size effect on structural strength: a review," *Archive of Applied Mechanics*, vol. 69, no. 9-10, pp. 703–725, 1999.
- [5] K. L. Pickering, G. W. Beckermann, S. N. Alam, and N. J. Foreman, "Optimising industrial hemp fibre for composites," *Composites A*, vol. 38, no. 2, pp. 461–468, 2007.
- [6] S. Jain, R. Kumar, and U. C. Jindal, "Mechanical behaviour of bamboo and bamboo composite," *Journal of Materials Science*, vol. 27, no. 17, pp. 4598–4604, 1992.
- [7] F. T. Peirce, "Tensile tests for cotton yarns, V: 'the weakest link'—theorems on the strength of long and short composite specimens," *Journal of the Textile Institute Transactions*, vol. 17, pp. 355–368, 1926.
- [8] W. Weibull, "A statistical distribution function of wide applicability," *Journal of Applied Mechanics*, vol. 18, no. 3, pp. 293–297, 1951.
- [9] W. A. Curtin, "Size scaling of strength in heterogeneous materials," *Physical Review Letters*, vol. 80, no. 7, pp. 1445–1448, 1998.
- [10] J. Andersons, R. Joffe, M. Hojo, and S. Ochiai, "Glass fibre strength distribution determined by common experimental

- methods," *Composites Science and Technology*, vol. 62, no. 1, pp. 131–145, 2002.
- [11] G. Foray, A. Descamps-Mandine, M. R'Mili, and J. Lamon, "Statistical flaw strength distributions for glass fibres: correlation between bundle test and AFM-derived flaw size density functions," *Acta Materialia*, vol. 60, no. 9, pp. 3711–3718, 2012.
  - [12] L. Afferrante, M. Ciavarella, and E. Valenza, "Is Weibull's modulus really a material constant? Example case with interacting collinear cracks," *International Journal of Solids and Structures*, vol. 43, no. 17, pp. 5147–5157, 2006.
  - [13] A. S. Virk, W. Hall, and J. Summerscales, "Multiple Data Set (MDS) weak-link scaling analysis of jute fibres," *Composites A*, vol. 40, no. 11, pp. 1764–1771, 2009.
  - [14] N. Defoirdt, S. Biswas, L. D. Vriese et al., "Assessment of the tensile properties of coir, bamboo and jute fibre," *Composites A*, vol. 41, no. 5, pp. 588–595, 2010.
  - [15] H. Takagi and Y. Ichihara, "Effect of fiber length on mechanical properties of "green" composites using a starch-based resin and short bamboo fibers," *JSME International Journal A*, vol. 47, no. 4, pp. 551–555, 2004.
  - [16] C. M. Landis, I. J. Beyerlein, and R. M. McMeeking, "Micromechanical simulation of the failure of fiber reinforced composites," *Journal of the Mechanics and Physics of Solids*, vol. 48, no. 3, pp. 621–648, 2000.
  - [17] Y. Zhang, X. Wang, N. Pan, and R. Postle, "Weibull analysis of the tensile behavior of fibers with geometrical irregularities," *Journal of Materials Science*, vol. 37, no. 7, pp. 1401–1406, 2002.
  - [18] V. Lavaste, J. Besson, and A. R. Bunsell, "Statistical analysis of strength distribution of alumina based single fibres accounting for fibre diameter variations," *Journal of Materials Science*, vol. 30, no. 8, pp. 2042–2048, 1995.
  - [19] K. L. Pickering and T. L. Murray, "Weak link scaling analysis of high-strength carbon fibre," *Composites A*, vol. 30, no. 8, pp. 1017–1021, 1999.
  - [20] W. A. Curtin, "Stochastic damage evolution and failure in fiber-reinforced composites," *Advances in Applied Mechanics*, vol. 36, pp. 163–253, 1998.
  - [21] J. Zhang and F. Wang, "Modeling of progressive failure in ductile matrix composites Including local matrix yielding," *Mechanics of Advanced Materials and Structures*, vol. 16, no. 7, pp. 522–535, 2009.
  - [22] L. S. Sutherland, R. A. Shenoi, and S. M. Lewis, "Size and scale effects in composites: I. Literature review," *Composites Science and Technology*, vol. 59, no. 2, pp. 209–220, 1999.

## Research Article

# Vibration Analysis of Cylindrical Sandwich Aluminum Shell with Viscoelastic Damping Treatment

Tai-Hong Cheng, Zhen-Zhe Li, and Yun-De Shen

*College of Mechanical and Electrical Engineering, Wenzhou University, Zhejiang Province 325035, China*

Correspondence should be addressed to Yun-De Shen; shenyunde63@163.com

Received 11 July 2013; Accepted 6 September 2013

Academic Editor: Yan Yang

Copyright © 2013 Tai-Hong Cheng et al. This is an open access article distributed under the Creative Commons Attribution License, which permits unrestricted use, distribution, and reproduction in any medium, provided the original work is properly cited.

This paper has applied the constrained viscoelastic layer damping treatments to a cylindrical aluminum shell using layerwise displacement theory. The transverse shear, the normal strains, and the curved geometry are exactly taken into account in the present layerwise shell model, which can depict the zig-zag in-plane and out-of-plane displacements. The damped natural frequencies, modal loss factors, and frequency response functions of cylindrical viscoelastic aluminum shells are compared with those of the base thick aluminum panel without a viscoelastic layer. The thickness and damping ratio of the viscoelastic damping layer, the curvature of proposed cylindrical aluminum structure, and placement of damping layer of the aluminum panel were investigated using frequency response function. The presented results show that the sandwiched viscoelastic damping layer can effectively suppress vibration of cylindrical aluminum structure.

## 1. Introduction

The cylindrical curved structure has been employed in many engineering applications, such as aircrafts, automobiles, ships, and other industrial machines. Which structures are usually vibrated with different level due to external regular or random loads. And the structural failures can originate from the vibration by severe dynamic load and structural resonances. So the study of vibration and dynamic characteristics of cylindrical structure is an important work in engineering field.

Numerical researches have been studied for vibration of the shells with different theories. Studies on the vibrations characteristics of the cylindrical shells have been carried out extensively using numerical methods. Love [1] modified the Kirchhoff hypothesis for plates and established the assumptions used in the so-called classic theory of thin shells. Arnold and Warburton, Chung, Bhimaraddi, Soldatos, and Hadji-georgiou analyzed vibration of a cylindrical structure based on Love hypothesis [2–5]. Constrained layer damping is a mechanical engineering technique for suppression of vibration. Typically a viscoelastic or another damping material is

sandwiched between two sheets of stiff materials that lack sufficient damping by themselves. Ross et al. presented a general analysis of the viscoelastic structures [6]. They described the damping mechanism of the viscoelastic material as in-plane and transverse shear deformations, RKU assumptions. Mead and Markus developed sixth-order equations of motion for the transverse displacement of the damped sandwich beams with arbitrary boundary conditions [7]. Blasingame and DiTaranto added the extensional stiffness of the dissipative core layer to Kerwin's formulation of the laminated sandwich plate [8]. Siu and Bert investigated the material damping of laminated anisotropic rectangular plates, considering the thickness-shear flexibility and rotary and coupling inertia [9]. Chen and Huang presented a study on optimal placement of PCLD treatment for vibration suppression of the plates [10]. In their optimization, the structural damping plays the main performance index and the frequencies' shift and constraint layer damping thickness act as penalty functions. Zheng et al. have adopted genetic algorithm based penalty function method that is employed to find the optimal layout of rectangular passive constrained layer damping patches aiming to minimize the structural volume displacement

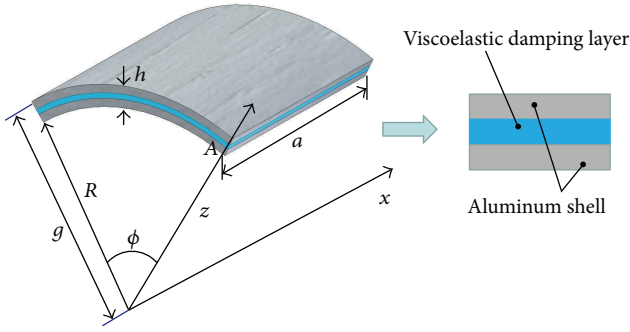


FIGURE 1: Geometry of cylindrical aluminum shell with viscoelastic damping layer.

of constraint layer damping treated cylindrical shell [11]. An optimization solution of rectangular constraint layer damping patches locations and dimensions is obtained under the constraint of total amount of constraint layer damping in terms of percentage added weight to the base structure. Ro and Baz presented optimal damping studies with an active constrained viscoelastic damping treatment distributed over regions of high strain energy on a plate [12]. Masti and Sainsbury have investigated the effectiveness of using a strain energy-based partial coating approach for vibration attenuation of the cylindrical shells [13]. The isogeometric analysis with nonuniform rational B-spline based on the classical plate theory is developed for free vibration analyses of functionally graded material thin plates [14].

In this study, a viscoelastic constrained layer damping treatment was employed to minimize vibration of a cylindrical aluminum panel using layerwise finite element theory, the base structure, and the constraining layer. The transverse shear, the normal strains, and the curved geometry are exactly taken into account in the present layerwise shell model, which can depict the zig-zag in-plane and out-of-plane displacements. The frequency response functions, the mode shapes, and the modal loss factor of a cylindrical sandwich aluminum panel were investigated with viscoelastic damping treatment.

## 2. Description of Finite Element Modeling

Figure 1(a) shows the geometry of a cylindrical aluminum shell with a viscoelastic damping layer. In this study, the layerwise shell theory is proposed to accurately predict the vibration and damping characteristics of the cylindrical aluminum panels with the viscoelastic damping layers. Based on the full layerwise shell theory, the displacement fields ( $u$ ,  $v$ , and  $w$ ) on the cylindrical coordinate system can be expressed by introducing the piecewise interpolation function along the thickness direction and finite element shape functions

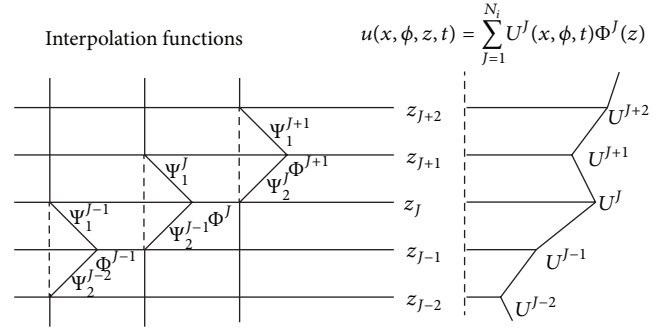


FIGURE 2: In-plane displacement based on the layerwise theory.

$$u(x, \phi, z, t) = \sum_{J=1}^{Ni} U^J(x, \phi, t) \Phi^J(z), \quad (1a)$$

$$v(x, \phi, z, t) = \sum_{J=1}^{Ni} V^J(x, \phi, t) \Phi^J(z), \quad (1b)$$

$$w(x, \phi, z, t) = \sum_{J=1}^{Ni} W^J(x, \phi, t) \Phi^J(z), \quad (1c)$$

where the linear interpolation function  $\Phi^J(z)$  along the thickness direction can be expressed by the following form:

$$\Phi^J(z) = \begin{cases} 0 & \text{for } z < z_{J-1}, \\ \Psi_2^{J-1}(z) = \frac{z - z_{J-1}}{z_J - z_{J-1}}, & \text{for } z_{J-1} < z < z_J, \\ \Psi_1^J(z) = -\frac{z - z_{J+1}}{z_{J+1} - z_J}, & \text{for } z_J < z < z_{J+1}, \\ 0, & \text{for } z_{J+1} < z. \end{cases} \quad (2)$$

Based on the sublaminate layerwise shell theory, an in-plane displacement can be described with a zig-zag deformation along the thickness direction as shown in Figure 2 [15]. The relationship between strains and displacement fields can be expressed as follows:

$$\varepsilon_{xx} = \frac{\partial u}{\partial x} = \sum_{J=1}^{Ni} \frac{\partial U^J}{\partial x} \Phi^J, \quad (3a)$$

$$\varepsilon_{\phi\phi} = \frac{1}{g_\phi} \left( \frac{\partial v}{\partial \phi} + w \right) = \frac{1}{g_\phi} \sum_{J=1}^{Ni} \left( \frac{\partial V^J}{\partial \phi} + W^J \right) \Phi^J, \quad (3b)$$

$$\varepsilon_{zz} = \frac{\partial w}{\partial z} = \sum_{J=1}^{Ni} W^J \frac{d\Phi^J}{dz}, \quad (3c)$$

$$\begin{aligned}\varepsilon_{\phi z} &= \frac{1}{g_\phi} \left( \frac{\partial w}{\partial \phi} - v \right) + \frac{\partial v}{\partial z} \\ &= \frac{1}{g_\phi} \sum_{j=1}^{Ni} \left( \frac{\partial W^j}{\partial \phi} - V^j \right) \Phi^j + \sum_{j=1}^{Ni} V^j \frac{d\Phi^j}{dz},\end{aligned}\quad (3d)$$

$$\varepsilon_{xz} = \frac{\partial w}{\partial x} + \frac{\partial u}{\partial z} = \sum_{j=1}^{Ni} \left( \frac{\partial W^j}{\partial x} \Phi^j + U^j \frac{d\Phi^j}{dz} \right), \quad (3e)$$

$$\varepsilon_{x\phi} = \frac{\partial v}{\partial x} + \frac{1}{g_\phi} \frac{\partial u}{\partial \phi} = \sum_{j=1}^{Ni} \left( \frac{\partial V^j}{\partial x} + \frac{1}{g_\phi} \frac{\partial U^j}{\partial \phi} \right) \Phi^j. \quad (3f)$$

$g_\phi$  is defined as a function of  $z$  in the following form:

$$g_\phi = R \left( 1 + \frac{z}{R} \right) = R + z. \quad (4)$$

### 3. Governing Equations of Cylindrical Panel

To derive the governing equation of motion for the cylindrical panels with the viscoelastic layers, Hamilton's variational principle was applied in the following form:

$$\underbrace{\int_V \rho \ddot{u}_i \delta u_i dV}_{\delta T(\text{Kinetic Energy})} + \underbrace{\int_V \sigma_{ij} \delta \varepsilon_{ij} dV}_{\delta V(\text{Strain Energy})} = \underbrace{\int_V f_i \delta u_i dV + \int_S \tau_i \delta u_i dS}_{\delta W(\text{External Works})}, \quad (5)$$

where  $\rho$ ,  $f_i$ , and  $\tau_i$  are the density, body force, and surface force, respectively. The displacement field of  $j$ th interface was defined using shape function as follows:

$$U^j(x, \phi, t) = \sum_{I=1}^{NPE} U_I^j(t) \bar{\psi}_I(x, \phi), \quad (6a)$$

$$V^j(x, \phi, t) = \sum_{I=1}^{NPE} V_I^j(t) \bar{\psi}_I(x, \phi), \quad (6b)$$

$$W^j(x, \phi, t) = \sum_{I=1}^{NPE} W_I^j(t) \bar{\psi}_I(x, \phi), \quad (6c)$$

where NPE is node per element and  $\psi_I$  is linear interpolation function and by substituting (1a), (1b), (1c), (3a), (3b), (3c), (3d), (3e), and (3f) into (5), we can obtain the following equations of the finite element:

$$\mathbf{M}_e \ddot{\mathbf{u}}_e + \mathbf{K}_e \mathbf{u}_e = \mathbf{F}_e. \quad (7)$$

Consequently, we can obtain the global finite element equations of motion through the assembly process, resulting in the following complex form:

$$\mathbf{M} \ddot{\mathbf{U}} + \mathbf{K} \mathbf{U} = \mathbf{F}. \quad (8)$$

### 4. Dynamic Equation of Cylindrical Panel with Viscoelastic Damping Layer

Here, normal and shear moduli can be expressed in the form of complex numbers as follows:

$$\bar{E}_{II} = E_{II} (1 + i\eta_{II}) \quad \text{for } I = 1, 2, 3 \quad (9a)$$

$$\bar{G}_{12} = G_{12} (1 + i\eta_{12}), \quad (9b)$$

$$\bar{G}_{23} = G_{23} (1 + i\eta_{23}), \quad \bar{G}_{13} = G_{13} (1 + i\eta_{13}).$$

By considering the complex modulus of (9a) and (9b), the eigensystem matrices for undamped free vibration can be written in the following form:

$$\mathbf{M} \ddot{\mathbf{U}} + (\mathbf{K}(\omega) + i\mathbf{K}_D(\omega)) \mathbf{U} = \mathbf{F}(\omega). \quad (10)$$

The modal approach using the eigensolutions of undamped free vibration is applied to reduce the order of system matrices as follows:

$$\mathbf{M}^* \ddot{\mathbf{U}}^* + (\mathbf{K}^*(\omega) + i\mathbf{K}_D^*(\omega)) \mathbf{U}^* = \mathbf{F}^*(\omega), \quad (11)$$

where the reduced system matrices and vectors are given as

$$\mathbf{M}^* = \Psi^T \mathbf{M} \Psi, \quad (12a)$$

$$\mathbf{K}^* = \Psi^T \mathbf{K} \Psi, \quad \mathbf{K}_D^* = \Psi^T \mathbf{K}_D \Psi, \quad (12b)$$

$$\mathbf{F}^* = \Psi^T \mathbf{F}, \quad (12c)$$

$$\mathbf{U} = \Psi \mathbf{U}^*. \quad (12d)$$

From (11), natural frequencies and modal loss factors can be defined as follows:

$$\omega_n^2 = \text{Real}[\lambda_n^*], \quad \eta_n = \frac{\text{Imag}[\lambda_n^*]}{\text{Real}[\lambda_n^*]}. \quad (13)$$

The frequency response function is used to investigate the steady state dynamic characteristics of the linear system subject to harmonic excitation. Due to a harmonic excitation at a certain point, the reduced force vector with respect to modal coordinates is given as follows:

$$\mathbf{F}^* = \Psi^T \mathbf{F} = F_0 \Psi^T \mathbf{F}_{\text{input}} e^{i\omega t} = F_0 \mathbf{F}_{\text{input}}^* e^{i\omega t}. \quad (14)$$

Finally, the frequency response function obtained from the modal approach is given in the following form:

$$\begin{aligned}\mathbf{H} &= \frac{\mathbf{U}}{F_0} = \frac{\Psi \mathbf{U}^*}{F_0} \\ &= \Psi (\mathbf{K}^*(\omega, T) + i\mathbf{K}_D^*(\omega, T) - \omega^2 \mathbf{M}^*)^{-1} \mathbf{F}_{\text{input}}^*,\end{aligned}\quad (15)$$

$$\text{Magnitude} = |\mathbf{H}|, \quad (16a)$$

$$\text{Phase, } \varphi = \arctan \left( -\frac{\text{Imag}(\mathbf{H})}{\text{Real}(\mathbf{H})} \right). \quad (16b)$$

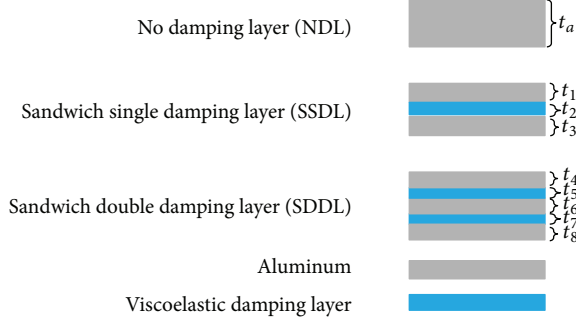


FIGURE 3: Three cases discussed in this study.

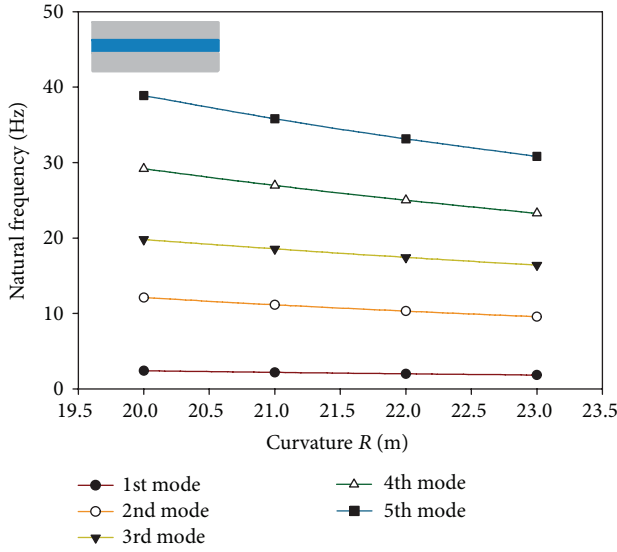
FIGURE 4: Variation of natural frequencies of cylindrical aluminum panel in case of SSDL with variation of curvature  $R$  ( $a = 0.2$  m,  $b = 0.1$  m,  $t_1 = 5$  mm,  $t_2 = 2$  mm,  $t_3 = 5$  mm, and  $\eta = 0.1$ ).

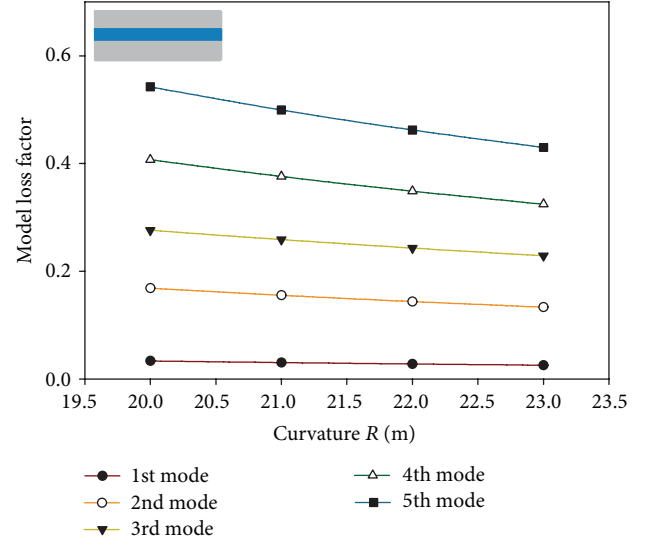
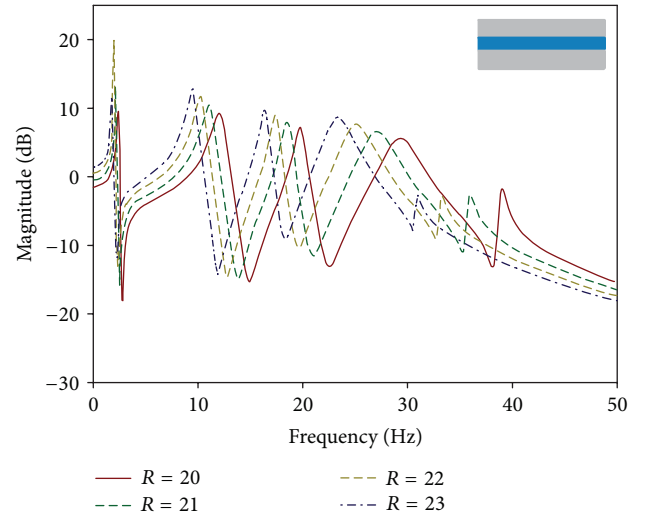
TABLE 1: Material properties of aluminum and viscoelastic material.

	Elastic modulus	Poisons ratio	Density
Aluminum	69 GPa	0.3	2800 kg/m <sup>3</sup>
Viscoelastic material	2.1 Mpa	0.499	970 kg/m <sup>3</sup>

## 5. Results and Discussion

For finite element analysis of the cylindrical aluminum panel, the nine-node  $2 \times 4$  meshes are used for the cylindrical panel and the material properties are given as in Table 1.

Figure 3 shows the three discussed cases in this study, which are no damping layer (NDL), sandwich single damping layer (SSDL), and sandwich double damping layer (SDDL). Figures 4 and 5 show the variation of the natural frequencies and the modal loss factor of cylindrical aluminum panel in case of SSDL with variation of the curvature  $R$ . The

FIGURE 5: Variation of modal loss factor of cylindrical aluminum panel in case of SSDL with variation of curvature  $R$  ( $a = 0.2$  m,  $b = 0.1$  m,  $t_1 = 5$  mm,  $t_2 = 2$  mm,  $t_3 = 5$  mm, and  $\eta = 0.1$ ).FIGURE 6: Frequency response of cylindrical aluminum panel in case of SSDL with variety of curvatures  $R$  ( $a = 0.2$  m,  $b = 0.1$  m,  $t_1 = 5$  mm,  $t_2 = 2$  mm,  $t_3 = 5$  mm, and  $\eta = 0.1$ ).

natural frequencies and the modal loss factor are decreased with increasing  $R$  except the first mode. Figure 6 shows the frequency response of the cylindrical aluminum panel in case of SSDL with variety of the curvatures  $R$ . As the radius of the cylindrical geometry was increased, the natural frequencies decreased except that the first mode and the magnitude of the second, the third, the fourth, and the fifth modes are increased due to the dominance of the transverse shear and the curvature effect.

Figure 7 shows the frequency response of the cylindrical aluminum panel in case of SSDL with variety of the central angles  $\phi$ . As the central angle of the cylindrical geometry was increased, the natural frequencies decreased except

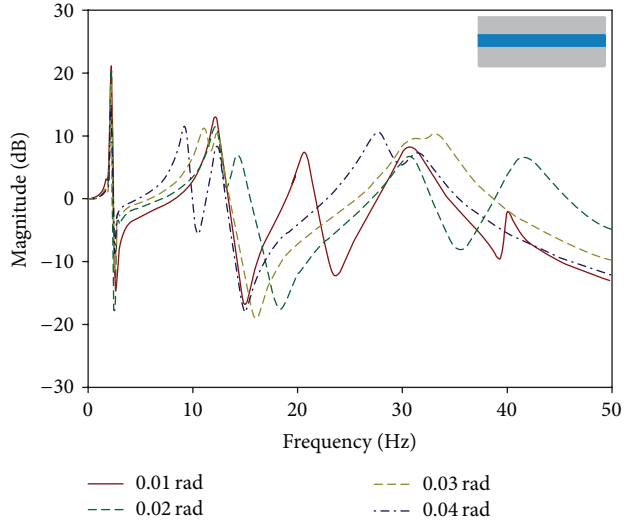


FIGURE 7: Frequency response of cylindrical aluminum panel in case of SSDL with variety of central angles  $\phi$  ( $a = 0.2$  m,  $R = 20$  m,  $t_1 = 5$  mm,  $t_2 = 2$  mm,  $t_3 = 5$  mm, and  $\eta = 0.1$ ).

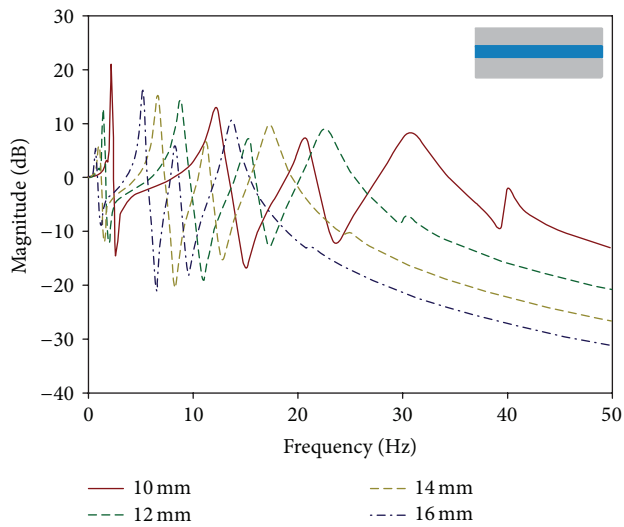


FIGURE 8: Frequency response of cylindrical aluminum panel in case of SSDL with variety of lengths  $a$  ( $\phi = 0.01$  rad,  $R = 20$  m,  $t_1 = 5$  mm,  $t_2 = 2$  mm,  $t_3 = 5$  mm, and  $\eta = 0.1$ ).

that the first mode and especially the second mode are more dominant with the central angle  $\phi$ . Figure 8 shows the frequency response of the cylindrical aluminum panel in case of SSDL with variety of the lengths  $a$ . With increasing the length value  $a$  the natural frequency has a decreasing trend in the frequency response function. The damping factor is an important parameter in the viscoelastic material. Figure 9 shows the frequency response of the cylindrical aluminum panel in case of SSDL with variety of the damping factors  $\eta$  of the viscoelastic damping material. As the damping factor increases, the magnitude of the first five modes decreased, because of good damping performance of the viscoelastic damping layer. Figure 10 shows the frequency response of

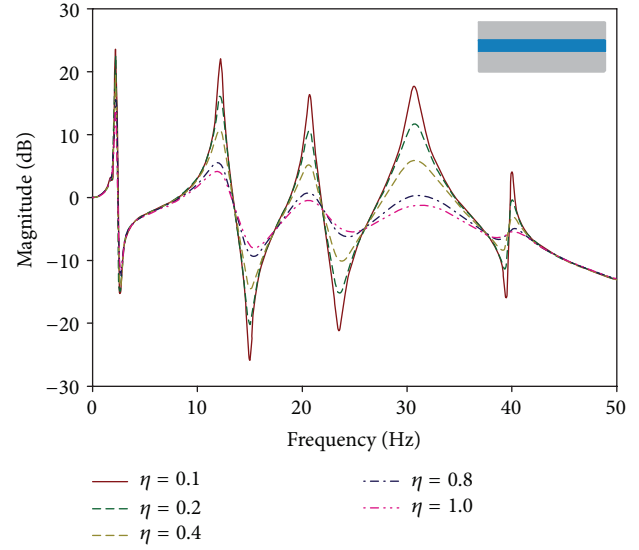


FIGURE 9: Frequency response of cylindrical aluminum panel in case of SSDL with variety of damping factors  $\eta$  of viscoelastic material ( $a = 0.2$  m,  $\phi = 0.01$  rad,  $R = 20$  m,  $t_1 = 5$  mm,  $t_2 = 2$  mm, and  $t_3 = 5$  mm).

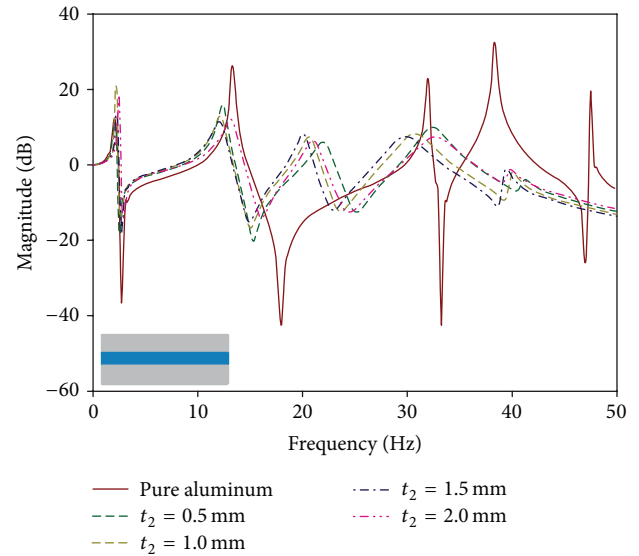


FIGURE 10: Frequency response of cylindrical aluminum panel in case of SSDL with variety of thicknesses of damping layer  $t_2$  ( $a = 0.2$  m,  $\phi = 0.01$  rad,  $R = 20$  m,  $ta = 10$  mm,  $t_1 = 5$  mm,  $t_3 = 5$  mm, and  $\eta = 0.1$ ).

the cylindrical aluminum panel in case of SSDL with variety of the thicknesses of the damping layer  $t_2$ . The magnitude of SSDL has good damping effect at the second, the third, the fourth, and the fifth modes, with shifting of the natural frequency. Figure 11 shows the frequency response function of the cylindrical aluminum panel in case of SSDL with

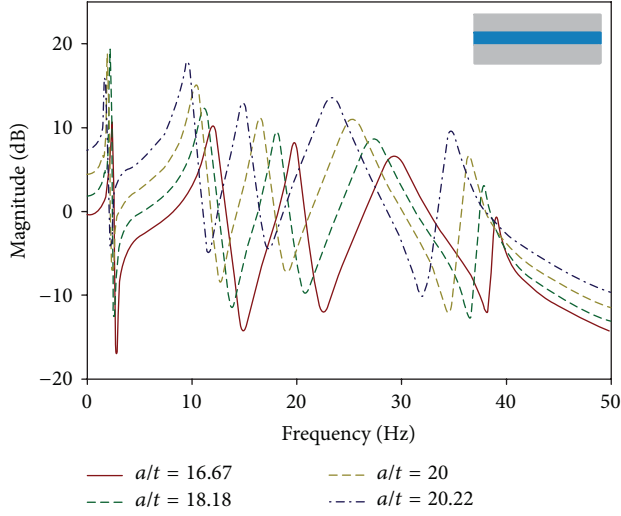


FIGURE 11: Frequency response of cylindrical aluminum panel in case of SSDL with variety of thickness ratios  $a/t$  ( $a = 0.2$  m,  $\phi = 0.01$  rad,  $R = 20$  m,  $t_2 = 2$  mm,  $t = t_1 + t_2 + t_3$ , and  $\eta = 0.1$ ).

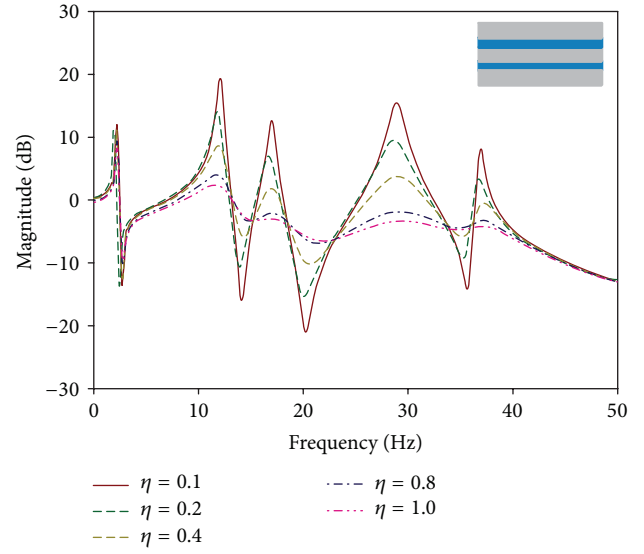


FIGURE 12: Frequency response of cylindrical aluminum panel in case of SSDL with variety of damping factors  $\eta$  of viscoelastic material ( $a = 0.2$  m,  $\phi = 0.01$  rad,  $R = 20$  m,  $t_4 = 3$  mm,  $t_5 = 1$  mm,  $t_6 = 4$  mm,  $t_7 = 1$  mm, and  $t_8 = 3$  mm).

variety of the thicknesses ratio. With increasing of the thickness ratio, the natural frequency has decreasing trend, because the thickness of panel becomes thin. Figure 12 shows the frequency response of the cylindrical aluminum panel in case of SSDL with variety of the damping factors of the viscoelastic material. As the damping factor increases, the magnitude of each mode decreased. Figure 13 shows the comparison of the frequency response of the cylindrical aluminum panel in case of pure aluminum, SSDL, and SDDL. The results show that the sandwiched viscoelastic damping layer has good damping performance compared with no damped thick aluminum panel. Figure 14 shows the mode shapes in case of NDL, SSDL, and SDDL. The first, the second, and the fourth modes show the bending mode and the third and the fifth modes show a twisting mode.

## 6. Conclusion

In this paper, the vibration characteristics of a sandwiched cylindrical aluminum shell with viscoelastic damping treatment were investigated using layerwise theories. The transverse shear, the normal strains, and the curved geometry are exactly taken into account in the present layerwise shell model, which can depict the zig-zag in-plane and out-of-plane displacements. The frequency response functions, the mode shapes, and the modal loss factor of a cylindrical sandwich aluminum panel were investigated with viscoelastic damping treatment. The damped natural frequencies, the modal loss factors, and the frequency response functions of the cylindrical viscoelastic aluminum shells are compared with those of the base thick aluminum panel without a viscoelastic layer. The thickness and the damping ratio of the viscoelastic damping layer, the curvature of proposed cylindrical aluminum structure, and placement of damping

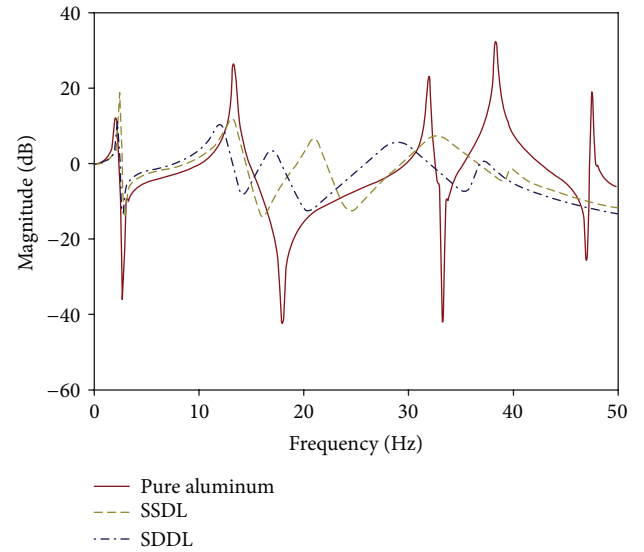


FIGURE 13: Frequency response of cylindrical aluminum panel in case of pure aluminum, SSDL, and SDDL ( $a = 0.2$  m,  $\phi = 0.01$  rad,  $R = 20$  m,  $t_1 = 5$  mm,  $t_2 = 2$  mm,  $t_3 = 5$  mm,  $t_4 = 3$  mm,  $t_5 = 1$  mm,  $t_6 = 4$  mm,  $t_7 = 1$  mm, and  $t_8 = 3$  mm).

layer of the aluminum panel were investigated using frequency response function. The presented results show that the sandwiched viscoelastic damping layer can effectively suppress vibration of the cylindrical aluminum structure.

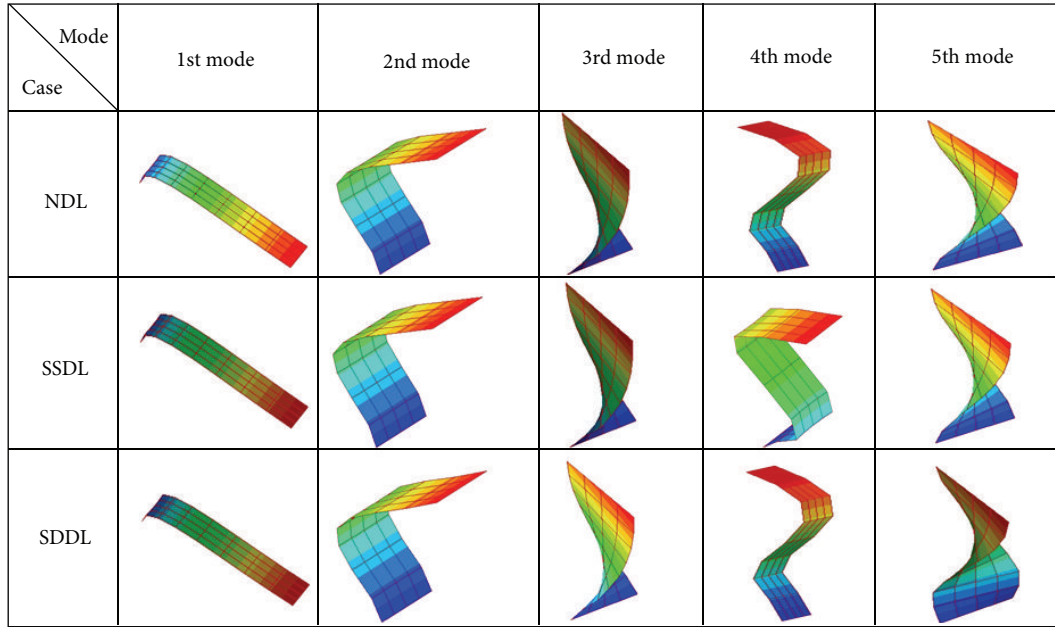


FIGURE 14: Mode shapes in case of NDL, SSDL, and SDDL.

## Acknowledgments

This material is based on the works funded by Zhejiang Provincial Natural Science Foundation of China under Grant no. LQ12E05013, Research on Public Welfare Technology Application Projects of Zhejiang Province of China under Grant no. 2013C31081 and Wenzhou Planned Science and Technology Project of China under Grant no. H20110005.

## References

- [1] A. E. H. Love, "The small free vibrations and deformations of thins elastic shell," *Philosophical Transactions of the Royal Society*, vol. 179, pp. 491–546, 1888.
- [2] R. N. Arnold and G. B. Warburton, "Flexural vibrations of the walls of thin cylindrical shells having freely supported ends," *Proceedings of the Royal Society of London A*, vol. 197, no. 1049, pp. 238–256, 1949.
- [3] H. Chung, "Free vibration analysis of circular cylindrical shells," *Journal of Sound and Vibration*, vol. 74, no. 3, pp. 331–350, 1981.
- [4] A. Bhimaraddi, "A higher order theory for free vibration analysis of circular cylindrical shells," *International Journal of Solids and Structures*, vol. 20, no. 7, pp. 623–630, 1984.
- [5] K. P. Soldatos and V. P. Hadjigeorgiou, "Three-dimensional solution of the free vibration problem of homogeneous isotropic cylindrical shells and panels," *Journal of Sound and Vibration*, vol. 137, no. 3, pp. 369–384, 1990.
- [6] R. Ross, E. E. Ungar E, and E. M. Kerwin, "Damping of plate of flexural vibrations by means of viscoelastic laminate," in *Proceedings of the Structural Damping-A Colloquium on Structural Damping Held at the ASME Annual Meeting*, pp. 49–88, 1959.
- [7] D. J. Mead and S. Markus, "Loss factors and resonant frequencies of encastré damped sandwich beams," *Journal of Sound and Vibration*, vol. 12, no. 1, pp. 99–112, 1970.
- [8] W. Blasingame and R. A. DiTaranto, "Composite loss factors of selected laminated beams," *The Journal of the Acoustical Society of America*, vol. 36, no. 5, pp. 1052–1052, 1964.
- [9] C. C. Siu and C. W. Bert, "Sinusoidal response of composite-material plates with material damping," *Journal of Engineering for Industry*, vol. 96, no. 2, pp. 603–610, 1974.
- [10] Y.-C. Chen and S.-C. Huang, "An optimal placement of CLD treatment for vibration suppression of plates," *International Journal of Mechanical Sciences*, vol. 44, no. 8, pp. 1801–1821, 2002.
- [11] H. Zheng, C. Cai, G. S. H. Pau, and G. R. Liu, "Minimizing vibration response of cylindrical shells through layout optimization of passive constrained layer damping treatments," *Journal of Sound and Vibration*, vol. 279, no. 3-5, pp. 739–756, 2005.
- [12] J. Ro and A. Baz, "Optimum placement and control of active constrained layer damping using modal strain energy approach," *Journal of Vibration and Control*, vol. 8, no. 6, pp. 861–876, 2002.
- [13] R. S. Masti and M. G. Sainsbury, "Vibration damping of cylindrical shells partially coated with a constrained viscoelastic treatment having a standoff layer," *Thin-Walled Structures*, vol. 43, no. 9, pp. 1355–1379, 2005.
- [14] S. Yin, T. T. Yu, and P. Liu, "Free vibration analyses of FGM thin plates by isogeometric analysis based on classicalplate theory and physical neutral surface," *Advances in Mechanical Engineering*, vol. 2013, Article ID 634584, 10 pages, 2013.
- [15] J. N. Reddy, *Mechanics of Laminated Composite Plates and Shells: Theory and Analysis*, CRC Press, Boca Raton, Fla, USA, 2004.

## Research Article

# Characteristics Analysis and Testing of SMA Spring Actuator

Jianzuo Ma,<sup>1</sup> Haolei Huang,<sup>1</sup> and Jin Huang<sup>2</sup>

<sup>1</sup> College of Mechanical Engineering, Chongqing Industry Polytechnic College, Chongqing 401120, China

<sup>2</sup> The Key Laboratory of Manufacture and Test Techniques for Automobile Parts, Chongqing University of Technology, Chongqing 400054, China

Correspondence should be addressed to Jin Huang; [jhuangcq@163.com](mailto:jhuangcq@163.com)

Received 19 July 2013; Accepted 8 September 2013

Academic Editor: Xing Chen

Copyright © 2013 Jianzuo Ma et al. This is an open access article distributed under the Creative Commons Attribution License, which permits unrestricted use, distribution, and reproduction in any medium, provided the original work is properly cited.

The biasing form two-way shape memory alloy (SMA) actuator composed of SMA spring and steel spring is analyzed. Based on the force equilibrium equation, the relationship between load capacity of SMA spring and geometric parameters is established. In order to obtain the characteristics of SMA spring actuator, the output force and output displacement of SMA spring under different temperatures are analyzed by the theoretical model and the experimental method. Based on the shape memory effect of SMA, the relationship of the SMA spring actuator's output displacement with the temperature, the stress and strain, the material parameters, and the size parameters is established. The results indicate that the trend of theoretical results is basically consistent with the experimental data. The output displacement of SMA spring actuator is increased with the increasing temperature.

## 1. Introduction

Shape memory alloy (SMA) is known as a kind of new intelligent material. SMA may undergo mechanical shape changes at relatively low temperatures, retain them until heated, and then come back to the initial shape [1, 2]. The outstanding quality characteristics of SMA are shape memory effect (SME) and super elasticity (SE) [3]. The shape memory effect, which allows the deformed material to recover a memorized shape when heated above the transformation temperature, can be exploited effectively in microrobots, automobile, automatic adjustment devices, aerospace, home appliances and daily necessities, [4–8] and so on.

An actuator based on these materials is made up of an SMA element that works against a contrasting element (a weight or other constant force, a conventional spring, or a second SMA element). At low temperature, the contrasting element overcomes the resistance of the easily deformable SMA element. The actuator is activated by heating the SMA element above the transformation temperature. The resulting increase in stiffness enables the SMA element to overcome the resistance of the contrast, thus generating useful displacements and producing mechanical work [3, 9–11].

In this paper, we present the biasing form SMA actuator, which is able to generate displacement and force. Based on

the force equilibrium equation, the output force and output displacement of SMA spring under different temperatures are analyzed by the theoretical model and the experimental method. Based on the shape memory effect of SMA, the relationship of the SMA spring actuator's output displacement with the temperature, the stress and strain, the material parameters, and the size parameters is established. The output displacement of SMA spring actuator is increased with the increasing temperature.

## 2. Properties of SMA

The most commonly used SMA elements for actuators are helical springs, which for this form produce a large displacement. The force that a spring of any material produces at a given deflection depends linearly on the shear modulus of the material. SMAs exhibit a large temperature dependence on the material shear modulus. The relationship between shear modulus and temperature for SMAs is given by

$$G = \begin{cases} G_M & \text{when } T < M_f \text{ and } T < A_s, \\ G(\gamma, T) & \text{when } M_f \leq T \leq A_f, \\ G_A & \text{when } T > A_f \text{ and } T > M_s, \end{cases} \quad (1)$$

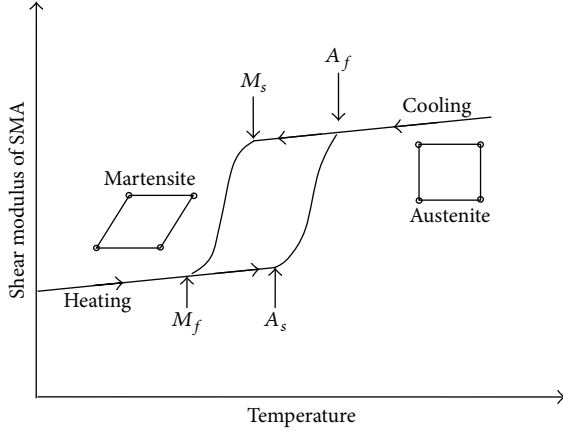


FIGURE 1: Transformation temperatures of martensite and austenite.

where  $G$  is the shear modulus of SMAs.  $T$  is temperature and  $M_s$ ,  $M_f$ ,  $A_s$ , and  $A_f$  are the start and finish transformation temperatures of martensite and austenite, respectively, as shown in Figure 1.  $G_M$  and  $G_A$  are the shear moduli of martensite and austenite, respectively. When  $M_f \leq T \leq A_f$ , in absence of stress, shear modulus of SMAs can be expressed approximately as

$$G(T) = G_M + \frac{G_A - G_M}{2} [1 + \sin \phi (T - T_m)]. \quad (2)$$

In the process of heating,  $T_m = (A_s + A_f)/2$ ,  $\phi = \pi/(A_f - A_s)$ ; in the process of cooling,  $T_m = (M_s + M_f)/2$ ,  $\phi = \pi/(M_s - M_f)$ .

When the SMA wire is heated or cooled, the heat balance equation is

$$\rho_1 c V \frac{dT}{dt} = -hA (T - T_f), \quad (3)$$

where  $\rho_1$  is the mass density of SMA,  $c$  is the specific heat,  $V$  is the volume of SMA exposed in air,  $t$  is the time,  $h$  is the heat exchange coefficient,  $A$  is the superficial area of SMA, and  $T_f$  is the temperature of airflow.

If  $T = T_0$ , when  $t = 0$ , the temperature variation of SMA wire with time is

$$T = (T_0 - T_f) e^{-t/\varphi} + T_f, \quad (4)$$

where  $T_0$  is the initial temperature and  $\varphi$  is the time constant of SMA wire,  $\varphi = \rho_1 c V / hA$ .

If the material and structural parameters of SMA have been determined, the time constant is inversely proportional to the heat exchange coefficient. Under three different heat exchange coefficients, the temperature variation of SMA wire with the around airflow temperature is shown in Figure 2. As shown in Figure 2, in a different heat exchange coefficient, the temperature of SMA wire changes faster when the time constant is smaller and the lag of time is shorter. When the time constant is less than 2.5, the lag time is less than 2 seconds.

### 3. Operational Principle of SMA Actuator

The SMA drive element uses the properties of low yield stress at martensitic state and returns to the high yield stress at austenite phase state when heated. Thus, the action form of a single SMA part is one-way. To obtain two-way characteristics of SMA elements, the structures of differential form and biasing form are used commonly. The differential form uses two or more SMA elements to obtain the two-way characteristics. The biasing form combines the one-way SMA with other parts to obtain two-way characteristics, shown in Figure 3, with the SMA helical spring working against a conventional steel spring (referred here as the “biasing” spring). At low temperatures, the steel spring is able to completely deflect the SMA spring to its compressed length. When increasing the temperature of the SMA spring, it expands, compressing the steel spring and moving the push rod.

### 4. Property Analysis of SMA Spring

Relative to the free length of the spring, the SMA spring provides a large action stroke, shown in Figure 4.

The expression for shear stress in an SMA spring is described as

$$\tau = \kappa \frac{8FD}{\pi d^3} = \kappa \frac{8FC}{\pi d^2}, \quad (5)$$

where the axial load is  $F$ ,  $D$  is the average diameter of the spring,  $d$  represents the wire diameter,  $C$  is the spring index,  $C = D/d$ , and  $\kappa$  is known as the Wahl correction factor applied:

$$\kappa = \frac{4C - 1}{4C - 4} + \frac{0.615}{C}. \quad (6)$$

Shear stress  $\tau$  has a relationship with shear strain  $\gamma$  which is

$$\tau = G \cdot \gamma. \quad (7)$$

The stretch of spring under the load  $F$  is

$$\delta = \frac{8FD^3 n}{d^4 G}, \quad (8)$$

where  $n$  is the number of turns in the spring.

The relationship between compressed length  $\delta$  and shear strain  $\gamma$  for SMA spring is given by

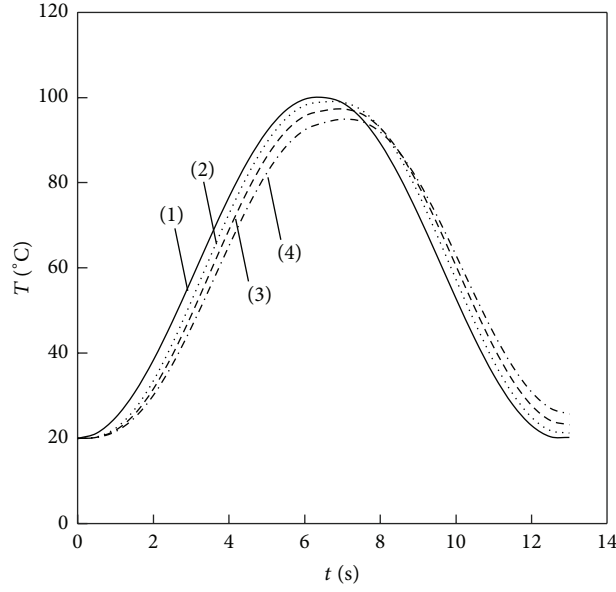
$$\delta = \frac{n\pi D^2}{d} \gamma. \quad (9)$$

The wire diameter for the actuator can be obtained from (5) for acceptable values of  $C$  ranging from 3 to 12:

$$d = \sqrt{\kappa \frac{8FC}{\pi \tau}}. \quad (10)$$

The number of turns in the spring can be obtained from (9):

$$n = \frac{\Delta \delta d}{\pi \Delta \gamma D^2}, \quad (11)$$



- (1) The around airflow temperature  
 (2) The temperature of SMA when the time constant is 1.5  
 (3) The temperature of SMA when the time constant is 2.0  
 (4) The temperature of SMA when the time constant is 2.5

FIGURE 2: The temperature variation of SMA wire with the around airflow temperature under three different heat exchange coefficients.

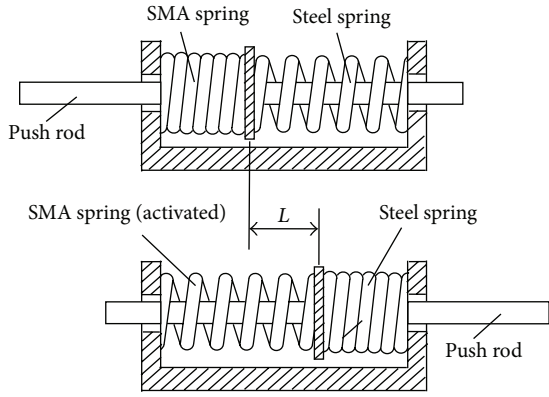


FIGURE 3: The operational principle of the SMA actuator.

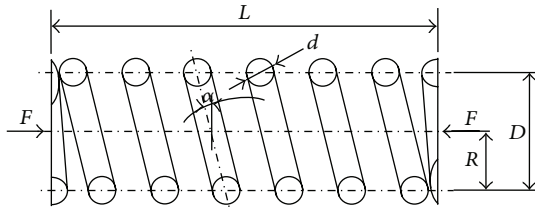


FIGURE 4: A compression helical SMA spring.

where  $\Delta\delta$  represents the stroke of the actuator and  $\Delta\gamma$  is the strain difference at high and low temperatures:

$$\Delta\gamma = \gamma_L - \gamma_H. \quad (12)$$

**4.1. The Output Force of SMA Spring under Different Temperatures.** The experimental system for the output force of SMA spring versus temperature under the constraint of displacement is shown in Figure 5 and the experimental device is shown in Figure 6.

As shown in (8), when  $M_f \leq T \leq A_f$ , the axial load at temperature  $T$  can be expressed as

$$F(T) = \frac{\delta(T) G(T)}{\delta_L G_L} F_L. \quad (13)$$

The axial load at low temperature is expressed as

$$F_L = \frac{d^4 G_L}{8 D^3 n} \delta_L. \quad (14)$$

When the axial displacement of SMA spring is restricted, the compressed length of SMA spring is kept as

$$\delta(T) = \delta_L. \quad (15)$$

When  $M_f \leq T \leq A_f$ , the output force at temperature  $T$  can be obtained from (13), (14), and (15) as

$$F(T) = \frac{G(T) d^4}{8 D^3 n} \delta_L. \quad (16)$$

In this study, Ti-49.8at.%Ni SMA spring is used, shown in Figure 7; its start and finish temperatures of the martensitic and austenitic phase transformation are  $M_s = 78^\circ\text{C}$ ,  $M_f = 50^\circ\text{C}$ ,  $A_s = 74^\circ\text{C}$ , and  $A_f = 95^\circ\text{C}$ , respectively. The shear

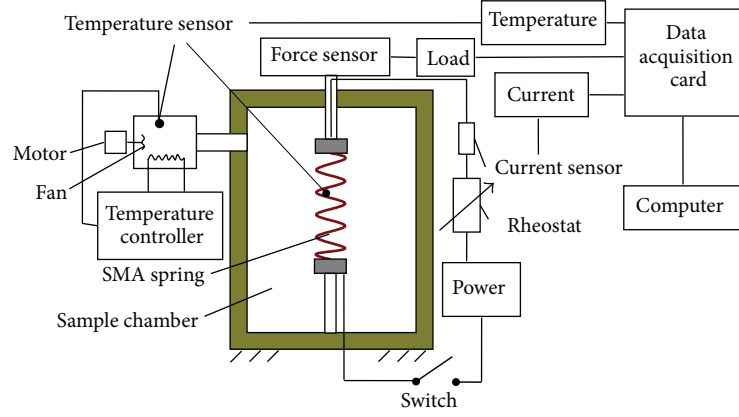


FIGURE 5: The experimental system for output force.

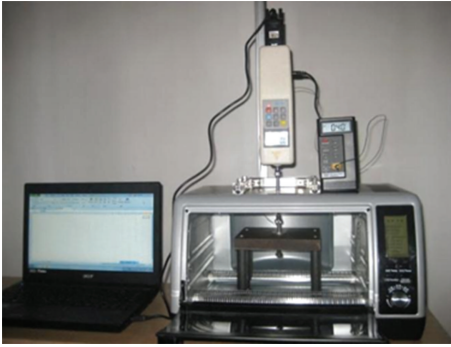


FIGURE 6: The experimental device for output force.

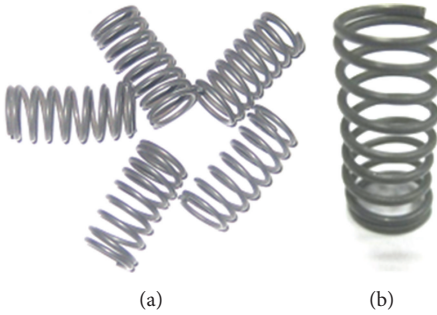


FIGURE 7: SMA spring sample.

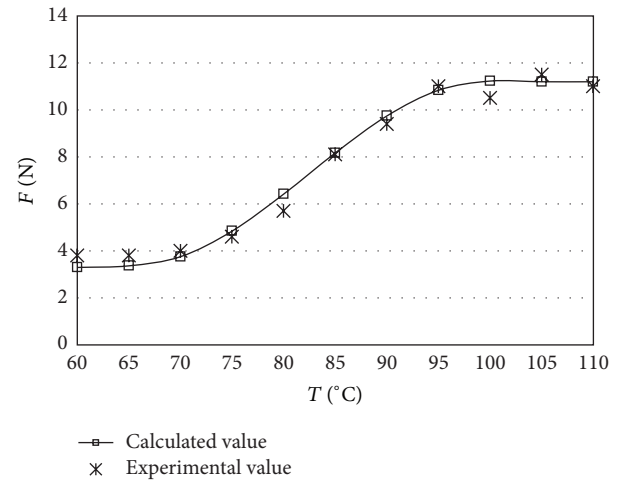


FIGURE 8: Output force versus temperature under the constraint of displacement.

4.2. *The Output Displacement of SMA Spring under Different Temperatures.* The experimental system for output displacement of SMA spring under different temperatures is shown in Figure 9 and the experimental device is shown in Figure 10.

As shown in (9), the compressed length can be expressed as

$$\delta = \frac{\pi D^2 n \gamma}{d}. \quad (17)$$

When  $M_f \leq T \leq A_f$ , shear strain  $\gamma$  is

$$\gamma = \frac{G_L \gamma_{\max}}{G}. \quad (18)$$

The output displacement can be obtained from (17) and (18) as

$$\Delta \delta = \frac{\pi D^2 n}{d} \left( 1 - \frac{G_L}{G} \right) \gamma_{\max}. \quad (19)$$

moduli of martensite and austenite are  $G_M = 7.5$  GPa and  $G_A = 25$  GPa, respectively. The wire diameter of SMA spring is  $d = 1$  mm, the angle of inclination is  $\alpha = 6^\circ$ , the diameter of SMA spring is  $D = 8.6$  mm, and the number of turns is  $n = 7$ . When  $\delta = 15$  mm, the theoretical and the experimental results of the relationship between the output force and temperatures of SMA spring are shown in Figure 8. The trend of theoretical results is basically consistent with the experimental data. The output force is increased with the rising of temperature.

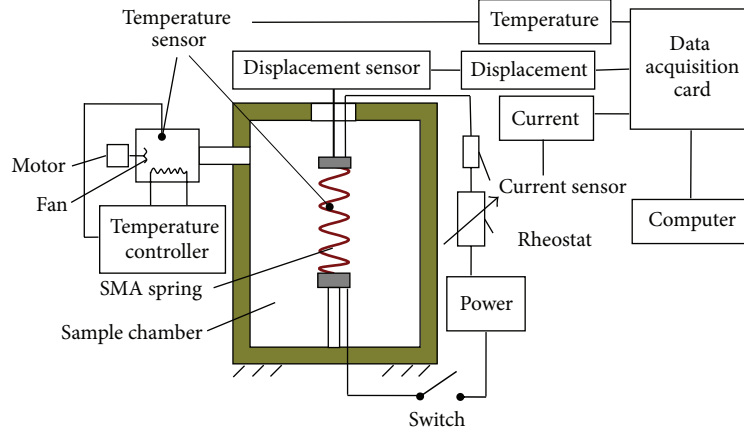


FIGURE 9: The experimental system for output displacement.



FIGURE 10: The experimental device for output displacement.

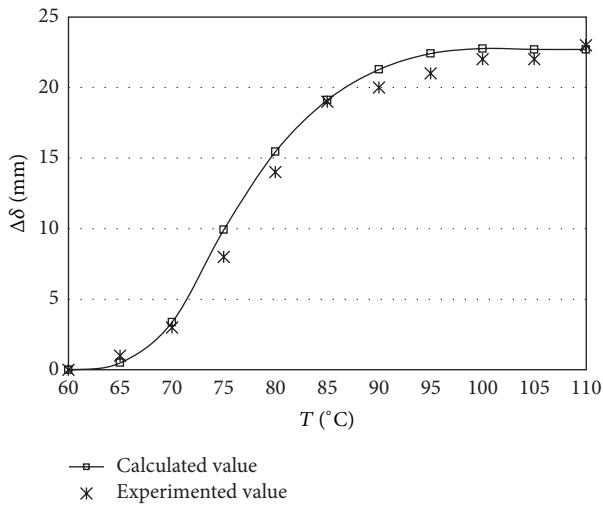


FIGURE 11: The output displacement of SMA spring versus temperature under constant load.

The typical SMA spring sample is shown in Figure 7; when the maximum shear strain is  $\gamma_{\max} = 2\%$ , the theoretical and the experimental results of the relationship between the output displacement and temperatures of SMA spring are shown in Figure 11. The trend of theoretical results is

basically consistent with the experimental data. The output displacement is increased with the rise of temperature.

## 5. Analysis of SMA Actuator

The scheme of the proposed actuator with an SMA spring and conventional steel against spring is illustrated in Figure 3, where at low temperature the SMA spring will be compressed and when heated will extend with a pushing actuation. For the SMA actuator in Figure 3, the axial load of SMA spring  $F$  has the relationship with the compressed length of SMA spring  $\delta$  as follows:

$$\frac{F(T)}{\delta(T)G(T)} = \frac{F_L}{\delta_L G_L}, \quad (20)$$

$$F(T) = F_L + \frac{F_H - F_L}{\Delta\delta} S(T),$$

where  $F(T)$ ,  $\delta(T)$ , and  $G(T)$  are the axial load, compressed length, and shear modulus of SMA spring at temperature  $T$ , respectively;  $F_L$ ,  $\delta_L$ , and  $G_L$  are the axial load, compressed length, and shear modulus of SMA spring at low temperature, respectively;  $F_H$  is the axial load at high temperature; and  $S(T)$  is the output displacement of SMA spring actuator:

$$S(T) = \delta_L - \delta(T). \quad (21)$$

The output displacement of SMA spring actuator can be obtained from (1), (2), (9), (20), and (21)

$$S(T) = \frac{(G(T) - G_L) \gamma_L}{(d/n\pi D^2) G(T) + ((F_H - F_L) / \Delta\delta F_L) G(T) \gamma_L}. \quad (22)$$

The experimental system for output displacement of SMA actuator under different temperatures is shown in Figure 12. The SMA helical spring works against a conventional steel spring to obtain the two-way SMA actuator. The typical SMA spring sample is shown in Figure 7. The stroke of the actuator is  $\Delta\delta = 10$  mm. The effect of temperature on the output displacement of SMA spring actuator is analyzed by

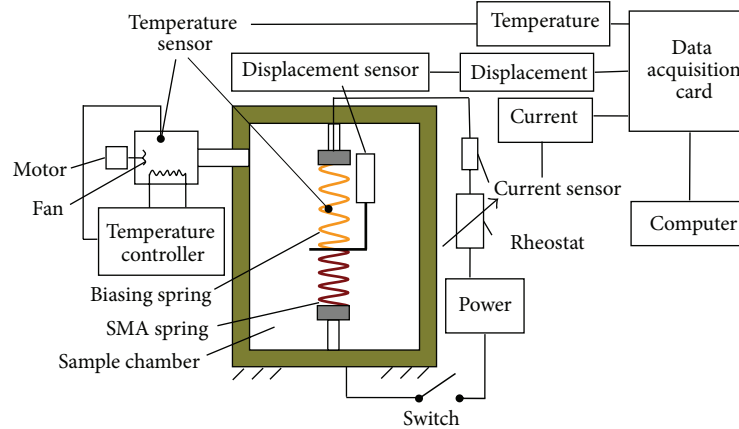


FIGURE 12: The experimental system for output displacement of SMA actuator versus temperature.

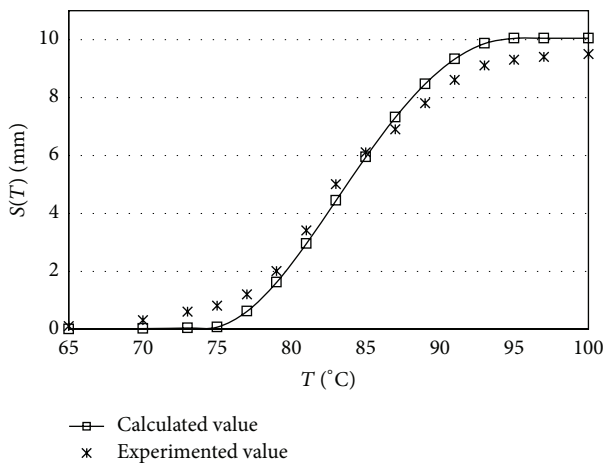


FIGURE 13: The output displacement versus temperature.

the theoretical model and the experimental method, shown in Figure 13. The axial loads of SMA spring at low and high temperatures are  $F_L = 10$  N and  $F_H = 30$  N, respectively. The low temperature shear strain is  $\gamma_L = 1.5\%$ . As shown in Figure 13, the output displacement of SMA spring actuator is increased with the increasing temperature.

## 6. Conclusions

The characteristics and test method of SMA spring and SMA actuator are analyzed in this paper. The output force and output displacement equations of SMA spring are derived. The output force and output displacement are increased with the rise of temperature. The relationship of the SMA spring actuator's output displacement with the temperature is investigated theoretically and experimentally. With the increase of the temperature acting on SMA actuator, the output displacement of SMA spring actuator is increased proportionally.

## Acknowledgments

This work was supported by the National Natural Science Foundation of China (51175532, 11272368) and by the Natural Science Foundation Project of CQ CSTC (Key Project CSTC, 2011BA4028).

## References

- [1] C. Yu, G. Kang, D. Song, and Q. Kan, "Micromechanical constitutive model considering plasticity for super-elastic NiTi shape memory alloy," *Computational Materials Science*, vol. 56, pp. 1–5, 2012.
- [2] S. Huang, M. Leary, T. Ataalla, K. Probst, and A. Subic, "Optimisation of Ni-Ti shape memory alloy response time by transient heat transfer analysis," *Materials & Design*, vol. 35, pp. 655–663, 2012.
- [3] G. Scire Mammano and E. Dragoni, "Increasing stroke and output force of linear shape memory actuators by elastic compensation," *Mechatronics*, vol. 21, no. 3, pp. 570–580, 2011.
- [4] A. Hadi, A. Yousefi-Koma, M. Elahinia, M. M. Moghaddam, and A. Ghazavi, "A shape memory alloy spring-based actuator with stiffness and position controllability," *Proceedings of the Institution of Mechanical Engineers, Part I: Journal of Systems and Control Engineering*, vol. 225, no. 7, pp. 902–917, 2011.
- [5] B. Kim, S. Lee, J. H. Park, and J.-O. Park, "Design and fabrication of a locomotive mechanism for capsule-type endoscopes using shape memory alloys (SMAs)," *IEEE/ASME Transactions on Mechatronics*, vol. 10, no. 1, pp. 77–86, 2005.
- [6] S. Langbein and A. Czechowicz, "Adaptive resetting of SMA actuators," *Journal of Intelligent Material Systems and Structures*, vol. 23, no. 2, pp. 127–134, 2012.
- [7] B. Kim, M. G. Lee, Y. P. Lee, Y. Kim, and G. Lee, "An earthworm-like micro robot using shape memory alloy actuator," *Sensors and Actuators A*, vol. 125, no. 2, pp. 429–437, 2006.
- [8] T. Georges, V. Brailovski, and P. Terriault, "Characterization and design of antagonistic shape memory alloy actuators," *Smart Materials and Structures*, vol. 21, no. 3, Article ID 035010, 2012.
- [9] R. Lahoz and J. A. Puértolas, "Training and two-way shape memory in NiTi alloys: influence on thermal parameters," *Journal of Alloys and Compounds*, vol. 381, no. 1–2, pp. 130–136, 2004.

- [10] M. Mertmann and G. Vergani, "Design and application of shape memory actuators," *European Physical Journal*, vol. 158, no. 1, pp. 221–230, 2008.
- [11] C. Mavroidis, "Development of advanced actuators using shape memory alloys and electrorheological fluids," *Research in Non-destructive Evaluation*, vol. 14, no. 1, pp. 1–32, 2002.

## Research Article

# Intelligent Detector of Internal Combustion Engine Cylinder Pressure and Sensitivity Temperature Coefficient Compensation

Beirong Zheng,<sup>1</sup> Chen Zhou,<sup>1</sup> Xiaomin Pan,<sup>1</sup> Quan Wang,<sup>2</sup> and Wei Xue<sup>1</sup>

<sup>1</sup> College of Mechanical and Electrical Engineering, Wenzhou University, Wenzhou 323035, China

<sup>2</sup> State Key Lab of Transducer Technology, Chinese Academy of Sciences, Shanghai 200050, China

Correspondence should be addressed to Wei Xue; [xue\\_wenzhou@163.com](mailto:xue_wenzhou@163.com)

Received 10 July 2013; Accepted 1 September 2013

Academic Editor: Yan Yang

Copyright © 2013 Beirong Zheng et al. This is an open access article distributed under the Creative Commons Attribution License, which permits unrestricted use, distribution, and reproduction in any medium, provided the original work is properly cited.

The detecting device based on mechanical mechanism is far from the measurement of internal combustion engine cylinder explosion and compression pressure. This pressure detection is under the environment of pulsed gas (over 500 times per one minute) and mechanical impactive vibration. Piezoresistive detection with silicon on insulator (SOI) strain gauges to pressure seems to be a good solution to meet such special applications. In this work, separation by implanted oxygen (SIMOX) wafer was used to fabricate the high temperature pressure sensor chip. For high accuracy and wide temperature range application, this paper also presents a novel pressure sensitivity temperature coefficient (TCS) compensation method, using integrated constant current network. A quantitative compensation formula is introduced in mathematics. During experiments, the absolute value of the compensated TCS is easy to be  $10 \times 10^{-6}/^{\circ}\text{C} \sim 100 \times 10^{-6}/^{\circ}\text{C}$  by individual adjustment and calibration of each device's temperature compensation. Therefore, the feasibility and practicability of this technology are tested. Again, the disadvantages are discussed after the research of the experiment data and the improvement methods are also given in the designing period. This technology exhibits the great potential practical value of internal combustion engine cylinder pressure with volume manufacturing.

## 1. Introduction

Explosion pressure and compression pressure of internal-combustion engine cylinder are two significant technical parameters which affect its work [1, 2]. Grasping its regularity of pressure is a main basis for designing and evaluating working performance of the internal-combustion engine. Currently, tools used to detect this pressure mainly are detection devices such as old mechanical watches. These mechanical detection watches are old-fashioned, which cause the low measuring accuracy (real measuring accuracy is far lower than marked accuracy). Besides, great swing of the clock pin makes it hard to read the number exactly and its service life is relatively short. It is far from meeting the operating requirement of internal-combustion engine cylinder's explosion pressure and compression pressure at the environment of striking by high temperature and pressure pulsed gas (over 500 times per one minute) and mechanical vibration.

There are three internal defects of mechanical pressure gauges [3, 4]. They are mechanical hysteresis, stagnation or creeping, and elastic effect. Elastic effect certainly causes

performance deviation. Besides, elastic modulus and rigidity modulus of elastic material are low, which leads to a bad dynamic response and affects its use severely [5]. The device presented in this paper equipped with amplified circuit and eight characters LCD screen avoids the detection device and utilizes high temperature piezoresistive pressure sensors as detecting units. The sensor makes it convenient to operate and has high testing precision and more scientific results. At the same time, it possesses several functions of data detection and record.

## 2. Fabrication of High Temperature Piezoresistive Pressure Sensor

Silicon pressure sensors were the first micromechanical devices developed. Using piezoresistive effect and microelectronic technology of semiconductor silicon, they have many advantages: large output signal, high SNR (signal-to-noise), convenient circuit processing, and high frequency responses [6].

The conventional piezoresistive pressure sensor chip functions as a Wheatstone bridge, formed by four diffused or ion implanted strain gauges in the thin silicon diaphragm. Silicon exhibits a high gauge factor and is principally applicable as a piezoresistive material up to temperatures of 400°C [7]. However, a known limitation of these silicon-based devices using isolation by reverse biased pn-junctions is the rising junction leakage current at elevated temperatures. The promising attempts for fabrication of high temperature piezoresistive pressure sensors is to cancel pn-insulation of the piezoresistors. One of the basic ideas is silicon on insulator (SOI) technology to remedy this by electrically insulating the thin layer at the wafer surface carrying the electronic device from the bulk wafer used as mechanical support [8, 9].

Two mainstream technologies of manufacturing SOI wafer are separation by implantation of oxygen [10, 11] (SIMOX) and bonding technology. SIMOX technology refers to the technology where large dose oxygen ions are implanted into initial silicon, then SOI structure is formed after high temperature annealing. Bonding technology includes bonding and etch back SOI technology and Smart Cut (or UNI-BON) technology [12, 13]. This paper adopted SIMOX technology, implanting oxygen ions into n-type silicon to obtain silicon dioxide dielectric isolated SOI wafer with high quality and commercial use. Then silicon chip is manufactured on micro fabrication platform. Since buried layer is isolated by silicon dioxide and pn-junction isolation is cancelled, the leakage current caused by temperature increasing between upper silicon measurement unit and bulk silicon is avoided. The sensor packaged with this kind of sensing chip is presented with high accuracy and a good long-term stability in high temperature testing experiments.

Figure 1 is the high temperature pressure sensor gauge chip based on SIMOX SOI wafer. One circular shape diaphragm is taken as the sensitive structure layer. The chip still retains silicon as the sensing material but has silicon oxide as an electrically isolating layer between it and the substrate. The sensor packaged with this kind of sensing chip is presented with high accuracy and a good long-term stability in high temperature testing experiments. The designed chip film thickness is 0.04 mm and effective radius of diaphragm is 2 mm.

When the sensor is subjected to pressure, the gas (or liquid) with high temperature and high pressure acts on the back of the chip and causes it to be deformed. The deformation is converted into the resistance variation in the gauges of the Wheatstone bridge on the other side. The Wheatstone bridge transforms the related stress, due to pressure, into an electrical output. Then this pressure can be measured. The diaphragm of the sensor can be optimized to make sensors of different ranges.

### 3. Testing of Dynamic Characteristics

The natural frequency of peripheral clamped circular diaphragm [14]  $f_n$  is

$$f_n = \frac{2.54h}{\pi r^2} \sqrt{\frac{E}{3(1-\nu^2)\rho}}, \quad (1)$$

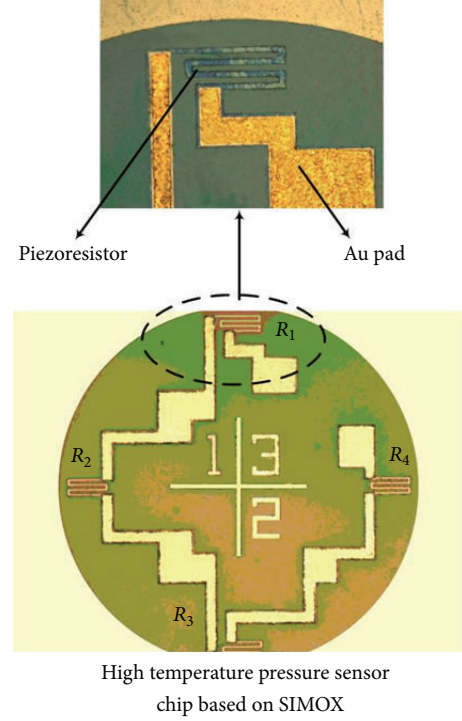


FIGURE 1: High temperature sensor chip based on SIMOX was used for strain gauges in detecting internal-combustion engine cylinder pressure.

where  $E$  is young modulus,  $\nu$  is Poisson's ratio,  $\rho$  is material density, and  $r$  is the effective radius of diaphragm.

Young's modulus of silicon is almost equal to steel material, but its density is only between 1/3 and 1/4 density of steel. So natural frequency of silicon film is higher than steel sheets by two times. The designed film thickness is 0.04 mm, and effective radius of diaphragm is 2 mm. It is easy to know that theoretic natural frequency is 44.22 kHz. It compared well with dynamic calibrated frequency of shock tube which is 38.46 kHz. It is shown in Figure 2 that it meets the requirement of high frequency measurement.

### 4. TCS Compensation

Piezoresistive pressure sensor is sensitive to the ambient temperature change. The temperature dependence of sheet resistance is one of the main limiting factors to improve the accuracy of the device and extend its application [15, 16].

Although various types of piezoresistive pressure sensors are available, for all integrated solid-state piezoresistive sensors, the basic operating principle of the sensor element remains unchanged. A pressure is applied to the resistors made with semiconductor materials in the arms of the bridge change by some amount. These devices use diffused or ion implanted resistors in an integral silicon diaphragm to transform the related stress, due to pressure, into an electrical output.

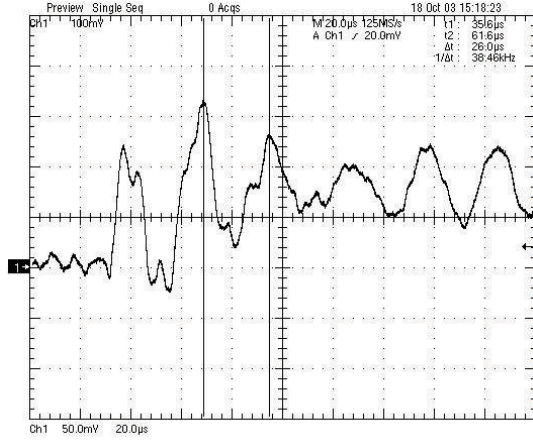


FIGURE 2: Dynamic response of the intelligent detector with the SIMOX silicon chip to meet mechanical impactive vibration.

They generally function as a Wheatstone bridge. That is,  $R_1 = R_2 = R_3 = R_4$ ,  $\Delta R_1 = \Delta R_3 = -\Delta R_2 = -\Delta R_4$ . So, the output voltage,  $V_0$ , is easily shown to be

$$V_0 = V_B \cdot \frac{\Delta R}{R}. \quad (2)$$

Since the change in resistance is directly proportional to pressure,  $V_0$  can be written as

$$V_0 = S \cdot P \cdot V_B \pm V_{OS}, \quad (3)$$

where  $V_0$  is the output in mV,  $S$  is the sensitivity in mV/V/Pa,  $P$  is the pressure in Pa,  $V_B$  is the bridge voltage in volts, and  $V_{OS}$  is the offset error (the differential output voltage when the applied pressure is zero). The offset voltage presents little problems in application since it can easily be compensated in the amplifier circuit or corrected digitally if a microprocessor is used in the system.

Looking at the derivative of (2) with respect to temperature and ignoring the  $V_{OS}$  term, we get

$$V_0' = P \cdot (S \cdot V_B' + S' \cdot V_B). \quad (4)$$

When a sensor is properly compensated, the output voltage does not change with the temperature.

Hence,

$$V_0' = 0, \quad S \cdot V_B' = -S' \cdot V_B, \quad \text{or } V_B'/V_B = -S'/S. \quad (5)$$

$S'/S$  is the temperature coefficient of sensitivity (TCS). TCS is always below zero due to the decrease in piezoresistive coefficient with increasing temperature. In order to compensate for the change in sensitivity, the bridge voltage must change with equal magnitude in the opposite direction, that is, using positive temperature coefficient of bridge voltage compensates negative TCS.

Although the basic piezoresistive pressure sensor elements are often referred to as either constant current or constant voltage driven sensors, the two basic methods of

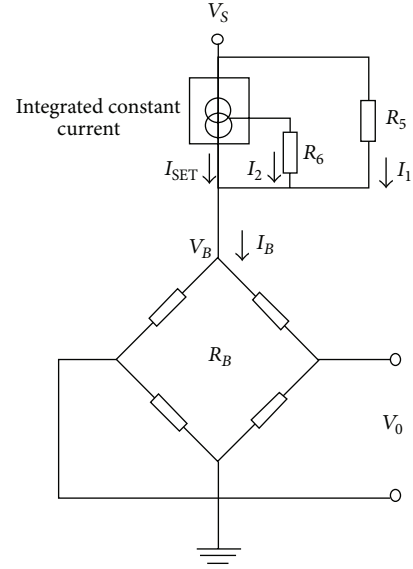


FIGURE 3: Sensitivity temperature coefficient compensation-based integrated constant current.

TCS compensation are using the internal characteristics of the die in conjunction with a constant source or using thermistors or other similar devices in conjunction with a constant voltage source [17, 18].

Thermistors can be used for TCS compensation. But they are inherently nonlinear, difficult to use in volume production, and more expensive than circuit approaches. The circuit is designed to incorporate a minimum number of adjustments and allow interchangeability of devices with little variation from device to device.

In this work, LM334 used for TCS compensation easily and inexpensively is shown in Figure 3. The LM334 is a three-pin programmable current source featuring an output current that rises linearly with temperature at  $+3360\mu\text{A}/^\circ\text{C}$ . In Figure 3, it is shown that

$$V_B = I_B R_B = (I_{SET} + I_2) R_B = \left( I_{SET} + \frac{V_S - V_B}{R_2} \right) R_B, \quad (6)$$

Where  $V_B$  is the Wheatstone bridge voltage,  $I_B$  is Wheatstone bridge current,  $R_B$  is Wheatstone bridge internal resistance  $I_{SET}$  is integrated constant current,  $I_1$  and  $I_2$  are the currents of the outer  $R_1$  and  $R_2$ , and  $V_S$  is the supply voltage.

Solving (6), it becomes

$$V_B = (I_{SET} R_2 + V_S) \frac{R_B}{R_B + R_2}. \quad (7)$$

As  $\alpha = R_B/(R_B + R_2)$ , taking the derivative with respect to temperature of (9) and normalizing it with respect to the bridge voltage, we obtain

$$\frac{V_B'}{V_B} = \left( \frac{R_B'}{R_B} \right) (1 - \alpha) + \left( \frac{I_{SET}'}{I_{SET}} \right) \left( 1 - \alpha \left( \frac{V_S}{V_B} \right) \right). \quad (8)$$

TABLE 1: TCS compensation measurement results.

$V_S$ (V)	$V_B$ (V)	Times	No.	Uncompensated TCS/ $\times 10^{-6}/^{\circ}\text{C}$	$R_5$ (K $\Omega$ )	$R_6$ (K $\Omega$ )	Compensated TCS/ $\times 10^{-6}/^{\circ}\text{C}$
6	4	1	1	-2529	82	9.1	21
6	4	2	1	-2529	82	9.1	32
6	4	3*	1	-2529	82	9.1	25
9	6	1	1	-2529	56	8.2	48
9	6	2	1	-2529	56	8.2	30
9	6	3*	1	-2529	56	8.2	35
12	9	1	1	-2529	36	7.5	-27
12	9	2	1	-2529	36	7.5	-14
12	9	3*	1	-2529	36	7.5	-20
6	4	1	2	-2617	75	9.1	-19
6	4	2	2	-2617	75	9.1	-26
6	4	3*	2	-2617	75	9.1	-37
9	6	1	2	-2617	56	10	45
9	6	2	2	-2617	56	10	36
9	6	3*	2	-2617	56	10	39
12	9	1	2	-2617	33	7.5	-20
12	9	2	2	-2617	33	7.5	-38
12	9	3*	2	-2617	33	7.5	-34

Note: 3\* is referred to the third measurement data of TCS after compensation of TCO.

Solving the equation for resistor  $R_2$ , we get

$$R_2 = \frac{R_B [I'_{\text{SET}}/I_{\text{SET}} ((V_S/V_B) - 1) + V'_B/V_B]}{(R'_B/R_B) + (I'_{\text{SET}}/I_{\text{SET}}) - (V'_B/V_B)}. \quad (9)$$

Substituting (7) into (9), we find that

$$R_2 = \frac{R_B [(I'_{\text{SET}}/I_{\text{SET}}) ((V_S/V_B) - 1) - (S'/S)]}{(R'_B/R_B) + (I'_{\text{SET}}/I_{\text{SET}}) + (S'/S)}. \quad (10)$$

According to the three-pin programmable current source  $I_{\text{SET}} = 0.0677/R_1$ , once  $R_2$  is known,  $R_1$  can be derived from the following equation:

$$R_1 = \frac{0.0677 R_B R_2}{V_B (R_B + R_2) - V_S R_B}. \quad (11)$$

To a sensor chip, if the  $V_S$  and  $V_B$  are assumed,  $R_B$ ,  $S'/S$ , and  $R'_B/R_B$  can be obtained. With  $I'_{\text{SET}}/I_{\text{SET}} = 3360 \times 10^{-6}/^{\circ}\text{C}$ , substituting the above values into (10) and (11),  $R_1$  and  $R_2$  can be obtained.

In experiments, 10 pieces of sensor chips are picked up randomly. Initially, before the compensation, the calibration is done with the temperature characteristic of the sensor (after ageing). The compensating value of TCS can be calculated from the data of calibration. The absolute value of the compensated TCS is easy to be  $10 \times 10^{-6}/^{\circ}\text{C} \sim 100 \times 10^{-6}/^{\circ}\text{C}$  by calibration of several temperature compensation cycles. Three experimental results of the ten sensors are listed in Table 1. Then the compensation of TCO (temperature compensation of offset) is measured [19]. The experiments show

that if the basic feature of the sensor is stable, the absolute value of the compensated TCO is easy to be controlled in  $10 \times 10^{-6}/^{\circ}\text{C} \sim 100 \times 10^{-6}/^{\circ}\text{C}$ . Meanwhile, it shows that the changes are not so obvious for measuring the overall TCS of the sensor once again, as referred to the third group data in Table 1. The feasibility of this method is subsequently demonstrated by the static calibrations and offset stability measurements, and then is promoted in line product of micropressure sensor.

For a pressure sensor, zero point stability for a long term is also an important parameter. The sensor zero point output under the ambient environment for 12 hours was measured. The output voltages are measured with recording the ambient temperature. Figure 4 shows the variation of output voltage. The pressure sensor has a strong anti-interference ability and can meet the requirement of high accuracy tests.

The intelligent detector of internal-combustion engine cylinder pressure is shown in Figure 5. It was packaged with high temperature piezoresistive pressure sensor to get the high frequency response as well as to perform under harsh environment. Equipped with preamplifier circuit, it was convenient to read the testing results, and the operating performance is reliable.

## 5. Discussion

Detectors were sent to Dalian Locomotive Works to carry contrast test with mechanical watch on DF4 locomotives testbed. The results presented that maximum power of the diesel engine is 2650 KW. Explosive pressure is over

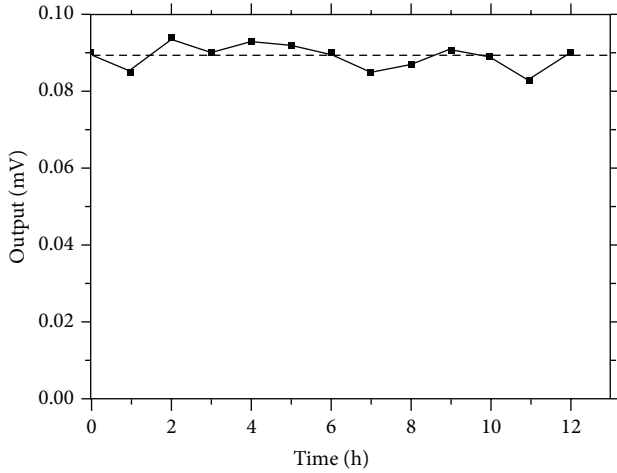


FIGURE 4: Intelligent detector's zero point stability under room temperature.



FIGURE 5: Intelligent detector of internal-combustion engine cylinder pressure with sensitivity temperature coefficient compensation-based integrated constant current.

12.55 MPa, and allowable error of air cylinders is 0.589 MPa. Contrast data of sixteen air cylinders is shown in Table 2.

Pressure recorded by detector was higher than testing result of mechanical watch. Mechanical watch produced major pressure loss during measurement process which was caused by its structure defect.

The head of mechanical watch consists of flattened and bent metal tube. The head produced deformation at the environment of high temperature and impure gas. There is a check valve of plane type inside. Its sealing is easy to be damaged by carbide in air, which will contribute to a much shorter life than detector. Sometimes mechanical watch may break down before finishing the test.

## 6. Conclusion

Intelligent detector of internal-combustion engine cylinder pressure with sensitivity temperature coefficient compensation-based integrated constant current is demonstrated in this paper. Separation by implanted oxygen (SIMOX) wafer was used to fabricate the high temperature pressure sensor chip. For high accuracy and wide temperature range

TABLE 2: Contrast testing data of the detector and the mechanical watch.

Cylinder number	Pressure value of mechanical watch (MPa)	Pressure value of the detector (MPa)
1	11.80	12.60
2	12.00	13.50
3	11.80	13.15
4	12.00	13.55
5	11.80	13.20
6	12.00	13.55
7	11.80	12.85
8	12.00	13.75
9	12.10	13.05
10	12.00	13.40
11	12.00	13.85
12	12.20	13.85
13	12.20	13.50
14	12.00	13.75
15	12.20	13.30
16	12.30	14.00

application, this paper also presents a novel pressure sensitivity temperature coefficient (TCS) compensation method, using integrated constant current network. A quantitative compensation formula is introduced in mathematics. During experiments, the absolute value of the compensated TCS is easy to be  $10 \times 10^{-6}/^{\circ}\text{C} \sim 100 \times 10^{-6}/^{\circ}\text{C}$  by individual adjustment and calibration of each device's temperature compensation. Intelligent detector effectively avoided the effect caused by high temperature and pressure pulsed gas, using high temperature piezoresistive pressure transducer. Meanwhile, the detector equipped with preamplifier circuit makes it convenient for the operator to read the results and guarantees the scientific and reasonable testing result.

## Acknowledgments

This work was financially supported by the science and technology development plan of Zhejiang province (public technology research and industrial projects, Grant no. 2012C21088), natural science foundation of Zhejiang province (Grant no. LY13E050016), and the opening foundation of Jiangsu province material tribology key laboratory (no. kjsmcx1001).

## References

- [1] S. Satoshi, O. Yasuhiro, M. Tetsuo et al., "Instantaneous 2D imaging of temperature in an engine cylinder with flame combustion," *International Journal of Heat and Mass Transfer*, vol. 62, pp. 382–390, 2013.
- [2] K. Halit, "Dynamic model of a two-cylinder four-stroke internal combustion engine and vibration treatment," *International Journal of Engine Research*, vol. 13, no. 6, pp. 616–627, 2012.

- [3] J. C. F. Millett, N. K. Bourne, M. Q. Chu, I. P. Jones, G. T. Gray III, and G. Appleby-Thomas, "The role of aging on the mechanical and microstructural response of aluminum 6061 to one-dimensional shock loading," *Journal of Applied Physics*, vol. 108, no. 7, Article ID 073502, 2010.
- [4] M. Cabrini, S. Lorenzi, P. Marcassoli, and T. Pastore, "NN-SCC assessment of steels for buried pipelines by means of 3 point bending tests," *Metallurgia Italiana*, vol. 102, no. 3, pp. 5–11, 2010.
- [5] L. Haifeng and N. Jianguo, "Mechanical behavior of reinforced concrete subjected to impact loading," *Mechanics of Materials*, vol. 41, no. 12, pp. 1298–1308, 2009.
- [6] M. H. Bao, *Micro Mechanical Transducers-Pressure Sensors, Accelerometers and Gyroscopes*, Elsevier, Amsterdam, The Netherlands, 2000.
- [7] A. Plöchl and G. Krauter, "Silicon on insulator: material aspects and application," *Solid-State Electronics*, vol. 44, no. 5, pp. 775–782, 2000.
- [8] G. K. Celler and S. Cristoloveanu, "Frontiers of silicon-on-insulator," *Journal of Applied Physics*, vol. 93, no. 9, pp. 4955–4978, 2003.
- [9] A. Diab, I. Ionica, G. Ghibaudo et al., "RC model for frequency dependence of split C-V measurements on bare SOI wafers," *IEEE Electron Device Letters*, vol. 34, no. 6, pp. 792–794, 2013.
- [10] Q. Wang, J. Ding, W. Xue, and Z. Ling, "Micro machining process of high temperature pressure sensor gauge chip based on SIMOX SOI wafer," *International Journal of Materials and Product Technology*, vol. 31, no. 2–4, pp. 375–385, 2008.
- [11] A. F. Saavedra, K. S. Jones, M. E. Law, and K. K. Chan, "Comparison of 311 Defect Evolution in SIMOX and Bonded SOI Materials," *Journal of the Electrochemical Society*, vol. 151, no. 4, pp. G266–G270, 2004.
- [12] H. Moriceau, F. Fournel, B. Aspar et al., "New layer transfers obtained by the SmartCut Process," *Journal of Electronic Materials*, vol. 32, no. 8, pp. 829–835, 2003.
- [13] A. F. Saavedra, J. Frazer, K. S. Jones et al., "Influence of the surface Si/buried oxide interface on extended defect evolution in silicon-on-insulator scaled to 300 Å," *Journal of Vacuum Science and Technology B*, vol. 20, no. 6, pp. 2243–2247, 2002.
- [14] D. F. Liu, *Mechanical Sensitive Device and Its Application*, Science Press, Beijing, China, 1987.
- [15] J. Scott and E. T. Enikov, "Novel temperature compensation technique for force-sensing piezoresistive devices," *Journal of Micromechanics and Microengineering*, vol. 21, no. 11, Article ID 115017, 2011.
- [16] N. P. Futane, S. R. Chowdhury, C. R. Chowdhury, and H. Saha, "ANN based CMOS ASIC design for improved temperature-drift compensation of piezoresistive micro-machined high resolution pressure sensor," *Microelectronics Reliability*, vol. 50, no. 2, pp. 282–291, 2010.
- [17] Q. Wang, J. Ding, and W. Wang, "Fabrication and temperature coefficient compensation technology of low cost high temperature pressure sensor," *Sensors and Actuators A*, vol. 120, no. 2, pp. 468–473, 2005.
- [18] P. Melvås and G. Stemme, "A diode-based two-wire solution for temperature-compensated piezoresistive pressure sensors," *IEEE Transactions on Electron Devices*, vol. 50, no. 2, pp. 503–509, 2003.
- [19] S. Vlassis and S. Siskos, "Signal conditioning circuit for piezoresistive pressure sensors with variable pulse-rate output," *Analog Integrated Circuits and Signal Processing*, vol. 23, no. 2, pp. 153–162, 2000.

## Research Article

# An Inverse Method to Reconstruct Complete Stiffness Information of Rubber Bushing

Gang Lei,<sup>1</sup> Qian Chen,<sup>2</sup> Ying Liu,<sup>2</sup> and Jingjing Jiang<sup>2</sup>

<sup>1</sup> Key Laboratory of Advanced Manufacturing Technology for Automobile Parts, Chongqing University of Technology, Ministry of Education, Chongqing 400054, China

<sup>2</sup> Faculty of Mechanical Engineering, Chongqing University of Technology, Chongqing 400054, China

Correspondence should be addressed to Gang Lei; [ganglei4786@126.com](mailto:ganglei4786@126.com)

Received 7 July 2013; Accepted 23 August 2013

Academic Editor: Xing Chen

Copyright © 2013 Gang Lei et al. This is an open access article distributed under the Creative Commons Attribution License, which permits unrestricted use, distribution, and reproduction in any medium, provided the original work is properly cited.

A specific rubber bushing, with only radial and axial stiffness data having been acquired, is studied. In terms of the hyperelastic material of this bushing, three-term Ogden law is utilized as the material constitutive model which requires to be characterized. Without the material mechanical tests provided, a parameter identification method is proposed for searching a group of acceptable parameters which are able to model rubber-like material of this rubber bushing. In this case, based on the nonlinear finite element analysis method and optimization technique, the parameters of material law are determined, and the rotational stiffness of this bushing is also evaluated. The complete stiffness information has been established.

## 1. Introduction

Rubber is recognized as an engineering material since the vulcanization of rubber being pioneered by Charles Goodyear in 1839 [1]. Unlike metals which require relatively few properties to characterize their mechanical behavior, the rubber-like materials present more complex with nonlinearity in terms of both geometric and material behavior. The traditional method to characterize rubber-like materials constitutive laws is evaluated through the sets of experimental data of different types of deformation. Uniaxial tension, planar tension, and biaxial tension tests are as the recommendations to identify the model parameters. Charlton et al. [1] utilized synthetic test data to characterize the mechanical behavior of rubber via FEA. Chen et al. [2] proposed a tension model for analyzing the rubber layers based on the theory of elasticity. Suphadon and Busfield [3] proposed a demanding test at solving a large strain elasticity problem of a rubber cylinder subjected to a combination of tension and torsion based on the applicable FE method. The validity of different stored energy functions was also studied. The image analysis is also used in material parameter of rubber; see [4]. However, obtaining the rubber-like material behavior without material

experimental information due to the shortage of necessary experimental appliances also needs to be considered.

Several methods are proposed at solving problems of parameter identification. Baker and Shrot [5] calculated material parameters from descriptors which involve inverse parameter identification methods without finite element simulations. Florentin and Lubineau [6] have explained how an appropriate use of the constitutive equation gap method can help in verification of material model parameters.

In this paper, an inverse finite element method for parameters identification is introduced, which involves the stiffness information of a specific component. More specifically, we focus on the parameters identification for one of the material constitutive laws and the evaluation for rotational stiffness of one certain rubber bushing.

## 2. Constitutive Laws

Generally, vulcanized rubber is assumed as an incompressible hyperelastic material [7]. Hyperelastic material is described as a “strain energy potential,” which defines the strain energy stored in the material per unit of reference volume as a function of the deformation at that point in the material. The most

common constitutive laws for modeling the hyperelastic materials behavior are the Mooney [8], Rivlin [9], Twizell and Ogden [10], and Yeoh [11] models. Each constitutive model is a special form of the strain energy potential [12].

Li and Yang [13] have pointed out that Ogden, Yeoh, and Martins models are the best ones that fit the silicone-rubber experimental data. Considering these hyperelastic models, the model whose parameter determination is the most complicated is the Ogden model [10] due to its relatively large number of parameters [14].

The Ogden strain energy potential is expressed in terms of the principal stretches ( $\lambda_1$ ,  $\lambda_2$ , and  $\lambda_3$ ). Thus, the constitutive equation of Ogden takes the form [1, 15]

$$U = \sum_{i=1}^N \frac{2\mu_i}{\alpha_i^2} (\lambda_1^{\alpha_i} + \lambda_2^{\alpha_i} + \lambda_3^{\alpha_i} - 3) + \sum_{i=1}^N \frac{1}{D_i} (J - 1 - R)^{2i}, \quad (1)$$

where  $\mu_i$ ,  $\alpha_i$  are material constants,  $N$  is the number of terms in the function, the stretch ratios  $\lambda_1$ ,  $\lambda_2$ , and  $\lambda_3$  are eigenvalues of the deformation tensor,  $J$  is the ratio to the deformed volume to the undeformed volume, and  $D_i$  defines the material compressibility (when  $D_i = 0$ , the material is considered completely incompressible). An ideal incompressible material maintains constant volume:

$$j = 1, \quad R = 0. \quad (2)$$

The Ogden model, (1), then becomes

$$U = \sum_{i=1}^N \frac{2\mu_i}{\alpha_i^2} (\lambda_1^{\alpha_i} + \lambda_2^{\alpha_i} + \lambda_3^{\alpha_i} - 3). \quad (3)$$

Note that as required by the definition of a strain energy potential, Ogden's strain energy vanishes when the material is in its natural, undeformed state [16]:

$$\lambda_1 = \lambda_2 = \lambda_3 = 1. \quad (4)$$

Ogden constitutive law is considered one of the most successful functions in describing the large deformation range of rubber-like materials. In this paper, therefore, the constitutive equation of three-term Ogden, with six coefficients, is utilized to define the property of this rubber material.

### 3. Parameter Identification for Rubber-Like Material of Rubber Bushing

In this paper, based on the combination of the nonlinear FE method and optimization technique, the parameters of hyperelastic material will be defined to describe the mechanical characteristics of rubber bushing. Meanwhile, the complete stiffness information about rubber bushing can be obtained.

During the identification process, two FE simulations are performed to replicate the radial and axial stiffness tests. The parameters of the material constitutive law are determined to fit the experimental result. Firstly, a set of initial values are assigned to the parameters of constitutive law. Simulate the translational stiffness of rubber bushing described by

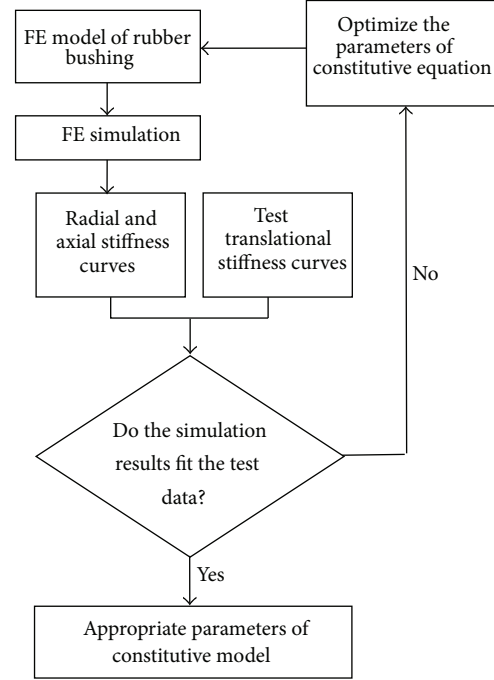


FIGURE 1: Typical steps in parameters identification cycle.

the foregoing parameters. If this result fails to fit the experimental data, an optimization procedure needs to be conducted to find the appropriate parameters which are able to model an effective hyperelastic material achieving to describe the mechanical characteristics of rubber bushing. Figure 1 demonstrates the main steps in parameters identification cycle.

**3.1. Translational Stiffness Tests.** The axial and radial stiffness tests were conducted due to the axisymmetrical structure of rubber bushing and limited test equipment. As shown in Figure 2, the axial stiffness is along  $x$  direction, and the radial stiffness is along  $y$  or  $z$  direction.

The translational stiffness tests provide axial and radial stiffness information which will be utilized as the standard data in the next parameter identification process.

**3.2. Translational Stiffness Simulations.** In this work, a CAD model of rubber bushing is imported to the FE software. This model is meshed to finite elements, material properties and appropriate boundary conditions are set subsequently to acquire a completely rubber bushing FE model. To simulate the radial and axial stiffness data, the software ABAQUS is used. This process is the preparation for the next stage—parameter identification.

More specifically, two load steps are set as the boundary conditions to fully assess the models fit. In the first step, a forced displacement was applied on the outer surface of bushing simultaneously intermediate shaft fixed. This is a preloaded step for fixing the bushing and establishing nonlinear contact steadily. In the second step, the loads were applied on the pipe around the center hole, incrementally from 0.0 N

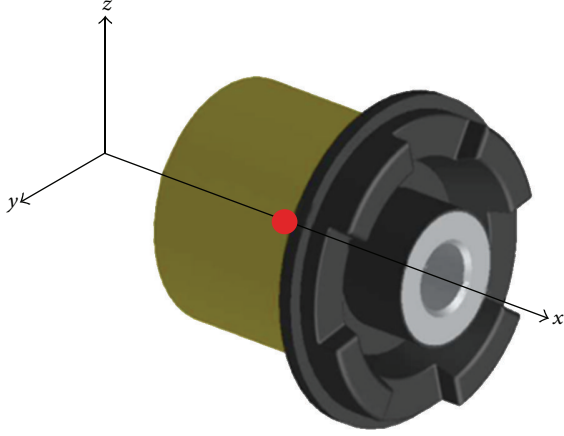


FIGURE 2: CAD model of rubber bushing.

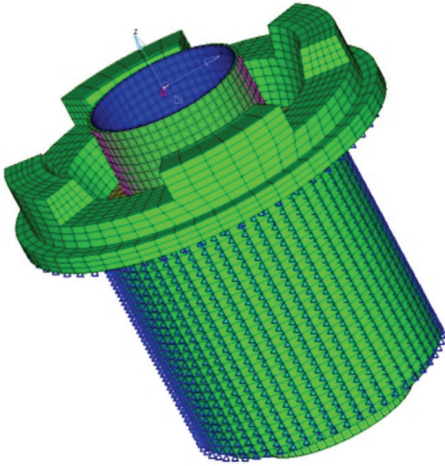


FIGURE 3: FE model of rubber bushing.

to 1000 N in  $x$  direction and 0.0 N to 3000 N in  $y$  direction which enables the axial stiffness and the radial stiffness to be evaluated by the FE software, respectively. The three-term Ogden law is applied as constitutive model for this rubber bushing, and a set of initial guesses are defined:

$$\begin{aligned} \mu_1 &= 1, & \mu_2 &= 0.00029, & \mu_3 &= 5e-06, \\ \alpha_1 &= 1.1, & \alpha_2 &= 11.5, & \alpha_3 &= -10. \end{aligned} \quad (5)$$

Figure 3 shows the FE model of rubber bushing with completely boundary conditions and material information.

The simulations were carried out for the two test described earlier: a radial stiffness test and an axial stiffness test. The simulated versus experimental displacement-stress curvilinear relationship is shown in Figure 4. Comparatively, there is a considerable gap between two curves which represent the stiffness steamed from the test and simulation, respectively. It is apparent that the initial coefficients of Ogden constitutive model do not suit this rubber bushing,

TABLE 1: The values of design variables.

Design variables	Lower bound	Upper bound
$\mu_1 = 1.0$	0.5	2.0
$\mu_2 = 2.9e-04$	$2.0e-04$	$3.8e-04$
$\mu_3 = 5e-06$	$4e-06$	$6e-06$
$\alpha_1 = 1.1$	0.6	1.6
$\alpha_2 = 11.5$	10	13
$\alpha_3 = -10.0$	-5	-15

and parameter identification is needed to find accurate coefficients of material constitutive model consequently.

**3.3. Parameter Identification.** Parameters of the constitutive equation of rubber are determined based on the combination of translational stiffness test data and finite element optimization techniques. When the results of simulation present apparent deviations from test data, the coefficients of the constitutive model should be redefined. This process can be completed by optimization software.

The six coefficients ( $\mu_1, \mu_2, \mu_3, \alpha_1, \alpha_2$ , and  $\alpha_3$ ) in the three-term Ogden strain energy model are selected as the design variables, since all their values influence stiffness of rubber bushing. Based on experimental data, a company provided, the values with lower and upper bounds that are defined in Table 1.

Two FE simulations are performed to replicate the radial and axial stiffness tests. If the simulated curves overlap the experimental counterpart, it means that the parameters of the constitutive equation having been selected could model this rubber-like material of rubber bushing accurately. To minimize the gap between simulated load-displacement curves and the experimental data, four subobjectives are proposed as follows.

**Subobjective 1.** The area enclosed by the simulated axial stiffness curve and abscissa axis is introduced as a response for this subobjective, while the experiment counterpart is applied as the target value.

**Subobjective 2.** The area enclosed by the simulated radial stiffness curve and abscissa axis is introduced as a response for this subobjective, while the experiment counterpart is applied as the target value.

**Subobjective 3.** The endpoint value on axial stiffness simulated curve is expected to approximate the experimental counterpart.

**Subobjective 4.** The endpoint value on radial stiffness simulated curve is expected to approximate the experimental counterpart.

Since the experimental and simulated curves are linear ranging from the minimum to the maximum value of the loads applied in this research, the above four subobjectives are able to make the simulated curves overlap the experimental

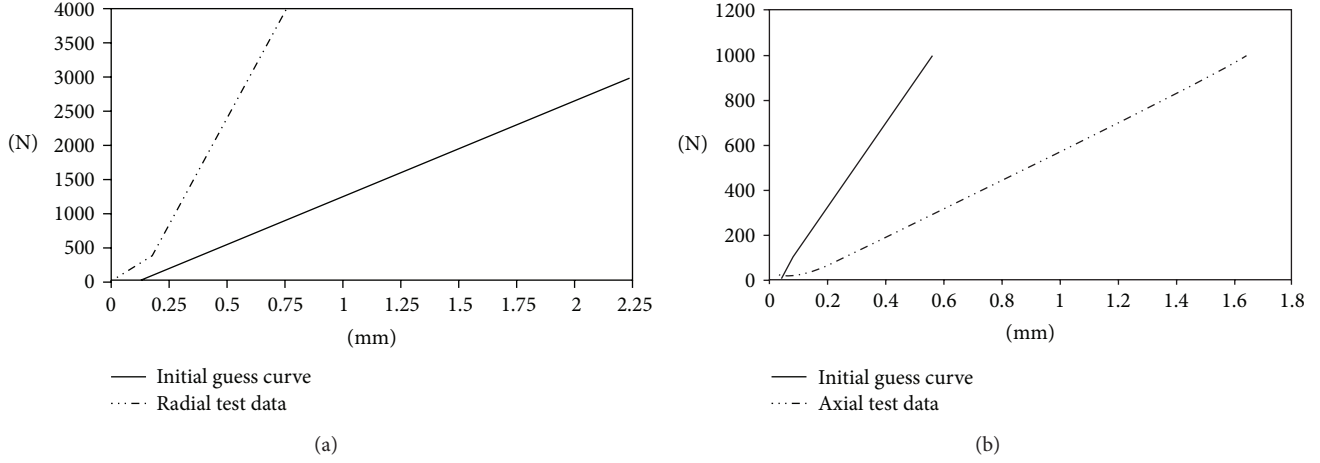


FIGURE 4: The initial load-displacement curves.

TABLE 2: The coefficient of material law (after optimized evaluation).

Constitutive equation	$\mu_i$	$\alpha_i$
Ogden $N = 3$	$\mu_1 = 1.273$	$\alpha_1 = 0.985$
	$\mu_2 = 2.58e - 04$	$\alpha_2 = 11.495$
	$\mu_3 = 5.8e - 06$	$\alpha_3 = -9.99$

counterpart and then replicate the radial and axial stiffness tests.

In a usual optimization problem, only one design object should be defined, while in this specific case four subobjectives are involved in the identification process. A weighted equation is employed, therefore, to integrate the four goals mentioned above into one general objective:

$$C_W = \sum_{i=1}^4 \omega_i C_i, \quad (6)$$

where  $C_W$  is the general objective as the weighted sum;  $\omega_i$  are weights in this optimization procedure,  $\omega_1 = \omega_2 = \omega_3 = \omega_4 = 1$ ; and  $C_i$  are the subobjective function.

Genetic algorithm [17] is introduced as the optimization method to find optimum value of the constitutive parameters of rubber-like material, due to its implicit parallelism and capability searching for the global optimum solution. The optimization procedure is carried out by FE optimization software. The iteration history plot will show the graph of the objectives. Figure 5 reveals the objectives history plot which converges to the specified values.

Having experienced 10 iterations, the result converges. Then it is extracted from the simulated model with parameters of constitutive model characterized simultaneously. The simulated versus experimental displacement-stress curvilinear relationship is shown in Figure 6, and a detailed parameters after the characterizing of the three-term Ogden law are provided in Table 2.

Figure 6 reveals good fit in both radial and axial stiffness with a slight relative errors involved which are acceptable in the engineering project. Consequently, the parameters of

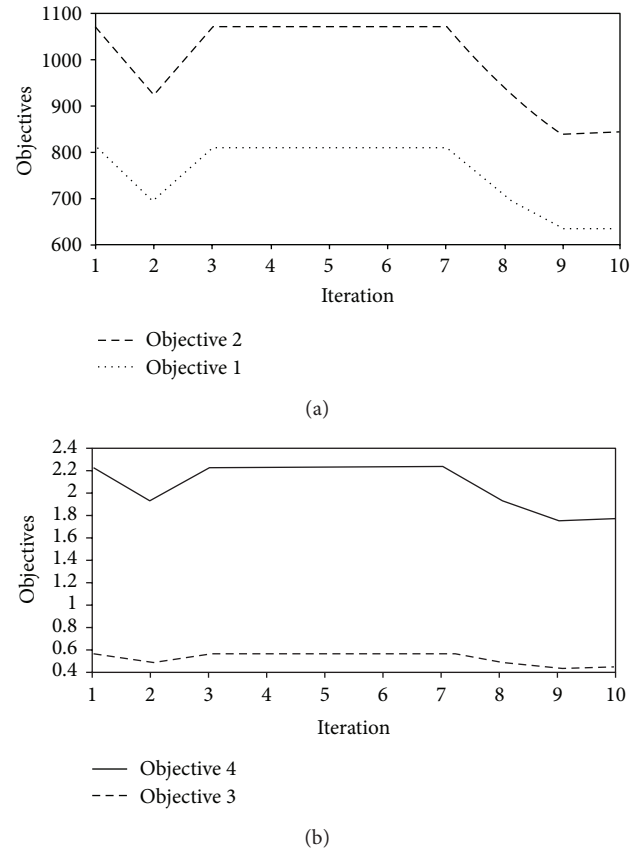
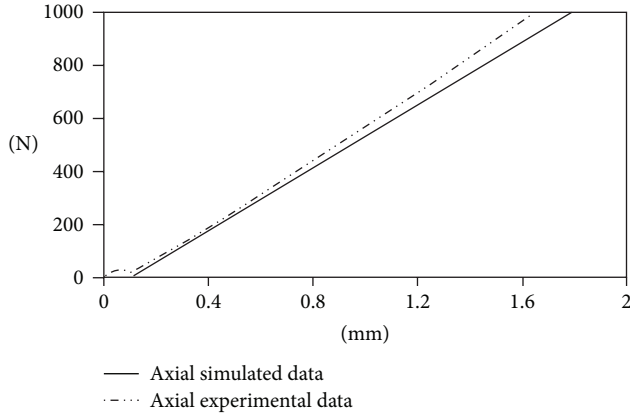


FIGURE 5: Histories of design variable.

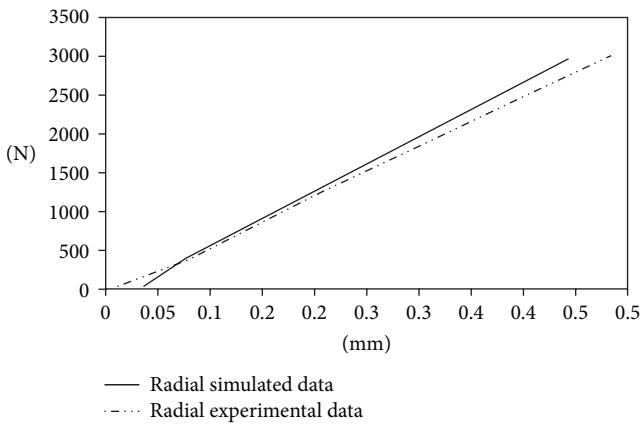
constitutive model, obtained after final iteration, are proved validly to simulate the rotational stiffness.

#### 4. Rotational Stiffness Analysis

Due to the limited amount of experimental appliances, the rotational stiffness tests are not conducted. Instead, they will



(a)



(b)

FIGURE 6: The load-displacement curves (after optimization).

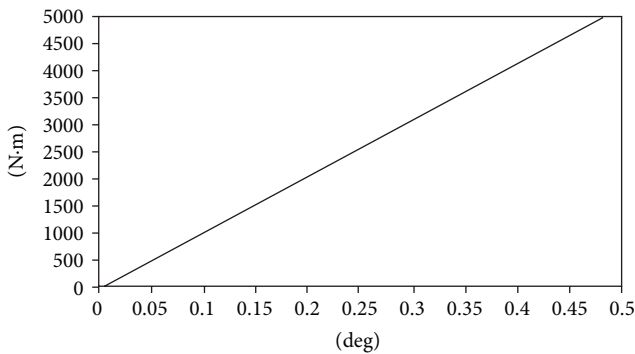
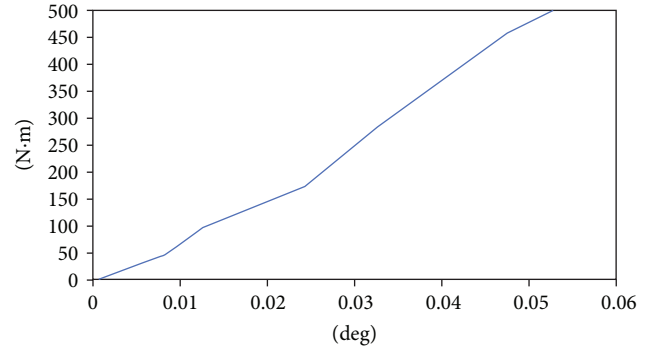


FIGURE 7: Rotational stiffness curve (around y or z direction).

be obtained through simulated software based on FE theory. The rotational stiffness information can be obtained by applying torques incrementally from 0 N·mm to 5000 N·mm around  $x$  and 0 N·mm to 500 N·mm around  $y$  ( $z$ ) direction, respectively. The simulated torque-angle curves are provided in Figures 7 and 8.

FIGURE 8: Rotational stiffness curve (around  $x$  direction).

## 5. Conclusions

In this study, the parameters of the three-term Ogden law used for modeling hyperelastic material have been identified. A nonlinear simulation is performed to replicate experimental radial and axial stiffness test for a specific rubber bushing, while the parameters of the material law are determined to fit the experimental results. Comparing the experimental and simulated data, only petty errors are found which indicates that the parameters of the constitutive equation are valid for modeling the material of this rubber bushing.

Subsequently, an accurate model is established relying on the determinate parameter of the material law in order to evaluate two rotational stiffness curves which have not been obtained due to the lack of rotational test data. In this procedure, the complete information about stiffness of rubber bushing can be acquired.

This parameter identification method is proved to model the appropriate hyperelastic material for rubber bushing validly when material tensile tests data are not provided. Additionally, the whole information about rubber bushing stiffness can be established practically.

## Acknowledgment

This work was funded by the 2012 open-ended foundation of Key Laboratory of Advanced Manufacturing Technology for Automobile Parts, Ministry of Education by Project of cstc2013yykfb0198.

## References

- [1] D. J. Charlton, J. Yang, and K. K. Teh, "Review of methods to characterize rubber elastic behavior for use in finite element analysis," *Rubber Chemistry and Technology*, vol. 67, no. 3, pp. 481–503, 1994.
- [2] S. C. Chen, X. K. Tian, and W. M. Yan, "Modeling and analysis of laminated rubber bearings under axial tensile loading," *Materials and Structures*, 2013.
- [3] N. Suphadon and J. J. C. Busfield, "Elastic behaviour of rubber cylinders under combined torsion and tension loading," *Plastics, Rubber and Composites*, vol. 38, no. 8, pp. 337–342, 2009.
- [4] K.-J. Gong, Y.-T. Wei, and J.-X. Ye, "Constitutive parametric experiment of tire rubber hyperelastic laws with application,"

Gongcheng Lixue/*Engineering Mechanics*, vol. 26, no. 6, pp. 193–198, 2009.

- [5] M. Baker and A. Shrot, “Inverse parameter identification with finite element simulations using knowledge-based descriptors,” *Computational Materials Science*, vol. 69, pp. 128–136, 2013.
- [6] E. Florentin and G. Lubineau, “Identification of the parameters of an elastic material model using the constitutive equation gap method,” *Computational Mechanics*, vol. 46, no. 4, pp. 521–531, 2010.
- [7] P. Martins, R. Jorge, and A. Ferreira, “A comparative study of several material models for prediction of hyperelastic properties: application to silicone-rubber and soft tissues,” *Strain*, vol. 42, no. 3, pp. 135–147, 2006.
- [8] M. Mooney, “A theory of large elastic deformation,” *Journal of Applied Physics*, vol. 11, no. 9, pp. 582–592, 1940.
- [9] R. Rivlin, “Large elastic deformations of isotropic materials. iv: further developments of the general theory A,” *Philosophical Transactions of the Royal Society of London*, p. 379, 1948.
- [10] E. Twizell and R. Ogden, “Non-linear optimization of the material constants in Ogden’s stress-deformation function for incompressible isotropic elastic materials,” *Journal of the Australian Mathematical Society*, pp. 424–434, 1983.
- [11] O. Yeoh, “Some forms of the strain energy function for rubber,” *Rubber Chemistry and Technology*, vol. 66, no. 5, pp. 754–771, 1993.
- [12] J. Martins, E. Pires, R. Salvado, and P. Dinis, “A numerical model of passive and active behavior of skeletal muscles,” *Computer Methods in Applied Mechanics and Engineering*, vol. 151, no. 3-4, pp. 419–433, 1998.
- [13] X.-F. Li and X.-X. Yang, “A review of elastic constitutive model for rubber materials,” *China Elastomerics*, vol. 15, no. 1, pp. 50–58, 2005.
- [14] A. Andrade-Campos, P. Pilvin, J. Simões, and F. Teixeira-Dias, *Software Development for Inverse Determination of Constitutive Model Parameters*, Software Engineering: New Research, Nova Science, New York, NY, USA, 2009.
- [15] Hibbit.Karlsson & Sorensen, *ABAQUS Theory Manual Version 6.7*, Hibbit.Karlsson & Sorensen, Providence, RI, USA, 2007.
- [16] “Mechanics and thermomechanics of rubberlike solids,” G. Saccomandi and R. W. Ogden, Eds., Springer, New York, NY, USA, 2004.
- [17] Z. Michalewicz, *Genetic Algorithms Data Structures Evolution Programs*, Springer, New York, NY, USA, 1996.

## Research Article

# Analysis and Testing of MR Shear Transmission Driven by SMA Spring

Jin Huang,<sup>1</sup> Xu Chen,<sup>2</sup> and Lirong Zhong<sup>1</sup>

<sup>1</sup> College of Mechanical Engineering, Chongqing University of Technology, Chongqing 400050, China

<sup>2</sup> College of Vehicle Engineering, Chongqing University of Technology, Chongqing 400050, China

Correspondence should be addressed to Xu Chen; [chenxu12@cqut.edu.cn](mailto:chenxu12@cqut.edu.cn)

Received 11 July 2013; Accepted 27 August 2013

Academic Editor: Xing Chen

Copyright © 2013 Jin Huang et al. This is an open access article distributed under the Creative Commons Attribution License, which permits unrestricted use, distribution, and reproduction in any medium, provided the original work is properly cited.

A transmission method of magnetorheological (MR) fluid in cylindrical-type driven by shape memory alloy (SMA) spring with the thermal effect was proposed. The torque can change rapidly with temperature. Based on the thermal effect of SMA, the expression for displacement of SMA spring was established. The rheological property of MR fluid under the magnetic fields was described by Bingham model. Based on momentum equation, the shear flow of MR fluid between two cylinders was analyzed and the expressions of flow velocity and torque have been obtained. The experimental results show the output displacement of SMA spring and the transmit torque of MR fluid is directly proportional to the temperature and the applied magnetic field, respectively.

## 1. Introduction

MR fluids and SMAs are known as smart materials for their properties can change rapidly on different external conditions. By applying a magnetic field, the fluids show the viscoplastic behavior with yield strength [1, 2]. Altering the strength of the magnetic field will precisely control the shear yield stress of the fluid. MR fluids are useful for the efficient control of the torques and forces transmission, and they can be used in clutches [3–7], brakes [8, 9], dampers [10–12], valves [13, 14], and so on. SMAs may undergo mechanical shape changes at relatively low temperatures and retain them until heated and then coming back to the initial shape [15, 16]. This makes SMAs unique compared to other smart materials that can be used for actuator applications [17, 18].

MR transmission is a device that transmits torque by the shear stress of the MR fluids. It has the property that their transmitting torque changes quickly in response to an external magnetic field. A literature review indicates that the transmission using MR fluids can be classified as having either disc-type or cylindrical-type [6]. In the disc-type, the MR fluid within the activation region between two parallel discs is a circular plate. In the cylindrical-type, the activated MR fluid between two concentric cylinders is an annular cylinder.

In order to rationally design the MR transmission devices driven by SMA spring under thermal effect a designer should analyzes the output displacement of SMA spring under thermal effect, and the torque transmission ability of MR fluid. In this paper, Bingham model is used to describe the constitutive characteristics of MR fluids subject to an applied magnetic field. The expressions for the output displacement of SMA spring and the torque of the cylindrical type MR transmission are established to provide the theoretical foundation for the design of MR device.

## 2. Transmission Principle

The schematic of the cylindrical MR transmission driven by SMA spring under thermal effect is shown in Figure 1. The driving shaft and driving cylinder are initiative members, and the shell is the driven one. The initiative members rotate at definite velocity  $\omega_1$ . At low temperature, MR fluid is saved at oil chamber, and the transmission system is in the state of separation. When the temperature gets higher, the SMA driving spring will pushes the MR fluid filling into the working gap between the driving-cylinder and shell through pipe rapidly. The cylindrical MR transmission device depends on the shear stress of the MR fluid to transmit torque. In the absence of

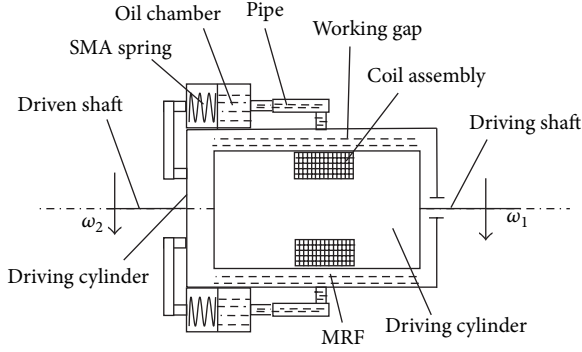


FIGURE 1: MR fluid shear transmission driven by SMA between two cylinders.

an applied magnetic field, MR fluid keeps flowing, so its transmission torque is only a very small viscous torque. However, in the course of operation, a magnetic flux path is formed when electric current is put through the coil assembly. As a result, the MR particles are gathered to form chain-like structures, in the direction of the magnetic flux path. These chain-like structures increase the shear stress of the MR fluid. With the increase of the applied magnetic field, the shear stress developed by the MR fluid goes up rapidly. When the shear stress is large enough, the initiative and driven members can finish a synchronous rotation. The amount of torque can be adjusted continuously by changing the input current in coil assembly.

### 3. Thermal Characteristics of SMA Spring

The displacement of bias type SMA actuating device based on SMA spring can be expressed as follows [19]:

$$S(T) = \frac{(G(T) - G_M) \Delta \delta F_L \gamma_{1L}}{(d/n\pi D^2) G(T) \Delta \delta F_L + (F_H - F_L) G_M \gamma_{1L}}, \quad (1)$$

where  $S(T)$  is the displacement of temperature control switch at temperature  $T$ ,  $d$  is the diameter of SMA wire,  $D$  is the diameter of spring,  $n$  is the number of spring turns,  $G_M$  is the elasticity modulus of martensite phase,  $\gamma_{1L}$  is the shear strain of martensite at low temperature,  $F_L$  and  $F_H$  are axial loads of SMA spring in martensite phase and austenitic phase, respectively,  $\Delta \delta$  is the maximum displacement of bias type SMA temperature controlled switch, and  $G(T)$  is the shear elasticity modulus of SMA spring at temperature  $T$ .

Consider

$$G(T)$$

$$= \begin{cases} G_M & T < M_f, T < A_s \\ G_M + \frac{G_A - G_M}{2} [1 + \sin \varphi (T - T_m)] & M_f \leq T \leq A_f \\ G_A & T > A_f, T > M_s, \end{cases} \quad (2)$$

where  $G_A$  is the elasticity modulus of austenitic phase and  $M_s$  and  $A_s$  are the starting values of phase change temperature for martensite and austenitic, respectively.  $M_f$  and  $A_f$  are the final values of phase change temperature, respectively. In the heating process,  $T_m = (A_s + A_f)/2$  and  $\varphi = \pi/(A_f - A_s)$ .

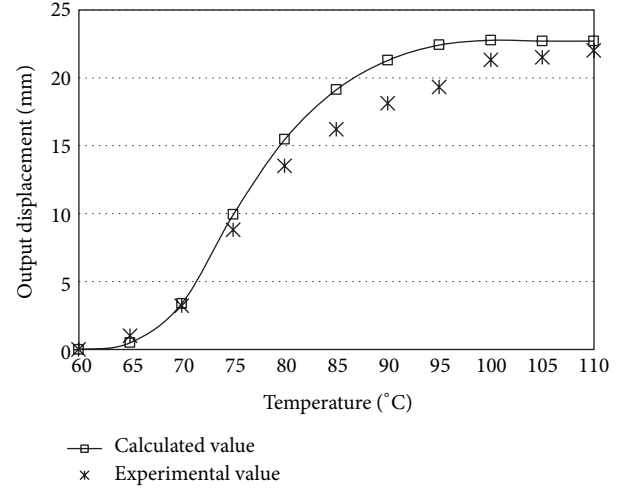


FIGURE 2: The displacements of SMA spring versus temperatures.

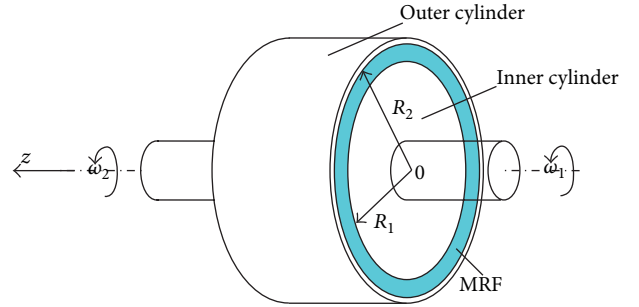


FIGURE 3: Circular flow of MR fluid between two cylinders.

In the cooling process,  $T_m = (M_f + M_s)/2$  and  $\varphi = \pi/(M_s - M_f)$ .

The theoretical and the experimental results of the relationship between output displacements and temperatures of SMA spring are shown in Figure 2. The SMA is NiTi alloy, and the phase transition temperatures are  $M_f = 50^\circ\text{C}$ ,  $M_s = 78^\circ\text{C}$ ,  $A_s = 74^\circ\text{C}$ , and  $A_f = 95^\circ\text{C}$ . The shear elasticity modulus at austenitic and martensite phase is  $G_A = 25\text{ GPa}$  and  $G_M = 7.5\text{ GPa}$ , respectively; the shear strain of martensite at low temperature is  $\gamma_{1L} = 2\%$ . The parameters of spring are as follows:  $D = 8.5\text{ mm}$ ,  $d = 1\text{ mm}$ ,  $n = 7$ , and the angle of inclination  $\alpha = 6^\circ$ .

### 4. The Shear Transmission of MR Fluid between Two Cylinders

Figure 3 shows the circular flow of an MR fluid within the operational gap between two cylinders. When the inner cylinder is rotated by the rotating speed  $\omega_1$ , the MR fluid is sheared and flowed at the rotating speed  $\omega_r$  in  $\theta$  direction. The outer cylinder is rotated by the rotating speed  $\omega_2$  because of the shear stress of the fluid.

In the cylindrical coordinate system, the momentum equation of the shear flow in  $\theta$  direction can be expressed by

$$\begin{aligned} \rho \left( \frac{\partial v_\theta}{\partial t} + \frac{v_\theta}{r} \frac{\partial v_\theta}{\partial \theta} + v_z \frac{\partial v_\theta}{\partial z} \right) \\ = f_\theta - \frac{1}{r} \frac{\partial p}{\partial \theta} + \frac{\partial \tau_{r\theta}}{\partial r} + \frac{1}{r} \frac{\partial \tau_{\theta\theta}}{\partial \theta} + \frac{\partial \tau_{z\theta}}{\partial z} + \frac{2}{r} \tau_{r\theta}, \end{aligned} \quad (3)$$

where  $\rho$  is the density of MRF,  $v_\theta$  is the flow velocity of the fluid in the  $\theta$  direction,  $t$  is time,  $f_\theta$  is the mass force in  $\theta$  direction, and  $\tau_{ij}$  is the shear stress.

In order to analyze the behavior of MR fluids flow in the gap between two cylinders, the following assumptions are given: the fluid is incompressible. There is no flow in radial direction and axial direction, but only tangential flow. The flow velocity of MR fluid is a function of radius. The pressure in the thickness direction of MR fluid is a constant one. The strength of magnetic field in the working gap of the activation region is well distributed. In the cylindrical coordinate system ( $r, \theta, z$ ),  $z$ -direction is coincident with the axis of two cylinders, and the distribution of the flow velocity is

$$v_r = 0 \quad v_\theta = r\omega(r) \quad v_z = 0, \quad (4)$$

where  $v_r$  and  $v_z$  are the flow velocity of the fluid in the  $r$ -direction and  $z$ -direction, respectively.  $\omega(r)$  is the rotation angular velocity of the fluid in the  $\theta$  direction. The angular velocity  $\omega(r)$  is the function of  $r$ -coordinate.

In the mode of flow, assume that the MR fluid within the gap is regarded as a cylindrical fluid. The momentum equation of the shear flow at the narrow gap may be approximated by

$$\frac{d\tau_{r\theta}}{dr} + \frac{2}{r} \tau_{r\theta} = 0, \quad (5)$$

where  $\tau_{r\theta}$  is the shear stress developed by MR fluid.

Ignore the wall slip effect, and the boundary conditions of MR fluid flow can be expressed as

$$v_\theta|_{r=R_1} = R_1\omega_1, \quad (6a)$$

$$v_\theta|_{r=R_2} = R_2\omega_2. \quad (6b)$$

The behavior of MR fluids is similar to Newtonian fluid without applied magnetic field. When a magnetic field is applied, the characteristics of MR fluids can be described by Bingham model [20]:

$$\begin{aligned} \tau_{r\theta} &= \tau_y + \eta \dot{\gamma} \quad \tau \geq \tau_y, \\ \dot{\gamma} &= 0 \quad \tau < \tau_y. \end{aligned} \quad (7)$$

Integrating the momentum equation (5), shear stress can be indicated as

$$\tau_{r\theta} = \frac{c_1}{r^2}, \quad (8)$$

where  $c_1$  is the integrating constant. Because the rotating speed decreases with the increase of the radius  $r$ , and the shear rate  $\dot{\gamma}$  in (7) can be calculated by

$$\dot{\gamma}_{r\theta} = -r \frac{d\omega(r)}{dr}. \quad (9)$$

The flow velocity  $\omega(r)$  can be obtained from (7), (8), and (9) as

$$\omega(r) = \frac{\tau_y}{\eta} \ln r + \frac{c_1}{2\eta r^2} + c_2, \quad (10)$$

where  $c_2$  is the integrating constant.

Applying the boundary conditions in ((6a) and (6b)), the integrating constants can be determined as

$$c_1 = \frac{2R_1^2 R_2^2 \tau_y}{R_2^2 - R_1^2} \ln \frac{R_2}{R_1} + \frac{2\eta R_1^2 R_2^2}{R_2^2 - R_1^2} (\omega_1 - \omega_2), \quad (11a)$$

$$c_2 = \frac{R_2^2 \omega_2 - R_1^2 \omega_1}{R_2^2 - R_1^2} - \frac{\tau_y}{\eta} \left( \frac{R_2^2 \ln R_2}{R_2^2 - R_1^2} - \frac{R_1^2 \ln R_1}{R_2^2 - R_1^2} \right). \quad (11b)$$

Submit ((11a) and (11b)) into (10), and the velocity distribution can be obtained as

$$\begin{aligned} \omega(r) &= \frac{\tau_y}{\eta} \ln r + \frac{R_1^2 R_2^2}{R_2^2 - R_1^2} \left( \frac{\tau_y}{\eta} \ln \frac{R_2}{R_1} + \omega_1 - \omega_2 \right) \frac{1}{r^2} \\ &+ \frac{R_2^2 \omega_2 - R_1^2 \omega_1}{R_2^2 - R_1^2} - \frac{\tau_y}{\eta} \left( \frac{R_2^2 \ln R_2}{R_2^2 - R_1^2} - \frac{R_1^2 \ln R_1}{R_2^2 - R_1^2} \right). \end{aligned} \quad (12)$$

As shown in Figure 3, MR fluids flow between two cylinders. The transmission torque of MR fluid can be expressed as

$$M = 2\pi r^2 L \tau, \quad (13)$$

where  $L$  is the width of the working gap. There are two parts of transmission torque of MR fluids between two cylinders, which are torque  $M_\eta$  produced by viscosity of MR fluids and torque  $M_H$  produced by yield stress  $\tau_y$ . If all of the MR fluids in working gap between two cylinders are yielded in shear mode, the transmission torque  $M_\eta$  produced by viscosity of MR fluids can be derived by combining (7), (9), (12), and (13):

$$M_\eta = 4\pi\eta L \frac{(\omega_1 - \omega_2) R_1^2 R_2^2}{R_2^2 - R_1^2}. \quad (14)$$

The torque  $M_H$  produced by yield stress of MR effect can be described as

$$M_H = \frac{\pi L_e (R_2 + R_1)^2}{2} \tau_y, \quad (15)$$

where  $L_e$  is the effective width of the MR effect developed by the MR fluid. The transmission torque of MR fluids between two cylinders is

$$M = M_H + M_\eta = \frac{\pi L_e (R_2 + R_1)^2}{2} \tau_y + 4\pi\eta L \frac{(\omega_1 - \omega_2) R_1^2 R_2^2}{R_2^2 - R_1^2}. \quad (16)$$

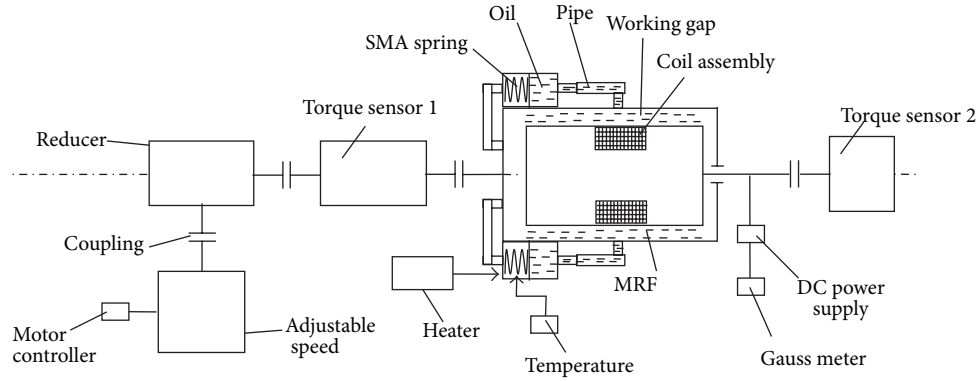


FIGURE 4: The overall sketch of performance experimental system for cylindrical-type MR fluid transmission driven by shape memory alloy.

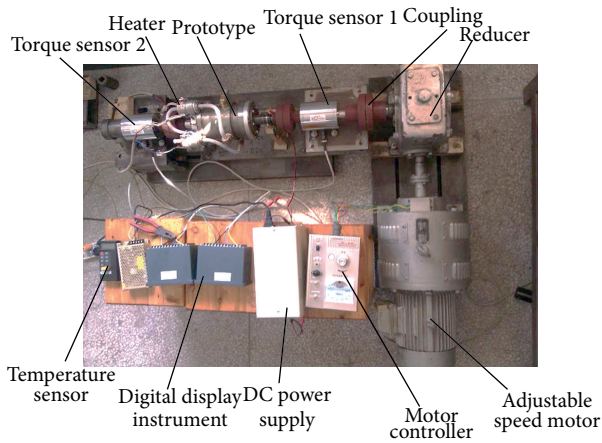


FIGURE 5: The performance experimental system for cylindrical-type MR fluid transmission driven by shape memory alloy.

## 5. Test and Analysis

Figure 4 shows the overall sketch of performance experimental system for cylindrical-type MR fluid transmission driven by shape memory alloy. Based on this system, the transmission torques of MR fluids between two cylinders under different applied magnetic fields are analyzed. The shearing rate of MR fluids between two cylinders can be adjusted by motor in the test system; see Figure 5. The magnetic field strength can be controlled by electric current in coil. All parameters in system are measured in real time by temperature sensor, speed, and torque sensors.

For this example, we use a typical MR fluid. Figure 6 shows the relation, obtained from the experiment, between the dynamic yield stress and the magnetic field strength for a typical MR fluid. The result shows that the shear stress is heavily influenced by applied magnetic field. In this study, the following parameters are given:  $\eta = 0.86$  Pa·s,  $L = 140$  mm,  $L_e = 50$  mm,  $R_1 = 50$ , and  $R_2 = 52$ .

When temperature is  $60^\circ\text{C}$  and the speed of driving shaft is 60 r/min, the relationship between the transmission torque of MR fluid between two parallel cylinders and the field current in coil assembly was obtained according to the test

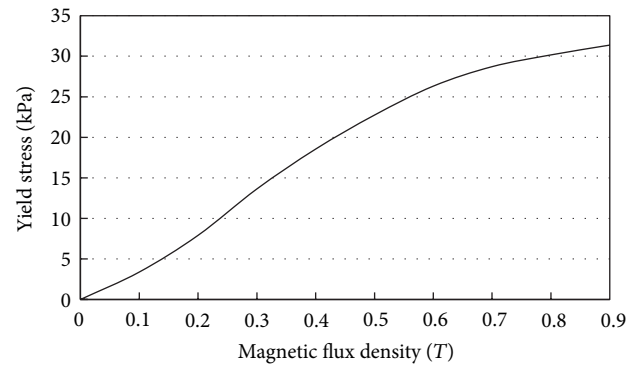


FIGURE 6: Yield stress versus magnetic flux density.

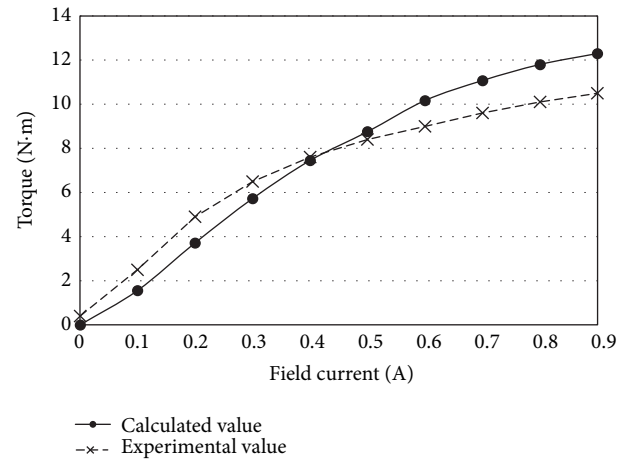


FIGURE 7: Torque versus field current.

system in Figure 5. The comparison of the theoretical and the experimental results is shown in Figure 7. When the currents are 0 A, 0.2 A, 0.4 A, 0.6 A, and 0.8 A, the experimental results of transmit torque are 0.6 N·m, 4.9 N·m, 7.6 N·m, 9.0 N·m, and 10.1 N·m, respectively. The transmit torque developed by MR fluid goes up rapidly with the increase of the applied magnetic field. The transmit torque with a variation of shear rate under field currents in coil assembly is shown in Figure 8.

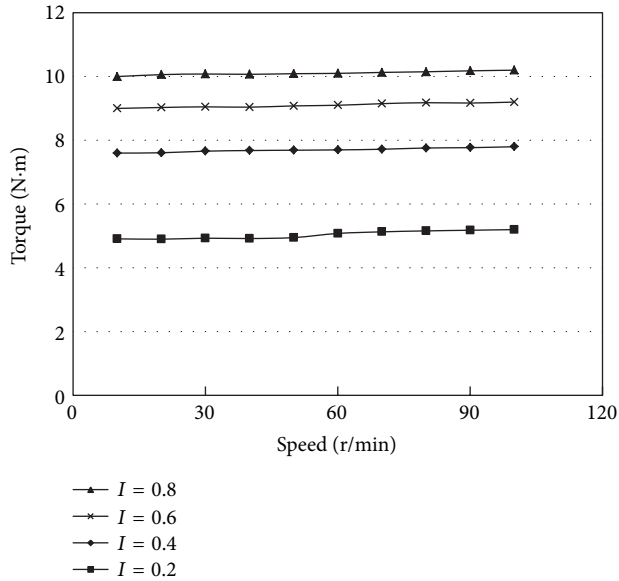


FIGURE 8: Torque versus speed.

In a variety of input speeds, the transmit torque remains generally stable.

The results show that the torque measured by experiment has the same trend with the calculated value basically. The deviation between experimental and theoretical values is brought by the error of yield stress, the structural error, the magnetic flux leakage, the simplification of theoretical analysis model, and so on.

## 6. Conclusions

- (1) Based on the heating and driving characteristics of SMA, the relationship between displacement and temperature of SMA spring was analyzed. The experimental results were well satisfied with the theoretical results. In the range of phase transition temperature, the output displacement of SMA spring increases with the rising of temperature.
- (2) The MR fluid can be driven into working chamber by SMA Spring. The volume of MR fluid in working chamber increases with the increasing of output displacement of SMA spring.
- (3) Based on rheological characteristics of MR fluid, the flow and transmission of MR fluid between two cylinders were analyzed, and the equations of flow velocity and transmit torque of MR fluid between two cylinders were obtained. The transmit torque of MR fluid between two cylinders increases with the increasing of applied magnetic field.

## Acknowledgments

This work was supported by the National Natural Science Foundation of China (51175532 and 11272368) and by the Natural Science Foundation Project of CQ CSTC (key project CSTC, 2011BA4028).

## References

- [1] M. S. Kim, Y. D. Liu, B. J. Park, C.-Y. You, and H. J. Choi, "Carbonyl iron particles dispersed in a polymer solution and their rheological characteristics under applied magnetic field," *Journal of Industrial and Engineering Chemistry*, vol. 18, no. 2, pp. 664–667, 2012.
- [2] J. Zhang, J.-Q. Zhang, and J.-F. Jia, "Characteristic analysis of magnetorheological fluid based on different carriers," *Journal of Central South University of Technology*, vol. 15, no. 1, pp. 252–255, 2008.
- [3] A. S. Shafer and M. R. Kermani, "On the feasibility and suitability of mr fluid clutches in human-friendly manipulators," *IEEE/ASME Transactions on Mechatronics*, vol. 16, no. 6, pp. 1073–1082, 2011.
- [4] T. Kikuchi, K. Otsuki, J. Furusho et al., "Development of a compact magnetorheological fluid clutch for human-friendly actuator," *Advanced Robotics*, vol. 25, no. 9-10, pp. 1363–1363, 2011.
- [5] P. Kielan, P. Kowol, and Z. Pilch, "Conception of the electronic controlled magnetorheological clutch," *Przegląd Elektrotechniczny*, vol. 87, no. 3, pp. 93–95, 2011.
- [6] J. Huang, L. Fu, and L. Zhong, "Analysis of a magnetorheological transmission for fan clutch," *Advanced Materials Research*, vol. 287-290, pp. 173–177, 2011.
- [7] Z. Herold, D. Libl, and J. Deur, "Design and testing of an experimental magnetorheological fluid clutch," *Strojarsvo*, vol. 52, no. 6, pp. 601–614, 2010.
- [8] J. Huang, J. Q. Zhang, Y. Yang, and Y. Q. Wei, "Analysis and design of a cylindrical magneto-rheological fluid brake," *Journal of Materials Processing Technology*, vol. 129, no. 1-3, pp. 559–562, 2002.
- [9] A. Farjoud, N. Vahdati, and Y. F. Fah, "Mathematical model of drum-type MR brakes using herschel-bulkley shear model," *Journal of Intelligent Material Systems and Structures*, vol. 19, no. 5, pp. 565–572, 2008.
- [10] J. Huang, J. He, and G. Lu, "Analysis and design of magnetorheological damper," *Advanced Materials Research*, vol. 148-149, pp. 882–886, 2011.
- [11] X. C. Zhu, X. J. Jing, and L. Cheng, "Magnetorheological fluid dampers: a review on structure design and analysis," *Journal of Intelligent Material Systems and Structures*, vol. 23, no. 8, pp. 839–873, 2012.
- [12] E. Dragašius, V. Grigas, D. Mažeika, and A. Šulginas, "Evaluation of the resistance force of magnetorheological fluid damper," *Journal of Vibroengineering*, vol. 14, no. 1, pp. 1–6, 2012.
- [13] M. Y. Salloom and Z. Samad, "Design and modeling magnetorheological directional control valve," *Journal of Intelligent Material Systems and Structures*, vol. 23, no. 2, pp. 155–167, 2012.
- [14] J. Huang, J. M. He, and J. Q. Zhang, "Viscoplastic flow of the MR fluid in a cylindrical valve," *Key Engineering Materials*, vol. 274-276, no. 1, pp. 969–974, 2004.
- [15] G. Costanza, M. E. Tata, and C. Calisti, "Nitinol one-way shape memory springs: thermomechanical characterization and actuator design," *Sensors and Actuators A*, vol. 157, no. 1, pp. 113–117, 2010.
- [16] S. Huang, M. Leary, T. Ataalla, K. Probst, and A. Subic, "Optimization of Ni-Ti shape memory alloy response time by transient heat transfer analysis," *Materials and Design*, vol. 35, pp. 655–663, 2012.

- [17] S. Langbein and A. Czechowicz, "Adaptive resetting of SMA actuators," *Journal of Intelligent Material Systems and Structures*, vol. 23, no. 2, pp. 127–134, 2012.
- [18] S. Degeratu, P. Rotaru, G. Manolea, H. O. Manolea, and A. Rotaru, "Thermal characteristics of Ni-Ti SMA (shape memory alloy) actuators," *Journal of Thermal Analysis and Calorimetry*, vol. 97, no. 2, pp. 695–700, 2009.
- [19] J. Ma, H. Shu, and J. Huang, "MR continuously variable transmission driven by SMA for centrifugal fan in nuclear power plant," *Science and Technology of Nuclear Installations*, vol. 2012, Article ID 205675, 6 pages, 2012.
- [20] J. D. Carlson and M. R. Jolly, "MR fluid, foam and elastomer devices," *Mechatronics*, vol. 10, no. 4, pp. 555–569, 2000.

## Research Article

# Flexural Vibration Test of a Beam Elastically Restrained at One End: A New Approach for Young's Modulus Determination

Rafael M. Digilov and Haim Abramovich

*Faculty of Aerospace Engineering, Technion—Israel Institute of Technology, 32000 Haifa, Israel*

Correspondence should be addressed to Rafael M. Digilov; [edurafi@technion.ac.il](mailto:edurafi@technion.ac.il)

Received 1 May 2013; Accepted 11 July 2013

Academic Editor: Xing Chen

Copyright © 2013 R. M. Digilov and H. Abramovich. This is an open access article distributed under the Creative Commons Attribution License, which permits unrestricted use, distribution, and reproduction in any medium, provided the original work is properly cited.

A new vibration beam technique for the fast determination of the dynamic Young modulus is developed. The method is based on measuring the resonant frequency of flexural vibrations of a partially restrained rectangular beam. The strip-shaped specimen fixed at one end to a force sensor and free at the other forms the Euler Bernoulli cantilever beam with linear and torsion spring on the fixed end. The beam is subjected to free bending vibrations by simply releasing it from a flexural position and its dynamic response detected by the force sensor is processed by FFT analysis. Identified natural frequencies are initially used in the frequency equation to find the corresponding modal numbers and then to calculate the Young modulus. The validity of the procedure was tested on a number of industrial materials by comparing the measured modulus with known values from the literature and good agreement was found.

## 1. Introduction

The Young modulus is a fundamental material property and its determination is common in science and engineering [1, 2]. It is a key parameter in mechanical engineering design to predict the behavior of the material under deformation forces or more to get an idea of the quality of the material. Young's moduli are determined from static and dynamic tests. In static measurements [3, 4] such as the classical tensile or compressive test, a uniaxial stress is exerted on the material, and the elastic modulus is calculated from the transverse and axial deformations as the slope of the stress-strain curve at the origin. Dynamic methods [5–12] are more precise and versatile since they use very small strains, far below the elastic limit and therefore are virtually nondestructive allowing repeated testing of the same sample. These include the ultrasonic pulse-echo [6, 7] or bar resonance methods [4, 8–14]. In the sonic pulse technique, the dynamic Young modulus is determined by measuring the sound velocity in the sample. In the resonance method, the linear elastic, uniform, and isotropic material of density  $\rho$  usually in the form of a bar of known dimensions is subjected to transverse

or flexural vibrations, the natural frequency of  $n$ th mode of which  $f_n$  related to Young's modulus  $E$  by the relation [15, 16]

$$f_n = \frac{\lambda_n^2}{2\pi l^2} \sqrt{\frac{EI}{\rho A}}, \quad n = 1, 2, 3, \dots \quad (1)$$

can be accurately measured. In (1)  $\lambda_n$  is the modal eigenvalue that depends on boundary conditions,  $l$  is the vibrating length of the bar,  $A$  is its cross-sectional area, and  $I$  is the second moment of the cross-section, equal to  $\pi r^4/4$  for a rod of radius  $r$  and  $dh^3/12$  for a rectangular beam with width  $d$  and depth  $h$ . Knowing the modal numbers, by simply measuring the resonance frequencies, geometry, and density of the specimen, the Young modulus can be determined from (1) as

$$E = \frac{4\pi^2 f_n^2 l^4 \rho A}{\lambda_n^4 I}. \quad (2)$$

The test sample is usually arranged in a manner to simulate free-free or clamped-free end conditions [10–12], when  $\lambda_n$ , associated with the  $n$ th flexural mode is a constant.

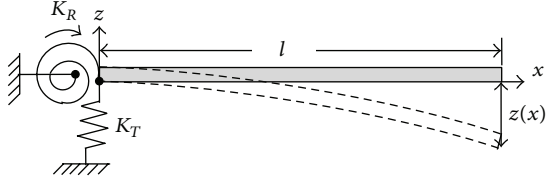


FIGURE 1: Model of a cantilever beam elastically restrained at  $x = 0$ .

In the present paper, we develop a new approach, in which a rectangular strip-shaped sample attached to a force sensor forms the Euler Bernoulli beam with partial translational and rotational restraints at the fixed end. This feature expands the capabilities of the resonant beam method making it suitable for materials with high stiffness and low density in which case, it is difficult to ascertain the flexural resonance frequencies with high certainty.

## 2. Theoretical Background

Consider a rectangular bar of uniform density  $\rho$ , cross-section dimensions of which width  $d$  and depth  $h$  are much less than length  $l$ . The bar is fixed at one end ( $x = 0$ ) to the force sensor with a linear ( $K_T$ ) and torsion ( $K_R$ ) springs constants (see Figure 1) and is otherwise free to move in the transverse  $z$ -direction. For small deflections, that is,  $\partial z(x, t)/\partial x \ll 1$ , the effects of rotary inertia and shear deformation can be ignored. In this case, neglecting the deflection due to the weight, the flexural displacement of a bar,  $z(x, t)$  at point  $x$  is governed by the Euler-Bernoulli equation [10]

$$\rho A \frac{\partial^2 z}{\partial t^2} + EI \frac{\partial^4 z}{\partial x^4} = 0 \quad (3)$$

with boundary conditions at  $x = 0$ :

$$-K_T z(0, t) = EI \left. \frac{\partial^3 z}{\partial x^3} \right|_{x=0}, \quad K_R \left. \frac{\partial z}{\partial x} \right|_{x=0} = EI \left. \frac{\partial^2 z}{\partial x^2} \right|_{x=0} \quad (4)$$

which correspond to the force and moment balance, respectively. At the free end  $x = l$  there are no moment and shear force acting, that is,

$$\left. \frac{\partial^2 z}{\partial x^2} \right|_{x=l} = 0, \quad \left. \frac{\partial^3 z}{\partial x^3} \right|_{x=l} = 0. \quad (5)$$

Equations (3)–(5) define completely the linear flexural vibration problem, in which the natural frequencies of the beam depend on spring constants  $K_T$  and  $K_R$ . Applying the separation of variables method, the solution of (3) can be cast in the following form:

$$z(x, t) = w(x) T(t) = \sum_{n=1}^{\infty} w_n(x) e^{i\omega_n t}, \quad (6)$$

where  $w_n(x)$  describes the  $n$ th normal mode and  $\omega_n$  ( $=2\pi f_n$ ,  $f$ : resonant frequency) is the angular frequency of

the  $n$ th mode. Substituting (6) into (3) gives an eigenvalue problem in the form of a fourth-order ordinary differential equation

$$\frac{\partial^4 w_n(x)}{\partial x^4} - \kappa_n^4 w_n(x) = 0, \quad (7)$$

where  $\kappa_n$  is related to the angular frequency  $\omega_n$  and the modal number  $\lambda_n$  by the dispersion relationship

$$\kappa_n^4 = \left( \frac{\lambda_n}{l} \right)^4 = \omega_n^2 \frac{\rho A}{EI}. \quad (8)$$

With the boundary condition, (4), the solution of (7) admits the form of  $n$ th flexural eigenmode:

$$w_n(x) = A_n (\cosh \kappa_n x + a_n \sinh \kappa_n x + b_n \sin \kappa_n x) + C_n (\cos \kappa_n x - b_n \sinh \kappa_n x - a_n \sin \kappa_n x), \quad (9)$$

where related coefficients  $b_n$  and  $a_n$  are defined as

$$a_n = \frac{1 - \lambda_n^4 R_n T_n}{2\lambda_n^3 R_n}, \quad b_n = \frac{1 + \lambda_n^4 R_n T_n}{2\lambda_n^3 R_n} \quad (10)$$

with  $R_n$  and  $T_n$  expressed through experimentally accessible quantities:

$$R_n = \frac{K_R}{(2\pi f_n)^2 \rho A l^3}, \quad T_n = \frac{K_T}{(2\pi f_n)^2 \rho A l}, \quad (11)$$

and integration constants  $A_n$  and  $C_n$  are related by the modal restriction equation (5) as

$$\frac{A_n}{C_n} = \frac{\cos \lambda_n + b_n \sinh \lambda_n - a_n \sin \lambda_n}{\cosh \lambda_n + a_n \sinh \lambda_n - b_n \sin \lambda_n} = -\frac{\sin \lambda_n - b_n \cosh \lambda_n + a_n \cos \lambda_n}{\sinh \lambda_n + a_n \cosh \lambda_n - b_n \cos \lambda_n}, \quad (12)$$

where the second equality implies the constraints on possible values of  $\lambda_n$ , known as the frequency equation:

$$\begin{aligned} & (1 + \lambda_n^4 R_n T_n) - (1 - \lambda_n^4 R_n T_n) \cos \lambda_n \cosh \lambda_n \\ & - \lambda_n [(\lambda_n^2 R_n + T_n) \sin \lambda_n \cosh \lambda_n \\ & + (\lambda_n^2 R_n - T_n) \sinh \lambda_n \cos \lambda_n] \\ & = 0. \end{aligned} \quad (13)$$

For given values of  $R_n$  and  $T_n$ , transcendental equation (13) has infinite (iterative or graphical) solutions. As  $T_n \rightarrow 0$  and  $R_n \rightarrow 0$  (13) becomes

$$1 - \cos \lambda_n \cosh \lambda_n = 0 \quad (14)$$

that is the frequency equation for the free-free beam. For  $T_n \gg R_n$  (13) reduces to the frequency equation derived by Chun [17], which in our case is written in the form

$$\begin{aligned} & R_n \lambda_n^3 (1 + \cos \lambda_n \cosh \lambda_n) \\ & - \sin \lambda_n \cosh \lambda_n - \sinh \lambda_n \cos \lambda_n = 0 \end{aligned} \quad (15)$$

which, in turn, at  $R_n \rightarrow \infty$  becomes the frequency equation for the clamped-free beam

$$1 + \cos \lambda_n \cosh \lambda_n = 0. \quad (16)$$

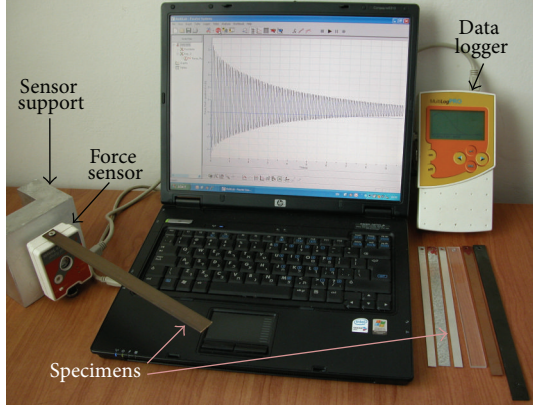


FIGURE 2: Equipment used for measuring Young's modulus with the force sensor.

### 3. Principles of Operation

The experimental setup consists of a commercial, Fourier Force Sensor DT 272 with rotation  $K_R$  ( $=17.837 \text{ N}\cdot\text{m}$ ) and translation  $K_T$  ( $=6400 \text{ N}\cdot\text{m}^{-1}$ ) spring constants, accuracy  $\pm 2\%$ , and resolution (12 bit)  $0.005 \text{ N}$  for a scale range  $\pm 10 \text{ N}$ . The force sensor mounted on a support is connected through data acquisition system and data studio software to a personal computer (PC) as is shown in Figure 2.

The strip-shaped specimen with a roughly mass of  $m \approx 10 \text{ g}$  is attached horizontally to a force sensor at one end and is free at the other end. By simply displacing the free end in the transverse direction and abruptly releasing it, the sample is subjected to free flexural vibrations, so that the condition  $\partial z / \partial x \ll 1$  was fulfilled. At a given sample rate,  $f_s = 1000 \text{ Hz}$  the force sensor detects the dynamic response and through the data acquisition system displays the damped oscillations of the restoring force versus time (Figure 3(a)). This vibration signal is analyzed and processed by an FFT implemented in acquisition software like MultiLogPRO [18] providing the direct information about natural frequencies up to  $f_s/2$ , which appears as single peaks in the frequency spectrum (Figure 3(b)). At this point, using data on the geometrical dimensions of the sample, its density, and spring constants of the force sensor  $K_R$  and  $K_T$ , identified resonance frequencies  $f_n$  are used in (11) to calculate dimensionless parameters  $R_n$  and  $T_n$ . Knowing  $R_n$  and  $T_n$ , modal number  $\lambda_n$  was found from the graphical solution of (13) using the mathematical packages MATHEMATICA [19]. The Young modulus is then determined from

$$E = 48\pi^2 \frac{\rho f_n^2 l^4}{\lambda_n^4 h^2}. \quad (17)$$

The relative error of the method arises from the uncertainties in the measurement of the quantities in (17). The relative error in the density  $\rho$  determined by the hydrostatic method is  $|d(\ln \rho)| \leq 0.7\%$ . The uncertainty in the thickness and length measurement are, respectively,  $|d(\ln h)| \leq 0.4\%$  and  $|d(\ln l)| \leq 0.25\%$ . The dispersion in the natural frequency

TABLE 1: Identified resonant frequencies  $f_n$  in Hz, modal numbers determined from (13), and Young's moduli in GPa evaluated by (17) for the brass specimens of different lengths,  $d = 16 \text{ mm}$ ,  $h = 1.5 \text{ mm}$ , and  $\rho = 8400 \text{ kg}\cdot\text{m}^{-3}$ .

$l/d$	$T_n/R_n$	$f_1$	$\lambda_1$	$E_1$	$f_2$	$\lambda_2$	$E_2$
8.13	60.6	37.82	1.595	111.6	232.79	4.068	100
9.06	75.4	31.14	1.619	110.3	193.83	4.14	100
9.813	88.4	26.84	1.638	107.4	170.23	4.179	102
10.69	104.9	23.07	1.653	107.9	147.82	4.215	104.7
12.25	137.8	17.9	1.679	105.2	115.24	4.276	103.7
14.69	198.2	13.0	1.701	108.9	84.10	4.326	109
15.5	220.7	11.75	1.709	108.2	76.25	4.372	106.5

determination is  $|d(\ln f_1)| \leq 0.25\%$ . By applying the error propagation technique, given by

$$|d(\ln E)| \leq 2|d(\ln f_1)| + |d(\ln \rho)| + 4|d(\ln l)| + 2|d(\ln h)| \quad (18)$$

we find that the relative error in Young's modulus does not exceed  $\pm 3\%$ . The greatest inaccuracies occurred in the measurement of the specimen dimensions.

### 4. Results and Discussion

To test the accuracy and validity of the present method, the effect of the sample length on the resonance frequency and Young's modulus was studied. A commercial brass strip of width  $d = 16 \text{ mm}$ , thickness  $h = 1.5 \text{ mm}$ , and density  $\rho = 8400 \text{ kg}\cdot\text{m}^{-3}$  was cut into samples of various length, so that one of the conditions of the Euler-Bernoulli beam theory  $l/h > 10$  remained unchanged, while the second  $l/d$  ranged from 8 to 16. Since the ratio  $T_n/R_n \gg 1$  (see Table 1) we used the approximated equation (15) to find the  $\lambda_1$ . The validity of this approach is illustrated in Figure 4, which shows that the solutions of both (15) and (13) practically coincide.

Based on the results of measurements of the natural frequencies and modal numbers presented in Table 1, a double logarithm plot of  $f_i/\lambda_i^2$  against  $l$  predicted by (1) to be linear with the gradient of  $-2$  shows that the slope of the line that best fits these data in a least-squares sense is  $-2.02$  for the first mode and  $-1.94$  for the second one. Based on the same set of data we show in Figure 5 the plot of the ratio  $f_i l^2/\lambda_i^2$  versus  $l/d$ . Most of the uncertainty in the ordinates of this plot arises from uncertainty of  $l$  rather than  $f_i$ . In the range of  $l/d > 10$ , the value of  $f_i l^2/\lambda_i^2$  is constant to within the experimental uncertainties, showing that  $f_i/\lambda_i^2 \propto l^{-2}$  is in agreement with (1). For  $l/d < 10$ , that is smaller for validity of the Euler-Bernoulli beam theory, the ratio  $f_i l^2/\lambda_i^2$  decreases (increases) with  $l$  for the first (second) mode. For  $l/d \geq 10$ , the mean value of Young's modulus  $E = 106 \pm 2 \text{ GPa}$  lies within the range  $95 \div 110 \text{ GPa}$ , listed in an extensive table of ASTM testing [20].

Below, we compare the results of measurements of elastic moduli at ambient temperature for a wide class of industrial materials with that accepted in the literature. A set of test specimens used were cut from the commercial sheet materials

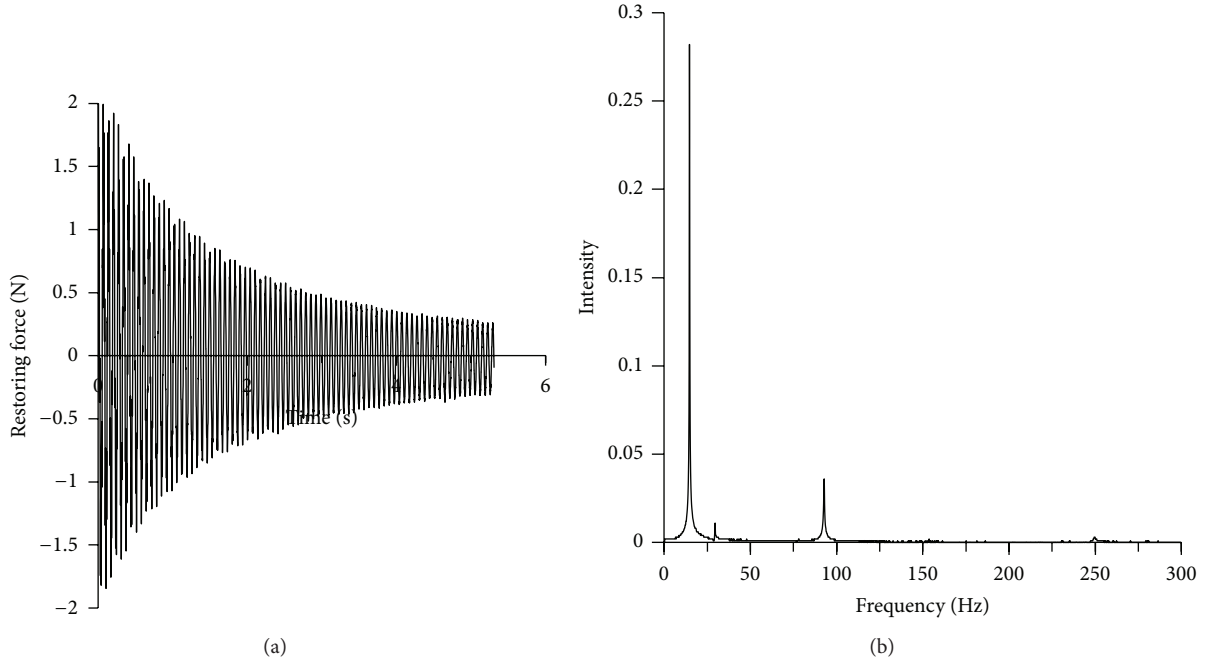


FIGURE 3: The flexural vibration test of partially restrained aluminum beam with  $l = 0.282$  m,  $d = 1.35$  cm, and  $h = 1.55$  mm. (a) Dynamic response detected by the force sensor at sample rate 1 kHz. (b) Identified resonance frequencies:  $f_1 = 14.7$  Hz;  $f_2 = 92.8$  Hz;  $f_3 = 249.5$  Hz.

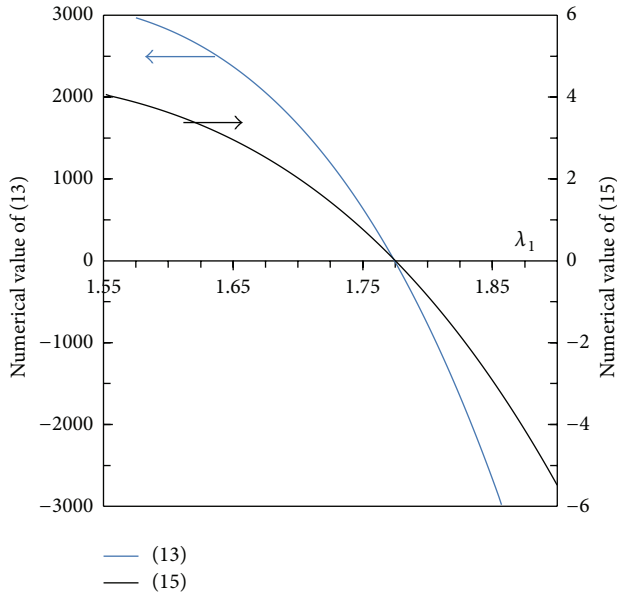


FIGURE 4: Graphical solutions of (13) and (15) for the first mode of flexural vibrations of partially restrained aluminum beam are, respectively,  $\lambda_1 = 1.7752$  and  $\lambda_1 = 1.7745$  against  $\lambda_1 = 1.8751$  for ideal clamped-free case.

into strips of the thickness ( $h$ ) from 0.5 to 3.3 mm, width ( $d$ ) from 5 to 16.5 mm, and length ( $l$ ) from 15 to 30 cm. For each specimen, the length, width, and thickness were altered and the value of the Young modulus calculated by (17) for each set varied within the experimental error. Table 2 summarizes data of the specimen dimension, material

density, natural frequencies, modal numbers, and Young's modulus calculated from the first resonant frequency. It can be seen that test results are in good agreement with the accepted those in the literature data.

In all cases, identified natural frequencies of the partially restrained cantilever beam are lower than those for the clamped-free case. However, this does not necessary mean that the elastic modulus determined from these frequencies should be smaller than in ideal clamped-free case as the modal number, being in the denominator equation (17) in fourth power, decreases as well. Interestingly, the plot of  $\lambda_1^4$  versus  $1/R_1$  in Figure 5 shows a linear dependence

$$\lambda_1^4 = \lambda_\infty^4 \left( 1 - \frac{1}{3R_1} \right), \quad (19)$$

where  $\lambda_\infty = 1.8751$  is the first modal number for the clamped-free flexural vibrations of the beam. Taking into account (11), after substituting (19) in (17), we obtain the working equation for the Young modulus determination through the first resonance frequency of flexural vibrations of the partially restrained cantilever beam (Figure 6)

$$E = \frac{48\pi^2 f_1^2 \rho l^4}{h^2 \lambda_\infty^4 \left( 1 - \left( 4\pi^2 f_1^2 \rho A l^3 / 3K_R \right) \right)}. \quad (20)$$

## 5. Summary

A new technique for the fast determination of the dynamic Young modulus was developed, yielding a substantial modification of the classical cantilever beam method. The procedure

TABLE 2: Young's moduli of materials  $E$  in GPa, determined at room temperature by (17) and specimen parameters: length  $l$  in mm, thickness  $h$  in mm, density  $\rho$  in  $\text{kg}\cdot\text{m}^{-3}$ , fundamental frequency  $f_1$  in Hz, and modal number  $\lambda_1$  calculated by (13).

Material	$l$	$h$	$\rho$	$f_1$	$\lambda_1$	$E$	$E_{\text{Literature}}$
Al 6061 sheet	282	1.55	2715	14.42	1.778	70.0	70–72
Zn coated steel	193	0.55	7820	12.0	1.868	201	206
Sheet steel 304	193	0.5	7970	11.0	1.864	210	190–213
Cooper alloy	214	1.0	8790	11.89	1.848	106	110–120
Brass stripe	248	1.5	8400	11.75	1.709	108	96–110
Perspex	190	3.0	1190	23.2	1.798	4.2	2.4–4.6
Wood, oak	252	3.5	674	30.3	1.664	12.6	11–12
Composite <sup>a</sup>	232	2.5	1600	33.0	1.429	92.0	36–150

<sup>a</sup> Graphite carbon epoxy.

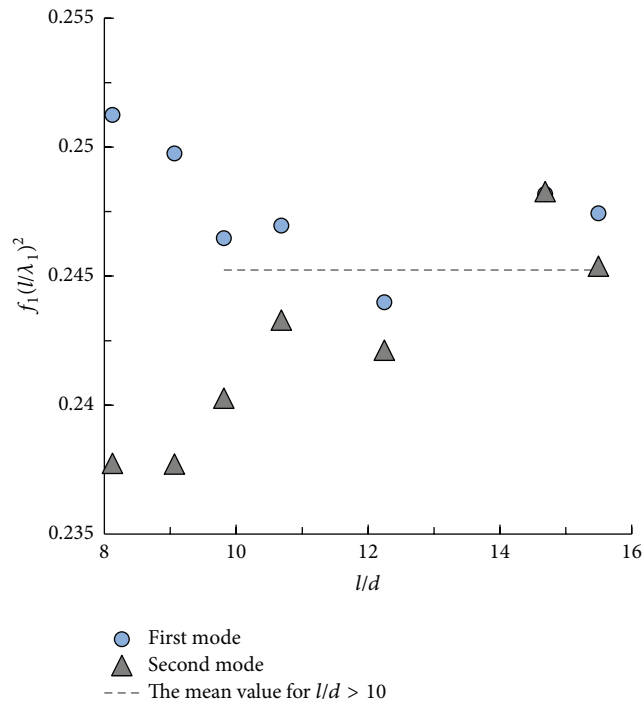


FIGURE 5: Plot of  $f_1(l/\lambda_1)^2$  versus  $l/d$  based on the flexural vibration test of a rectangular brass strip ( $d = 16.0$  mm and  $h = 1.5$  mm). For  $l/d \geq 10$ , the mean value 0.245 (broken line) is constant to within experimental uncertainty.

uses a rectangular beam, partially restrained at one end, flexural vibrations of which are detected with the aid of the force sensor. The relative experimental uncertainty is found to be less than 3%, which is mainly due to the uncertainty in the samples dimensions. The feasibility and accuracy of a new experimental procedure has been demonstrated by measuring the Young modulus for a number of test materials with different material properties. Comparison of obtained results with those accepted in the literature data is good. The relative deviation of measured values from the cited data is less than 5%. The method has potential advantages over other dynamic methods of being very simple and fast and requiring no additional equipment to excite resonance frequencies. It is particularly suitable for composite materials having a high

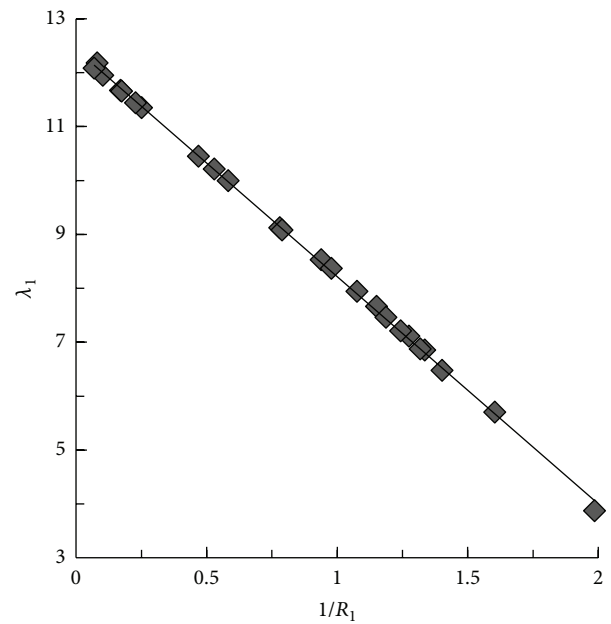


FIGURE 6: The modal number of the first mode of flexural vibrations of partially restrained cantilever beams in the fourth degree as a function of the inverse of the dimensionless frequency parameter,  $1/R_1$ . Symbols are experimental data taken from Tables 1 and 2. Solid line is by (19).

stiffness and low density, such as carbon fiber reinforced plastic. The accuracy can be significantly improved by more precise determination of specimen dimensions.

## Acknowledgment

This work was supported by the Ministry of Absorption and Immigration of Israel through the KAMEA Science Foundation.

## References

- [1] J. D. Lord and R. Morrell, "Elastic modulus measurement". Measurement good practice guide, No. 98," February 2007, <http://www.npl.co.uk/publications/guides/guides-by-title/>.

- [2] J. D. Lord, *Review of Methods and Analysis Software for the Determination of Modulus from Tensile Tests*, vol. 41, NPL Measurement Note MATC (MN), 2002.
- [3] P. E. Armstrong, *Measurement of Mechanical Properties, Techniques of Metals Research*, vol. 5, part 2 of Edited by R. F. Bunshan, John Wiley & Sons, New York, NY, USA, 1971.
- [4] M. Radovic, E. Lara-Curzio, and L. Riester, "Comparison of different experimental techniques for determination of elastic properties of solids," *Materials Science and Engineering A*, vol. 368, no. 1-2, pp. 56-70, 2004.
- [5] A. Wolfenden, Ed., *Dynamic Elastic Modulus Measurements in Materials*, American Society for Testing and Materials, 1990.
- [6] A. S. Birks and R. E. Green, *Nondestructive Testing Handbook*, vol. 7 of *Ultrasonic Testing*, American Society for Nondestructive Testing, 1991.
- [7] A. Migliori and J. L. Sarrao, *Resonant Ultrasound Spectroscopy: Applications to Physics, Materials Measurements and Nondestructive Evaluation*, John Wiley & Sons, New York, NY, USA, 1997.
- [8] A. Wolfenden, M. R. Harmouche, G. V. Blessing et al., "Dynamic Young's modulus measurements in metallic materials: results of an interlaboratory testing program," *Journal of Testing and Evaluation*, 1989.
- [9] G. Roebben, B. Bollen, A. Brebels, J. van Humbeeck, and O. van der Biest, "Impulse excitation apparatus to measure resonant frequencies, elastic moduli, and internal friction at room and high temperature," *Review of Scientific Instruments*, vol. 68, no. 12, pp. 4511-4515, 1997.
- [10] W. Lins, G. Kaindl, H. Peterlik, and K. Kromp, "A novel resonant beam technique to determine the elastic moduli in dependence on orientation and temperature up to 2000°C," *Review of Scientific Instruments*, vol. 70, no. 7, pp. 3052-3058, 1999.
- [11] K. Heritage, C. Frisby, and A. Wolfenden, "Impulse excitation technique for dynamic flexural measurements at moderate temperature," *Review of Scientific Instruments*, vol. 59, no. 6, pp. 973-974, 1988.
- [12] R. M. Digilov, "Flexural vibration test of a cantilever beam with a force sensor: fast determination of Young's modulus," *European Journal of Physics*, vol. 29, no. 3, p. 589, 2008.
- [13] American Society for Testing and Materials, "Standard test method for dynamic Young's modulus, Shear modulus, and poisson's ratio for advanced ceramics by impulse excitation of vibration," Standard C 1259-01, April 2001.
- [14] Comité Européen de Normalisation, "Determination of dynamic elastic modulus by measuring the fundamental resonant frequency," Standard EN 14146, 2004.
- [15] D. J. Inman, *Engineering Vibration*, Prentice-Hall, Englewood Cliffs, NJ, USA, 1994.
- [16] S. S. Rao, *Mechanical Vibrations*, Addison-Wesley, Menlo Park, Calif, USA, 3rd edition, 1995.
- [17] K. R. Chun, "Free vibration of a beam with one end spring-hinged and the other free," *ASME Journal of Applied Mechanics*, vol. 39, no. 4, pp. 1154-1155, 1972.
- [18] "Multilab software for MultiLogPRO," Fourier System, <http://fourieredu.com/>.
- [19] *Mathematica 7*, Wolfram Research, Champaign, Ill, USA, 2008.
- [20] J. R. Davis, Ed., *Metals Handbook*, ASM International, Materials Park, Ohio, USA, 1990.